Searches for New Physics in final states containing leptons, b-jets and $E_{\mathrm{T}}^{\mathrm{miss}}$ at the ATLAS detector

UNIVERSITY OF LIVERPOOL

Thesis submitted in accordance with the requirements of the University of Liverpool for the degree of Doctor in Philosophy by

Matthew James Sullivan

Department of Physics
Oliver Lodge Laboratory
University of Liverpool

February 2021

Abstract

This Thesis documents analyses targeting BSM processes in final states containing leptons, b-jets and missing transverse energy ($E_{\mathrm{T}}^{\mathrm{miss}}$) at the ATLAS detector, as well as studies relevant for the high luminosity upgrade of ATLAS.

The first analysis presented targets the pair-production of a supersymmetric chargino and next-to-lightest neutralino, decaying via a W boson and SM-like Higgs boson. This analysis used 36.1 fb^{-1} of ATLAS pp data taken between 2015-2016 at a centre-of-mass energy ($\sqrt{s}$) of 13 TeV, and placed exclusion limits on chargino/next-to-lightest neutralino masses up to 550 GeV for a massless neutralino [1]. An updated search is also presented, using 139 fb^{-1} data taken between 2015-2018, extending the sensitivity up to chargino/next-to-lightest neutralino masses up to 740 GeV [2]. Preliminary studies using machine learning classifiers to select this signal from the dominant Standard Model backgrounds are presented, showing promising classification performance.

In addition, a search for dark matter produced in association with a single top quark is presented. The result of this analysis is interpreted in the context of an extended Higgs sector model, where a pseudoscalar mediator couples the dark matter to the Higgs sector. The analysis used 139 fb^{-1} of data taken between 2015-2018, collected at $\sqrt{s} = 13$ TeV. The process was excluded for charged Higgs masses, originating from an extended Higgs sector New Physics model, up to 1250 GeV for a mediator mass of 100 GeV. The complimentary sensitivity of this analysis to dark matter produced in association with both a single top quark or a pair of top quarks was evaluated, excluding charged Higgs masses up to 1400 GeV [3].

Finally, work performed for the upcoming luminosity upgrade is presented. Performance studies of pixel modules for the ATLAS inner tracker are shown using data collected in test beams at DESY. The sensitivity to chargino/next-to-lightest neutralino pair-production at the upgraded ATLAS detector is evaluated using the expected dataset of 3000 fb^{-1} taken at $\sqrt{s} = 14$ TeV. Using machine learning classifiers, the expected exclusion limits on the chargino/next-to-lightest neutralino are set at 1280 GeV for a massless neutralino [4].

Declaration

I hereby confirm this work is my own, except where other works are referenced. This work has not previously been submitted to any institute, including this one. This thesis does not exceed the relevant word count.

Matthew James Sullivan

Acknowledgements

During my eight years at the University of Liverpool, the people helping to make it such a memorable period of my life have become innumerable, and to thank each and every person would require an equally long period of time. For those not acknowledged by name I can only give my thanks for being involved in this part of my life. It has been a true privilege to call this city my home and be a part of the Department of Physics throughout.

The first of many thanks goes to my mum, my dad and my sister, for their endless and unwavering support throughout my PhD. The level of support you all offer continues to astound me and I can only offer my gratitude in return. An honourable mention must go to my niece, Charlotte, who was born halfway through my PhD and has been the best niece one could ask for, although these words are, for now, lost on you.

Secondly, many thanks are owed to the non-physics friends, who have given me respite from the challenges of my PhD. Particularly, Holly, Brad, Pete, Alex, Ellie and Sean, who have supported and encouraged me through challenging professional and personal times. Your continued reminder to write this Thesis, however, is unforgiveable. Additionally, a big thanks to Hannah, who for the last ten years has been putting up with my nonsense, and hopefully will continue to do so. I hope over time I can begin to pay back the levels of support you have all given me.

These acknowledgements would be incomplete without a mention to the circumstances within which a large portion of it was written. The COVID-19 pandemic has had a devastating impact on individuals and families the world-over, causing both physical and mental struggle. On a personal level, numerous thanks are owed for enabling me to submit this work in this turbulent time. Firstly, to UKRI, for their generous financial support, enabling me to continue my work during these challenging times. Secondly, thanks are owed to the NHS, both due to their handling of the national crisis and for their continued healthcare support during, undoubtedly, the most stressful period of my life. However, the period of national lockdown due to the coronavirus has also provided unforeseen opportunities for personal development, and I submit this work having gained far more than anticipated. Countless thanks are owed to Jess, for managing to keep my stress-levels under control, for

the walks, the talks and the laughs. Without you, this work would have been submitted in a much heavier fashion.

Of course, many thanks are owed to the physics community within which I have been immersed. Firstly, to the Liverpool ATLAS group, who welcomed me into the collaboration in 2016 and have supported me throughout my PhD. The group, and the department, provided me with some incredible opportunities, for which I am extremely grateful. Secondly, to all of the physics friends, who have listened to my rants, help spot the bugs I couldn't find, and bluntly point out when I'm being stupid. Special thanks must go to James, Chips and Lauren for dealing with me when at my most difficult, and for the frequent trips to the pub, both in Liverpool and Geneva.

Finally, to my excellent supervisors, Monica D'Onofrio and Yanyan Gao. You have pushed me to levels beyond what I imagined I could achieve and have given me amazing opportunities for professional development. I can only apologise for being slow and stupid, and am extremely grateful for your patience in supervision.

Contents

List of Figures

List of Tables

Introduction

Since its inception the Standard Model (SM) of particle physics has withstood huge amounts of experimental scrutiny. The SM provides a mathematical framework in which to describe *all* non-gravitational interactions of the known fundamental particles. With the discovery of the Higgs boson, a cornerstone of the SM, by the ATLAS and CMS collaborations in 2012 [5, 6], the SM is complete.

While one cannot detract from the success of the SM's description of physics at the smallest scales, there are numerous open questions which have not yet been answered. The reconciliation of gravity with physics at the subatomic scale, the hierarchy problem, astrophysical evidence of dark matter, and the matter-antimatter asymmetry require explanations from physics Beyond the Standard Model (BSM). The experiments at the Large Hadron Collider (LHC) have a broad programme of direct and indirect searches for BSM physics. Aiding in this is the LHC itself, providing pp collisions at $\sqrt{s} = 13$ TeV at luminosities around $10^{34}\text{cm}^2\text{s}^{-1}$. The huge datasets collected by both ATLAS and CMS, afforded by the LHC and its excellent performance, provide an ideal environment for BSM searches.

The physics analyses presented in this Thesis target two BSM scenarios; searches for Supersymmetry (SUSY) and searches for Dark Matter (DM) production. In both scenarios, the SM Higgs sector is extended to include an additional Higgs doublet, hence these models being known as Two Higgs Doublet models (2HDM). SUSY extends the SM with an additional symmetry in which particles gain 'superpartners', particles which differ in spin by 1/2 from their SM counterpart. The superpartners to the SM gauge bosons and Higgs mix and form a rich particle spectrum containing charged and neutral states, known as charginos and neutralinos. The lightest supersymmetric particle (LSP), in this case the lightest neutralino, is a leading candidate for DM. A search for the weak production of SUSY particles, specifically a chargino-neutralino pair, decaying to the supersymmetric DM candidate is performed, through decays involving the SM Higgs and W boson. Aside from SUSY, by adding a pseudoscalar mediator, a, to a 2HDM model, DM can couple to the SM extended Higgs sector leading to a rich array of final states. The associated production of DM with a single top quark, a previously experimentally-uncovered final state, is studied in the context of the 2HDM+a model.

Both BSM scenarios studied in this Thesis are experimentally-challenging, due to the low rate of new particle production when compared to irreducible SM processes. Advanced signal selection techniques using machine learning (ML) methods are studied, enabling the efficient selection of signal while substantially rejecting the SM background. The upcoming High-Luminosity upgrade of the LHC and ATLAS will provide the opportunity to probe many BSM scenarios to levels never before possible, with an expected dataset of 3000 fb^{-1} being collected by ATLAS by the end of operations. To prepare for the HL-LHC phase of operation, ATLAS will undergo a major upgrade of many detector components. The ATLAS inner tracker (ITk) will provide high-precision tracking in conditions where as many as 200 inelastic proton-proton collisions are expected in each bunch-crossing. The efficiency of the pixel modules of the ITk are studied after being irradiated to the expected HL-LHC dose. Combining ML methods with the huge High Luminosity (HL) ATLAS dataset, the sensitivity to SUSY at the High-Luminosity LHC (HL-LHC) is also studied.

Part I provides an overall introduction in the context of physics models and the experimental setup. First, a theoretical overview of the SM is given, motivates the need for BSM physics, and then gives an overview of SUSY and the 2HDM+a model of DM production. It also gives a brief description of the LHC along with an overview of the ATLAS detector. Finally, the datasets used in this thesis are discussed, along with discussion of the simulation methods and object definitions used in the subsequent Chapters.

Part II describes the core work of this Thesis, encompassing three analyses using pp data at $\sqrt{s} = 13$ TeV, presented in separate Chapters. Chapter 6 presents a search for electroweak SUSY using 36.1fb^{-1} data and subsequently 139fb^{-1}. Chapter 7 presents a search for DM production in association with a single top quark using 139fb^{-1} data.

Part III presents studies and work relevant for the HL-LHC phase. Chapter 9 illustrates the prospect for a search for the electroweak production of SUSY particles using 3000fb^{-1}data at $\sqrt{s} = 14$ TeV. Chapter 8 presents work done on the studying the performance of hybrid pixel modules for upcoming upgrade for the HL-LHC.

Part I

Theoretical overview and experimental apparatus

Chapter 1

The Standard Model and Beyond

This chapter presents an overview of the Standard Model (SM), along with the extensions to it which form the basis of the analyses in Chapters 6 and 7. The SM is currently our best description of physics at the smallest scales but does not give a complete description of some fundamental physical phenomena, which motivates searches for physics beyond the SM (BSM).

1.1 The Standard Model

The SM is the name given to the theory describing the fundamentals of particle interactions. Since its inception over half a century ago, it has withstood experimental scrutiny, each time providing a theoretical description of experimental data. The particle content of the SM was deemed complete in 2012, with the discovery of a particle consistent with the Higgs boson by the ATLAS [5] and CMS [6] collaborations.

The SM describes matter in terms of quarks and leptons and their interactions via three of the four fundamental forces through the exchange of force-carriers known as bosons. As alluded to at the beginning of this Chapter, the SM provides an incomplete description of physics at the smallest scales, which will be discussed later in this Chapter.

1.1.1 Overview

The SM particles are easily separable into two categories; fermions, which obey Fermi-Dirac statistics and have half-integer spin, and bosons, which obey Bose-Einstein statistics and have integer spin.

The fermions are further separable into two families, quarks and leptons, both of which have three generations. The quarks can be separated into 'up-type' and 'down-type', having electric charge $+\frac{2}{3}$ and $-\frac{1}{3}$, respectively. The 'up-type' quarks are the up (u), charm (c)

and top (t) quarks, while the 'down-type' quarks are the down (d), strange (s) and bottom (b). The leptons can be separated into charged leptons and neutral leptons (known as neutrinos), with the charged leptons having an electric charge of -1. The charged leptons are the electron (e), the muon (μ) and the tau (τ), with a corresponding electron neutrino (ν_e), muon neutrino (ν_μ) and tau neutrino (ν_τ). The three generations of fermions are ordered in increasing mass, with the first generation containing the up and down quarks, the electron and its corresponding neutrino, the former three of which combine to make up everyday matter. In the SM neutrinos do not have mass, but experimental evidence of neutrino flavour oscillations [7] implies that neutrinos are in fact massive, although their mass hierarchy is not yet clear [8].

Composite particles can be formed from combinations of quarks when they undergo hadronisation. 'Hadrons' are defined as bound states of quarks, with mesons being formed from pairs of quarks and baryons being formed by three quarks. In recent years, more exotic bound states of quarks, such as tetra-quarks [9, 10] and penta-quarks [11, 12] have been observed by the LHCb collaboration. All quarks except the top quark undergo hadronisation after a period of time. The top quark, which has a much larger mass than the other quarks, has a lifetime around $\tau_t = 10^{-25}$ s and as such decays via the weak force before it can hadronise. The first generation quarks, i.e. the up quark and down quark, can be combined to produce protons (uud) and neutrons (udd). Combining protons and neutrons with the first generation charged lepton, the electron, we give rise to nuclear physics and all *visible* matter in our universe.

The SM bosons are responsible for the interactions of the SM particles. Electromagnetic interactions are mediated by the massless photon (γ), and only occur between electrically-charged particles. Gluons (g), massless and electrically-neutral bosons, mediate the interactions between quarks, which carry the colour charge. The $W^\pm$ and Z^0 bosons mediate the weak interaction, which all SM fermions are subject to. Both the $W^\pm$ and Z^0 bosons are massive, and acquire their mass through the spontaneous breaking of the electroweak symmetry, as discussed later in this Chapter.

The particle content of the SM is summarised in Table 1.1.

1.1.2 Mathematical formulation of the SM

The SM is a quantum field theory (QFT) based upon the product of symmetry groups:

$$\mathrm{SU}(3)_C \times \mathrm{SU}(2)_L \times \mathrm{U}(1)_Y \tag{1.1.1}$$

Name	Symbol	Charge (e)	Spin	Mass
Fermions - Generation-I				
Up-quark	u	$+2/3$	$1/2$	2.16 MeV
Down-quark	d	$-1/3$	$1/2$	4.67 MeV
Electron	e	-1	$1/2$	0.511 MeV
Electron-neutrino	ν_e	0	$1/2$	< 2 eV
Fermions - Generation-II				
Charm-quark	c	$+2/3$	$1/2$	1.27 GeV
Strange-quark	s	$-1/3$	$1/2$	93 MeV
Muon	μ	-1	$1/2$	105.66 MeV
Muon-neutrino	ν_μ	0	$1/2$	< 2 eV
Fermions - Generation-III				
Top-quark	t	$+2/3$	$1/2$	172.9 GeV
Bottom-quark	b	$-1/3$	$1/2$	4.18 GeV
Tau	τ	-1	$1/2$	1.78 GeV
Tau-neutrino	ν_τ	0	$1/2$	< 2 eV
Bosons				
W boson	$W^\pm$	± 1	1	80.4 GeV
Z boson	Z	0	1	91.2 GeV
Gluon	g	0	1	0
Photon	γ	0	1	0
Higgs boson	H	0	0	125.1 GeV

Table 1.1: A table describing the charge, mass and spin of the SM particles. Particle masses taken from [13].

The $\mathrm{SU}(3)_C$ component describes strong interactions, the $\mathrm{SU}(2)_L$ component describes the electroweak sector and $\mathrm{U}(1)_Y$ describes electromagnetic interactions.

In order to understand the mathematical formulation of the SM, the concepts of *groups* will be briefly discussed, following the discussion in Ref [14]. A group is a set of mathematical objects, G, along with an operation, which obey the following 'axioms' [15]:

- *Closure*: For all $a, b \in G$, $a \cdot b \in G$
- *Associativity*: For all a, b and $c \in G$, $(a \cdot b) \cdot c = a \cdot (b \cdot c)$
- *Identity element*: An identity element, I, exists such that $I \cdot a = a \cdot I = a$
- *Inverse element*: An inverse element of a, a^{-1}, exists such that $a \cdot a^{-1} = a^{-1} \cdot a = I$

The generating set of a group is a subset of the elements of the group which under repeated application of the operator generate all of the elements of the group. The commutation relations of the members of a group are important to know. As a reminder, the commutator of two elements of a group, a, b is defined as:

$$[a, b] = (a \cdot b - b \cdot a) \tag{1.1.2}$$

Groups where the commutator of any two elements is always 0 are known as 'abelian', while groups where this does not hold are called 'non-abelian'. Abelian groups have n^2 generators, while non-abelian groups have $n^2 - 1$. While this seems conceptually-abstract, the number of generators of a group physically corresponds to the number of 'force-carriers' present in a theory governed by that group.

In Equation 1.1.1, U(n) and SU(n) refer to unitary groups and special unitary groups, respectively. U(n) is the set of $n \times n$ unitary matrices ($U \cdot U^{-1} = I$), and SU(n) the subset of U(n) which have a determinant of 1. The individual symmetry groups will be discussed in more details in the following sections, starting with electromagnetic interactions and the U(1) group.

Quantum Electrodynamics

Electromagnetic interactions are described by Quantum Electrodynamics (QED). These interactions are unique in the SM, as they have infinite range. We will derive the Lagrangian describing QED, starting from the Dirac equation for free fermions:

$$\mathcal{L}_{\text{Dirac}} = \bar{\psi}(i\gamma^\mu \partial_\mu - m)\psi \tag{1.1.3}$$

Due to the U(1) symmetry, QED is symmetric under *global* phase transformations of the form:

$$\psi(x) \to \psi'(x) = e^{i\alpha}\psi(x),\ \bar{\psi}(x) \to \bar{\psi}'(x) = e^{-i\alpha}\bar{\psi}(x) \tag{1.1.4}$$

Under *local* transformations, where $\alpha \to \alpha(x)$, the Lagrangian in Equation 1.1.3 is not gauge invariant:

$$i\bar{\psi}'\gamma^\mu \partial_\mu \psi' = i\bar{\psi}\gamma^\mu \partial_\mu \psi - \bar{\psi}\gamma^\mu \left(\partial_\mu \alpha\right)\psi \tag{1.1.5}$$

To resolve this, we define the covariant derivative:

$$D_\mu \equiv \partial_\mu + ieA_\mu \tag{1.1.6}$$

Note, with the introduction of the covariant derivative comes the introduction of the vector field, A_μ, which transforms as:

$$A_\mu \to A'_\mu = A_\mu - \frac{1}{e}\partial_\mu \alpha(x) \tag{1.1.7}$$

The result of a local transformation on the Dirac equation is now:

$$i\bar{\psi}'\gamma^\mu D'_\mu \psi' - m\bar{\psi}'\psi' = i\bar{\psi}\gamma^\mu \partial_\mu \psi - \bar{\psi}\gamma^\mu e A_\mu \psi - m\bar{\psi}\psi \tag{1.1.8}$$

Rearranging Equation 1.1.6 for ∂_μ and substituting in, we see local gauge invariance holds thanks to the introduction of the covariant derivative. Of particular interest is the term $\bar{\psi}\gamma^\mu e A_\mu \psi$, which couples the fermion fields to the vector field, which we associate to the photon, γ, with the coupling constant e corresponding to the electrical charge of the fermion. To complete the QED Lagrangian, one must add the electromagnetic Lagrangian to the Dirac Lagrangian. (For concision, we now adopt the Feynman 'slash' notation: $\not{\partial} = \gamma^\mu \partial_\mu$).

$$\mathcal{L}_{QED} = \mathcal{L}_{Dirac} + \mathcal{L}_{EM} = \bar{\psi}(i\not{D} - m)\psi - \frac{1}{4}F^{\mu\nu}F_{\mu\nu} \tag{1.1.9}$$

As the interaction term, introduced by using the covariant derivative, couples fermions to the photon with a coupling e, QED interactions are only relevant for electrically-charged fermions. The strength of the interaction is not a constant but in fact increases with momentum transfer, Q^2, or at small distances. This is known as a running coupling. Figure 1.1 shows the QED interaction vertex.

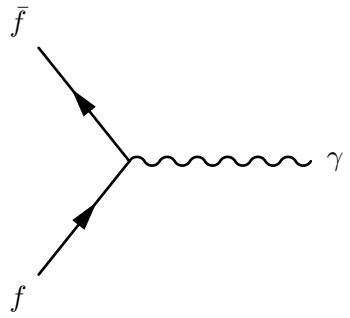

Figure 1.1: Feynman diagram showing the QED interaction vertex between a fermion and the photon.

Quantum Chromodynamics

Quantum Chromodynamics (QCD) addresses the interactions between quarks and gluons. It is governed by the $\mathrm{SU}(3)_C$ symmetry hence having $N_C^2 - 1 = 8$ mediators. By virtue of the symmetry group being a *special* unitary group, the theory is non-abelian, resulting in gluons being able to self-interact. Similarly to QED, we begin from the Dirac Lagrangian

and introduce a covariant derivative, in this case defined as:

$$\partial^\mu \Rightarrow D^\mu \equiv \partial^\mu \delta_{ij} - i g_s t^a_{ij} G^{a\mu} \tag{1.1.10}$$

where δ_{ij} is the Kroenecker delta (0 for $i \neq j$, 1 for $i = j$), g_s the strong coupling constant, $t^a = \frac{\lambda^a}{2}$ the generators of the SU(3)$_C$ symmetry group with λ^a being the Gell-Mann matrices and G^a being the gluon gauge fields. Using the covariant derivative from Equation 1.1.10, the Dirac equation from Equation 1.1.3 can be rewritten for QCD as

$$\mathcal{L}_{QCD} = \bar{\psi}_j (i\gamma_\mu \partial^\mu \delta_{ij} - m\delta_{ij})\psi_i - g_s(\bar{\psi}_j \gamma_\mu t^a_{ij} \psi_i) G^{a\mu} \,, \tag{1.1.11}$$

where i and j index the quarks from 1 to 3 and a indexes the gluons from 1 to 8. Adding in the kinetic term for the gluon fields and again using the Feynman slash notation, the full QCD Lagrangian is:

$$\mathcal{L}_{QCD} = \bar{\psi}(i\not{D} - m)\psi - \frac{1}{4} G^{\mu\nu}_a G^a_{\mu\nu} \tag{1.1.12}$$

Equation 1.1.12 is helpful to understand the gluon self-interaction, with 3-gluon and 4-gluon interactions present in the expansion of the $G^a_{\mu\nu} G^{\mu\nu}_a$. The gauge coupling of QCD

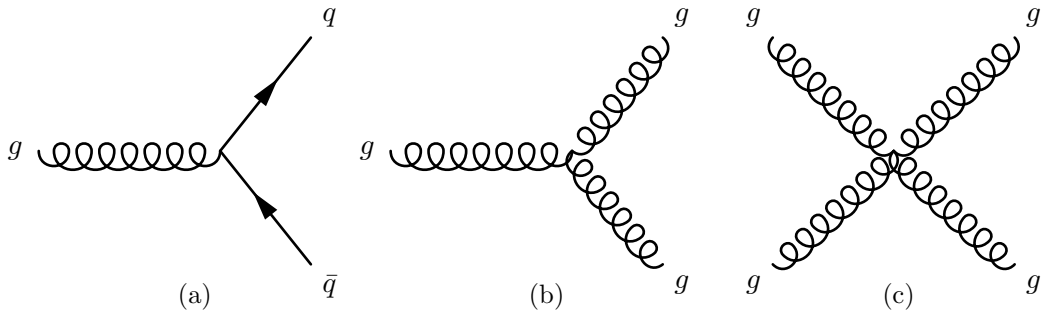

Figure 1.2: Feynman diagram showing the QCD quark-gluon interaction vertex (a), the triple gluon self-interaction (b) and the quartic gluon self-interaction (c).

depends upon the momentum transfer of a process, Q^2, as follows:

$$g_s(Q^2) = \frac{4\pi}{\beta_0 \ln\left(\frac{Q^2}{\Lambda^2_{\mathrm{QCD}}}\right)} \tag{1.1.13}$$

The Q^2 dependence of α_s means the coupling strength "runs" depending on the momentum transfer. At large Q^2, which corresponds to the high-energy or short-distance regime, quarks and gluons are treated as free particles. In this regime, perturbative QCD (pQCD) calculations can be used to make very accurate predictions. In pQCD, calculations proceed by performing a series expansion in α_s, where higher-order terms correspond to the contribution from Feynman diagrams with additional QCD vertices. Ultraviolet (UV) divergences can arise from internal loops in higher-order Feynman diagrams, which requires

the introduction of the *renormalisation scale*, μ_R, at which α_s is calculated. This means the evaluation of α_s is dependent upon μ_R, which is typically set to the mass of the Z boson, m_Z, at which the strong coupling has a value of 0.118.

In the low-energy limit, $Q^2 \rightarrow \Lambda^2_{\text{QCD}}$, where Λ^2_{QCD} is the energy at which quarks and gluons hadronise, known as the *hadronisation scale*, the strong coupling tends to infinity and hence perturbative calculations can no longer be used. This results in quarks being bound together into colour-neutral hadrons, a phenomena known as *colour confinement*. When the separation of a quark-antiquark pair is increased, so does the energy of the strong interaction between them. With increasing separation, it eventually becomes energetically-favourable to produce another quark-antiquark pair. This quark-antiquark pair forms colourless, bound states with the initial quark-antiquark pair. An additional result of colour confinement is that the range of the strong force is extremely short, around 1fm.

Weak interaction and Electroweak unification

The third force described by the SM is the weak interaction, which describes interactions between the left-handed fermions and is described by the $\text{SU}(2)_L$ symmetry group. It is therefore expected that the weak interaction has 3 mediators (from $N^2 - 1$); W^1_μ, W^2_μ and W^3_μ. The weak interaction also introduces new quantum numbers known as weak isospin, T, as well as its third component T_3. With these quantum numbers, we can define weak isospin doublets, using the first generation leptons and quarks as examples:

$$\begin{pmatrix} \nu_L \\ e_L \end{pmatrix} ; \begin{pmatrix} u_L \\ d_L \end{pmatrix} \tag{1.1.14}$$

Both of the weak isospin doublets shown in Equation 1.1.14 have $T = \frac{1}{2}$, with the fermion in the 'upper' position having $T_3 = +\frac{1}{2}$ and the fermion in the 'lower' position having $T_3 = -\frac{1}{2}$.

An extremely important concept for understanding the weak interaction is chirality. Chirality is an intrinsic property of particles, and determines how they behave in the weak interaction. The subscript 'L' is present as only fermions with 'left-handed' chirality (anti-fermions with 'right-handed' chirality) interact via the weak interaction. 'Left-handed' fermions, and 'right-handed' anti-fermions have $T = \frac{1}{2}$ and hence form isospin doublets, whereas 'right-handed' fermions and 'left-handed' anti-fermions have $T = 0$ and hence are isospin singlets.

The introduction of weak isospin doublets enables a mechanism for quarks to change flavour

through a charged-current interaction. For example, a 'down-type' quark can change into an 'up-type' quark through a transition of T_3. The Cabibbo-Kobayashi-Maskawa matrix, known as the CKM matrix, determines the probability of a quark, q, to transition to another flavour.

$$\begin{pmatrix} d' \\ s' \\ b' \end{pmatrix} = \begin{pmatrix} |V_{ud}| & |V_{us}| & |V_{ub}| \\ |V_{cd}| & |V_{cs}| & |V_{cb}| \\ |V_{td}| & |V_{ts}| & |V_{tb}| \end{pmatrix} \begin{pmatrix} d \\ s \\ b \end{pmatrix} \tag{1.1.15}$$

The CKM matrix has on-diagonal elements being close to one, while the off-diagonal elements can be as large as around 0.2. Therefore, the most probable quark flavour transitions are intra-generational, but inter-generation transitions are allowed.

It was shown by Glashow, Salam and Weinberg that the interaction can be unified with the electromagnetic interaction, with an overall symmetry group of $\mathrm{SU}(2)_L \times \mathrm{U}(1)_Y$. We now introduce the weak hypercharge, $Y = 2(Q - T_3)$, where Q is the electric charge. At low energies, the electromagnetic and weak interactions independently explain physical phenomena, such as hyperfine splitting and β decay in nuclei. The unification of these two interactions into the electroweak interaction must therefore preserve the two separate interactions at low energy. However, above the 'unification energy', the two separate interactions are merged into one. This new, unified interactions has four mediators; two massive, charged $W^{\pm}$ bosons, a massive, neutral Z and the massless, neutral γ. The interaction vertices of the three massive electroweak gauge bosons are shown in Figure 1.3. Note, Figure 1.3b shows the interaction of only the negatively-charged W boson interacting with leptons. The $\mathrm{SU}(2)_L \times \mathrm{U}(1)_Y$ symmetry group is non-abelian, and thus the

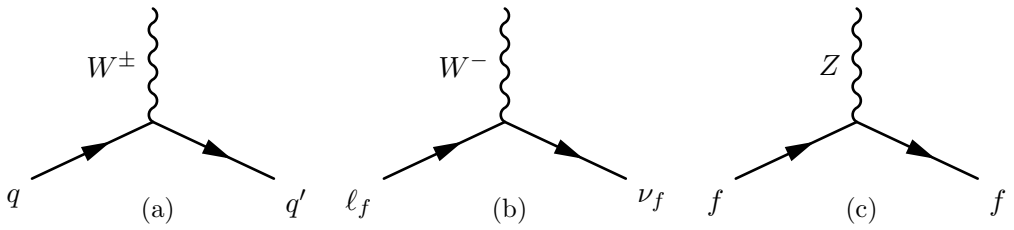

Figure 1.3: Feynman diagrams showing the massive electroweak gauge bosons fermion interaction vertices. Note, as shown in (b), only the W^- couples to the lepton isospin doublet, whereas for the quark isospin doublets (a) both the $W^{\pm}$ are involved.

electroweak gauge bosons can self-interact. Similarly to gluons in QCD, there are triple and quartic self-couplings; $W^{\pm}W^{\mp}Z/\gamma$, $W^{\pm}W^{\mp}Z/\gamma Z\gamma$ and $WWWW$.

As discussed previously, to ensure local gauge invariance of the SM electroweak Lagrangian,

we define the covariant derivative

$$\partial_\mu \rightarrow D_\mu \equiv \partial_\mu + \frac{i}{2} g \vec{\tau} \cdot \vec{W}_\mu + i g' \frac{Y}{2} B_\mu \, , \tag{1.1.16}$$

where $\vec{W}_\mu$ and B_μ are the gauge fields corresponding to the massless $W^{1,2,3}$ and B bosons, and g and g' are the couplings, of the $\mathrm{SU}(2)_L$ and $\mathrm{U}(1)_Y$ symmetries, respectively. The $W^{1,2,3}$ and B bosons must be massless, as the introduction of a mass term to the Lagrangian would violate gauge invariance. As the electroweak interaction only couples to 'left-handed' fermions, we can define projection operators, which project out the left- and right-handed components of a field:

$$P_L = \frac{1}{2}(1 - \gamma^5); P_R = \frac{1}{2}(1 + \gamma^5); \gamma^5 \equiv \begin{pmatrix} 0 & I_2 \\ I_2 & 0 \end{pmatrix} \tag{1.1.17}$$

We are then able to write the fermion field as $\psi = P_L\psi + P_R\psi = \psi_L + \psi_R$. The mass term in the Lagrangian, $m\bar{\psi}\psi$, now expands as:

$$m\bar{\psi}\psi = m\bar{\psi}_R\psi_L + m\bar{\psi}_L\psi_R \tag{1.1.18}$$

The left- and right-handed components of the fermion field, ψ, transform differently under the $\mathrm{SU}(2)_L \times \mathrm{U}(1)_Y$ symmetry and therefore the mass term in Equation 1.1.18 breaks local gauge symmetry. Therefore, we need to introduce a mechanism by which fermions, and also the electroweak gauge bosons, become massive.

The Higgs sector

The discovery of the $W^\pm$ bosons [16, 17] and Z boson [18, 19] happened in 1983 with masses around $m_W \sim 80$ GeV and $m_Z \sim 91$ GeV, proving there was a mechanism through which the gauge bosons acquire mass. The Higgs mechanism, first proposed in the 1960's, provided such a mechanism by introducing an $\mathrm{SU}(2)_L$ doublet of complex, scalar fields:

$$\Phi = \begin{pmatrix} \phi^+ \\ \phi^0 \end{pmatrix} = \frac{1}{\sqrt{2}} \begin{pmatrix} \phi_1 + i\phi_2 \\ \phi_3 + i\phi_4 \end{pmatrix} \tag{1.1.19}$$

This doublet has isospin $T = \frac{1}{2}$ and hypercharge $Y = 1$. This field has a scalar potential defined as:

$$V(\Phi) = \mu^2 \Phi^\dagger \Phi + \lambda (\Phi^\dagger \Phi)^2 \tag{1.1.20}$$

The two terms in Equation 1.1.20 can be identified as a mass term for the scalar boson and a self-interaction term, respectively. Dependent upon the choices for μ^2 ($\lambda > 0$), the potential can take on two shapes; parabolic for $\mu^2 > 0$ and a 'wine bottle' potential for

$\mu^2 < 0$. For reasons discussed later, the Higgs potential has $\mu^2 < 0$, and the shape of this potential is shown in Figure 1.4. The potential shown in Figure 1.4 evidently has a local

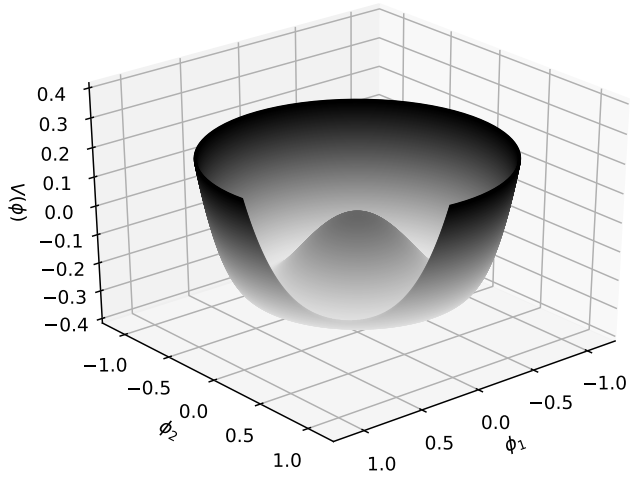

Figure 1.4: Schematic diagram showing the shape of the Higgs potential, known as the 'Mexican hat' potential.

minima at ϕ_1, $\phi_2 = 0$. However, the global minima is at non-zero values of ϕ, and is given by:

$$\phi_{min} = \sqrt{-\frac{\mu^2}{2\lambda}} \tag{1.1.21}$$

We define $v^2 = \mu^2/\lambda$, where v is the vacuum expectation value (VEV) of the the Higgs field, at ≈ 246 GeV. It is convenient to choose the VEVs of three of the four ϕ to zero, while the remaining field, conventionally ϕ_3, is given by:

$$\langle 0|\phi_3|0\rangle^2 = v^2 = \frac{\mu^2}{\lambda} \tag{1.1.22}$$

The choice for the spontaneous symmetry breaking to be done with the field ϕ_3 is to allow the photon to remain massless. Expanding the Higgs field around the minima with $\phi_3 = h + v$, we eventually acquire a term for the Higgs mass of $m_H = \sqrt{-2\mu^2}$. Inserting this field into 1.1.16, we obtain the mass terms for the electoweak gauge bosons:

$$\begin{aligned} m_W &= \frac{1}{2}gv \\ m_Z &= \frac{1}{2}\sqrt{g^2 + g'^2}\, v \\ m_\gamma &= 0 \end{aligned} \tag{1.1.23}$$

In Equation 1.1.23, g and g' are the coupling constants for the SU(2) and U(1) interactions, respectively, and are related to each other by $g \sin\theta_w = g' \cos\theta_w$, where θ_w is the weak mixing angle. The Higgs Lagrangian contains couplings to not only the electroweak gauge bosons but also the SM fermions. The strength of the couplings to the fermions are given by y_f, known as *Yukawa couplings*. This coupling enables the fermions to acquire masses in a gauge-invariant way through the Higgs mechanism. The mass of a fermion, f, is given by:

$$m_f = y_f \frac{v}{\sqrt{2}} \,. \tag{1.1.24}$$

Fermion masses are experimentally-determined, hence determining the Yukawa coupling of the Higgs to that fermion. The interactions of the Higgs with the electoweak gauge bosons and SM fermions are shown in Figure 1.5. The Higgs decay branching ratios (BR) depends

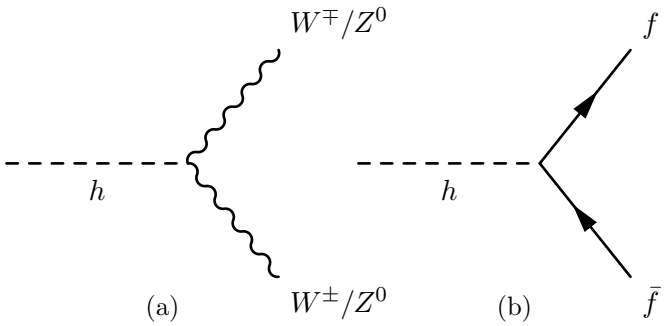

Figure 1.5: Feynman diagrams showing the Higgs interaction vertices with the electroweak gauge bosons (1.5a) and SM fermions (1.5b).

both upon the Higgs mass and the Yukawa coupling of the Higgs to the SM particles. Figure 1.6 shows the Higgs BRs for a SM Higgs boson with a mass in the range, 120-130 GeV. The largest Higgs BR is to a $b\bar{b}$-pair, which is important for the analyses detailed in Chapters 6 and 9.

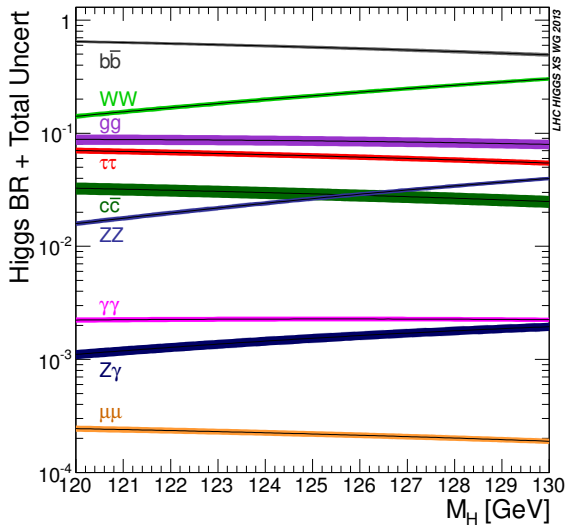

Figure 1.6: This plot shows the branching ratios of the SM Higgs decaying to SM particles in the mass range 120-130 GeV. [20]

1.2 Open questions in the SM

The first of the open questions to be discussed is the hierarchy problem. While the SM does not account for gravitational interactions, it is impossible to have a complete description of nature without its inclusion. The hierarchy problem arises when considering a unified theoretical description of all four, fundamental forces. Gravity is expected to become the dominant interaction at the Planck scale, which has an equivalent mass of $O(10^{19})$ GeV. This is 17 orders of magnitude higher than the electroweak scale and the Higgs mass, $O(10^2)$ GeV.

The Higgs mass consists of two terms; a 'bare' mass and the sum of the virtual corrections from particles coupling to the Higgs. We treat the Planck scale, Λ_P, as a cut-off value for the virtual contributions. Therefore, the physical Higgs mass can be written as:

$$m_H^2 = m_{H,\text{bare}}^2 + \delta m_H^2 = m_{H,\text{bare}}^2 - \frac{|g_f|^2}{8\pi^2}\Lambda_p^2 + \dots \tag{1.2.1}$$

Here, the neglected terms grows logarithmically in Λ_p. Assuming the SM is indeed valid upto the Planck scale, then the second term is $O(10^{19}\text{GeV})^2$, requiring an equally-large (to 1 part in over 10^{30} orders of magnitude) bare Higgs mass. While this in itself is not an issue with the SM, the amount of 'fine-tuning' required to give a 125 GeV Higgs boson mass is extremely large and for many physicists is deemed too large to attribute to a coincidence. The Anthropic Principle is sometimes invoked to justify this [21], while extensions to the SM such as Supersymmetry (SUSY) provide elegant, mathematical solutions to the hierarchy problem.

Within the SM, neutrinos do not have mass, but experimental observation of neutrino oscillations implies that they do have mass, and that each neutrino flavour is a mixture of the mass eigenstates. The SM includes only left-handed neutrinos, as described previously, while all other fermions are present in both left-handed and right-handed spinors. Neutrino mass may be explained by the presence of right-handed neutrinos which the SM does not include. Through the see-saw mechanism, right-handed neutrinos may also provide resolution to the unnaturally-small neutrino masses, orders of magnitude smaller than the other fermions [22]. Alternatively, neutrinos may be Majorana fermions, particles which are their own antiparticle [22]. The origin of neutrino masses and the question of why their mass is so small require explanation from BSM physics.

On larger scales, there are two troubling issues with the SM. Firstly, the SM predicts that at the Big Bang, the creation of the Universe, matter and antimatter should have been produced in equal quantity. If this were indeed true, the matter and antimatter should have all annihilated into photons ($f\bar{f} \to \gamma$), leaving a radiation dominated universe devoid of matter. However, at the present day, we can see this is not true. The Sakharov conditions [23] enable the necessary excess of baryons over antibaryons, to be produced, known as baryogenesis. The conditions state that a process can result in a matter-antimatter asymmetry if it violates baryon-number conservation, charge symmetry (C) and charge-parity (CP) symmetry. In the SM, CP violation is allowed to occur through the complex phase of the CKM matrix, but the amount of CP violation in the SM does not explain the universal imbalance. BSM models such as SUSY and GUTs can provide additional particles which satisfy the Sakharov conditions, hence explaining the matter-antimatter asymmetry.

Observations of anomalous gravitational behaviour, such as in the rotational curves of galaxies, enable us to infer the existence of DM. Since we do not *visibly* observe DM, it is inferred that DM does not interact electromagnetically, therefore being electrically-neutral. It is also required for DM to be stable, as its effects are observed from the early universe in the cosmic microwave background (CMB), the residual radiation from the Big Bang, until now.

Recent measurements of the DM abundance estimate that $\Omega_{DM}h^2 = 0.1200 \pm 0.0012$ [13], meaning that DM makes up as much as 26% of the universe. The only DM candidate within the SM are neutrinos as they are massive (inferred from neutrino mixing), neutral and stable. Therefore, neutrinos actually form part of the DM density. However, their contribution can be estimated as $\Omega_\nu h^2 \approx \frac{\sum_i m_i}{91\text{eV}} < 0.003$, a minor contribution to the total DM abundance.

There are countless proposed extensions to the SM, each of which can provide solutions to some of the open questions. One way of generating New Physics is to extend the symmetries of the SM. One such extension is supersymmetry (SUSY), which is described in Section 1.3. Another method postulates a DM candidate and couples it to the SM through some mediator. Section 1.4 describes one such model.

1.3 Supersymmetry

SUSY introduces an additional symmetry to the SM in which SM fermions can become bosons and SM bosons can become fermions. An operator. Q, is introduced which enables transformations between bosonic and fermionic states, as follows:

$$\begin{aligned} Q\,|\text{boson}\rangle &= |\text{fermion}\rangle \\ Q\,|\text{fermion}\rangle &= |\text{boson}\rangle \ . \end{aligned} \tag{1.3.1}$$

The symmetry group of SUSY is of the form $\text{SU}(3)_C \times \text{SU}(2)_L \times \text{U}(1)_Y \times \text{SUSY}$ such that when a SM particle undergoes a SUSY transformation, the SM quantum numbers are unchanged. Under this symmetry group, each of the SM particles gains a superpartner with spin differing by 1/2. The SM particles and their superpartners can be placed into either chiral multiplets or gauge multiplets.

The SM fermions and their bosonic, spin-0 superpartners form chiral multiplets. The superpartners to the SM fermions have an 's' prepended to their name, short for scalar. For example, the superpartner to the SM top quark is named the 'stop' quark. The SM bosons have 'ino' appended to their name, an example of this being the superpartners to the SM gluon being named gluinos. The SM vector bosons and their superpartners form gauge multiplets. In order to give masses to all of the particles, SUSY requires two Higgs doublets with weak isospin $Y = \pm 1/2$. This extended Higgs sector gives rise to four gauge eigenstates to the Higgs scalars: $\tilde{H}_u^+$, $\tilde{H}_u^0$, $\tilde{H}_d^0$ and $\tilde{H}_d^-$. The four eignenstates mix to form five mass eigenstates: h^0, H^0, A^0 and $H^\pm$. The SM Higgs boson discovered in 2012 is identified as the lightest CP-even SUSY Higgs, h^0, while the remaining mass eigenstates have much higher masses and are usually assumed to be decoupled. A summary of the chiral supermultiplets and gauge supermultiplets are shown in Tables 1.2 and 1.3, respectively.

Names	Symbol	Spin-0	Spin-1/2	$SU(3)_C \times SU(2)_L \times U(1)_Y$
squarks, quarks	Q	$(\tilde{u}_L\ \tilde{d}_L)$	$(u_L\ d_L)$	$(\mathbf{3}, \mathbf{2}, \frac{1}{6})$
(3 generations)	$\bar{u}$	$\tilde{u}_R^*$	$u_R^\dagger$	$(\bar{\mathbf{3}}, \mathbf{1}, -\frac{2}{3})$
	$\bar{d}$	$\tilde{d}_R^*$	$d_R^\dagger$	$(\bar{\mathbf{3}}, \mathbf{1}, \frac{1}{3})$
sleptons, leptons	L	$(\tilde{\nu}\ \tilde{e}_L)$	$(\nu\ e_L)$	$(\mathbf{1}, \mathbf{2}, -\frac{1}{2})$
(3 generations)	$\bar{e}$	$\tilde{e}_R^*$	$e_R^\dagger$	$(\mathbf{1}, \mathbf{1}, 1)$
Higgs, higgsinos	H_u	$(H_u^+\ H_u^0)$	$(\tilde{H}_u^+\ \tilde{H}_u^0)$	$(\mathbf{1}, \mathbf{2}, +\frac{1}{2})$
	H_d	$(H_d^0\ H_d^-)$	$(\tilde{H}_d^0\ \tilde{H}_d^-)$	$(\mathbf{1}, \mathbf{2}, -\frac{1}{2})$

Table 1.2: Chiral supermultiplets in the MSSM.

Names	Spin-1/2	Spin-1	$SU(3)_C \times SU(2)_L \times U(1)_Y$
gluino, gluon	$\tilde{g}$	g	$(\mathbf{8}, \mathbf{1}, 0)$
winos, W bosons	$\tilde{W}^\pm\ \tilde{W}^0$	$W^\pm\ W^0$	$(\mathbf{1}, \mathbf{3}, 0)$
bino, B boson	$\tilde{B}^0$	B^0	$(\mathbf{1}, \mathbf{1}, 0)$

Table 1.3: Gauge supermultiplets in the MSSM.

Mixing of mass eigenstates

The gauge eigenstates listed in Tables 1.2 and 1.3 are able to mix, resulting in mass eigenstates which are different from the gauge eigenstates. The gauge and mass eigenstates are presented in Table 1.4, showing the mixing between the gauge eigenstates.

Names	Spin	Gauge Eigenstates	Mass Eigenstates
Higgs bosons	0	H_u^+, H_u^0, H_d^0, H_d^-	h^0, H^0, A^0, $H^\pm$
Charginos	1/2	$\tilde{W}^\pm$, $\tilde{H}_u^+$, $\tilde{H}_d^-$	$\tilde{\chi}_1^\pm$, $\tilde{\chi}_2^\pm$
Neutralinos	1/2	$\tilde{H}_u^0$, $\tilde{H}_d^0$, $\tilde{W}^0$, $\tilde{B}^0$	$\tilde{\chi}_1^0$, $\tilde{\chi}_2^0$, $\tilde{\chi}_3^0$, $\tilde{\chi}_4^0$
Sleptons	0	$\tilde{e}_L$, $\tilde{e}_R$, $\tilde{\nu}_e$	same
		$\tilde{\mu}_L$, $\tilde{\mu}_R$, $\tilde{\nu}_\mu$	same
		$\tilde{\tau}_L$, $\tilde{\tau}_R$, $\tilde{\nu}_\tau$	$\tilde{\tau}_1$, $\tilde{\tau}_2$, $\tilde{\nu}_\tau$
Squarks	0	$\tilde{u}_L$, $\tilde{u}_R$, $\tilde{d}_L$, $\tilde{d}_R$	same
		$\tilde{c}_L$, $\tilde{c}_R$, $\tilde{s}_L$, $\tilde{s}_R$	same
		$\tilde{t}_L$, $\tilde{t}_R$, $\tilde{b}_L$, $\tilde{b}_R$	$\tilde{t}_1$, $\tilde{t}_2$, $\tilde{b}_1$, $\tilde{b}_2$
Gluino	0	$\tilde{g}$	same

Table 1.4: Table showing the SUSY gauge and mass eigenstates.

As shown in Table 1.4, mixing occurs between the superpartners of the electroweak gauge bosons and Higgs bosons, the squarks and sleptons. For the squarks and sleptons, the mix-

ing of the SUSY gauge eigenstates is proportional to the mass of their SM counterparts, and as such is only relevant for the superpartners of the top and bottom quarks and the tau lepton. The L and R subscripts denote that there are superpartners for both the left-handed and right-handed fermions, and do not denote the handedness of the superpartners themselves. The winos, bino and Higgsinos can mix to form a rich spectrum of electroweak mass eigenstates. The bino, $\tilde{B}^0$, the neutral wino $\tilde{W}^0$ and the neutralino higgsinos $\tilde{H}_u^0$ and $\tilde{H}_d^0$ can mix to form four neutral mass eigenstates known as neutralinos. The charged winos, $\tilde{W}^\pm$ and the charged higgsinos $\tilde{H}_u^+$ and $\tilde{H}_d^-$ can mix to form two charged mass eigenstates known as charginos. The neutralinos are denoted by $\tilde{\chi}_i^0$, where $i = 1, 2, 3, 4$, while the charginos are denoted by $\tilde{\chi}_i^\pm$, where $i = 1, 2$. By convention, the charginos and neutralinos are labelled in ascending mass. The lightest neutralino, $\tilde{\chi}_1^0$, is generally the lightest supersymmetric particle (LSP). The production cross-section for squarks, sleptons, charginos and neutralinos is shown in Figure 1.7. In the R-parity conserving case (defined

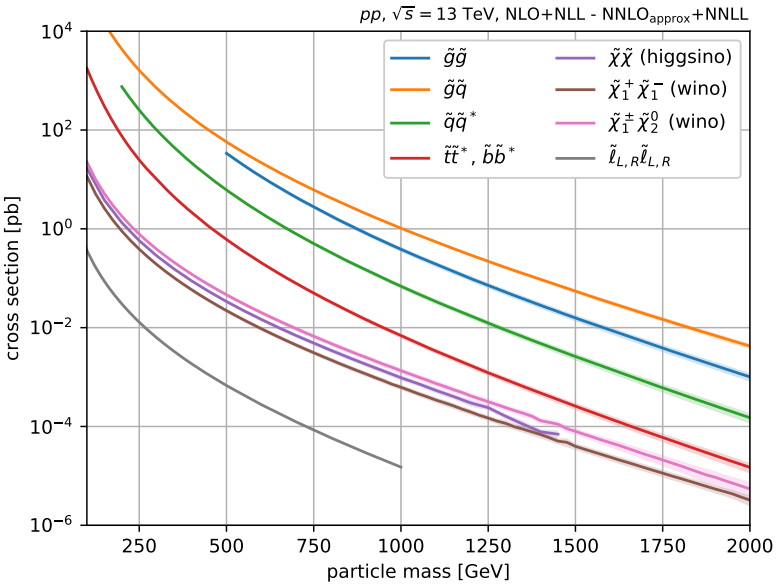

Figure 1.7: Figure showing the production cross-sections for pairs of SUSY particles at $\sqrt{s} = 13$ TeV.

later in this Chapter), the LSP is stable while the heavier charginos and neutralinos ($\tilde{\chi}_1^\pm$, $\tilde{\chi}_{2,3,4}^0$) can decay through a chain of decays until a final state containing LSPs and SM particles is reached. The two-body decay chains of charginos and next-to-lightest neutralinos are shown in Figure 1.8, assuming that the diagrams containing H^0, A^0 and $H^\pm$ are disfavoured compared to diagrams with h^0. In the case that the diagrams shown are kinematically-forbidden, decays can proceed via three-body decays involving SM fermions.

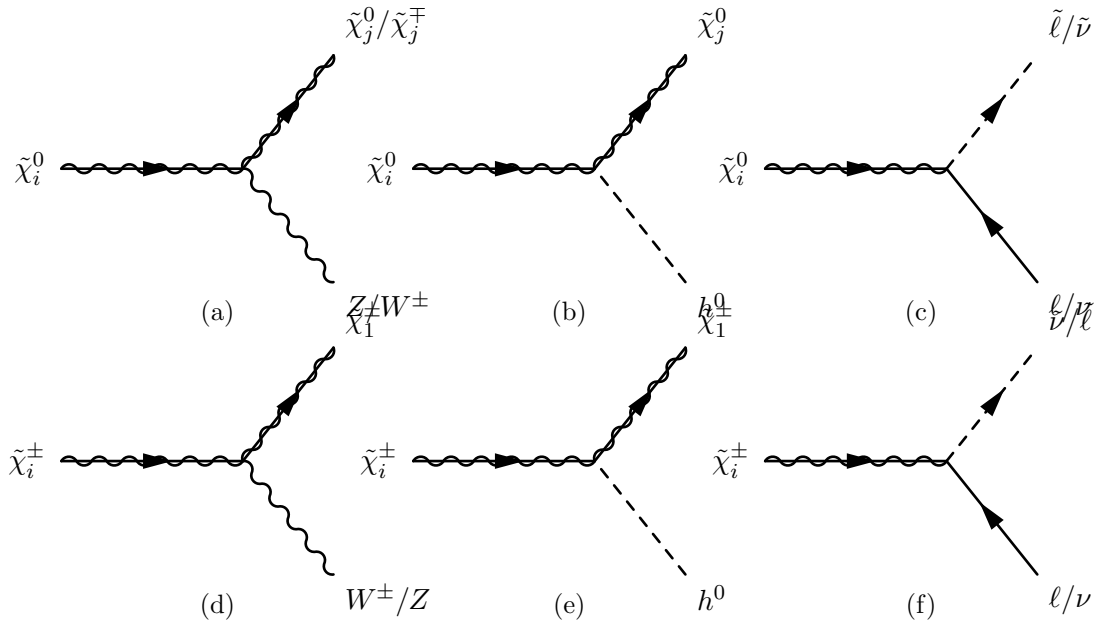

Figure 1.8: Diagrams showing the two-body decays of a given neutralino, $\tilde{\chi}_i^0$ (1.8a, 1.8b and 1.8c) and chargino, $\tilde{\chi}_i^\pm$ (1.8d, 1.8e and 1.8f).

Unification of fundamental interactions

As previously discussed, it was shown by Glashow, Salam and Weinberg that the electromagnetic and weak interactions unify above the electroweak scale, resulting in the combined electroweak interaction. It is postulated that above some grand unified theory (GUT) scale, the electromagnetic, weak and strong forces unify. However, in the SM, the evolution of the couplings of the three forces never converge. SUSY introduces additional particles which alter the running of the coupling constants, allowing them to unify at the GUT scale. The running of the couplings are shown in Figure 1.9 for both the SM and SUSY.

Resolution to the hierarchy problem

As previously discussed, the squared-mass of the Higgs boson, m_H^2, is comprised of two components; a bare mass, $m_{H,\text{bare}}^2$, and the quantum corrections to the Higgs mass through fermion couplings, δm_H^2. The correction to the Higgs mass for a given fermion, f, is given by

$$\delta m_{H,f}^2 = \frac{|y_f|^2}{16\pi^2}\left[-2\Lambda_p^2 + 6m_f^2 \ln\left(\Lambda_p/m_f\right)\right] \ , \tag{1.3.2}$$

where, m_f is the mass of the fermion and y_f is the Yukawa coupling of that fermion to the Higgs boson. From Equation 1.3.2, it is evident that the top quark which has $y_f \approx 1$, yields the largest correction at around 30 orders of magnitude larger than the measured Higgs

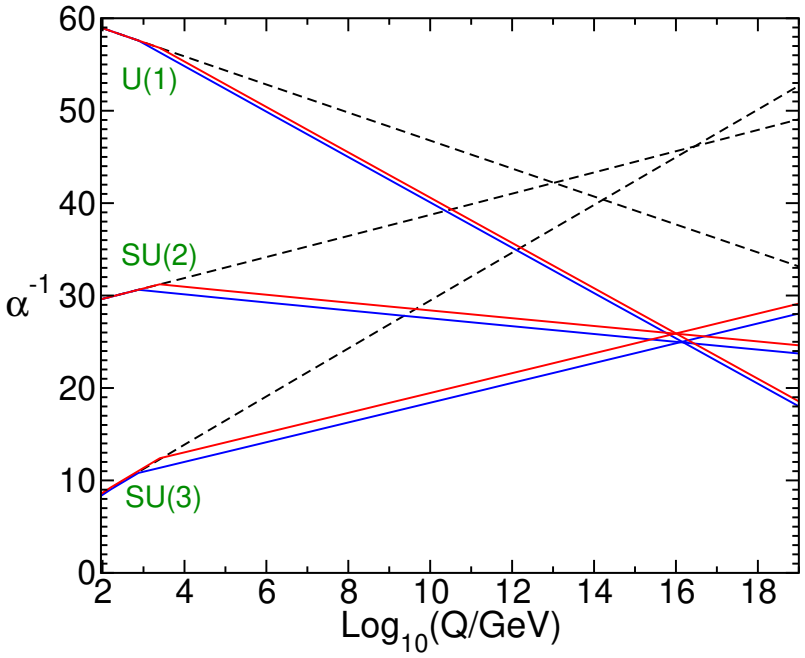

Figure 1.9: Diagram showing how the coupling constants evolve in SM-only (dashed) and SUSY (solid) scenarios. For the SUSY particles, the masses are varied from 750 GeV to 2.5 TeV, with the solid, red line showing the high mass scenario, while the solid, blue line shows the lower mass scenario. [24]

squared-mass, meaning there is either a high degree of 'fine-tuning' or there are additional quantum corrections from New Physics. SUSY introduces two scalars for each SM fermion (one for each of the left- and right-handed fields). The correction to the Higgs mass for a scalar, S is given by

$$\delta m_{H,f}^2 = \frac{\lambda_S}{16\pi^2}\left[\Lambda_p^2 - 2m_S^2 \ln\left(\Lambda_p/m_S\right)\right] \ , \tag{1.3.3}$$

where m_S is the mass of the scalar and $\lambda_S = |y_f^2|$. Assuming that the scalars have the same masses as their SM counterparts, the quadratic component of the corrections to the Higgs mass exactly cancel. However, if the superpartners and their SM particles have identical masses, observations of SUSY particles would have been made long before the LHC. At the time of writing however, no observation of a SUSY particle has been made. In light of this, it can be inferred that SUSY must be a spontaneously broken symmetry, in a similar manner to the electroweak symmetry of the SM. The exact mechanism through which this occurs is not yet known. However, it is possible to break the SUSY symmetry 'by hand' by introducing additional terms in the Lagrangian, as follows:

$$\mathcal{L} = \mathcal{L}_{\text{SUSY}} + \mathcal{L}_{\text{soft}} \ . \tag{1.3.4}$$

In Equation 1.3.4, $\mathcal{L}_{\text{SUSY}}$ contains all of the Yukawa and gauge interactions, while $\mathcal{L}_{\text{soft}}$ contains mass parameters which solve the heirarchy problem with a low level of fine-tuning. Naturalness [25] requires that the supersymmetric partners of the top quark and bottom quark, as well as the gluinos and Higgsinos, are light and have masses around the TeV scale.

R-parity

SUSY introduces an additional quantum number, known as R-parity, R_p. The R-parity is constructed using the spin (S), the baryon number (B) and lepton number (L) of the incoming and outgoing particles from an interaction vertex. The R-parity is defined as:

$$R_P = (-1)^{3(B-L)+2S} \, . \tag{1.3.5}$$

Using Equation 1.3.5, it can be seen that the SM particles all have $R_P = +1$, while the SUSY particles have $R_P = -1$. In SUSY models which conserve R-parity, processes which violate lepton and baryon number conservation are disallowed, which prevents the rapid decay of protons to leptons + mesons, a result which is consistent with experimental observation. The conservation of R-parity has three important consequences:

- The LSP is required to be stable. In models where the LSP is neutral and weakly-interacting with the SM, it becomes an excellent candidate for Dark Matter.
- Each SUSY particle must decay via a chain containing an odd number of LSPs, mostly just one.
- SUSY particles are pair-produced in pp collisions.

1.4 Extended Higgs sector and Dark Matter

There are numerous different approaches to study the potential of DM being produced at the LHC. Effective field theories (EFTs) enable the study of scenarios where the interactions between DM and the SM are mediated by particles which are much heavier than the energy scale of the interaction, and hence are difficult to reach kinematically. However, when the scale of the interaction of DM and the SM is similar to the scales accessible by the LHC, the EFT approach may become invalid. An alternative approach to model the DM-SM interactions is the use of simplified DM models. Such models should satisfy the following criteria:

- The DM candidate should be stable, or long-lived enough to escape ATLAS without detection. There must also be a mediator which couples the DM to the SM. Additional states can exist, but must be decoupled.

- The Lagrangian describing the model should be consistent with Lorentz invariance, should contain all SM gauge symmetries and allow DM stability.
- The additional interactions introduced in the simplified model should not violate any of the symmetries of the SM.

A set of simplified models satisfying these conditions is defined in [26], which add a real or complex spin-0 mediator to the SM. Simplified models make additional assumptions, such as assuming that the branching ratio of the process under consideration is 100%, or assuming other BSM particles are decoupled and hence do not contribute. The complex scalar contains both scalar and pseudoscalar particles, and it is assumed that the scalar is decoupled. Therefore, the set of simplified models are mediated by a scalar, ϕ or pseudoscalar, a. Two example diagrams of simplified model processes are shown in Figure 1.10.

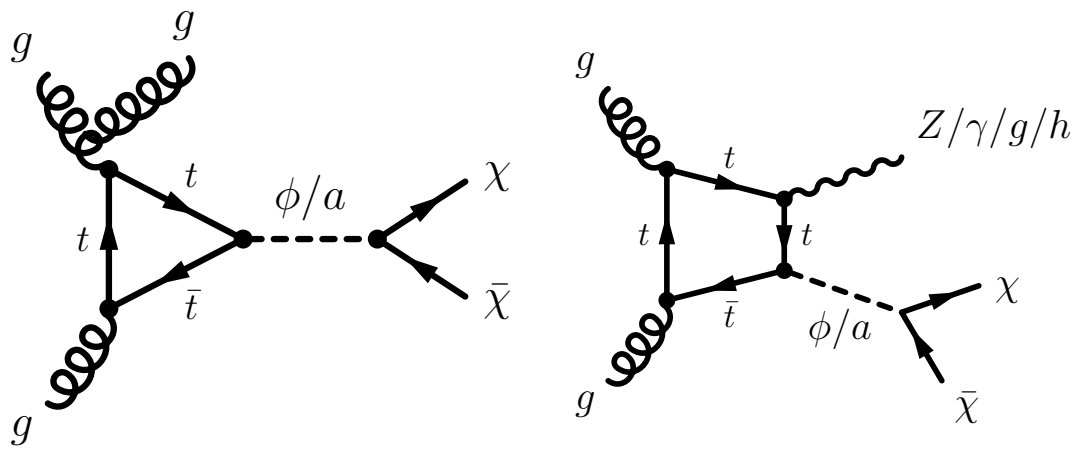

Figure 1.10: Feynman diagrams showing two of the dominant diagrams for the simplified DM model, where DM couples to the SM through a scalar (ϕ) or pseudoscalar (a) mediator [27].

While DM simplified models have provided an excellent benchmark for DM searches on ATLAS, the models themselves can suffer from theoretical inconsistency with the SM, violating both gauge invariance and unitarity [28]. The next generation of LHC DM models builds upon the DM simplified model framework, with the aim of resolving the theoretical inconsistencies previously described, while extending the phenomenology, such that a wider range of experimental signatures are available to be probed [29]. Of interest in this Thesis is the 2HDM+a model, the simplest, renormalisable extension of the simplified model of DM-SM interactions mediated by the pseudoscalar, a.

The 2HDM+a model introduces the same extended Higgs sector as introduced in Table 1.4 for SUSY, with a Higgs sector containing two Higgs doublets, Φ_1 and Φ_2, with the

addition of a pseudoscalar singlet, P. The introduction of an extended Higgs sector with two scalar doublets can lead to flavour-changing neutral currents (FCNCs), which in the SM are forbidden at tree-level [30]. Two coupling schemes can be used to avoid FCNCs, in which each Higgs doublet couples only to certain fermions. With the so-called type-II 2HDM structure, the up-type quarks (u, c, t) couple to one Higgs doublet, Φ_2, while the down-type quarks (d, s, b) and charged leptons couple to the other Higgs doublet, Φ_1. This is realised by setting the corresponding Yukawa couplings to 0; $y_u^1 = y_d^2 = y_\ell^2 = 0$. To ensure CP conservation in the Higgs sector, the parameters in the scalar potential are required to be real. As such, the most general, renormalisable scalar potential of the extended Higgs sector can be written as [29]

$$V = V_H + V_{HP} + V_P \ , \tag{1.4.1}$$

where V_H represents the potential for the Higgs doublets,

$$\begin{aligned} V_H =& \mu_1 \Phi_1^\dagger \Phi_1 + \mu_2 \Phi_2^\dagger \Phi_2 + \left(\mu_3 \Phi_1^\dagger \Phi_2 + \text{ h.c.}\right) + \lambda_1 \left(\Phi_1^\dagger \Phi_1\right)^2 + \lambda_2 \left(\Phi_2^\dagger \Phi_2\right)^2 \\ &+ \lambda_3 \left(\Phi_1^\dagger \Phi_1\right)\left(\Phi_2^\dagger \Phi_2\right) + \lambda_4 \left(\Phi_1^\dagger \Phi_2\right)\left(\Phi_2^\dagger \Phi_1\right) + \left[\lambda_5 \left(\Phi_1^\dagger \Phi_2\right)^2 + \text{ h.c.}\right] \ , \end{aligned} \tag{1.4.2}$$

V_{HP} represents the coupling of the Higgs doublets to the pseudoscalar singlet,

$$V_{HP} = P\left(i b_p \Phi_1^\dagger \Phi_2 + \text{h.c}\right) + P^2\left(\lambda_{P1} \Phi_1^\dagger \Phi_1 + \lambda_{P2} \Phi_2^\dagger \Phi_2\right) \ , \tag{1.4.3}$$

and V_P represents the potential of the pseudoscalar singlet,

$$V_P = \frac{1}{2} m_p^2 P^2 \ . \tag{1.4.4}$$

Above, μ_i represent the mass-squared terms, λ_j represent the quartic couplings, λ_{P1} , λ_{P2} represent the quartic portal couplings and both b_p and m_p are parameters with dimensions of mass. Upon rotation to the mass eigenstate basis, five physical Higgs mass states are obtained, h^0, H^0, A^0 and $H^\pm$, and the previously listed parameters become physical masses, mixing angles and quartic couplings. Each of the five physical Higgs states has a corresponding mass parameter, m_h, m_{H^0}, m_A and $m_{H^\pm}$, while the pseudoscalar mediator has a mass parameter m_a. The mixing of the CP-even Higgs states, h and H, is denoted by the mixing angle α, while the mixing between the CP-odd pseudoscalar A and a is denoted by θ. The ratio of the VEVs of the two Higgs doublets is denoted by $\tan\beta = v_2/v_1$, where $v_1 = v \sin\beta$ and $v_2 = v \cos\beta$, with $v \approx 246$ GeV as described previously. Finally, m_χ represents the mass of the Dirac fermion DM, and y_χ represents the DM coupling strength.

The 2HDM+a model forms the basis for the analysis detailed in Chapter 7, where the experimental signature and relevant assumptions and parameter choices are described in

the introduction.

Chapter 2

The LHC and the ATLAS Experiment

The physics analyses detailed in the forthcoming chapters made use of data collected by the ATLAS detector, one of the four main experiments situated around the Large Hadron Collider (LHC) at the European Organisation for Nuclear Research (CERN). CERN is home to the the largest particle physics accelerator to date, the LHC. Lying beneath the French-Swiss border at a depth of around 100 m, it spans a cirumference of almost 27 km. The LHC is a hadron-hadron collider, accelerating counter-circulating beams of protons (or heavy-ions for a short period every year) to provide collisions at four interactions points around the LHC; ATLAS, CMS, LHCb and ALICE. This thesis focuses entirely on proton-proton collisions recorded by the ATLAS experiment.

2.1 The LHC accelerator

The protons for the LHC beams are provided by a bottle of hydrogen gas. Protons are isolated by applying a strong electric field to hydrogen atoms, stripping away the electrons. These isolated protons are then transfered to a linear accelerator (LINAC2), where they undergo the initial acceleration to 50 MeV. Proton acceleration is achieved using Radio Frequency (RF) cavities. In the Proton Synchrotron (PS), the proton beam is divided into proton packets known as 'bunches', spaced by 25 ns intervals, with each bunch containing around $\mathcal{O}(10^{11})$ protons. The 50 MeV proton bunches are further accelerated to an energy of 1.4 GeV by the Proton Synchrotron Booster (PSB) and subsequently to an energy of 25 GeV by the PS. The Super Proton Synchrotron (SPS) is the penultimate stage of acceleration, accelerating the 25 GeV proton bunches to an energy of 450 GeV. These proton bunches are injected into the LHC to produce two counter-circulating beams and are accelerated from 450 GeV to 6.5 TeV by RF cavities. A diagram of the LHC accelerator complex is shown in Figure 2.1.

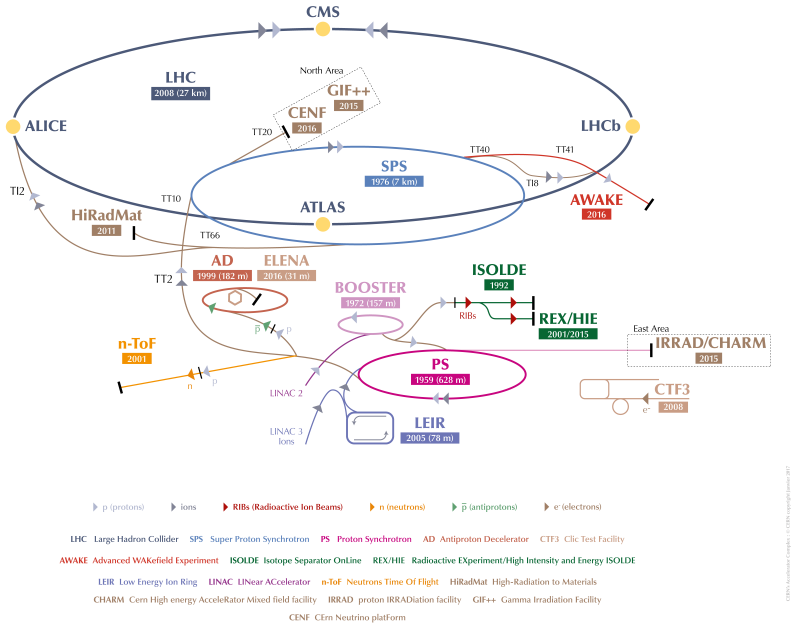

Figure 2.1: A diagram of the CERN accelerator complex. Of importance to the LHC accelerator are LINAC2, PSB, PS, SPS and LHC. [31]

2.2 Luminosity and pileup

The amount of data being delivered by LHC and recorded by its experiments is measured by the *luminosity*. For a circular collider, the expression for the instantaneous luminosity of two colliding beams is given by [32]:

$$\mathcal{L} = f\frac{N_p^2 n_b}{4\pi\sigma_x\sigma_y}F\ . \tag{2.2.1}$$

In Equation 2.2.1, N_p is the number of protons per bunch, n_b the number of bunches in each beam, f the frequency of bunch crossings ($1/25\text{ns} = 40\text{MHz}$), σ the size of the bunch at the interaction point (IP) and F a geometrical correction factor accounting for a non-zero crossing angle at the IP. The integrated luminosity (often shortened to 'luminosity'), is defined as the time-integral of the instantaneous luminosity: $L = \int \mathcal{L}dt$.

Due to the huge number of incident particles every second, the SI units for integrated luminosity of cm^{-1} are rarely used; instead, integrated luminosity is often quoted in units of 'barns', where 1 barn (b) is defined as 10^{-24}cm^2. The total number of expected events, N_{exp}, in a dataset with integrated luminosity L and cross-section $\sigma_{pp\to X}$ is given by $N_{\text{exp}} = \sigma_{pp\to X}L$.

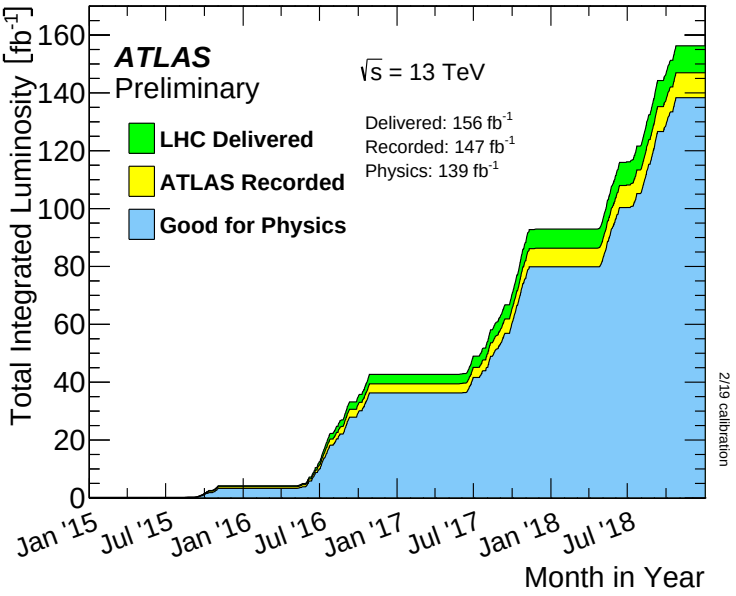

Figure 2.2: Plot showing the total integrated luminosity as a function of time during the Run-2 data-taking period. In total, the LHC delivered 156 fb^{-1} of data, with ATLAS recording 147 fb^{-1} and 139 fb^{-1} being established as suitable for physics analysis. [33]

Due to the bunched beam structure and the intensity of the bunches, multiple inelastic proton-proton collisions are possible per bunch crossing. Pileup is an important effect in high energy physics experiments such as ATLAS, as large amounts of pileup degrade the reconstruction performance of an experiment. Pileup events can come from either the same bunch crossing, known as in-time pileup, or from the bunch crossing just before or after the bunch-crossing being considered, known as out-of-time pileup. The collision, or vertex, with at least two tracks and with the highest Σp_T^2 is usually defined as the primary vertex, or 'hard scatter', in an event. All other vertices, and the resultant final state particles, from the same bunch crossing are considered 'pileup' events. Figure 2.3 shows the pileup profile for each data-taking year for Run-2 of the LHC. The mean number of interactions per bunch-crossing is taken as the mean of the Poisson distribution of the number of interactions per bunch-crossing calculated for each bunch. It is calculated using the per-bunch luminosity, defined as:

$$\mu = \mathrm{L}_{\mathrm{bunch}} \times \frac{\sigma_{\mathrm{inel}}}{f_r} \, . \tag{2.2.2}$$

In Eq. 2.2.2, $\mathrm{L}_{\mathrm{bunch}}$ is the per-bunch instantaneous luminosity, σ_{inel} is the inelastic cross-section (~ 80 mb for Run-2), and f_r is the bunch-crossing frequency.

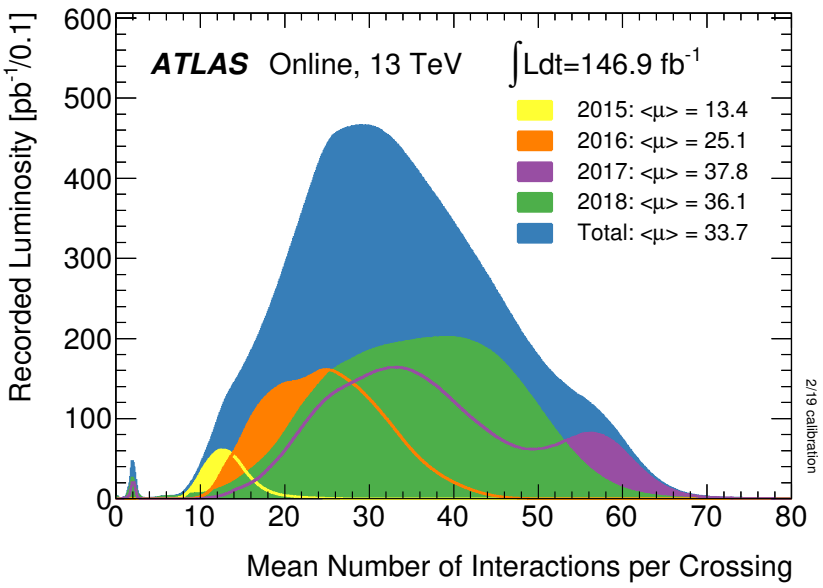

Figure 2.3: Mean number of proton-proton interactions per bunch crossing for Run-2 (2015-2018). The mean number of interactions per bunch-crossing is taken as the mean of the Poisson distribution of the number of interactions per bunch-crossing calculated for each bunch.

2.3 ATLAS overview

ATLAS, *A Toroidal LHC ApparatuS*, is one of the two general purpose detectors (GPDs) and is the largest of all of the LHC experiments, at 44m in length and 25m in width and weighing around 7000 tons. Figure 2.4 shows a schematic diagram of the ATLAS detector and its major subsystems. ATLAS is an almost hermetic detector, providing near-full 4π tracking and calorimetry through multiple detector subsystems. The ATLAS detector design was optimised for [34]:

- High-efficiency for charged particle reconstruction and identification.
- High-precision calorimetry, providing high-precision electron/photon identification and measurement along with accurate hadronic and missing transverse momentum measurements.
- Precise muon momentum measurements using only the muon system, at even the highest luminosity.
- Ability to trigger on objects with low momentum.

ATLAS has four major subsystems; the Inner Detector (ID), the Electromagnetic Calorimeter (ECAL), the Hadronic Calorimeter (HCAL) and the Muon Spectrometer (MS), arranged in concentric layers about the beam pipe. ATLAS is designed to be symmetric in the forward-backward plane about the interaction point (IP), and when discussed

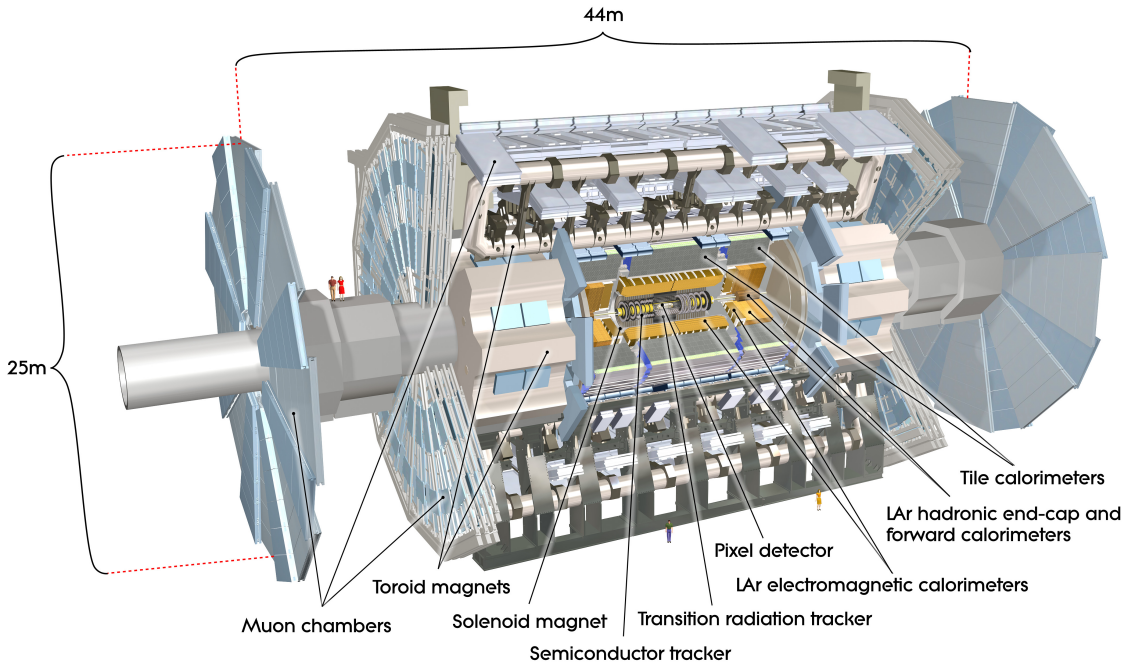

Figure 2.4: Cut-away diagram of the ATLAS detector. [35]

is often separated into the barrel region and the endcap region.

ATLAS uses a 'right-handed' coordinate system; the z-axis is defined in the beam direction, with the positive x-axis defined to point from the interaction point to the centre of the LHC and the positive y-axis being in the upwards direction. Side A of ATLAS, the side closer to Geneva Airport, is defined with positive z values, and Side C, closer to the Jura mountains, with negative z values.

The azimuthal angle, ϕ, and the polar angle, θ, are defined as the angle around the beam axis and the angle from the beam, respectively. From the polar angle, the pseudorapidity is defined as $\eta = -\ln\tan(\frac{\theta}{2})$. As the partons are highly boosted in the z-direction, and the partonic momentum fraction is not exactly known, object measurements are usually made in the plane perpendicular to the beam, the transverse plane, such as an object's transverse momentum, p_T or missing transverse momentum, $E_{\mathrm{T}}^{\mathrm{miss}}$. Differences in pseudorapidity between particles are independent of the momentum of the colliding partons and hence also make a useful observable.

2.4 Magnet system

When a charged particle of charge q moves with velocity v through a magnetic field of strength $|\vec{B}|$, the force on that particle is given by the Lorentz force,

$$\vec{F} = q\vec{v} \times \vec{B} \,, \tag{2.4.1}$$

where $\vec{v} \times \vec{B}$ denotes the cross-product of the velocity vector of the particle with the vector describing the magnetic field. Due to the presence of the a cross-product in the Lorentz force, the force experienced by the charged particle will be perpendicular to both the velocity vector and the magnetic field. The deflection of particle tracks by the magnet system enables the measurement of the momentum of an incident particle. The ATLAS magnet system is constructed from two superconducting magnet systems which enable this; a central solenoid (CS) which is surrounded by three toroid magnets. A diagram of the ATLAS magnet system is shown in Figure 2.5.

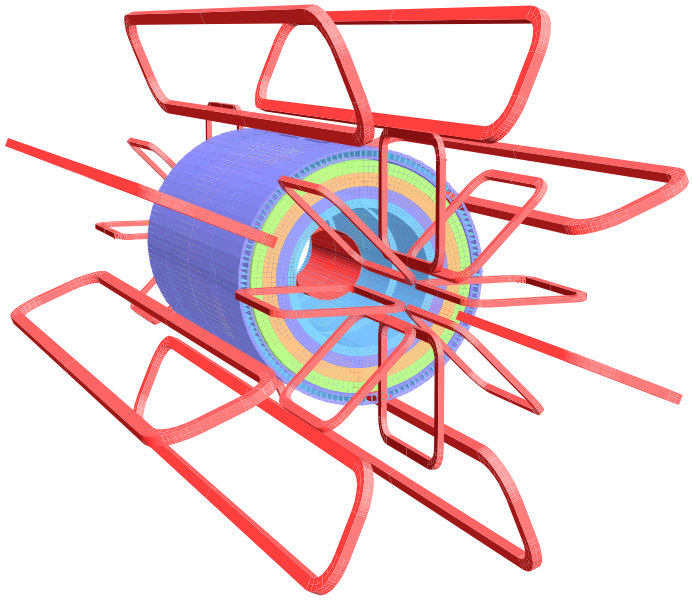

Figure 2.5: Diagram of the ATLAS magnet system, showing the barrel and end-cap toroids in red, while the CS is shown encased by calorimeter layers. [34]

The central solenoid (CS) provides a 2T magnetic field to the Inner Detector, peaking at around 2.6T at the magnet itself. The barrel toroid (BT) and endcap toroid (ECT) provide a magnetic field between 0.5-1 T for the muon spectrometer, peaking at 3.9T and 4.1T, respectively. Superconductivity of the magnet system is achieved using liquid helium cooled to around 4.5 K.

2.5 Inner Detector

The ATLAS Inner Detector (ID), shown in Fig. 2.6, is the innermost layer of the ATLAS detector. It is designed to provide high-precision tracking, vertex information, and for the identification of particles. The ID has 3 components; the Pixel detector, the Semiconductor Tracker (SCT) and the Transition Radiation Tracker (TRT). The Pixel detector and SCT use silicon pixels and strips, respectively, while the latter uses straw detectors to provide tracking information. The ID is immersed in a 2T magnetic field provided by the CS, allowing precise momentum measurement through the measurement of track deflection. The Pixel and SCT detectors provide coverage in $|\eta| < 2.5$, while the TRT provides further tracking information up to $|\eta| < 2.0$.

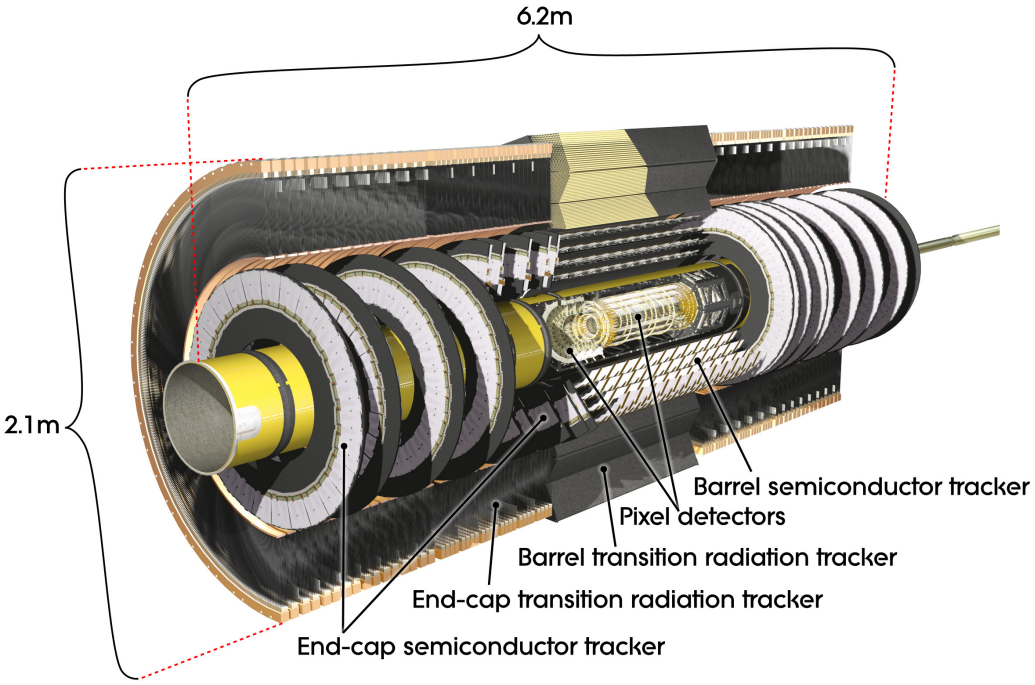

Figure 2.6: Cut-away diagram of the ATLAS Inner Detector. [35]

Pixel Detector

The Pixel Detector uses silicon semiconductor pixels to register particle hits from incident particles. Materials which exhibit semiconductive behaviour, such as silicon, have conductivity between that of an insulator and a conductor. The silicon pixels used in the Pixel Detector are constructed using a p-n junction. A p-n junction is the boundary between two silicon semiconductors which are doped to have excess of electrons (n-doped), or an excess of holes (p-doped). By applying a forward bias voltage to the pixel, the free electrons and holes can migrate across the junction through the depletion region. Conversely, when applying a reverse bias, the free electrons and holes are pulled away from the junction. When

Detector component	Modules	Pixel pitch [μm]	Resolution [μm]
Pixel Detector			
IBL	224	50 x 250	8 ($R-\phi$), 40 (z)
Barrel	1456	50 x 400	10 ($R-\phi$), 115 (z)
End-caps	288	50 x 400	10 ($R-\phi$), 115 (R)
SCT			
Barrel	2112	80	17 ($R-\phi$), 580 (z)
End-caps	1976	80	17 ($R-\phi$), 580 (R)

Table 2.1: Table giving a summary of the Pixel Detector and SCT module sizes and resolutions. [34, 36]

a sufficient reverse bias is applied, the pixel becomes fully depleted, meaning there is no current flow between the p-doped and n-doped side of the pixel. When a charged particle passes through a pixel, electrons and holes are liberated which drift to the electrodes of the pixel due to applied bias voltage, resulting in the collection of charge which is read out as a particle hit.

The Pixel Detector is the ID subsystem closest to the IP. It provides high-granularity, high-precision measurements of charged particles at radii as little as 5cm from the beam pipe. The system itself is constructed from three barrel modules at radii of $\sim$ 5cm, $\sim$ 9cm and $\sim$ 12cm, with five disks on either side at radii between 11cm and 20cm. The Pixel detector has 1744 silicon pixel sensors with a nominal pixel pitch of $50 \times 400\mu\text{m}^2$ and a thickness of 250μm. The barrel layers of the Pixel Detector contain 67 million readout channels, and the disks contain a further 13 million.

Since the initial detector design, a fourth layer has been added to the Pixel Detector, at a radius of $\sim$ 3cm. This layer is known as the 'Insertable B-Layer', or IBL. The IBL was developed and installed to improve the tracking and b-tagging performance of the ID in instantaneous luminosity conditions which exceeded the initial Pixel Detector design. The Pixel Detector's efficiency was expected to degrade due to the additional pileup produced by the higher-than-design instantaneous luminosity, but the inclusion of the IBL helped to combat this efficiency degradation while also providing an improvement to the impact parameter resolution. The pixel sensors used in the IBL have a pitch of $50 \times 250\mu\text{m}^2$. Table 2.1 summarises the semiconductor modules used in both the Pixel Detector and SCT.

Semiconductor Tracker

The SCT surrounds the Pixel detector, using detection techniques similar to that previously described for the Pixel detector. The SCT provides up to eight precision measurements

per track, aiding in high-precision measurement of charged particle momentum, as well as contributing to the measurement of the impact parameter and vertex position. The SCT is constructed from eight layers of silicon microstrip detectors, consisting of 4088 modules. The eight layers of barrel SCT modules have a total of 2112 microstrip modules with 80μm pitch, at radii between 30cm and 52cm. The SCT provides spatial resolution of 16μm in Rϕ and 580μm in z, allowing for tracks to be distinguished if they are separated by $\sim$ 200μm.

Transition Radiation Tracker

The TRT is the outermost layer of the ID, sitting at radii between 554mm $< r <$ 1106mm. The TRT is a straw-tube detector, utilising drift tube detectors to provide up to 36 additional measurements of each track. The drift tubes in the TRT are constructed from Kapton tubes, each of 4mm diameter, with a gold-plated tungsten wire in the centre of each drift tube with a diameter of 31 μm. The wire at the centre of each tube is at ground potential, while the wall of the tubes are at -1.5 kV. The tubes are filled with a mixture of xenon (70%), carbon dioxide (27%) and oxygen (3%). When a charged particle passes through a straw tube, electrons from the gas are liberated through ionisation processes. These electrons then drift toward the wire in the centre of the straw tube. The current flow created by the free electrons is registered as a particle hit. In total, the barrel TRT contains $\sim$ 50000 straws, while the end-caps contain 320000. Polymer fibres and foils fill the gaps between the straws in the barrel and endcap, respectively. The interface between the straws and the polymers used to fill the gaps can cause highly-relativistic particles to emit transition radiation. The probability of the emission of transition radiation depends upon the relativistic factor $\gamma = E/m$, and is hence strongest for lighter particles. Particle identification using transition radiation is performed to distinguish electrons from pions.

2.6 Calorimetry

The calorimeters in the ATLAS detector are designed to absorb and accurately measure the energy of incident particles. The calorimeter system can be separated into the Electromagnetic calorimeter (ECAL), the Hadronic calorimeter (HCAL) and the Forward Calorimeter (FCal) systems, all of which are sampling calorimeters. The ECAL is designed to measure the energies of incident electrons and photons, while the HCAL is designed for measuring the energy of hadrons which interact strongly.

The ATLAS calorimeter systems use alternating layers of absorber material and active detector material. When a particle enters the absorber material of a calorimeter, a cascade of particle decays is initiated, known as a shower. Particles which interact via the EM interaction produce EM showers, in which photons pair-produce electrons and positrons, both of which undergo Bremsstrahlung radiation of photons. Particles which interact via

the strong force produce much more complex showers. Particle-nucleus interactions in the calorimeters can produce additional hadrons, such as pions. Charged hadrons, will lose energy when traversing the absorber material through ionisation processes. In addition, neutral pions in their decay to two photons, $\pi^0 \to \gamma\gamma$, can induce an EM shower component.

The depth of the ATLAS calorimeters is optimised to contain showers, hence minimising punch-through into the next detector layer. The radiation length, X_0, of a material is the mean length over which an electron will lose all but $1/e$ of its initial energy through radiative processes, while the interaction length of a material, λ, characterises the mean distance a hadron will travel through a material before undergoing a nuclear interaction. The depth of each calorimeter is optimised to fully contain their respective shower type.

The two calorimeter systems provide full coverage in ϕ and calorimetry in the range $|\eta| < 4.9$. Complete ϕ coverage is needed for precise reconstruction of $E_{\mathrm{T}}^{\mathrm{miss}}$, a principle component of searches using ATLAS. A diagram of the ATLAS calorimeter system is shown in Fig. 2.7.

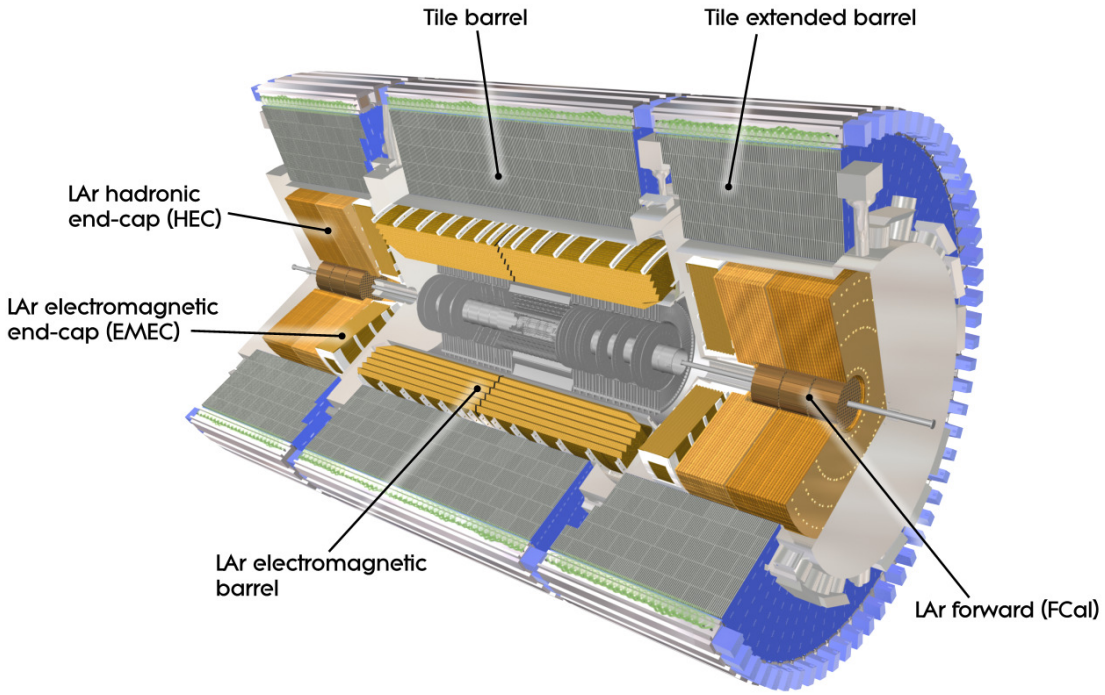

Figure 2.7: Cut-away diagram of the ATLAS Electromagnetic and Hadronic calorimeters. [35]

Electromagnetic Calorimeter

The ECAL is comprised of the barrel EM calorimeter which covers the pseudorapidity range $|\eta| < 1.475$ and the two end-cap EM calorimeters, each covering $1.375 < |\eta| < 3.2$. The ECAL is constructed using lead as the absorber material, while using liquid argon (LAr) as the active material. When a charged particle passes through the LAr, ionisation occurs, producing electrons. Using similar principles to the drift tubes described for the TRT, an electric field is applied, such that the ionisation electrons drift toward the electrodes. The thickness of the ECAL ranges from 22-38 radiation lengths to fully contain EM showers.

Hadronic Calorimeter

The Hadronic Calorimeter, as shown in Figure 2.7, can also be separated into several subsystems; the scintilating-tile calorimeter (HCAL), the LAr hadronic endcap calorimeter (HEC) and the forward calorimeter (FCal).

The tile calorimeter covers the range $|\eta| < 1.7$ and sits adjacent to the the ECAL. It is separated into a central barrel and two extended barrels. Each of these barrels is comprised of 64 modules with a size of $\Delta\phi \sim 0.1$ made of steel plate absorbers and scintillating plastic tiles. When charged particles pass through these scintillating tiles, photons with UV wavelengths are produced from polystyrene. These photons are collected by wavelength-shifting fibres, which are subsequently read out by photomultiplier tubes (PMTs).

The HEC is similar in construction to the ECAL, using LAr as the active medium, but instead of using lead as an absorber, uses copper. The HEC provides coverage in the range $1.5 < |\eta| < 3.2$. The HEC is constructed with two sets of wheels, one per end-cap, HEC1 and HEC2, respectively. Each of the four HEC wheels (a front and back wheel per end-cap) is constructed from 32 identical wedge-shaped modules.

Forward Calorimeter

The FCal provides coverage over $3.1 < |\eta| < 4.9$. Each FCal is split into three components; FCal1 is an electromagnetic module, while FCal2 and FCal3 are hadronic modules. FCal1 uses copper as an absorber material, whereas FCal2 and FCal3 use tungsten. All FCal modules use LAr as the active component.

2.7 Muon System

The Muon Spectrometer (MS) is the outermost part of ATLAS. Muons pass through the entire ATLAS detector before decaying, with a flight distance of $c\tau \sim 700$m, and do not undergo EM showering in the same way as electrons or photons. The main purpose of the

MS is to detect charged particles escaping the calorimeter systems and measure their momentum within the $|\eta| < 2.7$ range, also providing triggering capabilities within $|\eta| < 2.4$.

The MS comprises four subsystems; Monitored Drift-Tube (MDT) chambers, Cathode Strip Chambers (CSCs), Resistive Plate Chambers (RPCs) and Thin Gap Chambers (TGCs). The 1150 MDTs cover the $|\eta| < 2.7$ range with a resolution of 35μm per chamber. At the innermost layer of the MS, the MDTs are replaced by CSCs in the range $2.0 < |\eta| < 2.7$ due to their higher rate capability. The CSCs have a z resolution of 40μm, and a ϕ resolution of 5mm.

The triggering capability of the MS is provided by the RPCs and TGCs in the barrel and endcaps, respectively. The RPCs have a spatial resolution in z (ϕ) of 10mm (10mm) and a temporal resolution of 1.5ns, while the TGCs have a spatial resolution in R (ϕ) of 2-6mm (3-7mm) and a temporal resolution of 4ns.

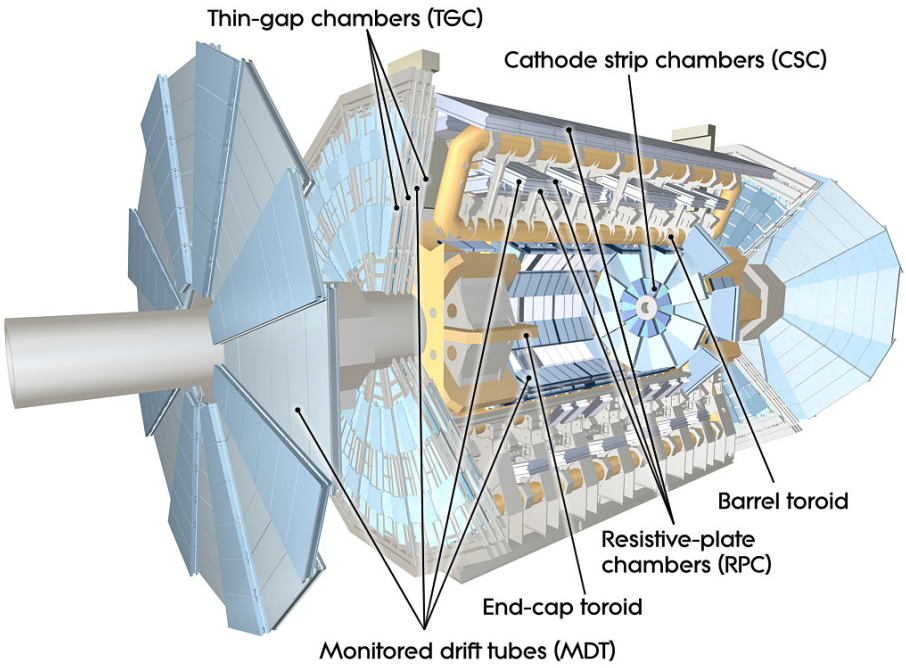

Figure 2.8: Cut-away diagram of the ATLAS Muon Spectrometer. [35]

2.8 ATLAS Trigger System

The temporal bunch-separation provided by LHC in Run-2 is 25ns, meaning the proton-proton bunch-crossing frequency is 40 MHz. However, saving all of these events to disk is not possible due to the huge bandwidth and storage required, with each event requiring around 1.3MB of storage. Saving all events to disk, however, is unnecessary as most events

will contain physics which is deemed 'uninteresting'. Figure 2.9 shows the dominant production cross-sections for SM processes at the LHC. As shown in Figure 2.9, processes such

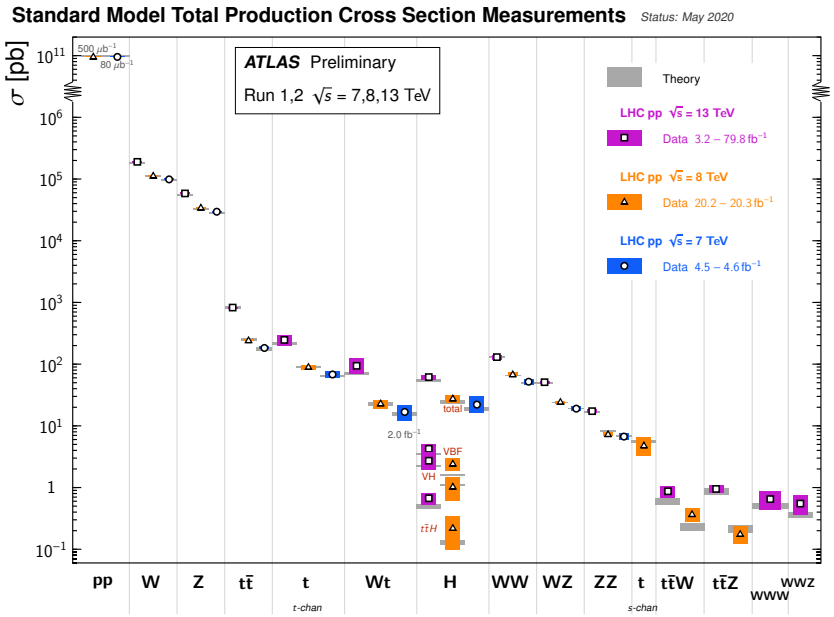

Figure 2.9: Plot showing the production cross-sections for the most dominant SM background processes at the LHC [37].

as multi-jet production are among the most-frequently produced at the LHC, and are of little experimental interest. ATLAS employs a trigger system which makes rapid decisions on whether to save the event to disk or not.

The ATLAS trigger system consists of the Level-1 (L1) hardware trigger and the software-based High-Level trigger (HLT). The L1 trigger uses coarse detector information from the calorimeters and MS to identify muons, electrons, photons, jets and hadronically-decaying taus with high transverse momentum, or events containing large amounts of total transverse energy and $E_{\mathrm{T}}^{\mathrm{miss}}$. The L1 trigger uses a subset of the ATLAS subsystems; the RPC and TGC are used for muons, while the calorimeter subsystems are used for EM clusters, jets, tau leptons, $E_{\mathrm{T}}^{\mathrm{miss}}$ and large total tranverse energy. The L1 trigger operates at a maximum of 100kHz, with each decision being made in less than 2.5μs. Regions-of-interest (RoIs) are identified by the L1 trigger; these are regions in η and ϕ containing potential physics objects. These RoIs are used as seeds in the HLT.

The software based HLT takes the full event information from the L1 RoI seeds and investigates the RoIs. The event reconstruction used in the HLT is then used to accept or reject the event. The HLT further reduces the event rate to around 1.5kHz. A functional diagram of the trigger and data acquisition system is shown in Figure 2.10.

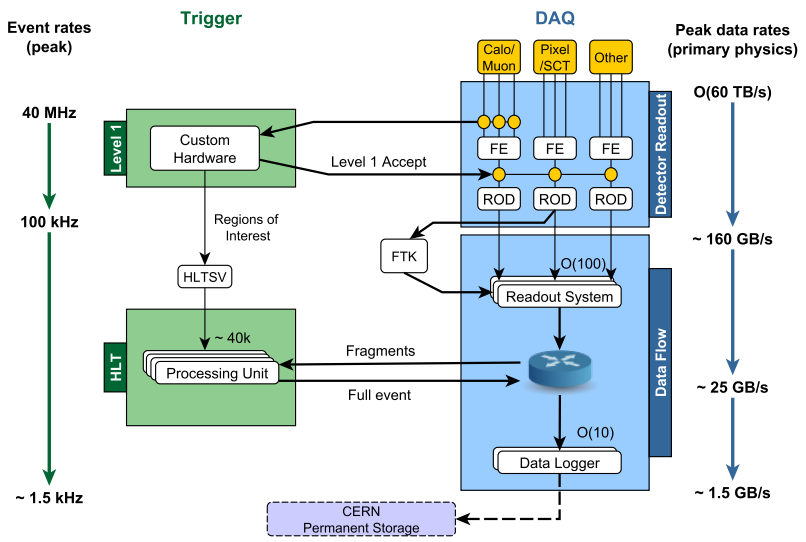

Figure 2.10: A functional diagram of the ATLAS trigger and data acquisition system (TDAQ). The diagram shows the flow of data from detector readout, through the L1 trigger, to the HLT and eventual disk storage. The steps following this are discussed in Chapter 4.

Chapter 3

Data and Monte Carlo samples

This Chapter discusses the datasets used in the physics analyses detailed in Chapter 6 and 7, detailing the running conditions during data-taking and the triggers used to collect the data. Along with the datasets, the procedure through which Monte Carlo (MC) samples are generated is discussed, along with a brief discussion of the generators used in the analyses in the subsequent Chapters. Finally, this Chapter discusses the complexities of simulating the single top Wt-channel process due to interference with the $t\bar{t}$ process, an effect which can generate uncertainties of $\mathcal{O}(100\%)$ on the predictions of the single top background. Studies are performed to quantify the impact of the interference in the analyses detailed in Chapters 6 and 7, where the single top process is one of the major SM backgrounds.

3.1 Datasets

The physics analyses discussed in Chapters 6 and 7 used data collected during the Run-2 data-taking period (2015-2018) in pp collisions at $\sqrt{s} = 13$ TeV, accumulating 139fb^{-1} ($\pm 1.7\%$) of collision data in total. The physics analysis described in Chapter 6 used a subset of this data, taken in 2015-2016, with a total integrated luminosity of 36.1fb^{-1} ($\pm 2.1\%$). The primary measurement of the luminosity is recorded by the LUCID detector [38], which sits 17m from the interaction point on both the A and C side of ATLAS and measures the visible number of interactions per bunch-crossing. In Run-2, proton bunches are separated by 25ns, compared to 50ns in Run-1. Each proton bunch contains $\mathcal{O}(10^{11})$ protons and as such each bunch-crossing can have multiple inelastic pp interactions. Each proton-proton collision which produces at least two tracks with $p_T > 0.4$ GeV is classed as an interaction point, being referred to as a collision vertex. The collision vertex in each bunch-crossing which has the highest $\sum p_T^2$ of tracks is identified as the Primary Vertex (PV). All other vertices are considered a background to the primary vertex, known as 'pileup', which is described in further detail in Chapter 2. Pileup at the LHC is one of the greatest challenges for accurate track reconstruction, and will continue to be so in the HL-LHC phase of operation. The pileup conditions for Run-2 are shown in Figure 2.3.

Triggers

As previously discussed, it is not possible to save all events to disk due to the huge bandwidth required to readout, partially-reconstruct and trigger on events in real-time. Events passing a L1 trigger are selected and processed with the HLT, and thus events are collected at a reduced rate. This reduced event rate integrated over Run-2 still provides a huge dataset in which to search for evidence of New Physics. For the New Physics models considered in this Thesis, a common signature of the production of BSM particles is the presence of large amounts of $E_{\mathrm{T}}^{\mathrm{miss}}$ in an event, due to the presence of non-SM particles in the final state. The analyses described in Chapter 6 and 7 both used $E_{\mathrm{T}}^{\mathrm{miss}}$ triggers to select events in data which may contain non-SM particles. Table 3.1 shows the list of triggers used in each data-taking year for the analysis detailed in Chapters 6 and 7. The names of

Year	Triggers
2015	HLT_xe70_mht
2016	HLT_xe90_mht_L1XE50
	HLT_xe100_mht_L1XE50
	HLT_xe110_mht_L1XE50
2017	HLT_xe90_pufit_L1XE50
	HLT_xe110_pufit_L1XE55
2018	HLT_xe110_pufit_xe70_L1XE50
	HLT_xe120_pufit_L1XE50
	HLT_xe110_pufit_xe65_L1XE50
	HLT_xe110_pufit_xe70_L1XE50

Table 3.1: A table showing the list of $E_{\mathrm{T}}^{\mathrm{miss}}$ triggers used in the analyses described in Chapter 6 and Chapter 7.

the triggers listed in Table 3.1 hold information of the trigger thresholds and algorithms used. The L1XE50 trigger threshold applies to the $E_{\mathrm{T}}^{\mathrm{miss}}$ (XE), and must satisfy $E_{\mathrm{T}}^{\mathrm{miss}} > 50$ GeV at the L1 trigger level. The HLT prefix indicates that an event must pass the HLT trigger where the trigger threshold is specified in the form xe110, where the 110 after xe indicates the HLT trigger threshold is $E_{\mathrm{T}}^{\mathrm{miss}} > 110$ GeV. The HLT algorithm used to calculate the $E_{\mathrm{T}}^{\mathrm{miss}}$, which are described in detail in [38], are denoted by mht or pufit where the former calculates the $E_{\mathrm{T}}^{\mathrm{miss}}$ based on jets while the latter uses a pileup-suppression technique to estimate the $E_{\mathrm{T}}^{\mathrm{miss}}$. The cell-based algorithm, which uses the uncalibrated energy deposits in the calorimeter to estimate the $E_{\mathrm{T}}^{\mathrm{miss}}$, omits any additional designation from the trigger name. Where two separate xe thresholds are present in a name, the former refers to the threshold for the pufit algorithm, while the latter refers to the threshold for the cell-based algorithm.

Due to the evolving conditions throughout each year of data-taking, there are frequently multiple triggers listed per year. These are 'period-dependent' triggers, and as instantaneous luminosities grow and the pileup profile shifts to higher $\langle\mu\rangle$, as defined in Chapter 2, so too do the trigger thresholds. The efficiency of the $E_{\mathrm{T}}^{\mathrm{miss}}$ trigger is determined by,

$$\epsilon(\mathcal{S}_i) = \frac{N\left(\text{trigger}|\mathcal{S}_i\right)}{N\left(\mathcal{S}_i\right)} \ , \tag{3.1.1}$$

where $\mathcal{S}_i$ denotes some event selection criteria, the denominator is the number of events passing the selection $\mathcal{S}_i$ and the numerator is the subset of those events which also pass the trigger requirements. The selection, $\mathcal{S}_i$, is relaxed to fully assess the trigger efficiency over a range of $E_{\mathrm{T}}^{\mathrm{miss}}$ values. When performing searches for New Physics processes which have low rates compared to the SM backgrounds, a high-trigger efficiency is required to retain as many candidate signal events as possible. The efficiency of the $E_{\mathrm{T}}^{\mathrm{miss}}$ trigger in the years 2015-2018 is shown in Figure 3.1 as measured in $Z \to \mu\mu$ events. $Z \to \mu\mu$ events are used as the muons have minimal interactions with the calorimeter material and thus the dimuon transverse momentum provides a good proxy for the $E_{\mathrm{T}}^{\mathrm{miss}}$.

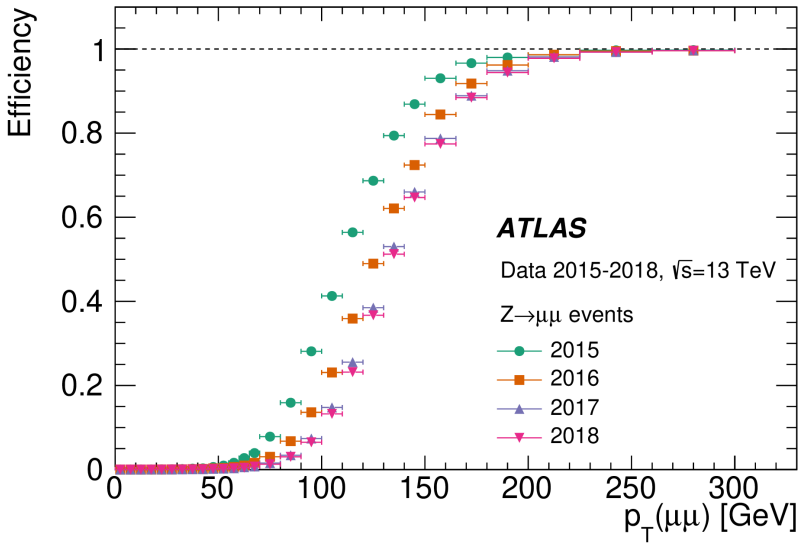

Figure 3.1: A plot showing the efficiency of the lowest unprescaled $E_{\mathrm{T}}^{\mathrm{miss}}$ trigger from 2015-2018, known as the 'turn-on' curve.

In order to ensure the trigger accepts events in data and from all MC processes with equal efficiency, the analyses detailed in Chapters 6 and 7 require all events are on the trigger 'plateau', the region of constant efficiency, shown in the 'turn-on' curve in Figure 3.1 at values above 200 GeV.

3.2 Monte Carlo simulation

An accurate, precise simulation procedure is required in order to make meaningful comparisons between SM predictions and the data collected by ATLAS. This is known as Monte Carlo (MC) simulation. A generic MC simulation works by randomly sampling a process-specific distribution many times to obtain a sample of predictions for that process. In the context of this Thesis, MC simulation is used to produce simulated samples of SM and BSM processes produced in pp collisions at the LHC and subsequently detected by ATLAS.

3.2.1 MC event generation

Typically, the procedure for simulating physical processes through MC simulation involves: *matrix element calculations (ME)*, *parton showering (PS)*, *hadronisation* and simulation of the *underlying event* (UE). This chain is represented in Figure 3.2.

The composite nature of protons is described by the parton model of hadrons, which describes the proton content as quarks and gluons collectively known as partons. In pp scattering events, the factorisation theorem enables the interaction of the protons to be *factorised* into terms describing the long-distance 'hard-scatter' interaction between two partons from the incoming protons and terms describing the short-distance distribution of the partons in the incident protons. The energy scale which separates the long-distance and short-distance phenomena is known as the factorisation scale, μ_F, and is introduced to remove low energy divergences from the cross-section calculation. Above the factorisation scale, the physics is modelled using the ME, while below the factorisation scale it is modelled by the parton distribution functions (PDFs) and the PS.

$$\sigma = \sum_{i,j} \overbrace{\int \mathrm{d}x_1 f_i\left(x_1, \mu^2\right) \int \mathrm{d}x_2 f_j\left(x_2, \mu^2\right)}^{\text{PDF}} \underbrace{\sigma_{ij}\left(Q^2\right)}_{\text{Hard scatter}} \tag{3.2.1}$$

The overall physics process can be therefore simulated in different steps as mentioned above. The incoming partons produce a primary interaction (the hard scatter) shown by the red circle and representing the ME calculation. The remaining partons from the incoming protons are also able to interact, producing multi-parton interactions (MPI), resulting in additional, softer particles. These softer interactions represent the UE and are shown by the additional blue partons and the purple oval. From the PV and the ME portion of the simulation, the PS is shown by the red cascade of partons being sequentially emitted. The light green ovals show the hadrons present after the PS and the subsequent green circles show the decay of these hadrons.

Each stage of the event generation procedure will be briefly discussed before summarising the MC simulations used to generate background samples used in the analyses detailed in Chapters 6 and 7. The details of the signal MC samples will be given in the relevant chapters.

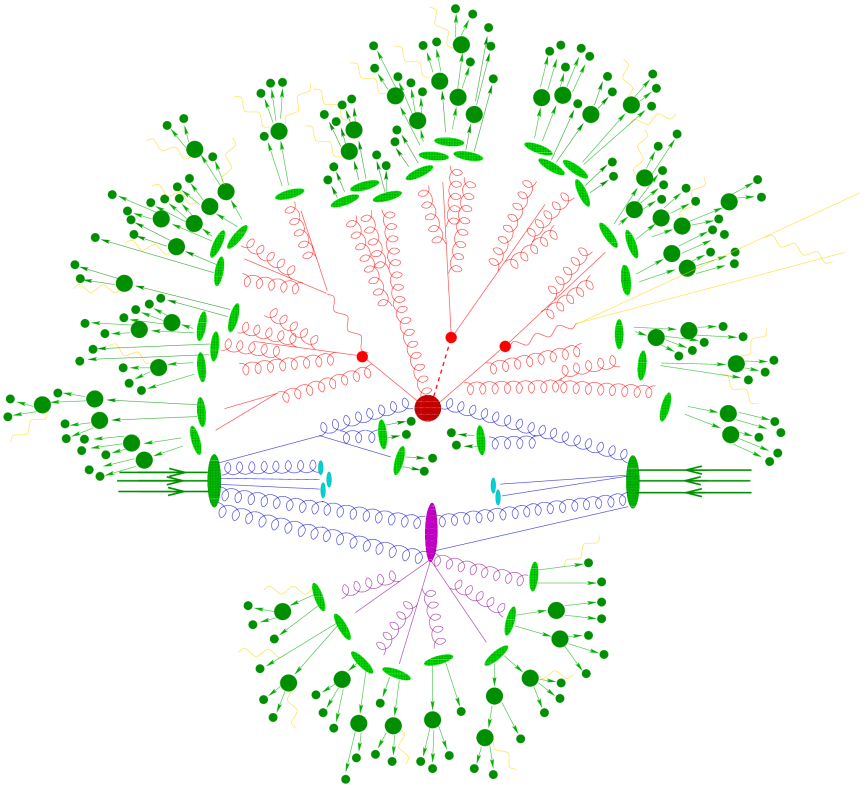

Figure 3.2: A representative diagram showing the MC simulation chain.

Hard scatter

The hard scatter calculation evaluates the process in which the incoming partons interact and undergo some transition into different final state particles, and is the highest-energy process evaluated during event generation. The hard scatter calculation is performed by evaluating the Feynman diagrams which represent the process of interest to yield the matrix element (ME). MEs can be calculated at different orders in QCD. Tree-level MEs have two vertices, and hence the ME goes like $\mathcal{M} \propto g_s^2$, while the cross-section goes like $\sigma \propto |\mathcal{M}^2| \propto g_s^4$. Most processes relevant at the LHC are calculated at next-to-leading order (NLO), with $\mathcal{M} \propto g_s^3$. As an example, representative tree-level diagrams for $t\bar{t}$ are shown in Figure 3.3. The hard scatter calculation often results in unstable particles in the final state. The subsequent stages of the event generation process evolve these hard, unstable particles from the highest energy levels down to softer, stable particles.

Figure 3.3: This figure shows tree-level Feynman diagrams for the $t\bar{t}$ process. These diagrams are also relevant for the discussion of $t\bar{t}$-Wt interference later in this Chapter.

Parton distribution functions

Due to the composite nature of protons, the collisions at the LHC are actually interactions of the partons within the proton; qq or gg, for example. Both the valence quarks (uud, for a proton) and sea quarks (virtual quark-antiquark pairs continually being created and annihilated inside the proton) contribute to the parton-parton collisions. Therefore, to accurately predict physical processes, the partons within the proton must be well-modelled, along with the fraction of the total proton momentum that each parton carries, known as the Bjorken x. PDFs predict the probabilty that a parton of a given type is present inside the proton with a given x, at a squared energy-scale Q^2. PDF sets are determined through fits to data, namely deep inelastic scattering (DIS) data, with data from ATLAS and CMS being included in the most recent global fits to data. [39]

PDFs can be calculated to differing orders in QCD, namely leading order (LO), next-to-leading order (NLO) and next-to-next-to-leading order (NNLO). The treatment of quark flavours is also a consideration when evaluating PDFs. The four-flavour scheme (4FS) and five-flavour scheme are the most common treatments of partons for PDFs. In the 4FS, b-quarks are treated as massive partons, unlike the other parton types, and the proton content is limited to gluons and the u, d, c and s quarks. In the 5FS, all partons are treated as massless and the proton can contain gluons and all quarks except the top quark. In both flavour-schemes, the b-quark is included in the final state.

Parton shower, Hadronisation and underlying event

The PS procedure evolves the hard scatter from an energy scale Q^2 down to the hadronisation scale Q_0^2, typically around the pion mass ($\sim$ 200 MeV), through sequential emissions of quarks and gluons, including soft and co-linear emissions. This procedure is repeated until all partons in the event reach the 'cut-off' point of the hadronisation scale. This procedure takes the event from one with only a few final state particles to a complex final state with many quarks and gluons.

Considerations must be made when applying a PS algorithm to events with additional partons in the final state, such as MEs calculated at NLO. For example, an event with n-jets in the final state can be produced in two ways; by evolving an event, through soft/-colinear emission, produced at the ME-level with n partons in the final state, or by introducing an additional hard parton emission in the PS procedure to an $n-1$ parton event. The overlap between these two possibilities is treated using a matching/merging procedure.

The hadronisation procedure starts after the PS at the cut-off scale of around 1 GeV. This procedure combines the partons present after the PS into colour-neutral states, as required by QCD. There are two widely-used models of hadronisation; the Lund String model [40], and the cluster model [41]. The former treats quark-antiquark pairs as the ends of a string, with a potential energy between the quarks that is proportional to its length such that the $q\bar{q}$ pair are linearly-confined. As the distance between the $q\bar{q}$ pair increases, so too does the potential energy, until it is energetically-favourable for the string to break, forming an additional quark-antiquark pair. The cluster model uses the property of *preconfinement* in QCD, in which the partons in a shower cluster together into colourless groups. These colour-singlets follow an invariant mass distribution which is independent of the hard scatter process. Unstable hadrons are able to decay through allowed SM transitions until all particles in the final state are stable.

The underlying event refers to all partonic interactions other than the hard scatter. These interactions can arise from the partons from the incoming protons not involved in the hard scatter as well as from any additional partons radiated in the event. Additional jets can arise from the UE, although these are typically much softer than jets produced in the hard scatter. ATLAS makes use of two MC tunings to data, the A14 tune [42] and the A3 tune [43], to improve the modelling of the UE.

3.2.2 Simulation of SM backgrounds

This section details the event generators used for simulating the SM background samples for the analyses described in the subsequent chapters. For the HL-LHC prospects study detailed in Chapter 9, the MC samples used were generated without being passed through the ATLAS detector simulation, but instead a parameterised detector simulation for the HL-LHC ATLAS detector. This is explained in more detail in Chapter 9 and Appendix A.

Pair production of top quarks, $t\bar{t}$, was generated using PowhegBox v2 [44–47] interfaced with Pythia8 v8.230 and the A14 tune with the NNPDF2.3 LO PDF set for the ME calculations. The h_{damp} parameter in PowhegBox, which controls the p_{T} of the first additional emission beyond the Born level and thus regulates the p_{T} of the recoil emission against the $t\bar{t}$ system, was set to 1.5 times the top-quark mass ($m_t = 172.5$ GeV) as a

result of studies documented in [48].

The generation of single top quarks in the Wt-channel, s-channel and t-channel production modes was performed by PowhegBox v2 [45–47, 49] similarly to the $t\bar{t}$ samples. For all processes involving top quarks, top-quark spin correlations were preserved. All events with at least one leptonically decaying W boson were retained; fully hadronic $t\bar{t}$ and single-top events do not contain sufficient $E_{\mathrm{T}}^{\mathrm{miss}}$ to contribute significantly to the background.

The production of $t\bar{t}$ pairs in association with electroweak vector bosons (W, Z) or Higgs bosons was modelled by samples generated at NLO using MadGraph v2.2.3 and showered with Pythia8 v8.212.

Events containing W or Z bosons with associated jets, including jets from the fragmentation of heavy-flavour quarks, were simulated using the Sherpa v2.2.1 [50] generator. Matrix elements were calculated for up to two additional partons at NLO and four partons at LO using the Comix [51] and OpenLoops 1 [52] ME generators and were merged with the Sherpa PS [53] using the ME+PS@NLO prescription [54]. The NNPDF3.0 NNLO [55] PDF set was used in conjunction with a dedicated PS tune developed by the Sherpa authors.

Diboson processes were also simulated using the Sherpa generator using the NNPDF3.0 NNLO PDF set. They were calculated for up to one (ZZ) or zero (WW, WZ) additional partons at NLO and up to three additional partons at LO.

3.3 Simulating Wt-channel single top at NLO

In many search channels, the $t\bar{t}$ and single top backgrounds are among the most prominent backgrounds due to their relatively high cross-sections and complex, irreducible, multi-particle final states which can exactly mimic the final states of many New Physics processes. Making predictions of these SM processes at the highest precision possible therefore enables searches for New Physics to set the best possible statistical limits, but particular care must be taken to treat the interference of $t\bar{t}$ and Wt-channel single top correctly. Both the $t\bar{t}$ and single top backgrounds are simulated at NLO and normalised to NNLO cross-section calculations. At LO, Wt-channel single top will almost always have a final state containing WWb, distinct from the $WWbb$ final state in $t\bar{t}$ production, as seen by comparing Figure 3.3 and 3.4.
However, simulating Wt-channel single top at NLO introduces diagrams which have a $WWbb$ final state, meaning the $t\bar{t}$ and Wt processes can interfere. NLO diagrams for Wt-channel single top are shown in Figure 3.5. When considering the $WWbb$ final state, the

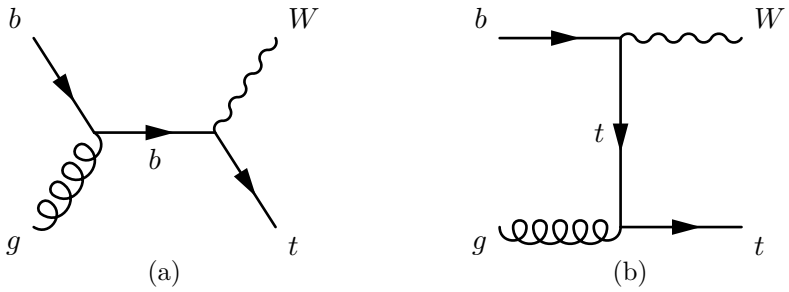

Figure 3.4: Feynman diagrams showing Wt-channel production at tree-level, where the final state is distinct from the $t\bar{t}$ process.

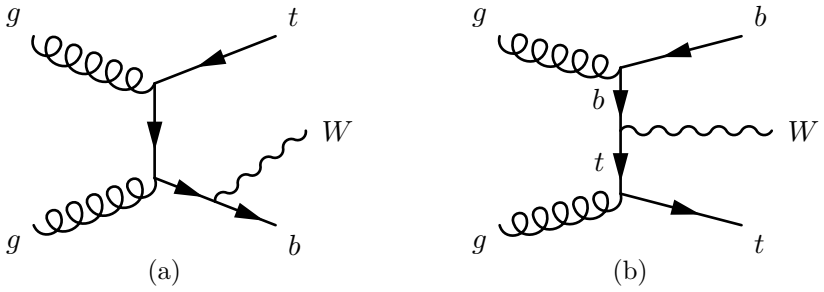

Figure 3.5: Feynman diagrams showing Wt-channel production at NLO. These diagrams interfere with the $t\bar{t}$ process due to their identical final state. The Wt diagrams at NLO can be separated into the number of resonant top quarks present. Figure 3.5b shows a 'single-resonance' diagram, while Figure 3.5a shows a 'double-resonance' diagram.

amplitude can be written as the sum of contributions from the $t\bar{t}$ and Wt process. As there is overlap between the two processes, diagrams with two resonant (on-shell) top quarks, known as 'double-resonance' diagrams are attributed to the $t\bar{t}$ process, while diagrams with a single resonant (on-shell) top quark are referred to as 'single-resonance' diagrams and are attributed to Wt production. Non-resonant $WWbb$ production is not considered. The amplitude can be written as:

$$\mathcal{A}_{WWbb} = \mathcal{A}_{DR} + \mathcal{A}_{SR} \tag{3.3.1}$$

where DR and SR correspond to the double-resonant and single-resonant components, respectively. The production goes with the square of the amplitude, which is where the interference terms arise:

$$|\mathcal{A}_{WWbb}|^2 = |\mathcal{A}_{SR}|^2 + |\mathcal{A}_{DR}|^2 + 2\mathcal{R}e(\mathcal{A}^*_{SR}\mathcal{A}_{DR}) \tag{3.3.2}$$

The first term on the right side is the contribution from DR diagrams, where there are two resonant top quarks, and the second term from SR diagrams, where there is a single resonant top quark, and the last term from interference between the two sets of diagrams.

All top-pair MC samples used in this Thesis are generated using only the diagrams which contribute to $\mathcal{A}_{DR}$, having exactly two resonant top quarks. The nominal choice for modelling the single top Wt-channel process uses only the diagrams which contribute to $\mathcal{A}_{SR}$, neglecting diagrams with two resonant top quarks and hence removing any interference from the cross-section. In regions where $t\bar{t}$ production dominates, the impact of the interference is small. However, it is important to assess the size and impact of the interference, especially in the extreme regions of phase space often covered by searches for New Physics, as the interference becomes important in regions where $m_{Wb} \sim m_t$. Two schemes for assessing the impact of the $t\bar{t}$-Wt interference are used in this Thesis and will be discussed in the following subsections.

3.3.1 Diagram removal vs. diagram subtraction

As previously mentioned, the nominal method of simulating the Wt-channel single top process is to remove all diagrams with two resonant top quarks; this method is known as the *diagram removal* (DR) scheme [56]. An alternate scheme of generation, known as *diagram subtraction* (DS) [56] is defined such that single- and double-resonance diagrams are included, and the contribution from the double resonance diagrams is subtracted at the cross-section level as follows:

$$d\sigma^{DS} = d\sigma^{WWbb} - d\sigma^{subt} \tag{3.3.3}$$

In Equation 3.3.3, the first term on the right is proportional to Equation 3.3.2. In the analysis detailed in Chapter 6, the differences between the DR and DS schemes for generating the Wt process were found to $\mathcal{O}(100\%)$ in *all* analysis regions due to poor MC statistics in the DS sample. The difference between the DR and DS predictions are evaluated in a control region (CR). In this region, the contribution of single top is expected to be large and MC predictions can be tested. The predictions for the two simulation schemes in the single top control region can be seen in Table 3.2.
As seen in Table 3.2, the DR and DS schemes make drastically different predictions for the single top yield in this region. The data-MC difference of the two predictions can be seen in Figure 3.6, showing the $E_{\mathrm{T}}^{\mathrm{miss}}$ distributions in CRST with both the DR and DS Wt samples. When comparing the predictions to data, it is clear that the DS predictions are much further from the observed yield than the DR prediction, and thus the DS prediction is underestimating the process in this region.
Given that the DS predictions do not correctly represent the data, an uncertainty estimated as the difference of the DR and DS predictions would be incorrect, and hence an alternative assessment must be found for estimating the interference uncertainty.

In the analysis detailed in Chapter 7, studies were performed to find a kinematic region to

Process	MC prediction
$t\bar{t}$	17.72 ± 1.85
Single top (DR)	28.54 ± 1.72
Single top (DS)	6.61 ± 1.9
W+jets	5.80 ± 1.32
$t\bar{t}V$	3.14 ± 0.27
Diboson	0.84 ± 0.26
Small backgrounds	0.10 ± 0.05
Total MC (DR)	56.1 ± 2.9
Total MC (DS)	34.2 ± 3.0
Data	64

Table 3.2: A table showing the estimated yields from MC of SM processes in the single top CR, defined in Table 6.3 corresponding to 36.1 fb^{-1} data. The data-MC discrepancy is much larger with the DS Wt prediction and the region becomes dominated by top-pair production. The uncertainty on the MC prediction is from the MC statistical uncertainty.

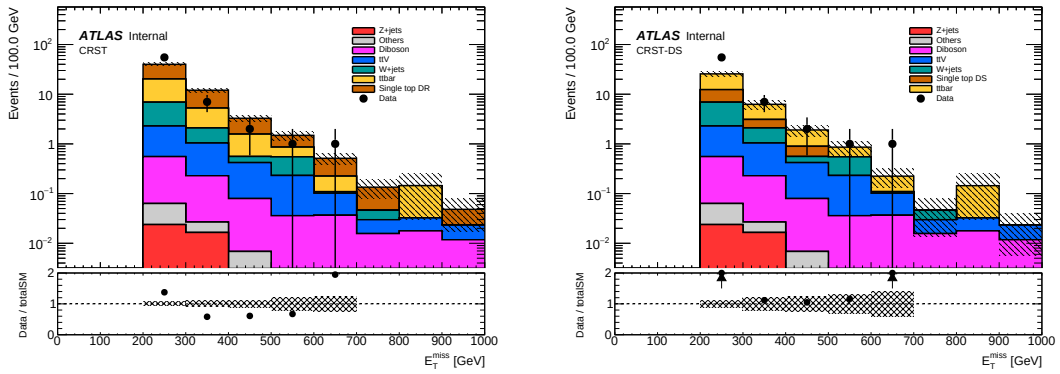

(a) (b)

Figure 3.6: Plots showing the E_T^{miss} distribution in the single top CR of the analysis detailed in Chapter 6. Figure 3.6a shows the data-MC comparison using the DR single top sample, while Figure 3.6b shows the same comparison using the DS single top sample.

use as a CR for the Wt background, a relatively minor but irreducible background. Using a similar method to those used to optimise the signal selection, as described in Section 5.3, a region where the single top background was dominant was found using a combination of an adapted random grid search and a genetic algorithm. The kinematic selections for this region are summarised in Table 3.3.

The estimated yields and purity obtained using these selections are given in Table 3.4.

The distributions of the subleading b-jet p_T and $\Delta\phi(\ell, E_T^{miss})$, used to define and isolate the Wt background, is shown in Figure 3.7 for both the DR and DS schemes.

Variable	Selection
am_{T2}	> 220 GeV
m_W^{had}	< 60 GeV
m_T	$\in [40, 100]$ GeV
p_T^{b2}	> 50
$\Delta\phi(\ell, E_T^{miss})$	< 0.5

Table 3.3: This table shows the selections used, in addition to the preselection cuts listed in Table 7.2, for the single top CR study for the analysis detailed in Chapter 7.

Process	MC prediction
$t\bar{t}$	135.52 ± 1.87
Single top (DR)	253.39 ± 8.04
Single top (DS)	39.08 ± 3.2
W+jets	134.75 ± 4.35
$t\bar{t}V$	3.41 ± 0.25
Z+jets	0.83 ± 0.14
Diboson	7.66 ± 0.85
ttH	1.37 ± 0.1
tWZ	0.02 ± 0.03
Purity (DR)	47.2%
Purity (DS)	12.1%
Data	363

Table 3.4: This table shows the predicted background yields for all SM backgrounds considered using the selections defined in Table 3.3, along with the purity of single top for both the DR and DS schemes, and finally the observed data in this region, corresponding to 139 fb^{-1} data. As can be seen there is a huge discrepancy between the two Wt generation schemes, with the data being enveloped by the two predictions.

Once again, it was found that the differences in the predictions between the DR and DS MC samples are large, with the DS scheme underestimating the data in the CR. The predictions from the DR scheme were used for the analysis, and the proposed CR was not used in the final analysis.

3.3.2 Coherent $WWbb$ simulation

An alternative approach evaluated for the search detailed in Chapter 6 uses three sets of complementary MC samples, 'singleres', 'doubleres' and 'sum', to simulate the $WWbb$ final state, generated at LO and at truth-level. The 'singleres' samples include diagrams with exactly one resonant top quark, corresponding to $\mathcal{A}_{SR}$, the 'doubleres' samples include di-

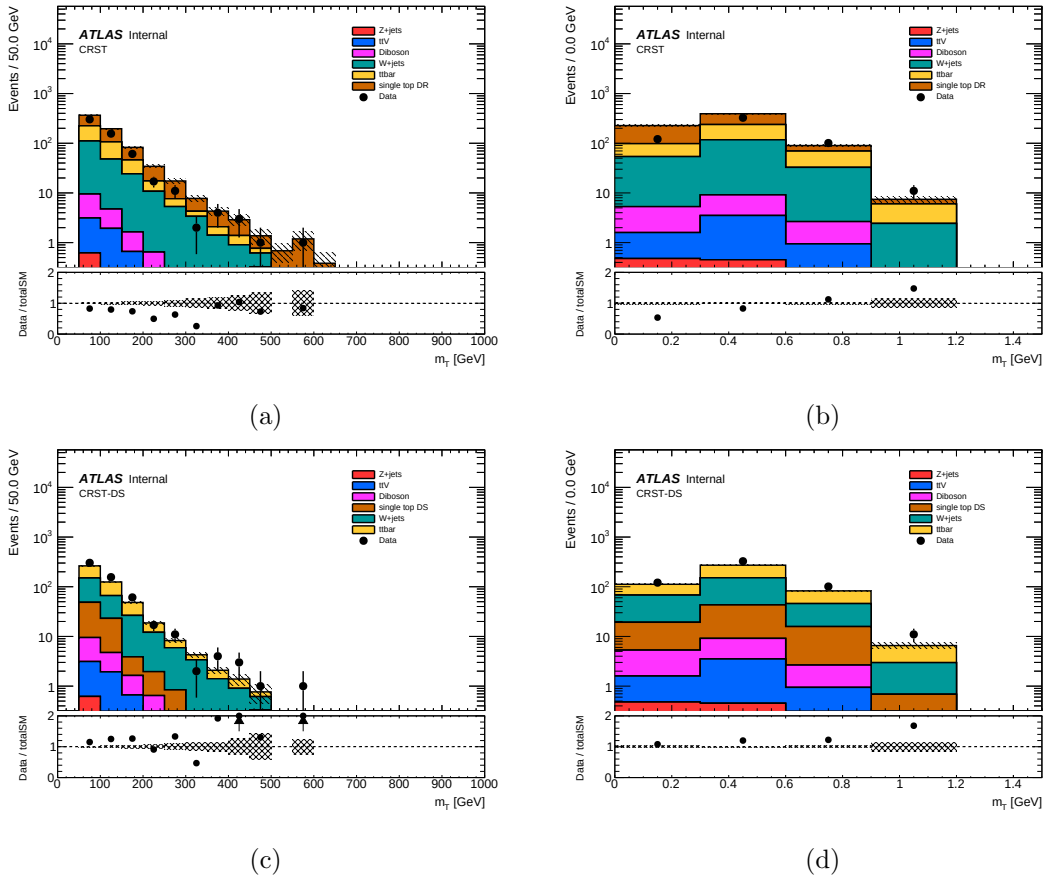

Figure 3.7: This Figure compares the two key variables used to isolate the Wt background for the DR and DS schemes. Figures 3.7a and 3.7c show the transverse momentum of the second b-jet in the event for the DR and DS schemes, respectively, while Figures 3.7b and 3.7d show the difference in ϕ between the lepton and $E_{\mathrm{T}}^{\mathrm{miss}}$ in the events for the DR and DS schemes, respectively. Large differences are observed between the DR and DS schemes, with the observed data being enveloped by the two.

agrams with two resonant top quarks, corrsponding to $\mathcal{A}_{DR}$ and the 'sum' samples include all diagrams with at least one resonant top quark, corresponding to $\mathcal{A}_{WWbb}$. As these samples are generated at LO, these samples are used only as a comparison between themselves, and not the nominal DR prediction, generated at NLO. Figure 3.8 shows comparisons of the shape and normalisation of the m_T and m_{CT} distributions, defined in Section 5.2 among the key discriminating variables used in this analysis, for the three samples at preselection level and in the single top CR.

Using the three sets of samples, it is possible to directly estimate the impact of the interference, by comparing the MC prediction for the Wt process with and without interference effects. The estimated yield for the Wt process with the interference effects, N_{MC}^{Wt+int}, is given by:

$$N_{MC}^{Wt+int} = N_{MC}^{sum} - N_{MC}^{doubleres} \tag{3.3.4}$$

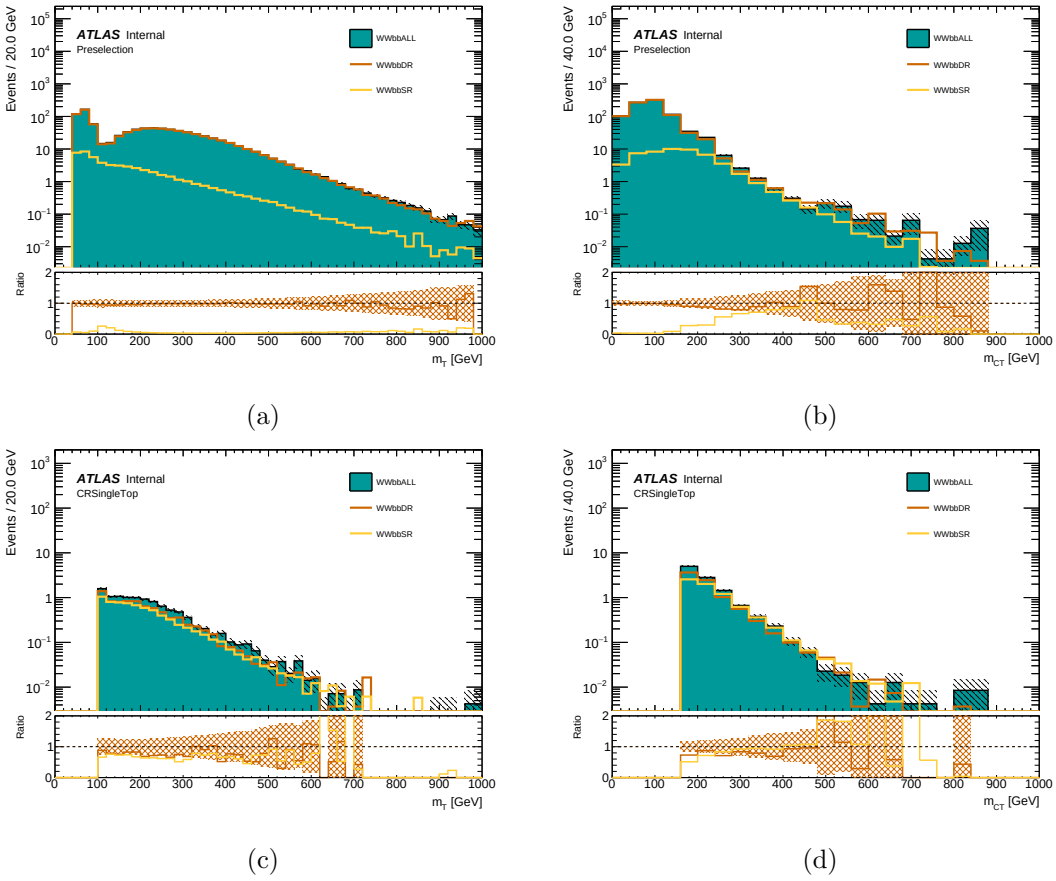

Figure 3.8: This figure shows the difference in shape and normalisation of for the $WWbb$ singleres, doubleres and sum samples. The ratio in the bottom panel shows the ratio of the singleres and doubleres to the sum, while the hatched error bar shows the sum in quadrature of the MC statistical uncertainty of the sum and doubleres sample. This error is equivalent to the statistical uncertainty on the estimate of the Wt singleres + interference.

This estimated yield can be directly compared with the prediction for the Wt process, N_{MC}^{Wt}. Table 3.5 shows a comparison of the nominal Wt DR prediction compared with the DS prediction, along with the predictions for the dedicated $WWbb$ samples, and finally showing the predicted Wt yield including interference effects, calculated using Equation 3.3.4.

The coherent simulation of the $WWbb$ final state, with contributions from both single- and double-resonance processes, provides a much more reasonable estimate of the uncertainty arising from the interference between the $t\bar{t}$ and Wt-channel processes when compared with the comparison of the DR and DS schemes. This method was used for evaluating the interference uncertainty in the analysis detailed in Chapter 6.

Region	TRLM	TRMM	TRHM	STCR
Single top (DR)	22.81 ± 3.12	19.67 ± 1.51	53.11 ± 2.51	28.54 ± 1.72
Single top (DS)	12.25 ± 2.17	13.22 ± 2.16	28.43 ± 2.97	6.61 ± 1.9
WWbb singleres	6.68 ± 0.05	8.62 ± 0.06	21.38 ± 0.1	23.44 ± 0.11
WWbb doubleres	23.28 ± 0.38	80.73 ± 0.48	598.7 ± 1.29	22.26 ± 0.3
WWbb sum	25.37 ± 0.4	84.94 ± 0.5	610.37 ± 1.34	29.97 ± 0.34
WWbb singleres + interference	2.09 ± 0.55	4.21 ± 0.69	11.67 ± 1.86	7.71 ± 0.45

Table 3.5: This table shows a comparison of the nominal DR Wt prediction with the DS prediction, and the predictions of the three sets of $WWbb$ samples, corresponding to 139 fb^{-1} data. The regions used in this Table are defined later in Table 6.3. The value quoted for the $WWbb$ singleres + interference prediction is calculated using Equation 3.3.4. The DR and DS predictions both use samples reconstructed with the full ATLAS detector simulation, while the $WWbb$ samples are generated at truth-level. The uncertainty on the MC prediction is from the MC statistical uncertainty.

Chapter 4

Object reconstruction

Particles produced in the pp collisions inside ATLAS can interact with the detector subsystems, as described in Chapter 2, with each type of particle leaving a unique signature. The combination of the tracking and calorimetry information enables the reconstruction of the underlying physics of an event. When combining this information, particles are referred to as physics 'objects', with the objects of interest to this Thesis being leptons, jets and $E_{\mathrm{T}}^{\mathrm{miss}}$. This Chapter begins by giving an overview of the different signatures of each particle type, before summarising the reconstruction techniques for each object.

4.1 Reconstruction overview

The interaction of particles with the detector subsystems is determined by several factors. Firstly, charged particles create small electrical signals when passing through the tracking layers of the detector due to ionisation effects, whereas neutral particles pass through the tracking layers without leaving a signature. Secondly, the particle type will determine the type of particle shower that occurs when entering the calorimeters, with electrons and photons depositing almost all of their energy in the ECAL, and particles which interact via the strong interaction depositing energy in both the ECAL and the HCAL. Finally, the presence of particles which do not interact with the detector subsystems, namely neutrinos and any massive, weakly-interacting new particles produced in the event, can be inferred from the total transverse momentum imbalance of the system, the $E_{\mathrm{T}}^{\mathrm{miss}}$. This is defined as the magnitude of the negative vector sum of all of the visible particles measured by ATLAS in an event. Figure 4.1 shows a representative diagram of the signatures of various particle types which are reconstructed within ATLAS.

By introducing loose requirements on the combination of the tracking and calorimetry information, 'baseline' objects are defined, placing requirements on the p_{T}, η and isolation of the object. Particle signatures in the same region of the detector can be reconstructed into multiple objects simultaneously, and thus to circumvent double counting a procedure

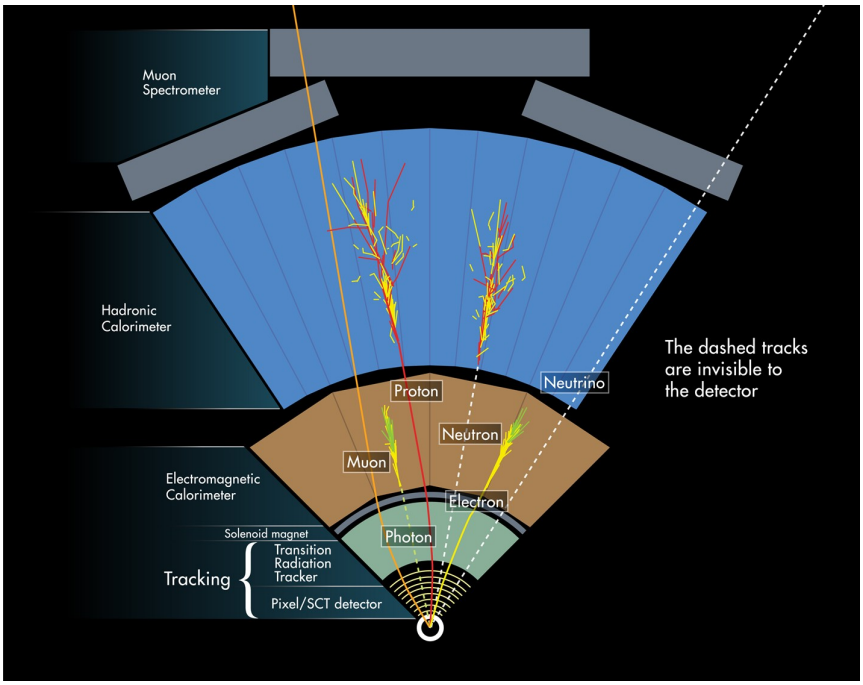

Figure 4.1: This diagram shows the various signatures left by different particles in the ATLAS detector. Solid lines represent a signature left in the corresponding detector subsystem, while dashed lines show the particle did not interact with that detector subsystem. [57]

is defined to remove overlap between objects, described later in this Chapter. Finally, a tighter set of requirements is placed upon the objects on a per-analysis basis, known as 'signal' requirements, which define the objects ultimately used in a specific analysis.

4.2 Leptons

The signals of interest in the analyses detailed in Chapters 6 and 7 have a single, charged lepton in the final state, which is required to be either an electron or muon. In both cases, this lepton originates from the decay of a W boson to $\ell\nu$. This Section will describe the reconstruction of electrons and muons, as well as briefly discussing the reconstruction of photons and tau leptons.

Electrons and photons

The reconstruction of electrons and photons uses information from the ID and ECAL. While electrons interact with both subsystems, photons leave no hits in the ID, with their only signature being an EM shower in the ECAL. However, photons can undergo a conversion to an electron-positron pair when they interact with detector material, and hence the reconstruction of electrons and photons proceeds in the same way. Both electrons and photons are reconstructed within the range $|\eta| < 2.47$, such that full tracking coverage

from the pixel detector and SCT are available [58, 59]. For the first step of electron/γ reconstruction, the ECAL is segmented into a 200×256 grid in η, ϕ. The energy deposited by an electron or photon at a given η, ϕ grid point is evaluated by summing the energy deposits in all layers of the ECAL, forming a 'tower'. A sliding-window of size 3×5 towers is scanned over the η, ϕ grid; any point of the grid where the summed E_{T} of all towers within the window exceeds 2.5 GeV is used as a seed for the clustering step. In order to identify the ECAL cluster as an electron or photon, the seed clusters are loosely matched to tracks in the ID. Tracks are extrapolated from the ID to the middle layer of the ECAL, with any track satisfying $\Delta\eta < 0.05$ and $-0.10 < \Delta\phi < 0.05$ considered as matched to the seed cluster. Seed clusters with at least one matched track are electron candidates while seed clusters with 0 matched tracks are photon candidates. Finally, the reconstructed energy of the candidate is determined by extending the window around the seed cluster to a size of 3×7 towers for $|\eta| < 1.37$ and 5×5 for $1.52 < |\eta| < 2.47$ and summing the energy deposits within the extended window.

Identification algorithms are applied to electron and photon candidates in order to quantify the quality of reconstruction and evaluate any potential misidentification. Photons radiated by electrons through Bremmstrahlung can produce electron-positron pairs, which subsequently interact with the detector material, providing a background to the prompt electron from the PV. Electron identification is performed in the region $|\eta| < 2.47$ using a likelihood discriminant, which takes as inputs tracking and calorimetry information, as well as quantities constructed from a combination of both tracking and calorimetry information. Photon identification is performed using selections on calorimeter quantities, such as quantities related to the shape of the EM shower in the ECAL, as described in [59].

In order to be applicable to a range of analyses, each with various electron selection efficiency and background rejection requirements, three working points are defined. The working points, Loose, Medium and Tight, have efficiencies of 93%, 88% and 80% for a prompt electron with $E_{\mathrm{T}} = 40$ GeV, respectively [58]. The efficiencies of the three working points are shown as a function of electron E_{T} and η in Figure 4.2.

A characteristic signature of the prompt production of electrons is that there is relatively little activity surrounding the particle when compared to the semileptonic decay of heavy-flavour quarks, from misidentification or from photon conversion. The *isolation* of an electron can be exploited as a tool for rejecting such backgrounds. Two sets of isolation variables are defined, track-based and calorimeter-based, to evaluate how much activity surrounds an electron. Nine electron isolation working points are defined, to enable a balance of signal electron efficiency and background rejection to be achieved by analyses [58].

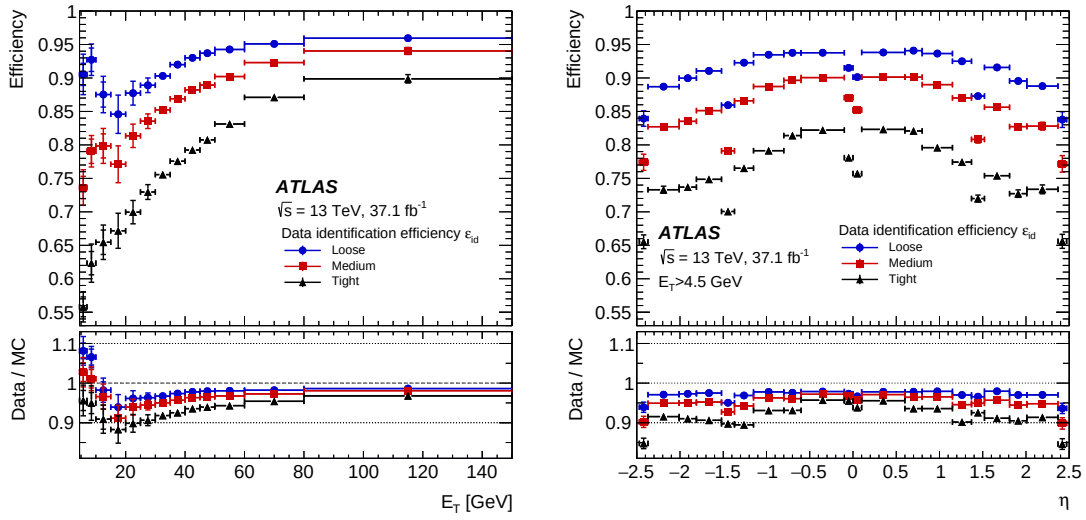

(a) (b)

Figure 4.2: Plots showing the electron identification efficiencies for the Loose, Medium and Tight working points, measured in $Z \to ee$ events [58], as a function of electron p_{T} (4.2a) and η (4.2b).

Muons

Muons are identified using inputs from the ID and MS, with additional information being provided by the calorimeters. The ID provides tracking information in the range $|\eta| < 2.5$, while the MS provides tracking information in the range $|\eta| < 2.7$. Muon reconstruction proceeds independently in the ID and MS; in the ID, tracks are built using information from the IBL, Pixel detector, SCT and TRT, in the same way as for all charged particles. Muon reconstruction in the MS proceeds by first searching for hit patterns in the individual MS cells, known as segments, and then fitting segments together from different layers to form track candidates. There are four types of reconstructed muon in ATLAS; *Combined (CB)*, *Segment-tagged (ST)*, *Calorimeter-tagged (CT)* and *Extrapolated (ME)* muons. Combined muons use hits in both the ID and MS detectors to build muon tracks, typically taking an 'outside-in' approach by starting reconstruction in the MS and matching the track candidate to a track in the ID.

Similarly to electrons, working points are defined for muon identification, enabling analyses to find an optimum balance of muon selection efficiency and background rejection. There are four muon ID working points defined; Loose, Medium, Tight and High-p_{T}, determining the quality of a muon reconstruction based upon the q/p significance and ρ' as well as the normalised χ^2 of the combined track fit. The q/p significance is defined as the absolute value of the difference between the measured charge-to-momentum ratio in the ID and MS, divided by the square root of the quadratic sum of the uncertainties on the measurements,

while ρ' is defined as the absolute value of the difference in the measured p_{T} in the ID and MS, divided by the p_{T} of the combined track [60]. The muon reconstruction efficiency as a function of the η is shown in Figure 4.3 for each of the muon identification working points. Muons originating from heavy particles such as the W boson are often well separated from

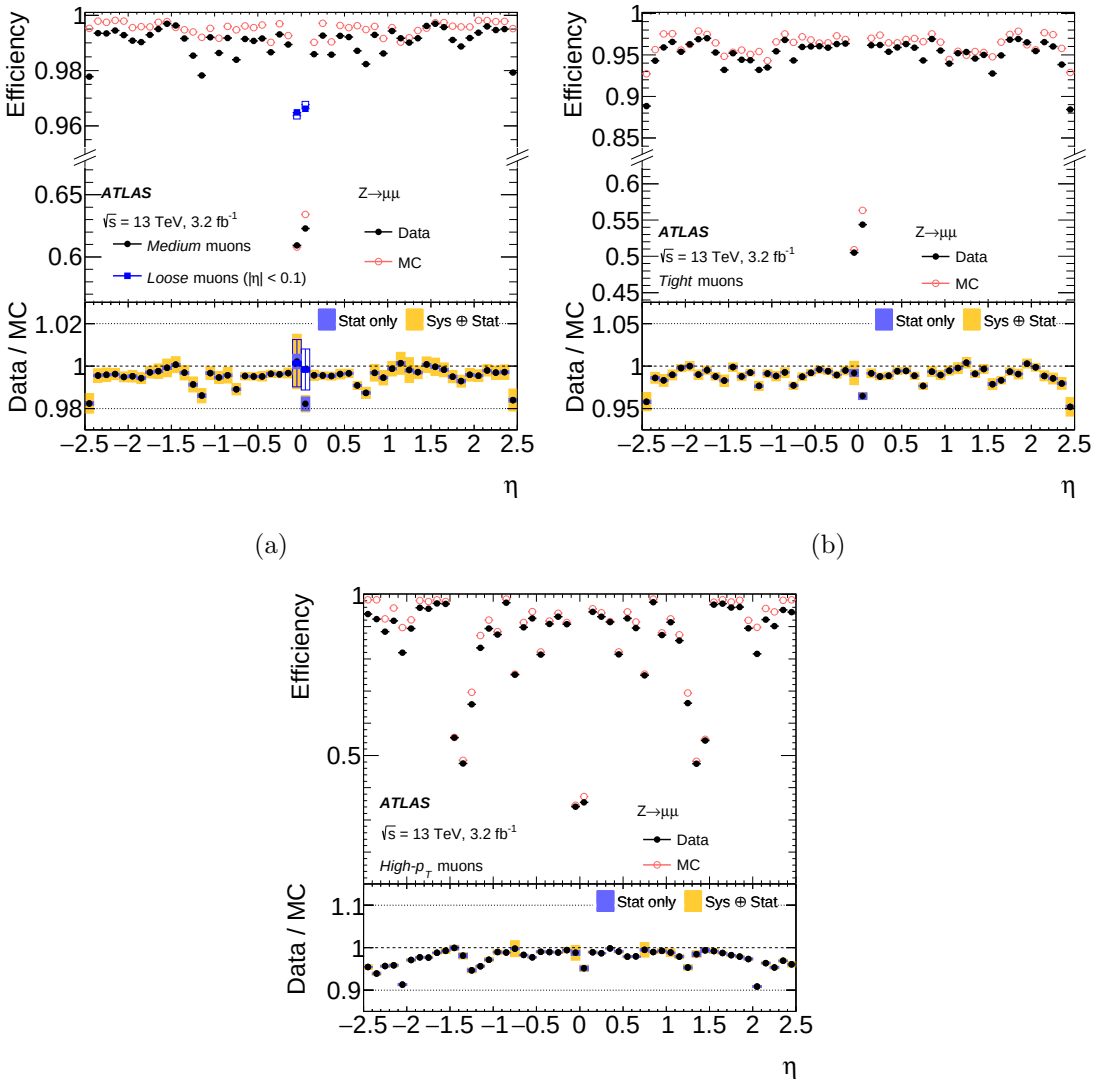

Figure 4.3: Plots showing the muon reconstruction efficiencies for the Loose and Medium (4.3a), Tight (4.3b) and High-p_{T} (4.3c) working points. All efficiencies are measured in $Z \to \mu\mu$ events.

any surrounding particles. Requiring that there is no surrounding activity from a muon, known as the isolation criteria, can be extremely useful for rejecting background multi-jet production. Two muon isolation variables, one track-based and one calorimeter-based, are used to evaluate if a muon is isolated. The distributions of the track- and calorimeter-based isolation variables can be seen in Figure 4.4. Seven muon isolation working points

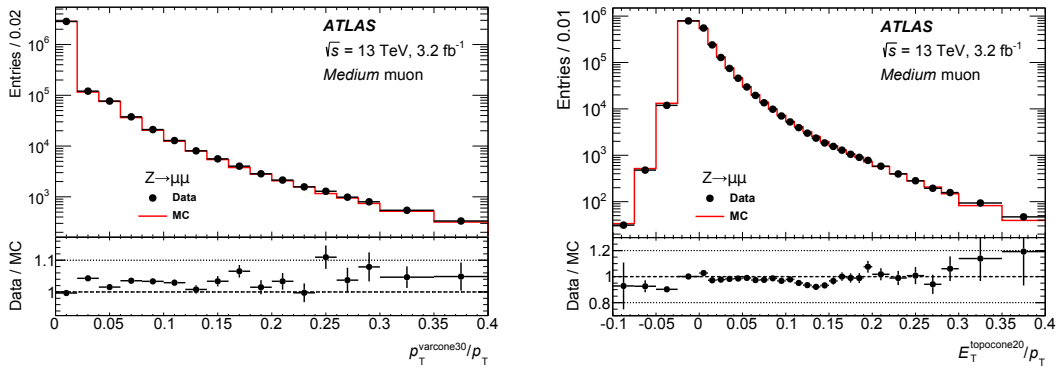

(a) (b)

Figure 4.4: Plots showing the distribution of the muon track-based (4.4a) and calorimeter-based (4.4b) for muons identified in $Z \to \mu\mu$ events with the Medium working point. $p_{\mathrm{T}}^{\mathrm{varcone30}}$ and $E_{\mathrm{T}}^{\mathrm{topocone20}}$ are defined as the scalar sum of the transverse momentum of tracks with a cone of variable radius $\Delta R = \min\left(10\mathrm{GeV}/p_{\mathrm{T}}^{\mu}, 0.3\right)$ of the muon and the scalar sum of transverse energy of topoclusters within a radius of $\Delta R = 0.2$ of the muon, respectively.

are defined to enable analyses to select an appropriate level of isolation for the signal under investiagation. The explicit definitions of the muon isolation working points is given in [60].

Taus

Taus, the heaviest of the charged leptons, can decay either leptonically ($\tau \to \ell\,\nu_\ell\,\nu_\tau$, $\ell = e, \mu$) or hadronically ($\tau \to$ hadrons ν_τ). The case with a leptonically-decaying tau, denoted by τ_{lep}, is simply reconstructed as either an electron or muon, with the neutrinos contributing to the real component of the $E_{\mathrm{T}}^{\mathrm{miss}}$. However, there is a dedicated reconstruction and identification flow for hadronically-decaying taus, denoted by τ_{had}. The τ_{had} candidates are seeded from jets (the reconstruction of which is detailed later in this Chapter), which proceeds by matching tracks with $p_{\mathrm{T}} > 1$ GeV which lie within $\Delta R < 0.2$ of a seed jet to a collision vertex. Tau identification is then performed using a BDT, trained to reject QCD backgrounds, using tracking information and the calorimeter clustering information used to reconstruct jets [61].

4.3 Jets

When proton bunches cross inside ATLAS, the environment is extremely dense with quarks and gluons. Strong interactions between partons in the incoming bunches of protons can result in the ejection of quarks and gluons in the transverse plane. The outgoing quarks and gluons evolve through a sequence of hadronisation, gluon splittings and radiations, as

described in Section 1.1.2 into a complex, highly-collimated collection of particles known as *jets*. The parton-dense environment of each bunch-crossing means pp collision events usually have numerous jets which can be from the hard scatter event, the proton remnants, or from pileup events. Jets provide an experimental tool for studying the strong interactions of the hard scatter, and are extremely important in the analyses presented in Chapters 6 and 7, with both signal processes containing jets originating from the presence of b-quarks.

For the analyses detailed in Chapters 6 and 7, jet reconstruction begins by first clustering calorimeter cells which are topologically-connected in 3-dimensions, known as 'topoclusters' [62]. The requirement of cells being topologically-connected helps minimise the misidentification of jets due to electronic noise and pileup, and makes use of the high-granularity of the ATLAS calorimeters. Each calorimeter cell is expected to have a baseline level of noise, σ_{noise}, which is defined as:

$$\sigma_{\text{noise}} = \sqrt{\left(\sigma_{\text{noise}}^{\text{electronic}}\right)^2 + \left(\sigma_{\text{noise}}^{\text{pileup}}\right)^2} \tag{4.3.1}$$

The first step in reconstructing jets using topoclusters proceeds by finding calorimeter cells where the energy deposit is $E_{\text{cell}} > 4\sigma_{\text{noise}}$. All cells with $E_{\text{cell}} > 4\sigma_{\text{noise}}$ form the seed for 'proto-clusters', the seed for the following steps of the algorithm. The clustering algorithm then proceeds by finding all cells neigbouring a seed which satisfy $E_{\text{cell}} > 2\sigma_{\text{noise}}$. Finally, the clustering algorithm stops when no neighbouring cells satisfies $E_{\text{cell}} > 2\sigma_{\text{noise}}$ but satisfy $E_{\text{cell}} > 0$. In the context of this clustering algorithm, 'neighbouring cells' can be either adjacent cells in the same layer of the calorimeter, or cells in different calorimeter layers which have some overlap in η, ϕ space. Any protocluster containing more than one local maxima, a cell which has a greater energy deposition than its surrounding cells, are separated around their respective maxima so as not to bias the jet clustering algorithm.

All topoclusters are calibrated to an appropriate energy scale, either hadronic or EM, to account for the energy losses in reconstruction. The ATLAS calorimeters are non-compensating, meaning that an incoming electron, e, and hadron, h, both of energy E, will have a ratio of measured energy $E_e/E_h > 1$. A fraction of the energy of hadronic showers goes unmeasured as it is absorbed in the binding energy of nucleons which are released as the shower evolves in the calorimeters [63].

Jet clustering algorithms

Jet reconstruction proceeds by clustering together the topoclusters described in the previous Section into jets which are determined to have originated from the same parton. Jet clustering algorithms can be separated into cone algorithms and sequential algorithms.

Cone algorithms The first jet clustering algorithm was developed in the 1970's and used in $e^+e^- \to q\bar{q} \to 2j$ events. Events were identified as containing two jets if at least 1-ϵ of the event's total energy was contained in two cones with opening half-angle δ. The choice of the parameters ϵ and δ is almost entirely arbitrary, and hence the algorithm can reconstruct vastly different final state jets and multiplicities depending entirely upon the parameter choice. In addition, in pp collisions the concept of total energy is obfuscated by the fact that the interacting protons contain partons with only a fraction of the total proton energy, with the residual energy either forming the underlying event or escaping down the beam pipe.

Most cone algorithms reconstruct jets through an iterative procedure, hence being known as iterative cones (IC). These algorithms proceed by first selecting a seed particle, i, and summing the momenta of all particles, j, satisfying the below condition:

$$\Delta R_{ij} = \sqrt{(y_i - y_j)^2 + (\phi_i - \phi_j)^2} < R \, . \tag{4.3.2}$$

In the equation above, R represents the jet radius, which is the modern-day equivalent of the δ parameter discussed earlier. This process is repeated, each time taking the result of the previous iteration as the new seed, until the resulting jet cone is stable. This class of algorithms are not fully specified without specifying a definition for seed particles, and without defining a procedure for removing overlap between cones. Cone algorithms are also plagued by infrared and collinear (IRC) unsafety. An infrared-safe jet clustering algorithm will reconstruct the same set of final state jets regardless of additional soft emissions in an event, while a collinear-safe jet clustering algorithm will reconstruct the same set of final state jets if a parton of energy E is replaced by two collinear partons whose summed energy is equal to E. Most IC jet clustering algorithms use the hardest particle in an event as the seed which can violate collinear safety if the hardest particle in the event is replaced by two collinear particles. In this case, the hardest particle in the event may change, meaning the reconstructed final state jets may also change.

Sequential algorithms Sequential jet clustering algorithms work in a similar, iterative manner as for IC algorithms, except using a 'bottom-up' approach to the clustering. The first use of a sequential clustering algorithm was also in the context of electron-positron collisions. There are three widely-used sequential clustering algorithms today; the inclusive-k_t algorithm, the Cambridge/Aachen algorithm and the anti-k_t algorithm. All three of these algorithms can be specified by the following equations.

$$d_{ij} = \min\left(p_{\mathrm{T},i}^{2p}, p_{\mathrm{T},j}^{2p}\right) \frac{\Delta R_{ij}^2}{R^2} \tag{4.3.3}$$

$$\Delta R_{ij}^2 = (y_i - y_j)^2 + (\phi_i - \phi_j)^2 \tag{4.3.4}$$

$$d_{iB} = p_{\mathrm{T},i}^{2p} \tag{4.3.5}$$

In Equation 4.3.3 and 4.3.5, $p_{\mathrm{T,i}}^{2p}$ and $p_{\mathrm{T,j}}^{2p}$ represent the transverse momentum of the ith and jth particle, respectively, raised to the power $2p$, where p is determined by the clustering algorithm being used. In the inclusive-k_t algorithm, the value of p is set to $+1$. This algorithm proceeds by iterating over all particles j within a radius R of i, calculating all d_{ij} and d_{iB} and finding the minimum. If $d_{ij} < d_{iB}$, the two particles are combined into a new particle and the algorithm proceeds from the start. If $d_{ij} > d_{iB}$, the particle i is determined to be a final-state jet and is removed from the list of particles, before the algorithm restarts from the beginning. As seen from the construction of d_{ij}, the inclusive-k_t algorithm begins by clustering soft particles first, and thus the algorithm is sensitive to pileup and the underlying event. The anti-k_t algorithm follows the same procedure as for the inclusive-k_t algorithm, but provides resolution to this issue by setting $p = -1$ in Equation 4.3.5. Therefore, in the anti-k_t algorithm, jet clustering proceeds from hard seeds, and sequentially adds softer particles until the jet is stable and is classified as a final-state jet. In this thesis, the anti-k_t algorithm is used to clustering all jets, with the jet radius parameter R set equal to 0.4 in all analyses detailed in the subsequent Chapters.

Once jets are clustered, they must be calibrated to account for detector performance and resolution effects. The jet energy scale (JES) calibration is applied to account for the non-compensating behaviour of the ATLAS hadronic calorimeters, as described in Chapter 2, as well as the effect of dead material. The JES calibration depends upon the jet p_{T} and η, as well as the pileup conditions and the flavour composition of the jet. These calibrations are derived by comparing data and MC samples in dijet, Z+jets and γ+jets p_{T} balance measurements. Jets arising from pileup events are suppressed using the Jet Vertex Tagger (JVT) discriminant [64]. The JVT uses information of the fraction of the transverse momentum of a given jet to originate from the PV to give a likelihood that a given jet is from the hard scatter event. By default, analyses require that the JVT value is > 0.59, with jets scoring less than this being rejected.

4.4 Flavour-tagging

For both measurements of SM processes and searches for BSM physics, identifying jets originating from heavy flavour (c, b) quarks is extremely important. b-quarks produced in the hard scatter hadronise and then travel a significant distance before decaying. The lifetime of b-hadrons is relatively long at around $1.5ps$ because of suppression in the CKM elements for V_{ub} and V_{cb}, meaning a b-hadron can travel several millimetres before decay-

ing. The result of this is the presence of a second decay vertex distinct from the PV, with tracks which have large impact parameters. The impact parameters of a track, d_0 and z_0, represent the transverse and longitudinal distance of closest approach to the PV, respectively. This distinctive signature enables jets originating from a b-quark to be 'tagged'.

The MV2c10 b-tagging algorithm is used to flavour-tag all b-jets in the analyses detailed in this Thesis. This algorithm utilises a Boosted Decision Tree (BDT) classifier which has 21 input variables, such as the jet p_{T} and η as described in [65]. The MV2c10 algorithm aims to distinguish b-jets from jets originating from a charm quark, named c-jets, jets originating from hadronic tau decays, named τ-jets and all other jets, originating from light-flavour quarks (u, d, s) and gluons, named 'light-jets'. The algorithm is trained using a simulated sample of both $t\bar{t}$ events and events containing a heavy Z' boson, the latter of which is used to optimise tagging performance for jets with high transverse momentum. The simulated Z' decays hadronically, with equal branching ratios of 33% to $b\bar{b}$, $c\bar{c}$ and a pair of light-jets. The output of the MV2c10 BDT is shown in Figure 4.5, applied to a simulated set of $t\bar{t}$ events with dileptonic final states.

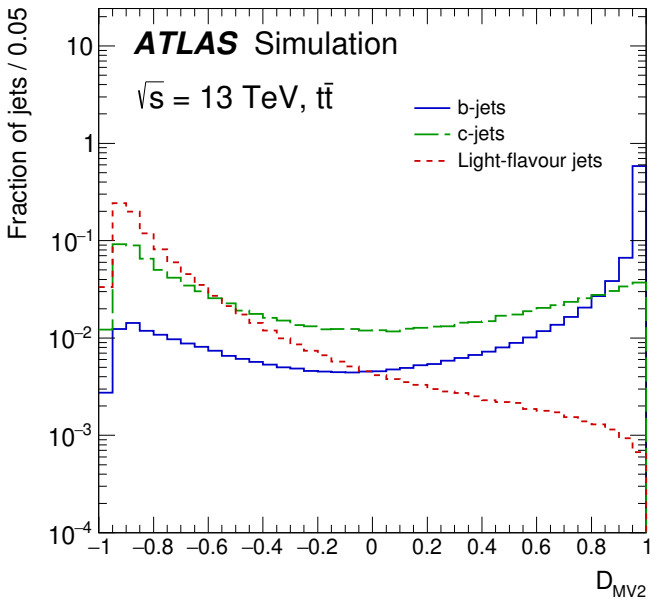

Figure 4.5: Figure showing the output of the BDT used by the MV2c10 algorithm to tag jets originating from b-quarks, applied on a sample of simulated $t\bar{t}$ events.

As shown in Figure 4.5, the discriminant, D_{MV2} peaks at values $\rightarrow 1$ for b-tagged jets (detailed further for any generic ML classifier in Chapter 5), while showing strong rejection of light-flavour jets. This discriminant is used by applying a lower-bound selection on the output of the BDT, such that any jet satisfying this requirement is tagged as a b-jet. Four b-tagging efficiency working points are defined, each corresponding to a different se-

lection on the ouput of the BDT, providing an optimal balance of b-tagging efficiency, ϵ_b, and c/τ/light-jet rejection. The working point used in the analyses detailed in Chapters 6 and 7 is the $\epsilon_b = 77\%$ working point, corresponding to a selection on the BDT output > 0.64, which has a c-jet rejection of 4.9, a τ-jet rejection of 15 and a light-jet rejection of 110. The jet rejection rate is defined as the inverse of the selection efficiency, $1/\epsilon_j$, where $j = c, \tau, \text{light}$. The efficiency of the MV2c10 b-tagging algorithm as a function of jet p_{T} is shown in Figure 4.6, along with the corresponding MC scale factors. The data used to derive the b-tagging efficiency scale factors was collected in 2015, 2016 and 2017 at $\sqrt{s} = 13$ TeV, and requires that each event has at least one lepton identified by the trigger system, with an explicit dilepton requirement applied in the offline selection.

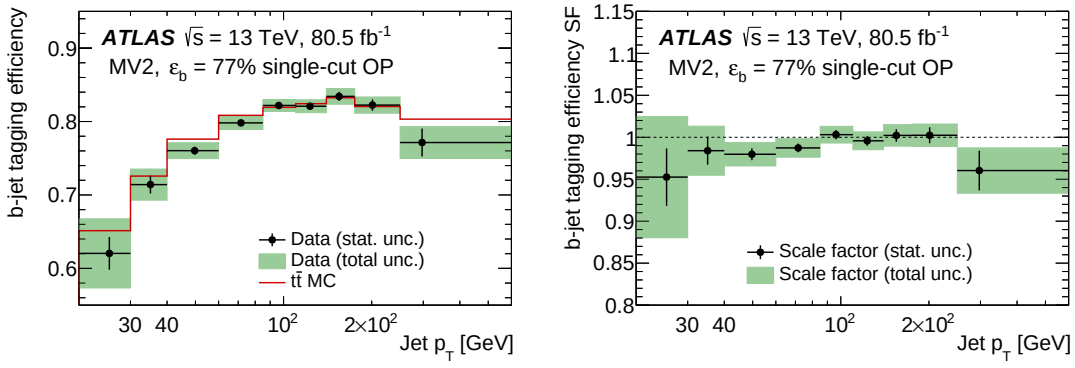

(a) (b)

Figure 4.6: Figure showing the efficiency of the MV2c10 b-tagging algorithm as a function of the jet p_{T} (4.6a) and the corresponding MC scale factors (4.6b) for the $\epsilon_b = 77\%$ working point.

4.5 $E_{\text{T}}^{\text{miss}}$

In searches for New Physics, it is expected that weakly-interacting BSM particles produced in pp collisions will escape direct detection. Therefore, in order to perform such searches, being able to reconstruct any momentum imbalance, indicating the presence of undetected particles, is crucial. The hermetic design of the ATLAS detector with near 4π solid angle coverage, as described in Chapter 2, enables the reconstruction of the momentum imbalance in each event, with the magnitude of this vector sum known as the missing transverse momentum, $E_{\text{T}}^{\text{miss}}$.

While the presence of $E_{\text{T}}^{\text{miss}}$ is a signature of the production of weakly-interacting BSM particles, it is not a unique signature of New Physics. As previously mentioned and as shown in Figure 4.1, neutrinos pass through the entirety of the ATLAS detector without interacting, and as such any SM decay involving neutrinos can be an irreducible background to a BSM signal. Aside from real $E_{\text{T}}^{\text{miss}}$ from neutrinos, the accurate measurement

of the $E_{\mathrm{T}}^{\mathrm{miss}}$ is complicated by detector imperfections; for example, physics objects being mismeasured, or particles passing through inactive detector material.

The $E_{\mathrm{T}}^{\mathrm{miss}}$ is calculated in x and y components, as shown in Equation 4.5.1, such that the $E_{\mathrm{T}}^{\mathrm{miss}}$ vector is given by $\mathbf{E}_{\mathrm{T}}^{\mathrm{miss}} = (E_x^{\mathrm{miss}}, E_y^{\mathrm{miss}})$.

$$E_{x(y)}^{\mathrm{miss}} = -\sum_i p_{x(y),i}^{\mathrm{hard}} - \sum_i p_{x(y),i}^{\mathrm{soft}}. \tag{4.5.1}$$

In Equation 4.5.1, the $p_{x(y),i}^{\mathrm{hard}}$ components are taken from the hard physics objects, while the $p_{x(y),i}^{\mathrm{soft}}$ components are taken from any tracks associated to the hard scatter vertex which are not associated to any of the objects contributing to the hard term. The vectoral representation of $E_{\mathrm{T}}^{\mathrm{miss}}$ allows both the magnitude and direction in ϕ to be used in physics analyses. The magnitude and direction of the $\mathbf{E}_{\mathrm{T}}^{\mathrm{miss}}$, $E_{\mathrm{T}}^{\mathrm{miss}}$ and ϕ^{miss}, are given by Equations 4.5.2 and 4.5.3, respectively.

$$E_{\mathrm{T}}^{\mathrm{miss}} = \sqrt{\left(E_x^{\mathrm{miss}}\right)^2 + \left(E_y^{\mathrm{miss}}\right)^2} \tag{4.5.2}$$

$$\phi^{\mathrm{miss}} = \tan^{-1}\left(\frac{E_y^{\mathrm{miss}}}{E_x^{\mathrm{miss}}}\right) \tag{4.5.3}$$

As previously mentioned, the reconstructed $E_{\mathrm{T}}^{\mathrm{miss}}$ in ATLAS is constructed from two components; the 'hard-event' component, $E_{\mathrm{T}}^{\mathrm{miss,\,hard}}$, and the 'soft-signal' component, $E_{\mathrm{T}}^{\mathrm{miss,\,soft}}$. The former arises from the reconstruction of the analysis-level electrons, photons, muons, τ_{had}, and jets, while the latter arises from tracks which are not associated with any of the final state objects. The analyses described in Chapters 6 and 7 use the Track Soft Term (TST) algorithm to calculate $E_{\mathrm{T}}^{\mathrm{miss,\,soft}}$, including all ID tracks associated with the PV but not associated with any final state object. As the TST algorithm makes use of the 'unused' tracks from the PV, any calorimeter deposits from soft, neutral particles are neglected, which makes the soft $E_{\mathrm{T}}^{\mathrm{miss}}$ term robust against pileup effects.

4.6 Overlap removal

It is possible for multiple objects to be reconstructed from the same detector signatures, such as calorimeter deposits, such that there are overlapping reconstructed objects. It is therefore necessary to define a prescription through which to resolve this overlap. The overlap removal procedure is performed on loosely reconstructed, 'baseline' objects and proceeds as follows:

- If two electrons share a track in the ID, the lower p_{T} electron is rejected.
- If an electron shares an ID track with a muon, the electron is rejected.

- Any non b-tagged jets within $\Delta R = 0.2$ of an electron are rejected, or within $\Delta R = 0.2$ of a muon if the jet has < 3 tracks or if the muon and jet are ghost-associated.

- For the remaining jets, any electrons or muons satisfying $\Delta R < \min(0.4, 0.04 + 10\text{GeV}/p_{\text{T}})$ are rejected.

To check if a muon is ghost-associated with a jet, the muon track is added to the jet with infinitesimally-small p_{T}. The muon is ghost-associated to the jet if the muon is still within the jet after this reclustering procedure. Objects remaining after the overlap removal procedure which pass the analysis-level reconstruction criteria form the final analysis objects.

4.7 Event cleaning

In order to ensure recorded data events entering analyses are of good quality, a set of event cleaning requirements are used. These requirements aim to remove any events which has noisy detector signals or which are poorly measured. These are summarised below.

Good Run List The Good Run List (GRL) is a record of all runs recorded by the ATLAS detector, which are deemed suitable for use in analyses. Typically, each run is broken down into 60s segments, known as *luminosity blocks*. Luminosity blocks in each run passing basic data quality requirements are included on the GRL. Events which were recorded in luminosity blocks or runs which are not included in the GRL are automatically rejected.

Trigger Each analysis has differing trigger requirements depending on the signal topology of interest. In this Thesis, the $E_{\text{T}}^{\text{miss}}$ triggers, listed in Table 3.1 are used.

Primary Vertex All events must have a primary vertex (PV). As previously described, the PV is defined as the vertex having at least two tracks with the highest $\sum p_{\text{T}}^2$. Events which do not have a vertex satisfying these requirements are rejected.

SCT, LAr and Tile calorimeter cleaning Noise bursts in the LAr calorimeter or Tile calorimeter trips can give incorrect measurements of the amount of electromagnetic or hadronic activity in an event, affecting the data quality. Events where such calorimeter activity was recorded are rejected. Events recorded during a reset of the SCT caused by a single particle upset (SEU) are also rejected. This occurs when there is a single particle upset (SEU) in a SCT module, which can cause the module to become extremely noisy until it is power-cycled.

Debug Stream Events which cause the ATLAS software-level trigger, the HLT, to crash or timeout form the input to the debug stream. These events are stored and reconstructed offline, where they are assigned to the debug stream. It is particularly important for analyses searching for New Physics to check events in the debug stream.

4.8 Object definitions summary

The working points and selections on acceptance used to define 'signal' objects in the analyses detailed in Chapters 6 and 7 are summarised in Table 4.1. The procedures through which objects are reconstructed have sets of associated systematic uncertainties which will be discussed in Chapter 5.

	SUSY $1\ell b\bar{b}$+$E_{\mathrm{T}}^{\mathrm{miss}}$		2HDM+a tW+$E_{\mathrm{T}}^{\mathrm{miss}}$
Dataset	36.1fb^{-1}	139fb^{-1}	139fb^{-1}
Electrons			
ID	TightLLH		
Isolation	Gradient (Loose)	FCLoose	FCLoose
		(FCHighPtCaloOnly for $p_{\mathrm{T}} > 200$ GeV)	
p_{T}	> 25 GeV	> 7 GeV	> 20 GeV
$\lvert\eta\rvert$	< 2.47		
Muons			
ID	Medium		
Isolation	Gradient (Loose)	FCLoose	FCLoose_FixedRad
p_{T}	> 25 GeV	> 6 GeV	> 20 GeV
$\lvert\eta\rvert$	< 2.7	< 2.5	< 2.5
Jets			
Algorithm	anti-k_t, R = 0.4		
p_{T}	> 25 GeV	> 30 GeV	> 30 GeV
$\lvert\eta\rvert$	< 2.8	< 2.8	< 2.5
b-jets			
Tagger	MV2c10		
p_{T}	> 25 GeV	> 20 GeV	> 20 GeV
$\lvert\eta\rvert$	< 2.5		
b-jet efficiency	FixedCutBEff, $\epsilon = 77\%$		

Table 4.1: A summary of the object definitions used in the analyses detailed in Chapters 6 and 7. The definition of the isolation working points for electrons and muons can be found in Refs [58] and [60], respectively, while the definition of the b-jet working point is given in Ref [65].

Chapter 5

Analysis methods

This Chapter aims to summarise the methods and tools used to perform the searches for New Physics described in the subsequent Chapters. Firstly, the general analysis strategy used in a search for New Physics is presented, with more relevant and specific detail given in Chapters 6 and 7. The key discriminatory variables used in this Thesis to select candidate signal events are described in Section 5.2. Section 5.3 of this Chapter describes some of the multivariate and machine learning (ML) methods used to select and optimise the acceptance of signal into the analyses, giving an overview of both conventional and more modern data selection techniques. Finally, Section 5.5 gives an overview of the statistical analysis performed and the methods used to draw statistical conclusions from the analyses detailed in the subsequent Chapters.

5.1 General search analysis strategy

Physics analyses targeting a BSM scenario generally define three classes of regions of phase space. *Signal regions* (SRs) are defined as regions of kinematic phase space which are enriched in the signal of interest. SRs can be defined by placing selections on kinematic and angular observables, such as the $E_{\mathrm{T}}^{\mathrm{miss}}$ or the angular difference between two jets $\Delta\phi(j_1, j_2)$, or through more abstract techniques such as placing a selection on some classifier trained to distinguish the signal of interest from the SM background. The latter will be discussed in Section 5.3.

Control regions (CRs) are defined as regions whose composition is dominated by a particular background process, such as $t\bar{t}$, while also having negligible signal contamination. Generally, SRs in searches are in an extreme part of kinematic phase space, far from where the SM background MC was validated, hence it is necessary to ensure reasonable agreement between data and the SM predictions for the background estimates in the CRs. A SM estimate is made for the controlled background in the corresponding CR by normalising the MC predictions to the observed data in that CR by fitting a floating normalisation

factor, typically denoted by μ_{process}. The background normalisation factor, μ_{process}, is both determined from and subsequently applied to all analysis regions included in the statistical analysis. This will be discussed further in Section 5.5.

Validation regions (VRs) are used as a method of ensuring the background estimation from the CR extrapolated to the SR is robust. Generally, this is achieved by defining VRs which differ from the SR definition by inverting only one SR selection. By defining multiple VRs, each with a different SR selection inverted, the extrapolation from CR to SR can be validated. However, VRs must also have low signal contamination, such that it is indeed the background estimate that is being validated.

A simplified diagram showing how CRs, VRs and SRs can be defined in terms of two observables is shown in Figure 5.1.

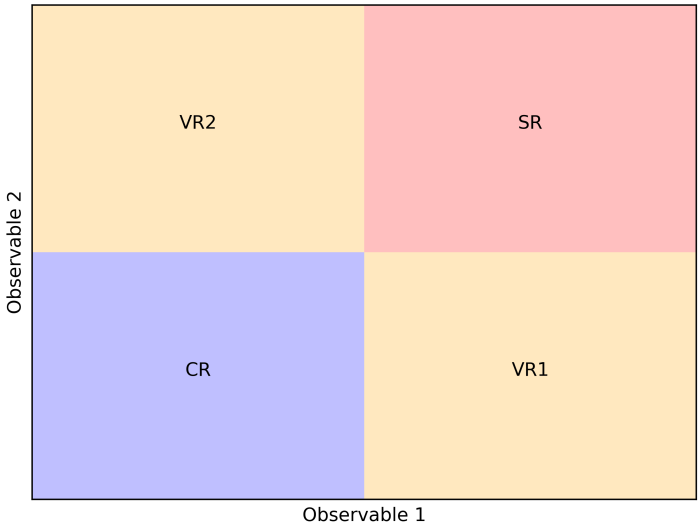

Figure 5.1: A simplified schematic diagram showing an example of a CR, VRs and an SR, all defined by placing orthogonal selections on two observables. The background estimation made in the CR is extrapolated and validated through VR1 and VR2 into the SR.

5.2 Discriminant variables

The analyses detailed in Chapters 6 and 7 have similar final states signatures including a single lepton, b-tagged jets and $E_{\text{T}}^{\text{miss}}$, and hence have very similar SM backgrounds to the respective signals. In particular, the presence of intermediate W bosons and $E_{\text{T}}^{\text{miss}}$ in the signal processes presented in Chapters 6 and 7 makes SM processes involving W bosons which decay leptonically an irreducible background to the signal. In addition, backgrounds

containing at least one top quark, where an intermediate W boson from $t \to Wb$ decays leptonically, are also irreducible due to the presence of a lepton, $E_{\mathrm{T}}^{\mathrm{miss}}$ and b-tagged jets. In the analyses presented in Chapters 6 and 7, the $t\bar{t}$, Wt and W+jets processes are the largest, irreducible backgrounds to the signals of interest. This Section aims to summarise the variables used to reject these SM backgrounds while retaining the signal.

The first, and perhaps most obvious, variable used to discriminate between a BSM signal and the SM backgrounds is $E_{\mathrm{T}}^{\mathrm{miss}}$. The construction of the $E_{\mathrm{T}}^{\mathrm{miss}}$ is described in Chapter 4. Processes which contain BSM particles have real $E_{\mathrm{T}}^{\mathrm{miss}}$ if the BSM particles do not decay to visible particles and are weakly-interacting, and hence could produce an excess of events in the $E_{\mathrm{T}}^{\mathrm{miss}}$ distribution. In such events, the amount of $E_{\mathrm{T}}^{\mathrm{miss}}$ is expected to be larger than the SM background, due to the presence of the additional BSM particles. However, real $E_{\mathrm{T}}^{\mathrm{miss}}$ from neutrinos in $W \to \ell\nu$ or $Z \to \nu\nu$ decays as well as $E_{\mathrm{T}}^{\mathrm{miss}}$ from misreconstructed jets can obscure a BSM signal. Therefore, a combination of applying selections on the $E_{\mathrm{T}}^{\mathrm{miss}}$ distribution with other kinematic selections is employed.

The transverse mass variable, m_{T}, can be used to reconstruct a single, massive particle undergoing a semi-invisible decay to one visible particle and one invisible particle. In this Thesis, the m_{T} variable is used to reconstruct W bosons, decaying to a charged lepton and a neutrino. In the case of an event with no BSM contributions, the only source of $E_{\mathrm{T}}^{\mathrm{miss}}$ is from the neutrino produced in the decay of the W boson and as such the m_{T} distribution has a kinematic endpoint around m_W. Detector effects smear the kinematic endpoint of the m_{T} distribution to around 100 GeV. The presence of $E_{\mathrm{T}}^{\mathrm{miss}}$ from BSM particles will produce a significantly different m_{T} distribution with a significantly longer tail compared to a SM-only case, and is therefore a powerful discriminant. The definition of m_{T} is given in Equation 5.2.1.

$$m_{\mathrm{T}} = \sqrt{2p_{\mathrm{T}}(\ell)E_{\mathrm{T}}^{\mathrm{miss}}\left(1 - \cos\Delta\phi(\mathbf{p}_{\mathrm{T}}(\ell), \mathbf{p}_{\mathrm{T}}^{\mathrm{miss}})\right)} \tag{5.2.1}$$

In Equation 5.2.1, $p_{\mathrm{T}}(\ell)$ is the transverse momentum of the lepton in the event while $\Delta\phi(\mathbf{p}_{\mathrm{T}}(\ell), \mathbf{p}_{\mathrm{T}}^{\mathrm{miss}})$ specifies the azimuthal angle between the lepton and the $E_{\mathrm{T}}^{\mathrm{miss}}$.

For the signal process of interest in the analysis detailed in Chapter 7, there are two intermediate W bosons, producing the single lepton final state as follows: $Wt \to W(Wb) \to (\ell\nu)(qq')b$. In addition to reconstructing the leptonically-decaying W boson using the m_T variable, the mass of the hadronically-decaying W boson, m_W^{had}, was achieved using an iterative reconstruction procedure, as described in Ref. [66]. The algorithm begins by clustering all of the $R = 0.4$ anti-k_t jets in an event into large, $R = 3.0$ jets. The radius of these large jets is then iteratively reduced until a radius which matches the p_{T} of the jet, defined by $R(p_{\mathrm{T}}) = 2 \times m_W/p_{\mathrm{T}}$, is reached. m_W^{had} is then defined as the mass of the

newly-reclustered jet.

The contransverse mass [67, 68], m_{CT}, is designed to reconstruct the masses of pair-produced particles which both decay in the same, semi-invisible manner. This is particularly useful for rejecting the $t\bar{t}$ process, where both legs decay into a W boson and a b-quark, followed by a subsequent decay of the W bosons. The m_{CT} is defined in Equation 5.2.2.

$$m_{\mathrm{CT}}^2 = (E_{\mathrm{T}}(v_1) + E_{\mathrm{T}}(v_2))^2 - (\mathbf{p}_{\mathrm{T}}(v_1) - \mathbf{p}_{\mathrm{T}}(v_2))^2 \tag{5.2.2}$$

The version of m_{CT} shown in Equation 5.2.2 violates Lorentz invariance under boosts of the laboratory centre-of-mass frame, and hence a modified, 'boost-corrected' version [68] is used in the analysis detailed in Chapter 6. For this analysis, the visible particles v_1 and v_2 are identified as the two b-jets in the event, b_1 and b_2, in order to partially reconstruct the $t\bar{t}$ system. As described in Ref. [68], the m_{CT} distribution has a kinematic endpoint which can be calculated as shown in Equation 5.2.3.

$$m_{\mathrm{CT}}^{\mathrm{max}} = \frac{m_{heavy}^2 - m_{invisible}^2}{m_{heavy}} \tag{5.2.3}$$

Identifying $m_{heavy} = m_{top}$ and $m_{invisible} = m_W$ gives a kinematic endpoint around 135 GeV for $t\bar{t}$ production, which is the most dominant background in the analysis detailed in Chapter 6.

The stransverse mass variable, m_{T2} [69] is closely related to the transverse mass variable, m_{T}. It is again designed to reconstruct the mass of pair-produced particles, most relevantly here $t\bar{t}$, where each particle decays semi-invisibly. To calculate the m_{T2}, the $E_{\mathrm{T}}^{\mathrm{miss}}$ is decomposed into two components, $\mathbf{q}_{\mathrm{T},1}$ and $\mathbf{q}_{\mathrm{T},2}$, with all possible combinations tested. The m_{T2} is shown in Equation 5.2.4 for a two-lepton final state.

$$m_{\mathrm{T2}} = \min_{\mathbf{q}_{\mathrm{T},1}+\mathbf{q}_{\mathrm{T},2}=E_{\mathrm{T}}^{\mathrm{miss}}} \{\max\left[m_{\mathrm{T}}(\mathbf{p}_{\mathrm{T}}(\ell_1), \mathbf{q}_{\mathrm{T},1}), m_{\mathrm{T}}(\mathbf{p}_{\mathrm{T}}(\ell_2), \mathbf{q}_{\mathrm{T},2})\right]\} \tag{5.2.4}$$

An asymmetric form of m_{T2} [70, 71], known as am_{T2}, is used in the analysis detailed in Chapter 7. When a pair of top quarks are produced and subsequently decay semi-leptonically, a selection applied to m_{T} above the W boson threshold will reject most events. However, for dileptonic $t\bar{t}$ where one lepton is not reconstructed, cuts applied on the m_{T} variable will not be enough to reject this process, as there is $E_{\mathrm{T}}^{\mathrm{miss}}$ from both legs due to the neutrinos. Selections on the am_{T2} variable can be applied in combination with selection on m_{T} to reject both semi- and dileptonic $t\bar{t}$ decays. The explicit definition of the am_{T2} variable, calculated using the $E_{\mathrm{T}}^{\mathrm{miss}}$, the transverse momentum of the lepton, $p_{\mathrm{T}}(\ell)$, and the transverse momentum of the leading and subleading b-jets, $p_{\mathrm{T}}(b_1)$ and $p_{\mathrm{T}}(b_2)$,

respectively, as used in Chapter 7, is shown in Equation 5.2.5.

$$\begin{aligned} am_{\mathrm{T2}}^{1} &= \min_{\mathbf{q}_{\mathrm{T},1}+\mathbf{q}_{\mathrm{T},2}=E_{\mathrm{T}}^{\mathrm{miss}}} \{\max\left[m_{\mathrm{T}}(\mathbf{p}_{\mathrm{T}}(b_1), \mathbf{q}_{\mathrm{T},1}), m_{\mathrm{T}}(\mathbf{p}_{\mathrm{T}}(\ell + b_2), \mathbf{q}_{\mathrm{T},2})\right]\} \\ am_{\mathrm{T2}}^{2} &= \min_{\mathbf{q}_{\mathrm{T},1}+\mathbf{q}_{\mathrm{T},2}=E_{\mathrm{T}}^{\mathrm{miss}}} \{\max\left[m_{\mathrm{T}}(\mathbf{p}_{\mathrm{T}}(\ell + b_1), \mathbf{q}_{\mathrm{T},1}), m_{\mathrm{T}}(\mathbf{p}_{\mathrm{T}}(b_2), \mathbf{q}_{\mathrm{T},2})\right]\} \\ am_{\mathrm{T2}} &= \min\left(am_{\mathrm{T2}}^{1}, am_{\mathrm{T2}}^{2}\right) \end{aligned} \tag{5.2.5}$$

As shown in Equation 5.2.5, in the case of a single lepton and two b-jets, the am_{T2} variable is calculated twice, one for each combination of the lepton and one of the b-jets, with the am_{T2} being taken as the minimum value of these combinations.

When a particle decays into daughter particles, the mass of the parent can be reconstructed if the daughter particles are fully-visible and hence the energy and momenta of each particle is measured. For the signal process considered in Chapter 6, the invariant mass of the two b-jets in an event, m_{bb} is employed to reconstruct the Higgs boson.

$$m_{bb} = \left((E_{b,1} + E_{b,2})^2 - ||\mathbf{p}_{b,1} + \mathbf{p}_{b,2}||^2\right)^{1/2} \tag{5.2.6}$$

In Equation 5.2.6, $E_{b,i}$ represents the energy of the ith b-jet, while $\mathbf{p}_{b,i}$ represents the momentum vector of the ith b-jet. This can be generalised to any two daughter particles as long as they are visible, taking the same form for reconstructing the decay of a Z boson to two charged leptons, for example.

5.3 Selection optimisation methods

Searches for New Physics often involve signals which have cross-sections orders of magnitude lower than those of SM processes. It is therefore necessary to design analyses which minimise the background contributions in the SRs, while also maintaining a high acceptance and selection efficiency for the signal of interest. Optimising SRs to satisfy these criteria is non-trivial, particularly when considering a large number of observables, and can often result in unreasonable computing times and loads.

Placing simple selections on the discriminating variables described previously does not give sensitivity to the signals of interest due to the huge irreducible SM backgrounds. In order to separate signals from the SM background, more sophisticated optimisation methods are used which take advantage of numerous discriminative variables in parallel. The methods used for region optimisation in this Thesis can be divided into two categories; 'grid-based' methods, and machine learning methods.

Grid-based methods aim to find the optimum selection on each of the discriminative vari-

ables used in an analysis. For each variable, a set of proposed selections is defined. Each candidate region is defined as one combination of the proposed selections, with the full set of proposed regions forming a 'grid'. The total number of candidate regions is given by the product of the number of proposed selections for each variable, and hence rapidly grows as additional variables are added, or more proposed selections are tested. Therefore, for a grid with many candidate regions it is often impossible to test every region, and hence some grid-based algorithms aim to search the grid for an optimal solution without explicitly testing each candidate region.

Machine learning (ML) classifiers do not explicitly optimise selections on individual discriminative variables and instead aim to classify events based upon the values of the variables. The inputs to ML classifiers are generally the discriminative variables of interest in an analysis. The classifier is trained to discriminate between the signal and the SM backgrounds by repeatedly being given events from each class and learning the differences between the distributions. ML classifiers make predictions on an event being signal-like or background-like, by outputting a number in the range $\in [-1, 1]$ or $\in [0, 1]$, depending on the classifier implementation, where predictions $\to 1$ represent a signal-like event. For ML classifiers, the SRs are defined by applying a lower bound selection to the distribution of the ML classifier predictions. The location of this selection is optimised by scanning over cuts and determining the optimal selection.

In order to determine the optimal solution in grid-based methods and determine the location of the optimal cut on the ML classifier output, the *significance* metric is defined. The definition of the significance metric used to assess the sensitivity of a region in this Thesis, denoted by Z and described in detail in [72], is shown in Equation 5.3.1.

$$Z = k\sqrt{2\left(n\ln\left[\frac{n(b+\sigma^2)}{b^2+n\sigma^2}\right] - \frac{b^2}{\sigma^2}\ln\left[1+\frac{\sigma^2(n-b)}{b(b+\sigma^2)}\right]\right)} \tag{5.3.1}$$

In Equation 5.3.1, n is the number of observed events, b is the expected number of background events, and σ is the uncertainty on the prediction b. The factor $k = 1$ for $n \geq b$, while $k = -1$ for $n < b$. The significance is typically evaluated for several benchmark signal models with specific parameter choices, targeting a particular region of the signal kinematic phase space. In this Thesis, the σ is estimated as being 30%, representing a conservative estimate of the dominant modelling and experimental systematics. A well-optimised SR will maximise the significance for the targeted signal phase space, while keeping SM background contributions to a minimum. However, in maximising the significance, it must be ensured that the SR is robust against statistical limitations arising from the MC. A SR which is underpopulated in MC events can give an unreasonably-high estimated significance, and as such it is typically required that there are at least 10 events

in the MC for each major SM background, and also for the signal MC sample(s) used for region optimisation. Details on the specific grid-based and ML methods used are given in the following subsections.

Grid-based methods

Grid-based optimisation methods define a grid of proposed regions, each defined by unique selections on each of the discriminative variables. For each variable, there are N_i test cuts, where i denotes the given variable, such that the total number of combinations of cuts, N, is given by $N = \prod_{i=1}^{M} N_i$. As N is given by a product, the number of combinations rapidly grows with grid granularity and the number of variables tested. In addition, these methods are often run on several benchmark signal models, each with different parameter choices. This ensures good sensitivity can be achieved across a wide range of the available kinematic phase space. Numerous grid-based methods were used in this Thesis, and will now be discussed.

Inclusive grid search

An 'inclusive' grid search finds the optimal combination of selections by calculating the significance for each benchmark signal model for *every* candidate region and returning the region with highest signficance for each signal. While this method is guaranteed to find the region with the highest significance for each benchmark signal model, the number of tests rapidly grows with increasing numbers of input variables or with a large number of proposed regions. The limiting factor of this method is the computational time required to find the optimal region through evaluating the significance for every combination. The subsequent grid-based methods evade this issue by randomly sampling points on the grid of candidate regions.

Random grid search

The random grid search (RGS) algorithm samples random points from the grid of candidate regions, evaluating the significance for each. To alleviate the computational requirements of the 'inclusive' grid search, the RGS algorithm typically samples a small portion of the grid, running for i iterations, calculating the significance with that set of cuts, and then removing that point from the grid. Due to the random nature of the RGS algorithm, it is never guaranteed that the algorithm will find an optimal solution without sampling the entire grid. Therefore, the RGS algorithm is run numerous times to ensure the highest significance combination it achieved can not be improved. Additionally, the RGS algorithm is run for several benchmark signal models, to ensure sensitivity across the kinematic phase space.

Adaptive random grid search

The RGS algorithm enables a large portion of a potential signal phase space to be probed without the computational expensive of studying the phase space grid at every point inclusively. However, the RGS method, by definition, randomly samples the grid of points with no 'awareness' of the significance. Hence, the RGS algorithm can sample a point with high significance, potentially close to the optimal solution, before randomly moving to a region of low significance. To circumvent this, a modified version of the RGS algorithm, known as the *adaptive* random grid search (ARGS), was developed. Instead of allowing the movement between any two points on the grid, the ARGS algorithm adapts the step size in a significance-aware way. Around regions of high significance, where $Z \geq 2$, the step size shrinks to allow a high-granularity study of the phase space around the point of interest. Once the significance falls below $Z = 2$, the step size grows again to allow bigger steps between grid points. Finally, once the significance drops below the activation threshold, $Z = 0.5$, the algorithm is free to move between any points on the grid, and is equivalent to the RGS algorithm.

Genetic algorithm

The genetic algorithm (GA) takes inspiration from the process of natural selection, in which the 'fittest' individuals survive the sequential evolution of the system. The GA starts by generating a 'population' of N combinations of cuts. The significance of each combination is calculated, with the lowest 50% of combinations discarded. The surviving 50% of combinations, known as the 'parents', are then copied, and undergo 'cross-over' and 'mutation', to produce 'offspring'. For the cross-over step, the offspring are ordered in terms of significance. In the cross-over step, adjacent offspring randomly switch values of cuts, while in the subsequent mutation step, random cut values are smeared using a Gaussian distribution. The significance of both the parents and the offspring are re-evaluated, and the process repeats, selecting the best-performing 50%. This process repeats for a predefined number of iterations, $i = 100$, terminating early if the best significance found doesn't improve in 10 iterations.

Machine learning methods

Machine learning (ML) techniques are a wide and active area of research, and this section does not aim to review the state of ML research. Instead, it aims only to give an overview of the usage of ML in this context and describe the ML methods used in this Thesis, in particular the use of supervised learning ML *classifiers* to separate a signal from the SM background. Two types of classifier are relevant in this Thesis; Boosted Decision Trees (BDTs) and Deep Neural Networks (DNNs). Each will be described in their own section, along with details of their implementation.

ML models are, when first created, a completely general model described by a set of parameters, known as *hyperparameters*. The set of hyperparameters used are chosen to maximise the performance of the model, while allowing the model to be robust against unseen data. The ML models used in this Thesis, as previously mentioned, act as classifiers, predicting on an event-by-event basis which of a finite number of classes an event belongs to. This is particularly useful in searches, where one wishes to discriminate a signal from an often irreducible SM background. To give these models the ability to discriminate between the SM backgrounds and signal, they undergo *training*. The models are trained on MC, meaning the class of each event is known during the training phase, which is known as *supervised* learning. ML models can be susceptible to learning the input events and hence become unable to make meaningful predictions about unseen data, known as *overtraining*. In order to overcome this, the performance of the model is evaluated on a statistically-independent sample of events, known as the *validation* sample.

While the structure of each type of ML model is different, the inputs to and outputs of the models are the same. The inputs to the ML models used in this Thesis are physical observables, such as the amount of $E_{\mathrm{T}}^{\mathrm{miss}}$ or the transverse momentum of the objects in the event. The outputs of the ML models used are a number within in a fixed range. In the case of binary classification, where only two classes are defined, the output of the ML model is in the range $\in [-1, 1]$ for classifiers implemented in TMVA [73], and otherwise $\in [0, 1]$. For multiclass classification, where the number of classes $N_{\mathrm{class}} > 2$, the ML model outputs N_{class} values in the range $\in [0, 1]$, the sum of which are 1, where each value represents the prediction for a given class. In this case, events are assigned a class based upon which class score was highest.

Boosted Decision Trees

Boosted Decision Trees (BDTs) are constructed from an ensemble of decision trees, known as *weak classifiers*. Decision trees are constructed from nodes and leaves, where each node represents a test condition on one of the input variables, and each leaf represents a class label. Each individual decision tree has limited discrimination power when evaluated, and hence techniques such as *boosting* [74] are used to create an ensemble of weak classifiers with strong discrimination power. The boosting technique proceeds by iteratively creating trees and assigning each tree a corresponding weight, w_i, related to the classification accuracy of the tree.

During the training phase, the boosting procedure is used to minimise the differences between the prediction of the classifier, $F(\mathbf{x})$, given the inputs $\mathbf{x}$, and the true class of the input data, y_{truth}. The difference between the prediction of a classifier and the true class

of an event is calculated using a *loss function*. The BDTs implemented in the toolkit for multivariate analysis (TMVA) framework utilise the AdaBoost algorithm [75], while the BDTs implemented in XGBoost [76] use gradient boosting.

Neural Networks

Neural Networks (NNs) take inspiration from the structure of neural connections in the brain. A neural network is constructed from an input layer, an output layer and one or more hidden layers. A NN with 1 hidden layer is classed as a 'shallow' NN, while NNs with more than 1 hidden layer are classed as a 'deep' NN (DNN). Each layer in a NN is constructed from nodes, with the number of nodes in the input layer being determined by the number of input variables, and the number of nodes in the output layer being determined by the classification mode of the network. For binary classification, the NN will have a single node in the output layer, while for multiclass classification there will be N_{class} nodes, one for each class.

The connections between the nodes in the layers depends upon the structure of the NN. In this Thesis, the NNs used are 'fully-connected', meaning each node is connected to all of the nodes in the previous and next layer. These connections, known as *synapses*, each have a corresponding weight w_i, where i represents the index of the input node in the previous layer. The input to a node in a layer is given by the weighted sum of the outputs of the nodes in the previous layer, as follows:

$$y = \sum_i w_i x_i + b \, . \tag{5.3.2}$$

In Equation 5.3.2, w_i represents the synaptic weight connecting the ith node in the previous layer to the given node, x_i is the output of the ith node in the previous layer and b is the bias. Each layer in a NN has a defined *activation function*, which acts upon the input to a node to produce an output value. The hidden layers in the NNs used in this Thesis use a Rectified Linear Unit (ReLU) activation, which is defined as $y(x) = \max(0, x)$. For the output layer, the sigmoid activation function is used for binary classification, while the softmax activation function is used for the multiclass case.

5.4 Estimating systematic uncertainties

There are two, broad classes of systematic uncertainties that need to be considered when performing a high energy physics analysis; *experimental* uncertainties, related to uncertainties in the reconstruction of the physics objects in an event, and *modelling* uncertainties, related to choices made in the MC simulation employed to aid in the estimate of the SM background or signal process.

Experimental uncertainties

Uncertainties arise in the simulation and reconstruction of the physics objects described in Chapter 4. Experimental uncertainties can affect both the normalisation and shape of distributions, meaning the number of reconstructed objects, e.g. leptons, passing region selections can vary. This Section briefly describes the experimental systematics evaluated in the analyses detailed in Chapters 6 and 7.

Luminosity The integrated luminosity of the dataset is determined using van Der Meer scans, first described in [77] and elaborated upon for ATLAS in [78]. The luminosity uncertainty affects the normalisation of MC predictions, and ultimately the model-dependent and model-independent limits of an analysis. For the analysis detailed in Chapter 6, which uses data collected in 2015-2016, the luminosity uncertainty is determined to be 2.1%, while for the analysis detailed in Chapter 7, using the full Run-2 dataset collected between 2015-2018, the luminosity uncertainty is determined to be 1.7%.

Jets As previously described in Section 4.3, the energy of reconstructed jets must be corrected to account for calorimeter non-compensation, detector acceptance and defects and pileup. The JES calibration is derived using MC simulation and data [79], and the JES uncertainties arise from choices made when developing this calibration. The full JES uncertainty set totals around 100 sources of uncertainty, while a reduced set of JES uncertainties totalling 7-8 uncertainties is also provided for analyses which are insensitive to small variations in the calibration [80]. These uncertainties are derived from source such as the differences of jet response between data and MC, pile-up effects and the dependence of the energy scale on the flavour of the jets.
The energy of jets cannot be measured exactly, despite the corrections to the jet energy from the JES calibration. The Jet Energy Resolution (JER) is defined as the width of the Gaussian distribution describing the measured jet energy at the calibrated jet energy scale. The JER is determined from both data and MC [81], with its uncertainty arising from choices made when determining the JER.

Flavour-tagging Uncertainties on the b-tagging arise from the derived flavour tag efficiencies, as well as the rates which jet flavours are misidentified. The uncertainties, which depend on p_{T}, η and the jet flavour, are derived by varying the scale factors which correct the flavour tagging efficiency and mis-tag rates.

Leptons Uncertainties that arise in the reconstruction of leptons are related to the lepton energy resolution and scale calibrations, as well as the efficiencies corresponding to the reconstruction, identification and isolation. In this Thesis, lepton trigger efficiency

uncertainties are neglected due to the use of the $E_{\mathrm{T}}^{\mathrm{miss}}$ triggers in the analyses detailed in Chapters 6 and 7.

Missing transverse energy The uncertainties on the $E_{\mathrm{T}}^{\mathrm{miss}}$ are separated into uncertainties affecting the $E_T^{\mathrm{miss,\ hard}}$ and the $E_T^{\mathrm{miss,\ soft}}$ components, as described in Section 4.5. The uncertainties on the hard $E_{\mathrm{T}}^{\mathrm{miss}}$ term are derived by propagating the individual energy scale and resolution uncertainties on the physics objects in an event to the $E_{\mathrm{T}}^{\mathrm{miss}}$. The energy scale and resolution of the soft $E_{\mathrm{T}}^{\mathrm{miss}}$ term are evaluated using data and MC as described in [82].

Modelling uncertainties

Numerous sources of uncertainty arise in the modelling of SM backgrounds and signal. Typically, the dominant modelling systematics come from the specific choice of generator used to evaluate the ME and the choice of algorithm used to model the PS. In terms of specific modelling uncertainties, the interference between the $t\bar{t}$ and Wt processes is often large, as described in Section 3.3. Modelling systematics are evaluated by simulating the same physical process with two MC production configurations. This is done either exploiting the capability of modern MC generators to associate weights to the event such that the impact of different parameter choices can be evaluated, or by comparing two independent samples. This uncertainty is then applied in the statistical analysis as a 2-sided systematic affecting the normalisation and/or shape of the nominal distributions of the corresponding process. A general overview of the sources of modelling uncertainty are described here, while specific information on the procedure used to evaluate the individual modelling uncertainties are given in Chapters 6 and 7.

PDF uncertainties The PDF uncertainties are evaluated considering both comparisons of the predictions with alternative PDF sets with respect to the nominal, and comparisons between nominal and variations within the same PDF set. References on methods used can be found for example in [83]. The uncertainty due to the choice of the nominal PDF set was found to be $\mathcal{O}(1\%)$ using the internal weights of the W+jets samples which enable the choice of nominal PDF set to be varied, which is far less than the dominant systematics and statistical uncertainties. Hence, PDF uncertainties are neglected in this Thesis.

Generator uncertainties The choice of generator used to model the hard scatter is typically driven by the agreement between the MC predictions and data, with the generator which best reproduces the data across a range of phase space being deemed the nominal choice. In order to ensure the estimate of the nominal generator is robust in the analysis phase space, the uncertainty on the calculation of the ME is evaluated by generating an MC sample which uses a different generator for the hard scatter, but is interfaced to the same

PS algorithm. Variations of the generator uncertainty are not available for all processes; in this Thesis, the generator uncertainties are evaluated for the top-pair, single top and $t\bar{t}V$ processes.

Parton showering uncertainties Similarly to generator uncertainties, the nominal choice of PS algorithm is driven by the agreement between data and MC predictions. To estimate the impact of using a different PS algorithm, the nominal configuration is compared with a MC sample which is produced using the same generator for the hard scatter but using a different PS algorithm. Again, this is evaluated only for the top-pair, single top and $t\bar{t}V$ processes.

Scale uncertainties Numerous choices of scale are made when producing MC samples, such as the value of α_S, μ_R and μ_F. For the W/Z+jets, diboson and triboson backgrounds, the predictions of 7 variations of μ_R and μ_F are evaluated, with the values of μ_R and μ_F being evaluated at 0.5×, 1.0× and 2.0× the nominal values. The maximum downwards and upwards variation then define the asymmetric uncertainty on these scale choices. As mentioned in Section 3.2.1, there can be overlap between a LO with PS and NLO process, and hence matching and/or merging is used to remove the overlap. For the W/Z+jets backgrounds, the choice of scale used to perform such matching is varied from the nominal value of 20 GeV to 15 GeV and 30 GeV.

Uncertainty calculation As previously mentioned, modelling uncertainties are calculated by comparing two MC predictions and taking the difference as the 1σ variation, which is known as a 2-point systematic. For backgrounds which are estimated using MC-only, the systematic in a given analysis region is calculated using the difference of the predictions of the two MC samples, as shown in Equation 5.4.1. The MC sample used as a variation can either be a statistically-independent sample, generated in a different configuration, or a weight-based variation of the nominal sample, where an alternate MC weight is applied to the nominal MC.

$$\alpha_{\text{syst}}^{\text{process}} = \pm \left| \frac{N(\text{MC})_{\text{variation}}^{\text{process}} - N(\text{MC})_{\text{nominal}}^{\text{process}}}{N(\text{MC})_{\text{nominal}}^{\text{process}}} \right| \tag{5.4.1}$$

For the analysis detailed in Chapter 6, the modelling uncertainties on the $t\bar{t}$, Wt and W+jets processes are estimated using transfer factors between the CR and SR/VR. The transfer factor between the CR and SR for a given process is shown in Equation 5.4.2.

$$\text{TF}_{\text{syst}}^{\text{process}} = \frac{N(\text{MC, SR})_{\text{syst}}^{\text{process}}}{N(\text{MC, CR})_{\text{syst}}^{\text{process}}} \tag{5.4.2}$$

The uncertainty in the SR is then given by the difference in transfer factors estimated using the nominal and variation MC samples, as shown in Equation 5.4.3.

$$\alpha_{\text{syst}}^{\text{process}} = \Delta\text{TF}_{\text{syst}}^{\text{process}} = \pm \left| \frac{\text{TF}_{\text{variation}}^{\text{process}} - \text{TF}_{\text{nominal}}^{\text{process}}}{\text{TF}_{\text{nominal}}^{\text{process}}} \right| \tag{5.4.3}$$

The transfer factor approach is not used in the analysis detailed in Chapter 7 as the SR bins each have a very different $E_{\text{T}}^{\text{miss}}$ spectrum, while the CRs are defined using a single $E_{\text{T}}^{\text{miss}}$ bin, and hence the extrapolation from the single-bin CRs to SR bins is difficult to validate. Therefore, modelling uncertainties in this analysis are evaluated using the prescription described in Equation 5.4.1.

5.5 Statistical analysis

All statistical analyses performed in this Thesis were implemented in the HistFitter framework [84]. This framework requires an analysis structure similar to that shown in Figure 5.1. The use of CRs in the statistical analysis allows background process yields to be corrected to data, to minimise mismodelling of data by the MC in the SRs.

Statistical analysis are performed by constructing a likelihood function, L, depending upon the expected number of MC events in each CR and SR, the systematic uncertainties arising from statistical, experimental and theoretical sources on these backgrounds, and the observed number of events in each CR and SR. The likelihood function used by HistFitter is shown in Equation 5.5.1.

$$L(n, \theta^0 | \mu_{\text{sig}}, b, \theta) = P(n_S | \lambda_S(\mu_{\text{sig}}, b, \theta)) \times \prod_{i \in CR} P(n_i | \lambda_i(\mu_{\text{sig}}, b, \theta)) \times C_{\text{syst}}(\theta^0, \theta) \tag{5.5.1}$$

The likelihood function is constructed around a product of Poisson distributions of observed (n_S, n_i) and expected (λ_S, λ_i) events in the SR and CRs, respectively. The Poisson expectations, λ_S and λ_i, depend upon the background prediction, b and the corresponding nuiscance parameters representing the systematic uncertainties, θ, as well as the signal strength parameter, μ_{sig}. The signal strength parameter can be set to 0 to remove signal being considered in the fit, or if considering signal can be set to 1 to include the nominal signal yield estimate for a signal under consideration. The systematics term, $C_{\text{syst}}(\theta^0, \theta)$, shown in Equation 5.5.2 is defined as a product of Gaussian constraints, θ_j, each representing a systematic variation, which are varied around $\theta_j^0 = 0$ when maximising the likelihood function.

$$C_{\text{syst}}(\theta^0, \theta) = \prod_{j \in S} G(\theta_j^0 - \theta_j) \tag{5.5.2}$$

Likelihood fits using this framework utilise the background CRs to make estimates of the backgrounds in the SR by normalising the expected number of background events from the MC to data. Each background with a corresponding CR, known as a *normalised* background, acquire a normalisation factor, μ_p. This normalisation factor is extracted from the fit automatically, and is used to provide an estimate of the background in the SR. This extrapolation to the SR is enabled through the use of transfer factors (TFs), which are shown in Equation 5.5.3.

$$N^{SR}_{\text{process}}(\text{Exp}) = N^{CR}_{\text{process}}(\text{Obs}) \cdot \frac{N^{SR}_{\text{process}}(\text{Exp})}{N^{CR}_{\text{process}}(\text{Exp})} = \mu_p \cdot N^{SR}_{\text{process}}(\text{MC}) \tag{5.5.3}$$

In Equation 5.5.3, the number of expected events in the SR region for a given process, $N^{SR}_{\text{process}}(\text{Exp})$, is calculated by multiplying the expected number of events for that process in that region from the MC, $N^{SR}_{\text{process}}(\text{MC})$, by the process-specific normalisation factor, μ_p, which is calculated automatically when performing the fit. The differences between the number of expected and observed events in a CR is used to constrain the normalisation parameters in the fit. In searches for New Physics, test statistics are used to quantify the agreement between the expected and observed yields in a given region. Of particular interest in this Thesis are the p-value and the CL_s. The p-value, given a hypothesis H_0, is interpreted as the probability that the alternate hypothesis, H_1, can provide a result at least as incompatible with H_0 as the observed result. The definition of the p-value is given in Equation 5.5.4.

$$p = \int_{t_{\text{obs}}}^{+\infty} g(t|H_0)dt \tag{5.5.4}$$

In Equation 5.5.4, $g(t|H_0)$ is the probability density of the test statistic, t, under the assumption of the hypothesis, H_0. In the event of a discrepancy between the expected and observed results, it is desirable to be able to quantify the size of a discrepancy, which is done using the significance, Z. This significance is defined such that a result which is Z standard deviations from the mean of a Gaussian distribution has an integral equal to the p-value.

The test statistic used for the purposes of setting limits on New Physics signals is the profile log likelihood ratio, shown in Equation 5.5.5.

$$t_{\mu_{\text{sig}}} = -2\log\left(\frac{L(\mu_{\text{sig}}, \hat{\hat{\theta}})}{L(\hat{\mu}_{\text{sig}}, \hat{\theta})}\right) \tag{5.5.5}$$

In Equation 5.5.5, L is the likelihood function defined in Equation 5.5.1, where the denominator has parameter choices such that the likelihood is maximised, while the numerator has parameter choices that maximise the likelihood for the specific signal hypothesis under test.

In the context of searches for New Physics, the p-value can be used to claim a discovery of New Physics, or exclude a given signal hypothesis. To claim the discovery of New Physics, one must reject the hypothesis that only the SM background contributes to the observed result to a level of $Z = 5\sigma$, corresponding to $p < 2.87 \times 10^{-7}$. The requirements to exclude a signal hypothesis are less stringent, requiring the rejection of the SM background plus BSM signal hypothesis with values of $p < 0.05$, corresponding to $Z = 1.64$. This exclusion limit corresponds to a 95% confidence limit.

In the case where an analysis has little or no sensitivity to a signal, the p-value can be an unreliable metric to use. For a given signal plus background hypothesis, $s + b$, the probability that the number of events, t, will be greater than or equal to the number of observed events, t_{obs} is given by:

$$p_{s+b} = P(t \geq t_{\text{obs}}|s + b) = \int_{t_{\text{obs}}}^{+\infty} g(t|s + b)dt\,. \tag{5.5.6}$$

The confidence limit CL$\equiv 1-\alpha$, such that the signal plus background hypothesis is excluded if $p_{s+b} < \alpha$. Similarly, in the background-only hypothesis, b, the probability that the number of events is less than the number of observed events is given by:

$$p_b = P(t \leq t_{\text{obs}}|b) = \int_{-\infty}^{t_{\text{obs}}} g(t|b)dt\,. \tag{5.5.7}$$

In the case where the analysis has little or no sensitivity to the signal, the distributions of the test statistics $g(t|s + b)$ and $g(t|b)$ almost entirely overlap. In the case that the background fluctuates downwards, the signal plus background hypothesis can be excluded, known as 'spurious exclusion'. To circumvent this, the CL$_s$ method [85] was developed, where the CL_s is defined as shown in Equation 5.5.8.

$$\text{CL}_s = \frac{p_1}{1 - p_0} = \frac{\int_{t_{\text{obs}}}^{+\infty} g(t|H_1)dt}{1 - \int_{-\infty}^{t_{\text{obs}}} g(t|H_0)dt} \tag{5.5.8}$$

In Equation 5.5.8, p_1 corresponds to the p-value that the alternate hypothesis, H_1, is at least as incompatible with H_0 as the observed result, while p_0 corresponds to the p-value that the observed result is compatible with the null hypothesis, H_0. By dividing p_1 by 1-p_0, the previously mentioned issues where the distributions of the test statistic for the signal plus background and background-only hypotheses almost entirely overlap in the limit of low/no sensitivity is avoided, as the denominator term in Equation 5.5.8 forces the CL$_s$ values to be large in this scenario, and hence not be excluded.

Background-only fit

The background-only fit is independent of any signal model assumptions, including only SM background MC in the fit. In this scenario, μ_{sig} is set equal to 0. This fit type includes only the CRs in the fit, and hence is not affected by the observed events in the SRs. The purpose of this fit is to estimate the background yields in the SRs and VRs in a signal-agnostic way, under the assumption that the CRs have negligible signal contamination. Additionally, the results of the background-only fit can be used as an indication of the sensitivity of an analysis to a different signal model, by using the number of signal events in the SR and the results of the background-only fit to perform some hypothesis test.

Model-dependent fit

The model-dependent fit regime includes background events and a specific signal model, fitting all processes together in both the CRs and SRs, including a signal strength parameter μ_{sig}. The signal is included in *all* regions, to allow any signal contamination in the CRs to be correctly accounted for when calculating the background normalisation factors, μ_p.

Generally, many different signal hypotheses are tested to ensure coverage of a wide range of phase space. Typically, this is achieved by generating many MC signal samples and varying one or two of the free parameters, such as the masses of the BSM particles. The model-dependent fit is performed on every signal point generated, such that the entire phase space of signal parameters is probed.

Model-independent fit

The model-independent fit is used to set limits on a generic BSM process present in the SRs. This fit includes both the CRs and SRs, but does not include a specific signal model, using a 'dummy' signal instead, and also does not allow signal contamination in the CRs. In this fit regime, the SRs are implemented as an inclusive, single-bin region. The result of this fit is used to set upper limits on the visible cross-section, σ_{vis}, and the number of events from BSM processes in a given SR of a generic BSM process.

Part II

Searches for New Physics in Run-2 ATLAS data

Chapter 6

Searches for $\tilde{\chi}_1^{\pm}\tilde{\chi}_2^0$ pair-production

This Chapter presents an overview of searches for the pair-production of the chargino, $\tilde{\chi}_1^{\pm}$, and the next-to-lightest neutralino, $\tilde{\chi}_2^0$, performed during the Run-2 period of ATLAS data taking The chargino is assumed to decay via a W boson and the lightest neutralino, $\tilde{\chi}_1^{\pm} \rightarrow W\tilde{\chi}_1^0$, while a decay through the Higgs boson, $\tilde{\chi}_2^0 \rightarrow h\tilde{\chi}_1^0$ is assumed for the next-to-lightest neutralino. The main focus is on the analysis performed using data taken in 2015-2016, totalling 36.1 fb^{-1}. Later in this Chapter, the results of an updated analysis using the full Run-2 dataset of 139 fb^{-1} are also presented, along with additional studies using machine learning to improve the sensitivity to the signal. Sensitivity studies for this signal at the High-Luminosity LHC, using a dataset of 3000 fb^{-1} collected at $\sqrt{s} = 14$ TeV, are presented in Chapter 9.

The author's contributions to the analyses presented in this Chapter are as follows. For the analysis performed with the 36.1 fb^{-1} dataset, the contributions consisted of the optimisation of the SR targeting the smallest mass splittings (SRLM), deriving the single top and W+jets CRs and VRs, and deriving the theoretical systematics on the SM backgrounds in all regions. The analysis performed with the 139 fb^{-1} dataset, the contributions consisted of performing cutflow comparisons and assisting in the evaluation of the theory systematics. The contributions to the ML studies consisted of developing the software used to perform these studies, along with assisting in optimising the variable choices used for the upcoming publication.

A search for $\tilde{\chi}_1^{\pm}\tilde{\chi}_2^0$ pair-production decaying via the Wh signature was undertaken in Run 1 using 20.3 fb^{-1} of data taken at taken 8 TeV centre-of-mass energy [86], targeting leptonic W boson decays, and $h \rightarrow b\bar{b}$, $h \rightarrow \gamma\gamma$, $h \rightarrow WW^*/ZZ^*/\tau\tau$ decays. Exclusion limits at 95% CL were set on this signal, excluding the process up to $\tilde{\chi}_1^{\pm}/\tilde{\chi}_2^0$ masses of around 275 GeV for a massless $\tilde{\chi}_1^0$. The exclusion limit for the individual channels, as well as the statistical combination of all channels, is shown in Figure 6.1.

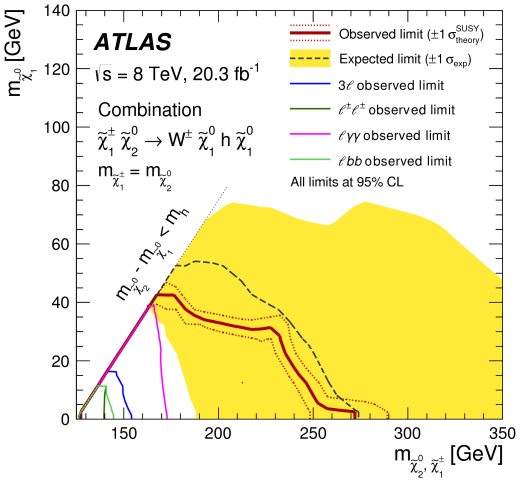

Figure 6.1: A plot showing the four exclusion limits obtained from searches for $\tilde{\chi}_1^{\pm}$ $\tilde{\chi}_2^0$ pair-production with the Wh signature during the Run-1 data taking period.

The Run-1 analysis had limited sensitivity to the signal model, as shown in Figure 6.1, where the yellow band around the combined limit shows the size of the statistical and systematic uncertainty on the SM background.

6.1 SUSY signal model

The decay channel targeted in this Chapter and in Chapter 9 require the W boson to decay leptonically, $W \rightarrow \ell\nu$, while the Higgs boson decays to two b-tagged jets, $h \rightarrow b\bar{b}$. In scenarios where the composition of the $\tilde{\chi}_2^0$ is Wino-like, the branching fraction of to the Higgs boson is large, and can become the dominant decay channel. The Higgs boson in this process, h, is the lightest CP-even Higgs from the extended SUSY Higgs sector and is assumed to be a SM-like Higgs boson, with $m_{\mathrm{h}} = 125$ GeV and with the branching fraction of BR($h \rightarrow b\bar{b}$) = 58%. Complimentary decay channels targeting the all-hadronic, $Wh \rightarrow qq'b\bar{b}$, and the single lepton plus photons, $Wh \rightarrow \ell\nu\gamma\gamma$, decays allow the reconstruction of the Higgs boson, while same-sign two-lepton and three-lepton signatures are sensitive to $h \rightarrow WW^*/ZZ^*/\tau\tau$ decays. A diagram of the signal process relevant for this Chapter is shown in Figure 6.2. Dedicated searches also target the decay of the $\tilde{\chi}_2^0$ to the Z boson [87, 88] as shown in Figure 6.2b, exploiting the decay of the Z boson into two charged leptons.

SUSY models have an enormous parameter space with over 100 free parameters, such as the sparticle masses and couplings. Simplified models vastly reduce the number of free parameters, such that a single analysis can be sensitive to a large region of the SUSY model phase space. This analysis has two free parameters, the mass of the chargino/next-to-lightest neutralino, m($\tilde{\chi}_1^{\pm}/\tilde{\chi}_2^0$), and the mass of the lightest neutralino, m($\tilde{\chi}_1^0$). Simulated signal samples are generated over a wide range on the m($\tilde{\chi}_1^{\pm}/\tilde{\chi}_2^0$)-m($\tilde{\chi}_1^0$) grid, as shown in

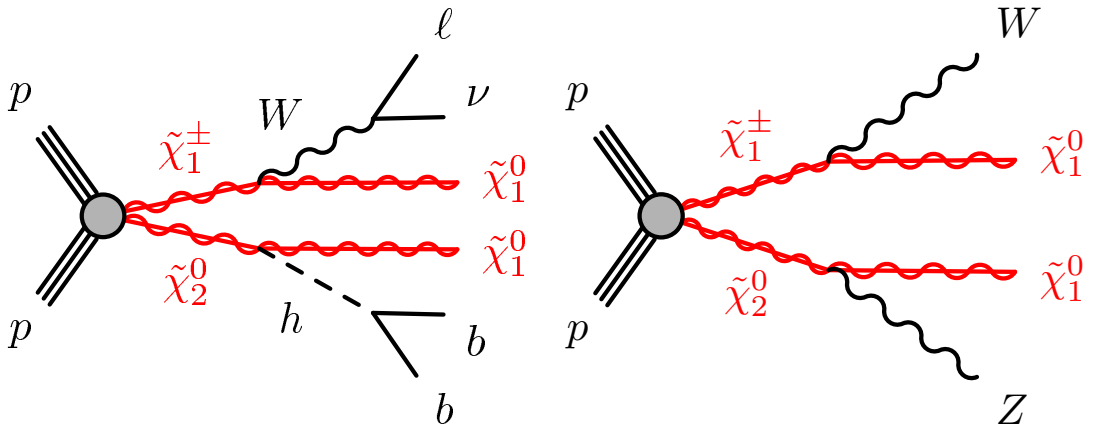

(a) (b)

Figure 6.2: Diagram showing $\tilde{\chi}_1^{\pm}\tilde{\chi}_2^0$ pair-production, with the chargino and neutralino decaying via a SM W boson and a Higgs (6.2a), and a Z boson (6.2b), respectively.

Figure 6.3.

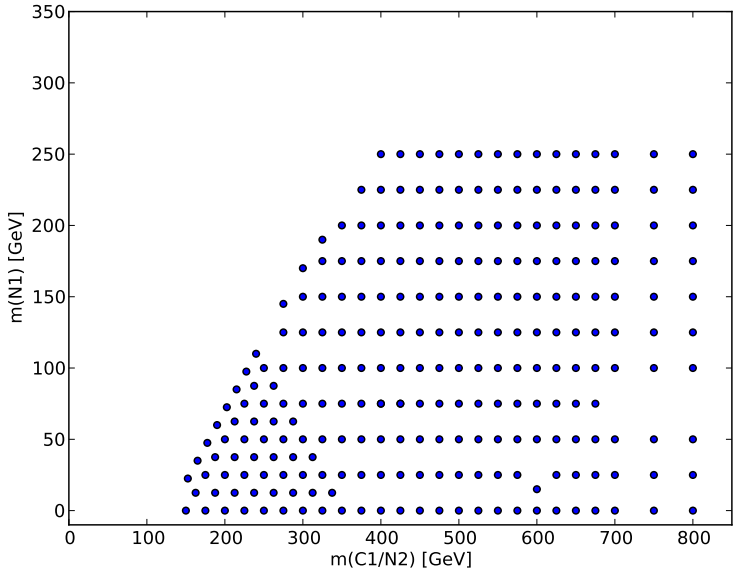

Figure 6.3: Plot showing the grid of MC signal samples generated for the analysis. The x-axis shows the masses of the $\tilde{\chi}_1^{\pm}/\tilde{\chi}_2^0$, and the y-axis shows the masses of the $\tilde{\chi}_1^0$.

6.2 Event selection

Candidate events for this analyses are first selected using a set of loose, preliminary selections, known as 'preselection'. The preselection requirements, summarised in Table 6.1, target events with an a topology characterised by the presence of a single lepton, two b-jets

and $E_{\mathrm{T}}^{\mathrm{miss}}$. All events are first required to pass one of the $E_{\mathrm{T}}^{\mathrm{miss}}$ triggers detailed in Section 3.1, which are determined to be 100% efficient in the subsequently-defined regions. All events are required to have exactly 1 electron or muon passing the signal lepton requirements, with any extra baseline leptons being vetoed. Events are required to have either 2 or 3 jets with transverse momentum greater than 25 GeV, with exactly two of these jets being b-tagged using the MV2c10 algorithm, described in Section 4.4. The b-tagged jets are also required to have transverse momentum greater than 25 GeV. The presence of upto one additional non-tagged jet is allowed as it was found to increase the SR statistics by upto 50% for the signal. Lower bound requirements are placed on the m_{bb} and m_{T} variables, introduced in Section 5.2, to reduce the combinatoric and multi-jet backgrounds.

Variable	Selection
$N_{\ell}^{\mathrm{baseline}}$	$= 1$
$N_{\ell}^{\mathrm{signal}}$	$= 1$
$p_{\mathrm{T}}(\ell_1)$	> 27 GeV
N_{jet}	$= 2$ or 3
$p_{\mathrm{T}}(\mathrm{jet})$	> 25 GeV
$N_{b-\mathrm{jet}}$	$= 2$
$p_{\mathrm{T}}(b-\mathrm{jet})$	> 25 GeV
m_{T}	> 40 GeV
m_{bb}	> 50 GeV

Table 6.1: A summary of the preliminary event selection used in the 36.1fb^{-1} search for $\tilde{\chi}_1^{\pm}\tilde{\chi}_2^0$ pair-production.

At the preselection level, the dominant SM backgrounds, estimated from MC-only are $t\bar{t}$ (67%), Wt-channel single top (17%) and W+jets (12%). Three SRs are defined, each targeting a different region of the m($\tilde{\chi}_1^{\pm}/\tilde{\chi}_2^0$)-m($\tilde{\chi}_1^0$) parameter space. SRLM is optimised to target scenarios where the mass-splitting of the m($\tilde{\chi}_1^{\pm}/\tilde{\chi}_2^0$) and m($\tilde{\chi}_1^0$), denoted by ΔM($\tilde{\chi}_1^{\pm}/\tilde{\chi}_2^0, \tilde{\chi}_1^0$), is similar to the Higgs mass. SRMM and SRHM target larger ΔM($\tilde{\chi}_1^{\pm}/\tilde{\chi}_2^0, \tilde{\chi}_1^0$), around 150-250 GeV and > 250 GeV, respectively. In addition to the $E_{\mathrm{T}}^{\mathrm{miss}}$, m_{T}, and m_{bb} variables, the m_{CT} observable, also introduced in Section 5.2, is exploited for the definition of the signal regions. Each of these variables are described in Section 5.2. The three SRs are defined in Table 6.2.

	SRLM	SRMM	SRHM
m_{bb}	$\in [105, 135]$ GeV		
m_{CT}	> 160 GeV		
$E_{\mathrm{T}}^{\mathrm{miss}}$	> 200 GeV		
m_{T}	$\in [100, 140]$ GeV	$\in [140, 200]$ GeV	> 200 GeV

Table 6.2: A summary of the signal region selections used in the SUSY Wh $1\ell + b\bar{b} + E_{\mathrm{T}}^{\mathrm{miss}}$ analysis.

The invariant mass of the two b-jets, m_{bb}, targets the Higgs boson mass, selecting events in the range $105 < m_{bb} < 135$ GeV. The contranservse mass, m_{CT}, is required to satisfy $m_{\mathrm{CT}} > 160$ GeV, to effectively suppress the $t\bar{t}$ process. The transverse mass, m_{T}, is required to be greater than 100 GeV to suppress the W+jets background, with three bins defined to target different $\Delta\mathrm{M}(\tilde{\chi}_1^{\pm}/\tilde{\chi}_2^0, \tilde{\chi}_1^0)$ scenarios.

6.3 Background estimation

The $t\bar{t}$, single top and W+jets backgrounds are the most dominant backgrounds in the three SRs. Each of these major backgrounds have corresponding CRs defined in which to evaluate the process-specific normalisations, μ_{process}. The $t\bar{t}$ CR is defined with 3 m_{T} bins, matching the m_{T} ranges of the 3 SR bins, named CR($t\bar{t}$)-LM, CR($t\bar{t}$)-MM and CR($t\bar{t}$)-HM, respectively. Each of these regions has a separate $t\bar{t}$ normalisation factor in the statistical analysis. These CRs invert the selection on the m_{CT} to target the production of a pair of top quarks, while the selection on m_{bb} is inverted as the distribution is not expected to peak around the Higgs masses. A single-bin CR for the single top background, CR(t), and a single-bin CR for the W+jets background, CR(W), are also defined. The single-top CR is defined by requiring the m_{bb} to be larger than 195 GeV to select b-quarks coming from the decay of a top quark and the initial state gluon splitting. Finally, the W+jets CR exploits the m_{T} variable, to target the decay of a single leptonic W boson, while rejecting the $t\bar{t}$ background. The full definitions of these regions are given in Table 6.3.

	Region				
Variable	CR($t\bar{t}$-LM)	CR($t\bar{t}$-MM)	CR($t\bar{t}$-HM)	CR(t)	CR(W)
m_{T} [GeV]	$\in [100, 140]$	$\in [140, 200]$	> 200	> 100	$\in [40, 100]$
m_{CT} [GeV]	< 160	< 160	< 160	> 160	> 160
m_{bb} [GeV]	$\notin [105, 135]$	$\notin [105, 135]$	$\notin [105, 135]$	> 195	< 80
$E_{\mathrm{T}}^{\mathrm{miss}}$ [GeV]	> 200	> 200	> 200	> 200	> 200

Table 6.3: Control region definitions for the SUSY Wh $1\ell + b\bar{b} + E_{\mathrm{T}}^{\mathrm{miss}}$ analysis.

Six VRs are defined, with three regions targeting m_{bb} values in a window around the Higgs peak, $m_{\mathrm{bb}} \in [105, 135]$ GeV, and three regions targeting m_{bb} values above and below this range, referred to as the 'sideband' region. The former VRs are referred to as 'on-peak' regions, denoted by $\mathrm{VR_{on}}$, while the latter are referred to as 'off-peak' regions and are denoted by $\mathrm{VR_{off}}$. Each set of VRs mirrors the SR binning in the m_{T} variable. The explicit VR definitions are given in Table 6.4.

	Region		
Variable	$\mathrm{VR_{on}}$(LM)	$\mathrm{VR_{on}}$(MM)	$\mathrm{VR_{on}}$(HM)
m_{T} [GeV]	$\in [100, 140]$	$\in [140, 200]$	> 200
m_{CT} [GeV]	< 160	< 160	< 160
m_{bb} [GeV]	$\in [105, 135]$	$\in [105, 135]$	$\in [105, 135]$
$E_{\mathrm{T}}^{\mathrm{miss}}$ [GeV]	> 200	> 200	> 200
	Region		
Variable	$\mathrm{VR_{off}}$(LM)	$\mathrm{VR_{off}}$(MM)	$\mathrm{VR_{off}}$(HM)
m_{T} [GeV]	$\in [100, 140]$	$\in [140, 200]$	> 200
m_{CT} [GeV]	> 160	> 160	> 160
m_{bb} [GeV]	$< 95 \,\|\|\, \in [145, 195]$		
$E_{\mathrm{T}}^{\mathrm{miss}}$ [GeV]	> 180	> 180	> 180

Table 6.4: Validation region definitions for the SUSY Wh $1\ell + b\bar{b} + E_{\mathrm{T}}^{\mathrm{miss}}$ analysis. The subscript 'on' and 'off' refer respectively to the m_{bb} requirement targeting the Higgs boson, hence 'on-peak', and targeting the sideband regions, or 'off-peak'.

6.4 Systematic uncertainties

Three types of uncertainty are considered in this analysis; statistical uncertainties, arising from the finite statistics in both data and MC samples, experimental systematics and modelling systematics. Section 5.4 describes the experimental systematics evaluated, along with the transfer factor prescription which is used to evaluate the modelling uncertainties in this analysis.

The dominant experimental systematics originate from the JER, totalling up to 20% of the background uncertainty in SRMM, with the subdominant experimental systematics arising from the b-tagging uncertainties. The SRs are statistically-limited and hence the size of the experimental uncertainties is driven by statistical fluctuations. The dominant theory uncertainties arise from the modelling of the $t\bar{t}$ process, estimated as 15-20% of the total background uncertainty in the SRs. The uncertainty due to the interference between the Wt-channel single top and $t\bar{t}$ processes ranges from 30% to 52% on the single top estimate in the SRs. A summary of the systematics in this analysis is shown in Table 6.5.

$1\ell + b\bar{b} + E_{\mathrm{T}}^{\mathrm{miss}}$ **channel**			
Uncertainty of region	SRLM	SRMM	SRHM
Total background expectation	5.7	2.8	4.6
Total background uncertainty	±2.3	±1.0	±1.2
Systematic, experimental	±1.3	±0.7	±0.6
Systematic, theoretical	±2.2	±0.9	±0.7
Statistical, MC samples	±1.1	±0.5	±0.6
Statistical, $\mu_{\mathrm{TT,ST,Wj}}$ scale-factors	±0.8	±0.6	±1.3

Table 6.5: Table showing a summary of the experimental and modelling uncertainties in the SUSY Wh $1\ell + b\bar{b} + E_{\mathrm{T}}^{\mathrm{miss}}$ analysis. The uncertainties are expressed in terms of the number of events.

6.5 Results

Background-only fit results

The results of the background-only fit in the CRs and SRs for the $1\ell+b\bar{b}+E_{\mathrm{T}}^{\mathrm{miss}}$ channel are shown in Tables 6.6 and 6.7, respectively. As explained in Chapter 5.5, the background-only fit configuration uses only the CRs to normalise the dominant backgrounds, in this case $t\bar{t}$, single top and W+jets. The $t\bar{t}$ background has 3 separate normalisation factors, one for each m_{T} bin, such that data/MC differences in each region can be corrected independently of each other. This is required as each m_{T} bin has a different composition of semi-leptonic and dileptonic $t\bar{t}$, with the LM region being dominated by semi-leptonic decays and the higher m_{T} bins being dominated by dileptonic $t\bar{t}$. The results of the background-only fit are then extrapolated to the VRs and SRs, such that an estimate of the backgrounds in the SR can be derived without bias from any potential excesses in the SRs, or assumptions on the signal model itself. Excellent data/SM agreement is observed in the CRs and most of the VRs. In $\mathrm{VR_{on}}$-HM and SRMM, there are excesses between $1.5-2\sigma$. These discrepancies were carefully investigated, with no reason identified as an explanation other than a potential statistical fluctuation. Excellent data/SM agreement is observed in the SRs.

The normalisation factors derived for the $t\bar{t}$, single top and W+jets backgrounds using the background-only fit configuration are given in Table 6.8, showing all values are compatible with unity.

Post-fit distributions in the CRs are shown in Figure 6.4, where excellent data/SM agreement is observed. In these plots, data and SM predictions are shown after all selections but the one on the variable shown, referred to as a 'N-1' distribution. The uncertainty band in the ratio includes all statistical and systematic uncertainties on the SM backgrounds.

Figure 6.5 shows the data/SM agreement in the VRs, where good agreement is observed within 2σ.

Control regions	CR($t\bar{t}$)-LM	CR($t\bar{t}$)-MM	CR($t\bar{t}$)-HM	CR(W)	CR(t)
Observed events	192	359	1115	72	65
Fitted bkg events	192 ± 14	359 ± 19	1115 ± 34	72 ± 9	65 ± 8
$t\bar{t}$	147 ± 33	325 ± 32	1020 ± 90	15 ± 14	20^{+23}_{-20}
Single top	28 ± 25	22^{+24}_{-22}	60^{+70}_{-60}	4^{+6}_{-4}	33 ± 25
W+jets	16 ± 7	7.3 ± 2.7	25 ± 11	51 ± 17	8 ± 4
$t\bar{t}V$	1.16 ± 0.20	2.8 ± 0.4	6.9 ± 1.1	0.079 ± 0.022	3.2 ± 0.6
Diboson	0.57 ± 0.24	0.92 ± 0.29	1.3 ± 0.4	2.1 ± 1.1	0.84 ± 0.28
Others	0.125 ± 0.032	0.20 ± 0.06	1.9 ± 0.5	0.24 ± 0.17	0.10 ± 0.04
MC exp. SM events	201 ± 16	310 ± 20	1150 ± 70	58 ± 15	58 ± 22
$t\bar{t}$	164 ± 10	282 ± 14	1070 ± 50	16 ± 14	20^{+21}_{-20}
Single top	24 ± 10	20 ± 14	50 ± 50	3^{+4}_{-3}	29.2 ± 2.3
W+jets	10.9 ± 2.8	5.1 ± 1.2	17 ± 4	35 ± 4	5.4 ± 1.9
Diboson	0.57 ± 0.24	0.92 ± 0.29	1.3 ± 0.4	2.1 ± 1.1	0.84 ± 0.28
$t\bar{t}$ +V	1.16 ± 0.20	2.8 ± 0.4	6.9 ± 1.1	0.079 ± 0.022	3.2 ± 0.6
Others	0.12 ± 0.03	0.6 ± 0.1	1.4 ± 0.4	0.3 ± 0.2	0.10 ± 0.05

Table 6.6: Table showing the results of the background-only fit in the CRs of the SUSY Wh $1\ell + b\bar{b} + E_{\mathrm{T}}^{\mathrm{miss}}$ analysis. Excellent data/SM agreement is observed in all regions.

Signal regions	SRLM	SRMM	SRHM
Observed events	6	7	5
Fitted bkg events	5.7 ± 2.3	2.8 ± 1.0	4.6 ± 1.2
$t\bar{t}$	3.4 ± 2.9	1.4 ± 1.0	1.1 ± 0.6
Single top (Wt)	$1.4^{+1.4}_{-1.4}$	$0.8^{+0.9}_{-0.8}$	1.2 ± 1.1
W + jets	0.6 ± 0.4	0.20 ± 0.11	1.6 ± 0.6
$t\bar{t}V$	0.10 ± 0.04	0.32 ± 0.09	0.54 ± 0.14
Diboson	$0.12^{+0.15}_{-0.12}$	0.05 ± 0.03	0.08 ± 0.02
Others	0.10 ± 0.05	0.03 ± 0.01	0.04 ± 0.02

Table 6.7: Table showing the background-only fit results in the SRs of the SUSY Wh $1\ell + b\bar{b} + E_{\mathrm{T}}^{\mathrm{miss}}$ analysis.

Background normalisations	
$\mu(t\bar{t}\text{-LM})$	1.02 ± 0.14
$\mu(t\bar{t}\text{-MM})$	1.15 ± 0.13
$\mu(t\bar{t}\text{-HM})$	$0.89^{+0.21}_{-0.20}$
$\mu(W)$	1.40 ± 0.5
$\mu(t)$	$1.10^{+0.7}_{-1.1}$

Table 6.8: Table showing the background normalisation factors for the SUSY Wh $1\ell + b\bar{b} + E_{\mathrm{T}}^{\mathrm{miss}}$ analysis, derived by performing a simultaneous fit of all CRs as described in Section 5.5.

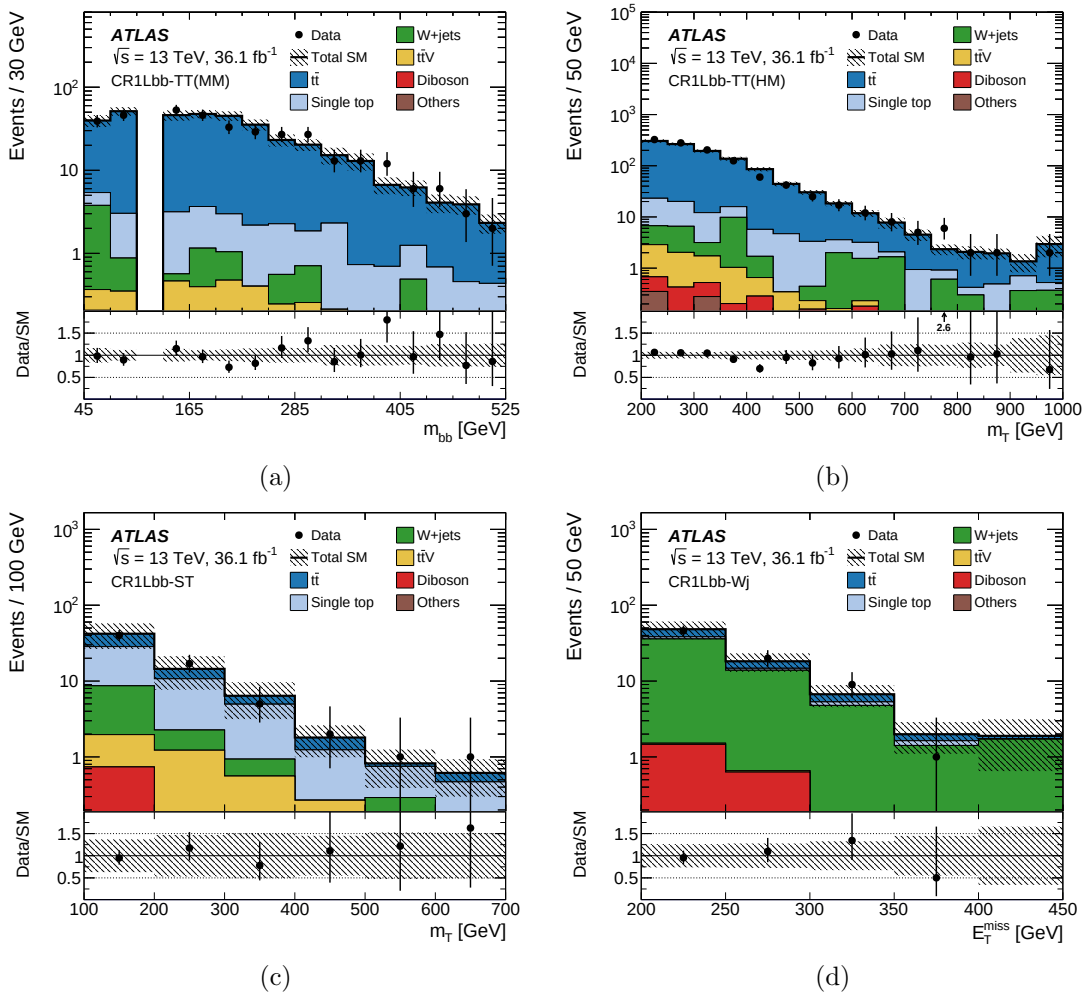

Figure 6.4: Plots showing the post-fit distributions after all CR selections except the one on the variable shown. The uncertainty band in the ratio plots contains MC statistical uncertainties and all systematic uncertainties.

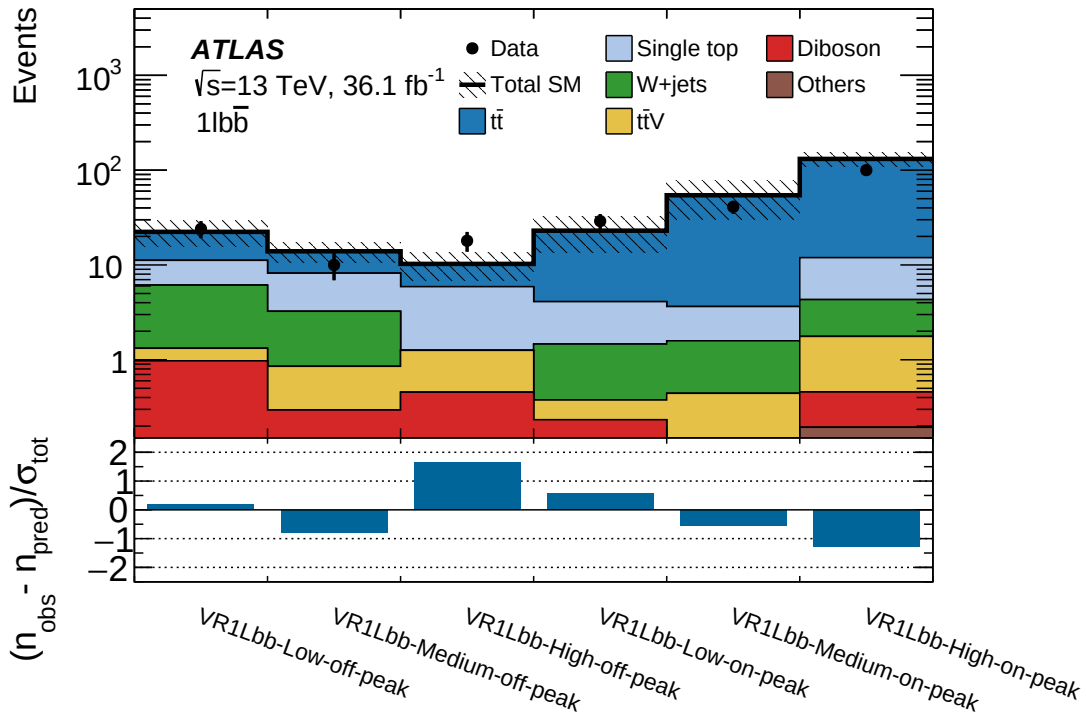

Figure 6.5: Summary plot showing the data/SM agreement in all VRs for SUSY Wh $1\ell + b\bar{b} + E_{\mathrm{T}}^{\mathrm{miss}}$ analysis. The uncertainty used to calculate the significance of the data/SM difference includes the statistical component on the MC and the data, as well as the total systematic uncertainty on the background estimate.

Model-dependent results

As shown in the background-only fit results presented previously, no significant excesses are observed in the SRs. Model-dependent exclusion limits are set on $\tilde{\chi}_1^{\pm}\tilde{\chi}_2^0$ pair-production decaying via the Wh signature to the $1\ell+b\bar{b}+E_{\mathrm{T}}^{\mathrm{miss}}$ final state. As described in Section 5.5, the model-dependent fit configuration uses both the CRs and SRs to set 95% confidence limits on the presence of a given signal model. The model-dependent exclusion limits for the analysis using a dataset of 36.1 fb^{-1} collected at $\sqrt{s} = 13$ TeV is shown in Figure 6.6, excluding $\tilde{\chi}_1^{\pm}/\tilde{\chi}_2^0$ masses up to 550 GeV for a massless $\tilde{\chi}_1^0$. The region enclosed by the solid and dashed lines represent the signal hypotheses which are excluded at 95% CL. The dashed line shows the expected exclusion region, which differs by 50-100 GeV from the observed exclusion line. This is caused by the small excess in SRMM, and is most evident in the intermediate $\Delta\mathrm{M}(\tilde{\chi}_1^{\pm}/\tilde{\chi}_2^0, \tilde{\chi}_1^0)$ range. The dotted red line represents the $\pm1\sigma$ variation in the observed limit due to theoretical uncertainties in the calculation of the signal cross-section.

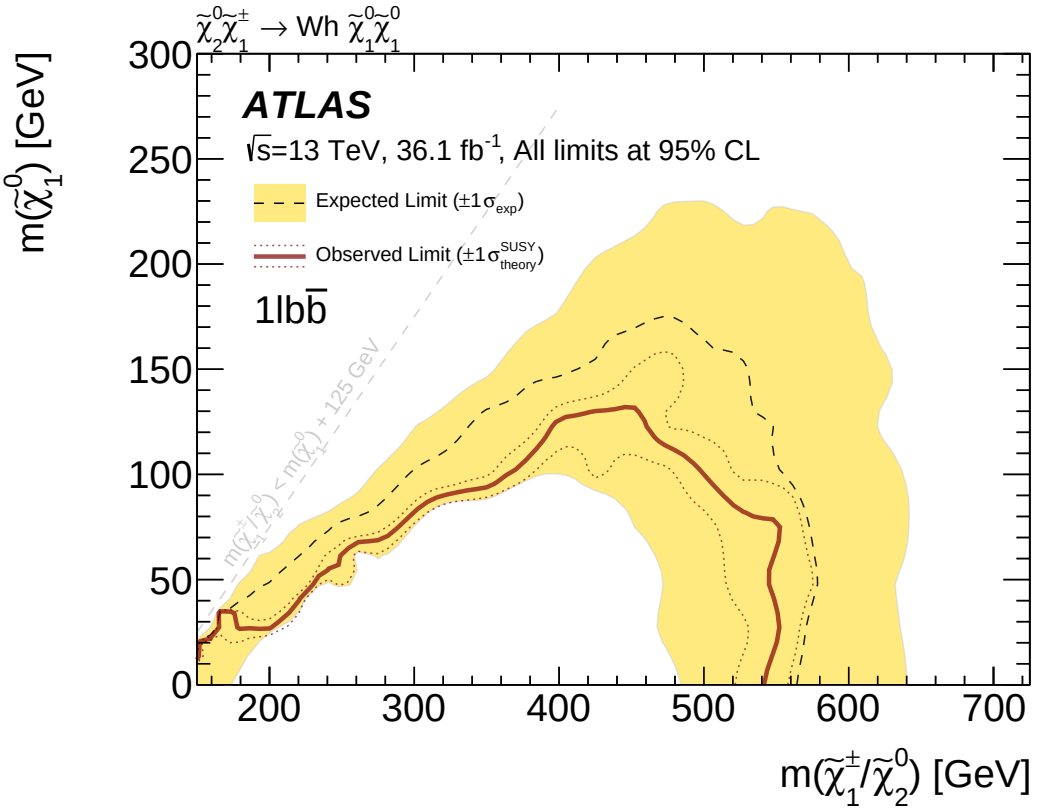

Figure 6.6: Plots showing the sensitivity to $\tilde{\chi}_1^{\pm}\tilde{\chi}_2^0$ pair-production with the Wh signature, decaying via the $1\ell + b\bar{b}+E_{\mathrm{T}}^{\mathrm{miss}}$ channel. The solid red line shows the observed exclusion limit. The yellow band shows the total experimental and theoretical uncertainties on the background, while the dotted red line shows the $\pm1\sigma$ variation in the observed exclusion limit due to theoretical uncertainties in the signal cross-section.

Model-independent limits

In addition to the model-dependent fit, 95% confidence limits are set on a generic BSM process using the model-independent fit strategy detailed in Section 5.5. A visible cross-section, σ_{vis}, is derived which represents the product of the signal selection efficiency, ϵ, the detector acceptance, A and the production cross-section for the BSM process, σ_{BSM}. The model-independent limits on σ_{vis} derived using the SRs defined early are shown in Table 6.9, as well as limits on the expected and observed number of signal events.

	σ_{vis} [fb]	S_{obs}^{95}	S_{exp}^{95}	p_0-value
SRLM	0.23	8.3	$8.0^{+3.3}_{-2.2}$	0.46
SRMM	0.28	10.0	$5.6^{+2.9}_{-1.7}$	0.04
SRHM	0.18	6.4	$6.1^{+3.1}_{-1.9}$	0.44

Table 6.9: From left to right, the observed 95% CL upper limits on the visible cross-sections σ_{vis}, the observed (S_{obs}^{95}) and expected (S_{exp}^{95}) 95% CL upper limits on the number of signal events with $\pm 1\sigma$ variations of the expectation, and the discovery p-value (p_0).

As shown in Table 6.9, the upper limit on the visible cross-section for a generic BSM process ranges from 0.18-0.28 fb.

6.6 Studies using 139 fb^{-1} data

The search for $\tilde{\chi}_1^{\pm}\tilde{\chi}_2^0$ described previously in this Chapter made use of 36.1 fb^{-1} pp collision data collected by ATLAS at $\sqrt{s} = 13$ TeV. An update to this analysis was performed using the full Run-2 dataset [2], collected between 2015-2018, and performing a reoptimisation of the selections described in Table 6.2. ML studies are currently underway to improve the sensitivity to the signal, with some initial studies presented in Section 6.6.

Reoptimised analysis using full Run-2 dataset

With the full Run-2 dataset of 139 fb^{-1}, the selections described in Table 6.2 were found to be no longer sensitive to the not-yet-excluded m($\tilde{\chi}_1^{\pm}/\tilde{\chi}_2^0$)-m($\tilde{\chi}_1^0$) parameter space of interest due to the low cross-section of the signal hypotheses. A reoptimised analysis strategy was developed, making use of multi-bin fits as described in Section 5.5, as well as the invariant mass of the lepton and the highest-p$_{\text{T}}$ b-tagged jet, $m(\ell, b_1)$, which is defined as:

$$m(\ell, b_1) = \left((E_{\ell,1} + E_{b,1})^2 - ||\mathbf{p}_{\ell,1} + \mathbf{p}_{b,1}||^2\right)^{1/2} . \tag{6.6.1}$$

When the lepton and the leading b-jet are both from the decay of a top quark, the $m(\ell, b_1)$ distribution has a kinematic endpoint at $\sqrt{m_t^2 - m_W^2}$, enabling good background rejection

	SRLM	SRMM	SRHM
N_{lepton}	$= 1$		
$p_{\text{T}}^{\ell_1}$ [GeV]	$> 7(6)$ for $e(\mu)$		
N_{jet}	$= 2$ or 3		
$N_{b\text{-jet}}$	$= 2$		
$E_{\text{T}}^{\text{miss}}$ [GeV]	> 240		
m_{bb} [GeV]	$\in [100, 140]$		
$m(\ell, b_1)$ [GeV]	–	–	> 120
m_{T} (excl.) [GeV]	$\in [100, 160]$	$\in [160, 240]$	> 240
m_{CT} (excl.) [GeV]	$\{\in [180, 230], \in [230, 280], > 280\}$		
m_{T} (disc.) [GeV]	> 100	> 160	> 240
m_{CT} (disc.) [GeV]	> 180		

Table 6.10: Overview of the selection criteria for the signal regions. Each of the three 'excl.' SRs is binned in three m_{CT} regions for a total of nine 'excl.' bins.

for processes with a leptonically-decaying top quark. This variable was used in addition to those described previously to improve discrimination between the signal and the SM backgrounds. The full SR definitions are given in Table 6.10. This analysis also makes use of $E_{\text{T}}^{\text{miss}}$ trigger, which is determined to be 100% efficiency in all analysis regions. The major difference in the SR definitions of the 36.1 fb^{-1} analysis (Table 6.2) and the 139 fb^{-1} analysis (Table 6.10) is the binning in the m_{CT} variable. Each of the three SR types, SRLM, SRMM and SRHM, is separated into three bins in m_{CT}. As described in Section 5.5, performing a statistical analysis on multiple bins simutaneously can increase the sensitivity to a signal model. The SRs demarcated by *(excl.)* are the SRs used for the model-dependent fit, while the SRs demarcated by *(disc.)* were the 'discovery' SRs used for the model-independent fit. The discovery regions are inclusive in both m_{T} and m_{CT} , to remove any assumption about the shape of these distributions for a generic BSM signal. The background estimation strategy is very similar to that defined in Section 6.3. The data/SM agreement in all regions is shown in Figure 6.7, where good agreement is seen in all regions within 2σ. In the absence of a significant excess, exclusion limits are set at 95% CL, as shown in Figure 6.8. As shown in Figure 6.8, $\tilde{\chi}_1^{\pm}/\tilde{\chi}_2^0$ masses up to 740 GeV were excluded by the analysis using a dataset of 139 fb^{-1}. The discrepancy between the expected and observed exclusion limits is due to the small overfluctuation of data between $1-2\sigma$ in several of the SR bins, as seen in Figure 6.7. These excesses seen in the updated SRMM and SRHM regions from Table 6.10 are closely related to the excess of data in SRMM shown in Table 6.7 due to the similarity in region definitions. The primary differences in these regions are the lepton transverse momentum threshold being lowered in the updated analysis, while the $E_{\text{T}}^{\text{miss}}$ and m_{CT} thresholds are increased in the updated

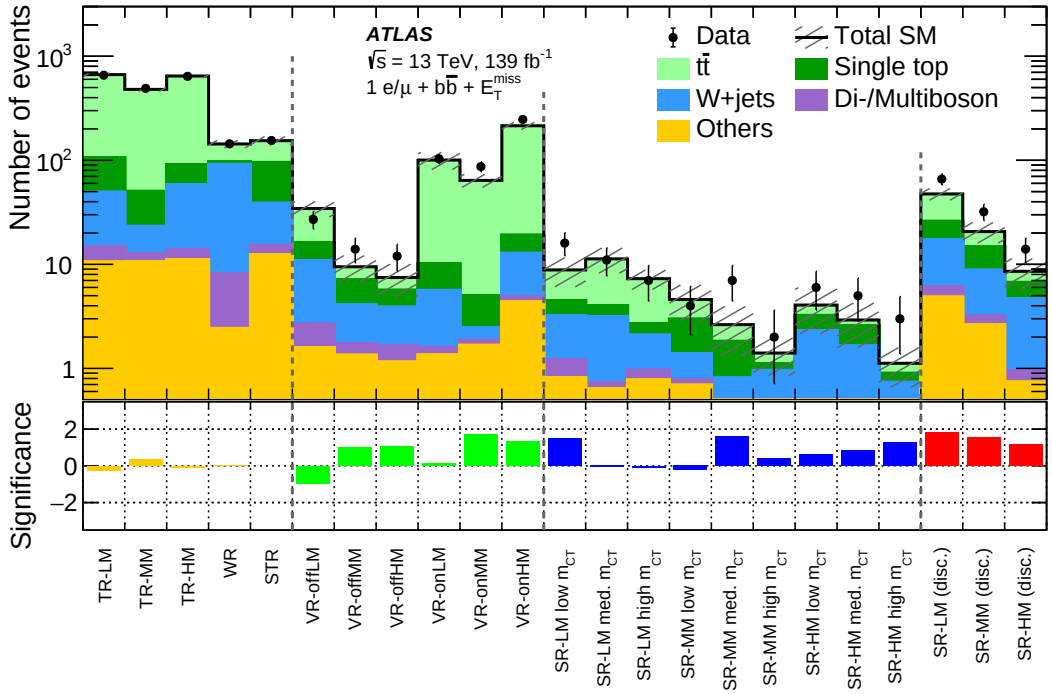

Figure 6.7: Plot showing the data/SM agreement in all CR/VR/SRs for the 139 fb^{-1} SUSY Wh $1\ell + b\bar{b} + E_{\mathrm{T}}^{\mathrm{miss}}$ analysis. Good agreement is seen in all regions.

analysis.

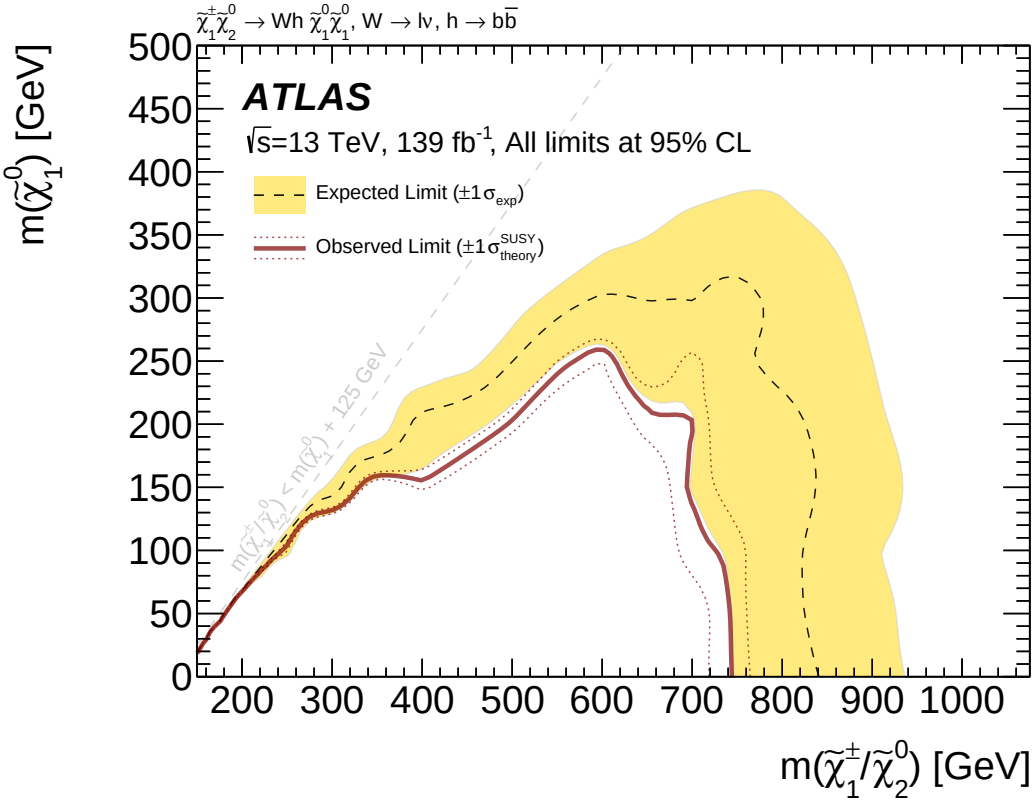

Figure 6.8: 95% CL exclusion limits for the SUSY Wh $1\ell+b\bar{b}+E_{\mathrm{T}}^{\mathrm{miss}}$ analysis, using the full Run-2 dataset of 139 fb^{-1}. $\tilde{\chi}_1^{\pm}/\tilde{\chi}_2^0$ masses up to 740 GeV are excluded for a massless $\tilde{\chi}_1^0$. The solid red line shows the observed exclusion limit, which is around 50-150 GeV lower than the expected exclusion limit, shown by the dashed black line, due to the excesses in SRMM and SRHM. The yellow band shows the total experimental and theoretical uncertainties on the background, while the dotted red line shows the $\pm 1\sigma$ variation in the observed exclusion limit due to theoretical uncertainties in the signal cross-section.

ML studies

Explorative studies were performed following the publication of the analysis described in the bulk of this Chapter to evaluate the possibility of using ML for signal selection. The bulk of the work presented here was in developing the ML framework which was used to perform initial prospect studies. In regions of phase space where the signal and background kinematics are very similar, applying selections to discriminative variables will generally result in poor sensitivity to a given signal. In this analysis, the separation of signal and background is particularly challenging in kinematically 'compressed' scenarios, where the mass-splitting of the $\tilde{\chi}_1^{\pm}/\tilde{\chi}_2^0$ and $\tilde{\chi}_1^0$ is similar to the Higgs boson mass. The use of ML methods to separate kinematically-challenging signal processes from the dominant backgrounds was studied. High-level variables, such as m_{T} and m_{CT}, defined as variables which are calculated using low-level inputs, such as the transverse momenta of the objects, can enable ML classifiers to achieve sensitivity to the signal.

Two ML classifiers were trained to separate the $t\bar{t}$ process, Wt-channel single top process and a compressed benchmark signal model process, with $\mathrm{m}(\tilde{\chi}_1^{\pm}/\tilde{\chi}_2^0) = 400$ GeV and $\mathrm{m}(\tilde{\chi}_1^0) = 250$ GeV. In this study, the W+jets background was ignored. A boosted decision tree, implemented using XGBoost, and a deep neural network, implemented using Keras and Tensorflow, the general principles of which are described in Chapter 5, were trained in the multiclass configuration on the following high-level and low-level variables:

- High-level: $E_{\mathrm{T}}^{\mathrm{miss}}$, m_{T}, m_{CT}, m_{bb}, $m(\ell, \mathrm{b}_1)$, $m(\ell, \mathrm{b}_2)$, $\Delta R(\mathrm{b}_1, \mathrm{b}_2)$
- Low-level: $p_{\mathrm{T}}(\ell_1)$, $p_{\mathrm{T}}(b_1)$, $p_{\mathrm{T}}(b_2)$, $\eta(\ell_1)$, $\eta(b_1)$, $\eta(b_2)$

It was found by testing the performance of models including both high-level and low-level variables and comparing to models with only high-level variables that no additional discrimination could be achieved when including the low-level variables, and thus they were not included in subsequent trainings. As both ML models were trained as multiclass classifiers, the output of both models is a prediction for each class. In practice, this means there are three values output for each event, corresponding to how $t\bar{t}$-like, how Wt-like and how signal-like each event is.

The receiver operating characteristic (ROC) curve shown in Figure 6.9 shows the signal efficiency versus background rejection for the $t\bar{t}$, Wt and signal classes.

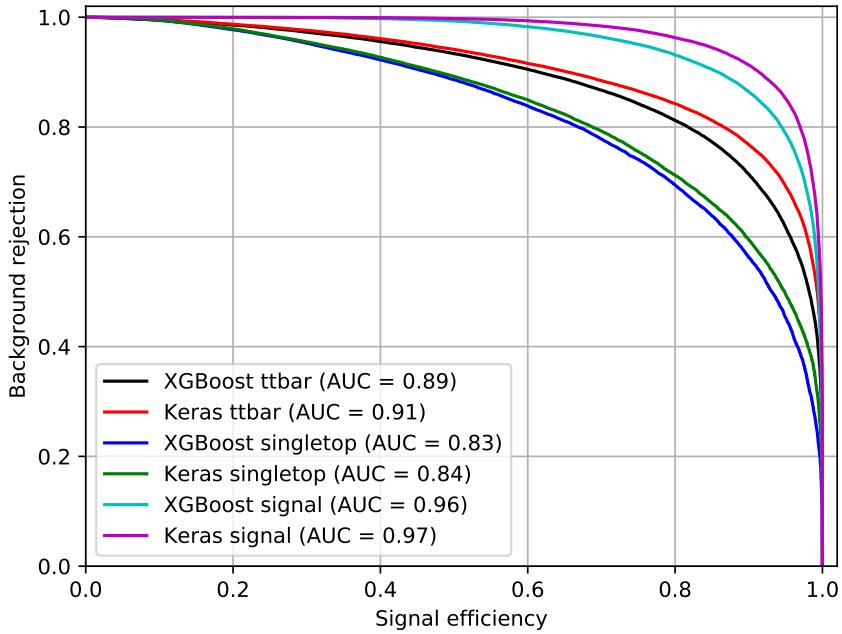

Figure 6.9: ROC curves showing the classification performance of the BDT and DNN for $t\bar{t}$, Wt-channel single top and signal classes.

Each ROC curve is a measure of how well a classifier separates one class from the others. The area under curve (AUC) value is the integral of the ROC curve, and is a measure of the classification accuracy of a model. As shown, the classification accuracy for both the BDT and DNN correctly selects signal events versus the background classes most frequently.

The results shown here have been considered promising by the analysis group and are being further pursued in the context of another Thesis from the University of Liverpool.

Chapter 7

Search for Dark Matter produced in association with a Top Quark

This Chapter presents a search for the production of DM in association with a single top quark, also referred to as DMt, using the full Run-2 dataset collected by ATLAS of 139 fb^{-1}. The results of the analysis are interpreted in the context of a simplified model of DM production, where the DM is coupled to an extended SM Higgs sector (2HDM) by a massive, spin-0, pseudoscalar mediator, a.

The Chapter focuses mainly on the $tW+E_{\mathrm{T}}^{\mathrm{miss}}$ signature, characterised by the presence of a single lepton arising from one of the two W bosons in the decay chain. The author's contributions to this analysis were defining the SRs, calculating the theoretical uncertainties for both the single lepton and two lepton channels, and developing and running the statistical analysis. A complementary analysis of the two lepton final state was also performed, as documented in [3], and will not be detailed here. In addition to the $tW+E_{\mathrm{T}}^{\mathrm{miss}}$ signature, it was found that the sensitivity of these analyses to DM produced in association with a $t\bar{t}$ pair, referred to as DM$t\bar{t}$, was non-negligble. The overall sensitivity of this analysis to the DM$t + t\bar{t}$ signal was evaluted and is detailed in the fit results. In addition to the independent analyses of the single- and two-lepton final states, both channels were statistically-combined to increase the sensitivity to the DMt and DM$t+t\bar{t}$ signals.

This Chapter begins with a description of the simplified DM model used to interpret the results, focusing on the experimental signature of interest, the $tW+E_{\mathrm{T}}^{\mathrm{miss}}$ signature. The SR optimisation and selections, as well as the background estimation strategy are documented, before finally presenting the analysis results.

7.1 2HDM+a signal model

The results of the search described in this Chapter are interpreted in the context of the 2HDM+a model, described in detail in Section 1.4. Models with a second Higgs doublet comprise five physical states; the CP-even scalars h and H, the CP-odd pseudoscalar A, and two charged Higgs bosons $H^{\pm}$. The coupling of the extended Higgs sector is of Type-II, such that one Higgs doublet couples to up-type fermions while the other couples to down-type fermions. The mixing in the extended Higgs sector is specified by three mixing angles, α, θ and β. α represents the mixing angle of the two CP-even states, θ represents the mixing of the CP-odd states, and tanβ represents the ratio of the VEVS of the two Higgs doublets.

In this Chapter a number of assumptions are made. The *alignment limit* is assumed, where $\cos(\beta - \alpha) = 0$, such that h can be identified with the SM Higgs boson. To enhance the sensitivity to this model, it is assumed that there is maximal mixing between the Higgs sector and the mediator, A and a, and as such it is assumed that $\sin\theta = 1/\sqrt{2}$. as described in Ref. [29], it is assumed the masses of the CP-even neutral Higgs, the CP-odd Higgs and the charged Higgs states are degenerate, and the mass of the DM, m_{χ} is set equal to 10 GeV. Finally, the DM coupling to a is set equal to unity, $y_{\chi} = 1$. Therefore, there are three free parameters; tanβ, $m_{H\pm}$ and m_a.

For the 2HDM+a model described in Chapter 1.4, the tW+$E_{\mathrm{T}}^{\mathrm{miss}}$ signature has not been previously studied, but has been shown to have promising potential in sensitivity studies [89]. The dominant Feynman diagrams for this signature are shown in Figure 7.1. The diagram shown in Figure 7.1a is present in the LHC DM simplified models, while the diagram shown in Figure 7.1b is only present in the 2HDM+a model. The latter diagram gives an approximate order-of-magnitude enhancement to the $pp \to tW\chi\chi$ cross-section through the on-shell production of the charged Higgs, H^{-}. The additional diagrams from the 2HDM+a model also interfere destructively with the diagrams from the LHC DM simplified model, restoring unitarity.

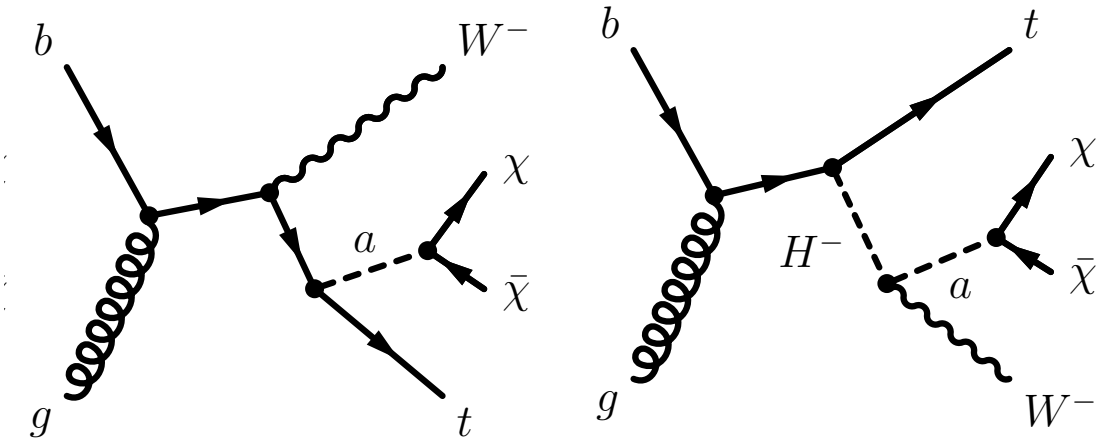

(a) (b)

Figure 7.1: Feynman diagram for dark matter production in the Wt channel, in the context of a 2HDM+a model. This chapter documents studies done in the single lepton channel, where one of the W bosons in the event decays leptonically.

In order to set model-dependent limits on this process, two planes are defined to cover the largest possible region of the available model phase space. The first is a scan in the $m_a, m_{H\pm}$ plane, assuming $\tan\beta = 1$, while the second is a scan in the $m_{H\pm}, \tan\beta$ plane, assuming $m_a = 250$ GeV. The cross-section dependence on $\tan\beta$ for the DMt and DM$t\bar{t}$ processes is shown in Figure 7.3, with $m_a = 250$ GeV and $m_{H\pm} = 600$ GeV. As seen in Figure 7.3, the cross-section for the DM$t\bar{t}$ process has a $1/\tan^2\beta$ dependence, while the DMt has a more complex dependence on the value of $\tan\beta$. A summary of the model parameter choices is given in Table 7.1, while Figure 7.3 describes the dependence of the cross-section of each process to $\tan\beta$, introduced in Section 1.4. This Figure also depicts the case where the DM is produced via a t-channel like process, which is not detailed here.

In addition to the $tW+E_{\mathrm{T}}^{\mathrm{miss}}$ signature, the analysis described in the later sections of this Chapter is also sensitive to the $t\bar{t}+E_{\mathrm{T}}^{\mathrm{miss}}$ signature of associated DM production. A rescaling procedure is applied to the DM$t\bar{t}$ process, which is generated, using the DMSimp framework [90], in the context of a simplified DM production model in which the pseudoscalar mediator a directly couples to the SM. The Feynman diagram for this process is shown in Figure 7.2. The predictions of this simplified model are rescaled to correctly model the prediction of the 2HDM+a model using the procedure described in [29], which also includes contributions from the heavy, CP-odd pseudoscalar A, as introduced in Section 1.4.

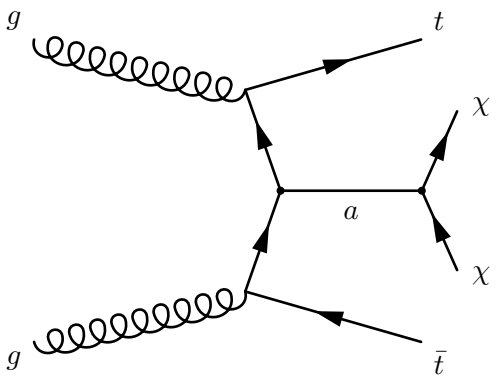

Figure 7.2: Diagram of DM produced in association with a $t\bar{t}$ pair, in the context of the 2HDM+a model under study in this Chapter. The sensitivity of the analysis described later in this Chapter to this signal is shown in Section 7.5.

Fixed parameters	Assumption
$\sin\theta$	$= 1/\sqrt{2}$
$\cos(\beta - \alpha)$	$= 0$
m_h	$= 125$ GeV
m_H, m_A, $m_{H\pm}$	Degenerate
m_χ	$= 10$ GeV
y_χ	$= 1$

Table 7.1: A table summarising the model parameter assumptions for the simplified 2HDM+a model of DM production as described in Ref. [29].

7.2 Event selection

The event selection for this analysis begins with a set of preliminary, loose selections, known as 'preselection'. The preselection requirements aim to select events matching the signal topology, while rejecting events with different topologies from the SM background processes. All events are required to have exactly 1 electron or muon in the final state, with any additional reconstructed leptons failing the 'signal' lepton requirements being rejected. At least three jets are required, two with transverse momenta greater than 50 GeV and one with transverse momentum greater than 30 GeV, to target events with at least one hadronically-decaying W boson, and at least one b-tagged jet, also with a transverse momentum greater than 50 GeV, is required to select events with a top quark. To minimise the background contribution from $t\bar{t}$, events with a second b-tagged jet are rejected if the transverse momentum of the jet is greater than 50 GeV. The jets and $E_{\mathrm{T}}^{\mathrm{miss}}$ must have an angular separation of at least 0.5 rad, to reject events which have mismeasured jets. All events are required to pass the event cleaning procedure described in Section 4.7, as well as passing one of the $E_{\mathrm{T}}^{\mathrm{miss}}$ triggers as described in Section 3.1. In order to ensure a constant $E_{\mathrm{T}}^{\mathrm{miss}}$ trigger efficiency, all events are required to have $E_{\mathrm{T}}^{\mathrm{miss}} > 250$ GeV. The full

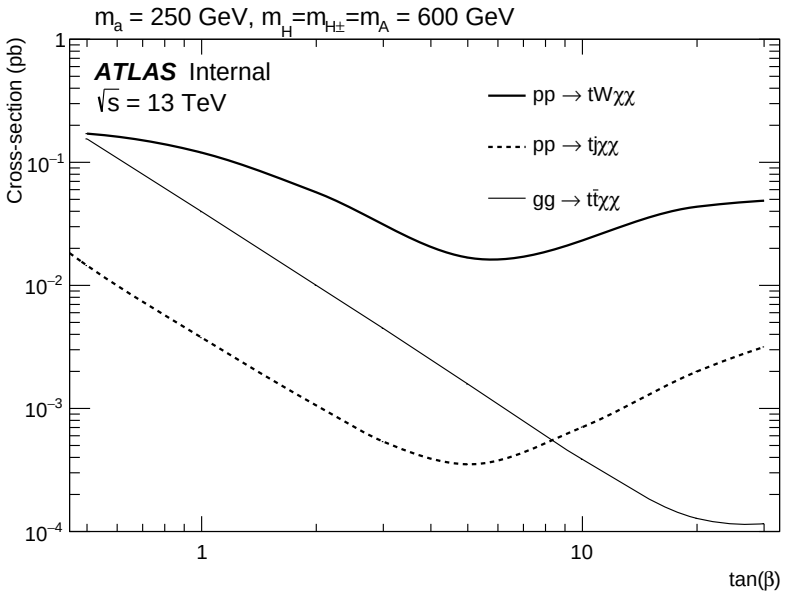

Figure 7.3: Diagram showing the production cross-section of DM produced in association with tW, t and $t\bar{t}$. The associated $t\bar{t}$ production cross-section is proportional to $1/\tan^2\beta$ as described in Ref. [91].

preselection requirements for this analysis are defined in Table 7.2.

Variable	Selection
N_ℓ^{baseline}	$= 1$
N_ℓ^{signal}	$= 1$
$p_{\text{T}}(\ell_1)$	> 30 GeV
N_{jet}	≥ 3
$p_{\text{T}}(jet)$	> 30 GeV
$N_{b-\text{jet}}$	≥ 1
$p_{\text{T}}(b-\text{jet})$	> 50 GeV
$E_{\text{T}}^{\text{miss}}$	> 250 GeV
m_{T}	> 30 GeV
$\lvert\Delta\phi\rvert$	> 0.5 [rad]

Table 7.2: Preliminary selections used for the $tW+E_{\text{T}}^{\text{miss}}$ analysis. All events are also required to pass the $E_{\text{T}}^{\text{miss}}$ trigger, and the event cleaning requirements detailed in Section 4.7.The object definitions used are detailed in Chapter 4.

At the preselection-level, the dominant backgrounds, estimated from MC-only, are $t\bar{t}$ (67%), W+jets (18%) and single top production (11%), where the percentages in parenthesis represents the contribution of that process to the total background. Four key variables were identified which enabled rejection of the backgrounds while maintaining a reasonably

high signal selection efficiency; $E_{\mathrm{T}}^{\mathrm{miss}}$, m_{T}, am_{T2} and $m_{\mathrm{W}}^{\mathrm{had}}$. These variables are defined in Section 5.2 and are shown at the preselection level in Figure 7.4. The am_{T2}, m_{T} and $m_{\mathrm{W}}^{\mathrm{had}}$variables formed the inputs to simultaneous adaptive random grid search and genetic algorithms, as described in Section 5.3. The selections used to define the SRs, which are binned in $E_{\mathrm{T}}^{\mathrm{miss}}$, are summarised in Table 7.3.

Variable	$\mathrm{SR}_{\mathrm{1L}}^{\mathrm{Bin0}}$	$\mathrm{SR}_{\mathrm{1L}}^{\mathrm{Bin1}}$	$\mathrm{SR}_{\mathrm{1L}}^{\mathrm{Bin2}}$	$\mathrm{SR}_{\mathrm{1L}}^{\mathrm{Bin3}}$	$\mathrm{SR}_{\mathrm{1L}}^{\mathrm{Bin4}}$
$p_{\mathrm{T}}(b_2)$ [GeV]	< 50	< 50	< 50	< 50	< 50
m_{T} [GeV]	> 200	> 200	> 200	> 200	> 200
am_{T2} [GeV]	> 220	> 220	> 220	> 220	> 220
$m_{\mathrm{W}}^{\mathrm{had}}$ [GeV]	> 60	> 60	> 60	> 60	> 60
$E_{\mathrm{T}}^{\mathrm{miss}}$ [GeV]	$\in [250, 300]$	$\in [300, 400]$	$\in [400, 500]$	$\in [500, 600]$	> 600

Table 7.3: Signal region definitions for the tW+$E_{\mathrm{T}}^{\mathrm{miss}}$ analysis.

7.3 Background estimation

The major backgrounds in the E_T^{miss} bins of the SR vary, depending on bin, between $t\bar{t}$ and W+jets, with smaller contributions from Wt-channel single top production, $t\bar{t}+V$ and the diboson backgrounds. A single-bin CR for the $t\bar{t}$ background, CR($t\bar{t}$), and a 2-bin CR for the W+jets background, CR(W), are defined. For the W+jets background, the CR is separated in terms of lepton charge to exploit the charge asymmetry of $W^{\pm}$ production. The difference in the distribution of u and d quarks (and their respective anti-quarks) in the proton, described by the PDFs, results in a difference of rates of production, with W^+ bosons being primarily produced by $u\bar{d}$, while W^- bosons being primarily produced by $\bar{u}d$ [92]. The definitions of the CRs are given in Table 7.4. Six validation regions are

Variable	CR($t\bar{t}$)	CR(W)
$N_{\ell}^{\mathrm{signal}}$	$= 1$	
$p_{\mathrm{T}}(b_1)$ [GeV]	> 50	
$p_{\mathrm{T}}(b_2)$ [GeV]	> 50	< 50
$E_{\mathrm{T}}^{\mathrm{miss}}$ [GeV]	> 250	
am_{T2} [GeV]	< 220	> 220
m_{T} [GeV]	> 200	$\in [40, 100]$
$m_{\mathrm{W}}^{\mathrm{had}}$ [GeV]	–	< 60

Table 7.4: Control region definitions for the tW+$E_{\mathrm{T}}^{\mathrm{miss}}$ analysis. The W+jets CR is split into two bins of lepton charge, such that the $W^{\pm}$ production charge asymmetry can be exploited.

defined in a region of kinematic phase space that is between the CRs and SRs. Two $t\bar{t}$

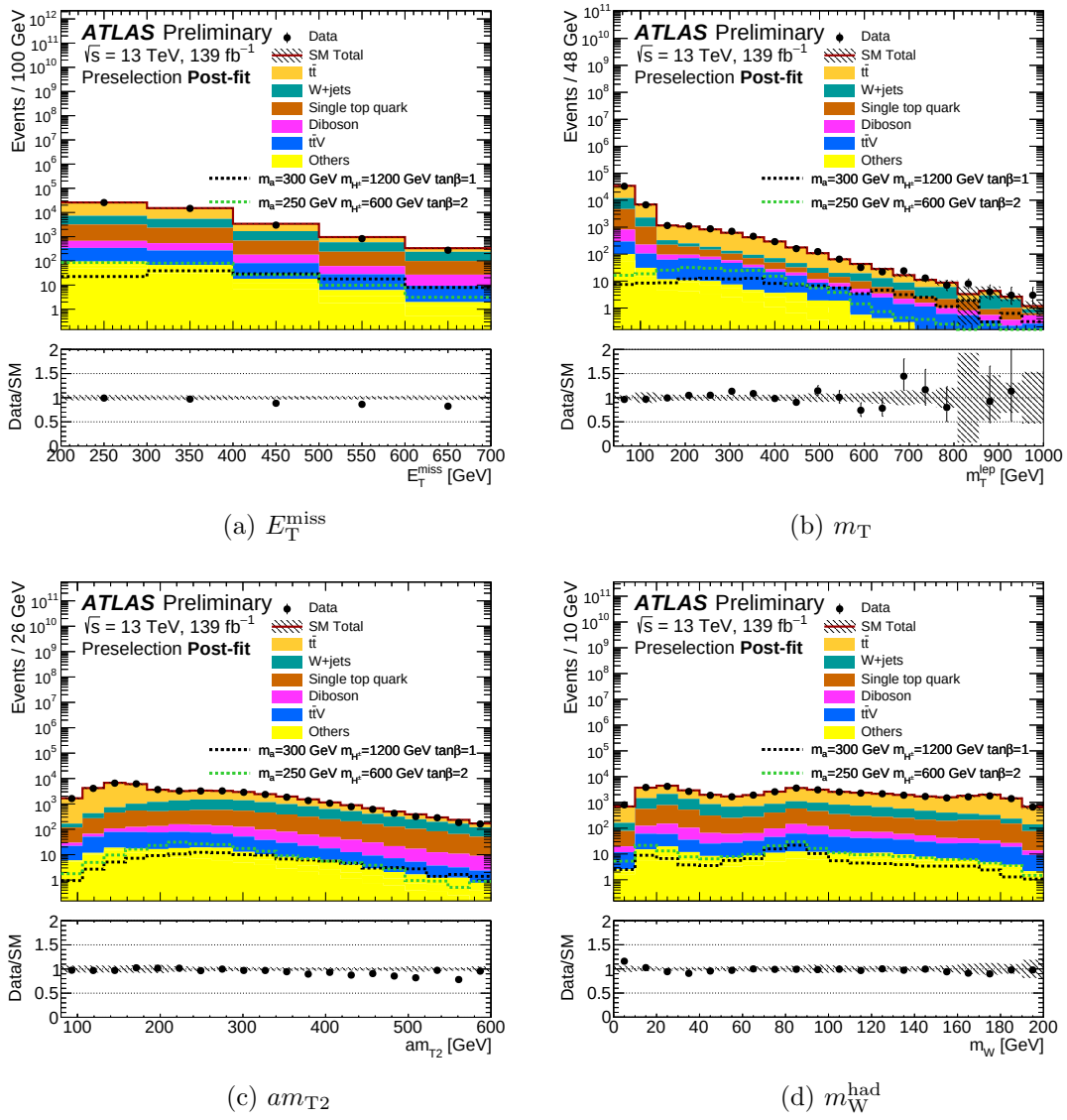

(a) $E_{\mathrm{T}}^{\mathrm{miss}}$ (b) m_{T}

(c) am_{T2} (d) $m_{\mathrm{W}}^{\mathrm{had}}$

Figure 7.4: Post-fit plots of the key kinematic variables. The uncertainty band in the ratio plot contains only the MC statistical uncertainty and the experimental uncertainties.

VRs are defined in order to validate the extrapolation of the $t\bar{t}$ background predictions as a function of the am_{T2} and m_W, while for the W+jets background, two VRs are defined to validate the extrapolation as a function of the m_T and m_W. Each of the W+jets VRs is split into two bins of lepton charge to mirror the CR definition. The VR definitions are explicitly defined in Table 7.5.

7.4 Systematic uncertainties

In addition to statistical uncertainties in the MC and on data, systematic uncertainties are evaluated on all MC background and signal samples, from both experimental and modelling

Variable	VR1($t\bar{t}$)	VR2($t\bar{t}$)	VR1(W)	VR2(W)
N_ℓ^{signal}		$= 1$		
$p_{\text{T}}(b_2)$ [GeV]		< 50		
$E_{\text{T}}^{\text{miss}}$ [GeV]		> 250		
am_{T2} [GeV]	< 220	> 220	> 220	> 220
m_{T} [GeV]	> 200	> 200	$\in [40, 100]$	> 100
$m_{\text{W}}^{\text{had}}$ [GeV]	–	< 60	> 60	< 60

Table 7.5: Validation region definitions for the tW+$E_{\text{T}}^{\text{miss}}$ analysis. The W+jets VRs, like the CR, are each split into two bins of lepton charge.

sources. The dominant experimental systematics in the SRs are from the JES, JER and b-tagging efficiency systematics. The modelling uncertainties on the $t\bar{t}$ and single top backgrounds are the dominant modelling systematics in the SRs. As previously described in Section 3.3, the uncertainty due to the modelling of the interference between the $t\bar{t}$ and Wt processes is evaluated by comparing the DR and DS schemes, with the derived uncertainty applied to the nominal Wt prediction. Table 7.6 gives an overview of the size of the dominant systematics in this analysis.

Uncertainty of region	$\text{SR}_{\text{1L}}^{\text{Bin0}}$	$\text{SR}_{\text{1L}}^{\text{Bin1}}$	$\text{SR}_{\text{1L}}^{\text{Bin2}}$	$\text{SR}_{\text{1L}}^{\text{Bin3}}$	$\text{SR}_{\text{1L}}^{\text{Bin4}}$
Total background expectation	169.1	171.3	54.7	20.2	15.6
Total background uncertainty	14.0	13.3	6.1	2.8	2.8
Systematic, experimental	6.6	2.6	1.24	0.7	0.4
Systematic, theoretical	4.5	7.3	3.4	1.06	1.12
Statistical, MC samples	4.1	4.1	2.3	1.1	1.2
Statistical, μ scale-factors	8.1	6.7	1.6	0.4	0.3

Table 7.6: Table showing a summary of the dominant experimental and modelling uncertainties.

7.5 Results

Background-only fit results

The background-only fit results in the CRs, VRs and SR bins for the single lepton channel are shown in Tables 7.7, 7.8 and 7.9, respectively. In addition, the background-only fit results in the SR for the two lepton channel is shown in Table 7.10. In this configuration, only the CRs enter the fit, allowing an estimate of the backgrounds in the VRs and SRs without any signal assumptions. Excellent data/MC agreement is observed in the CRs, VRs and the SRs. The correlations of the normalisation factors and the systematic uncer-

tainties from the background-only fit is shown in Figure 7.5.

The background normalisation factors for the $t\bar{t}$ and W+jets backgrounds, which are derived in the CRs, are shown in Table 7.11. These show excellent compatibility with the SM, agreeing with unity within 1σ.

Figures 7.6, 7.7 and 7.8 show the key kinematic variables for the CRs, VRs and SRs, respectively, including background normalisation factors from the background-only fit. Good modelling is seen in these variables.

As seen in Table 7.7, the contribution of the W+jets process in the W+jets CR is around three times larger in the positive lepton charge bin when compared to the negative lepton charge bin. As described in Chapter 1, the expected ratio of W^+ to W^- production at a proton-proton collider is around two-to-one, due to the quark content of the colliding protons. The MC estimate for the W+jets process in the W+jets CR at the pre-fit level predicts approximately three times as many events in the positive lepton charge bin versus the negative lepton charge bin, and hence is consistent with the fitted results.

In Table 7.8, it can be seen that the total uncertainty on the single top process in VR1($t\bar{t}$) is over 100%. This is due to the $t\bar{t}$-Wt interference systematic described in Chapter 3, which is evaluated as being a $\mp$113% uncertainty on the nominal single top prediction. All other single top theory systematics are around 10% in this region.

Control regions	CR($t\bar{t}$)	CR(W^+)	CR(W^-)
Observed events	911	3143	1653
Fitted bkg events	907 ± 31	3135 ± 57	1665 ± 38
$t\bar{t}$	847.0 ± 34.1	748.8 ± 83.4	720.8 ± 86.3
Single top	19.8 ± 11.5	276.6 ± 69.5	257.0 ± 70.2
W+jets	3.2 ± 0.8	2005 ± 98	625.4 ± 42.1
Z+jets	$0.1^{+0.2}_{-0.1}$	6.6 ± 1.0	8.4 ± 1.3
Diboson	0.9 ± 0.3	88.9 ± 15.6	46.1 ± 8.0
$t\bar{t}V$	31.0 ± 7.1	8.2 ± 2.7	6.0 ± 1.5
$t\bar{t}H$	4.4 ± 0.4	1.1 ± 0.2	1.2 ± 0.1
tWZ	1.1 ± 0.3	0.4 ± 0.1	0.3 ± 0.1

Table 7.7: Results of the background-only fit in the control regions for the single lepton channel of the search targeting the 2HDM+a tW+$E_{\mathrm{T}}^{\mathrm{miss}}$ signature. This fit includes only the control regions used to normalise the $t\bar{t}$ and W+jets backgrounds.

Validation regions	VR1($t\bar{t}$)	VR2($t\bar{t}$)	VR1(W^+)	VR1(W^-)	VR2(W^+)	VR2(W^-)
Observed events	1389	482	6127	4479	651	464
Fitted bkg events	1394 ± 87	464 ± 34	6722 ± 452	5026 ± 441	613 ± 70	475 ± 50
$t\bar{t}$	1221.1 ± 70.2	282.6 ± 28.5	3644.4 ± 331.6	3570.9 ± 354.9	282.2 ± 40.1	285.7 ± 41.2
Single top	$53.2^{+59.4}_{-53.2}$	57.0 ± 24.5	626.0 ± 280.2	612.9 ± 274.0	71.1 ± 36.1	73.4 ± 38.2
W+jets	39.1 ± 8.2	68.6 ± 11.9	2245.3 ± 131.2	719.1 ± 48.5	203.2 ± 42.1	70.1 ± 12.0
Z+jets	4.0 ± 2.1	2.7 ± 0.5	7.7 ± 1.1	7.3 ± 1.0	3.6 ± 0.9	2.4 ± 0.4
Diboson	15.3 ± 3.2	27.2 ± 5.5	160.2 ± 28.4	85.6 ± 15.6	34.5 ± 7.1	25.9 ± 5.8
$t\bar{t}V$	54.4 ± 12.1	22.5 ± 5.0	32.4 ± 2.8	23.9 ± 3.1	16.3 ± 3.8	15.3 ± 3.5
$t\bar{t}H$	3.6 ± 0.3	0.71 ± 0.04	4.5 ± 0.3	4.4 ± 0.4	0.69 ± 0.03	0.7 ± 0.1
tWZ	3.6 ± 0.8	2.5 ± 0.6	1.5 ± 0.2	1.6 ± 0.2	1.7 ± 0.4	1.8 ± 0.5

Table 7.8: Results of the background-only fit in the validation regions for the single lepton channel of the search targeting the 2HDM+a tW+$E_{\mathrm{T}}^{\mathrm{miss}}$ signature. This fit includes only the control regions used to normalise the $t\bar{t}$ and W+jets backgrounds.

Signal regions	SR1LBin0	SR1LBin1	SR1LBin2	SR1LBin3	SR1LBin4
Observed events	182	191	60	24	12
Fitted bkg events	169 ± 14	171 ± 13	55 ± 6	20.1 ± 2.8	15.6 ± 2.8
$t\bar{t}$	101 ± 12	84 ± 12	20 ± 5	5.1 ± 1.7	2.3 ± 1.5
Single top	16.3 ± 5.2	17.3 ± 5.2	5.4 ± 3.2	2.0 ± 1.8	$1.7^{+2.0}_{-1.7}$
W+jets	28 ± 4.0	37.0 ± 4.3	14.2 ± 2.4	6 ± 1	5.9 ± 1.1
Z+jets	2.0 ± 0.9	1.1 ± 0.7	0.3 ± 0.1	0.15 ± 0.04	0.15 ± 0.02
Diboson	7.2 ± 1.7	9.6 ± 2.00	4.6 ± 1.0	2.2 ± 0.5	2.7 ± 0.6
$t\bar{t}V$	12.3 ± 1.4	19.5 ± 3.5	8.7 ± 1.2	4.0 ± 0.7	2.5 ± 0.5
$t\bar{t}H$	0.6 ± 0.1	0.6 ± 0.1	0.17 ± 0.02	0.06 ± 0.02	0.03 ± 0.01
tWZ	1.7 ± 0.2	2.4 ± 0.5	1.17 ± 0.15	0.42 ± 0.09	0.39 ± 0.09

Table 7.9: Results of the background-only fit in the signal region for the single lepton channel of the search targeting the 2HDM+a tW+$E_{\mathrm{T}}^{\mathrm{miss}}$ signature. This fit includes only the control regions used to normalise the $t\bar{t}$ and W+jets backgrounds.

Signal regions	SR2L
Observed events	12
Fitted bkg events	5.9 ± 1.2
$t\bar{t}$	1.2 ± 0.9
Single top	$0.26^{+0.27}_{-0.26}$
W+jets	–
Z+jets	–
Diboson	0.5 ± 0.2
$t\bar{t}V$	2.9 ± 0.7
tWZ	0.8 ± 0.1
Others	0.16 ± 0.08

Table 7.10: Results of the background-only fit in the signal region for the two lepton channel of the search targeting the 2HDM+a tW+$E_{\mathrm{T}}^{\mathrm{miss}}$ signature. This fit includes only the control regions used to normalise the $t\bar{t}$, WZ and $t\bar{t}+V$ backgrounds. The category 'Others' includes triboson production, four-top production, $t\bar{t}WW$ production and Higgs boson production processes.

1ℓ analysis	
$\mu(t\bar{t})$	0.96 ± 0.08
$\mu(\mathrm{W})$	1.01 ± 0.05
$1\ell + 2\ell$ combination	
$\mu(t\bar{t}\ 1\ell)$	0.96 ± 0.08
$\mu(t\bar{t}\ 2\ell)$	1.00 ± 0.03
$\mu(\mathrm{W})$	1.01 ± 0.05
$\mu(\mathrm{WZ})$	0.75 ± 0.26
$\mu(t\bar{t}Z)$	0.81 ± 0.16

Table 7.11: Background normalisation factors the $tW+E_{\mathrm{T}}^{\mathrm{miss}}$ analysis

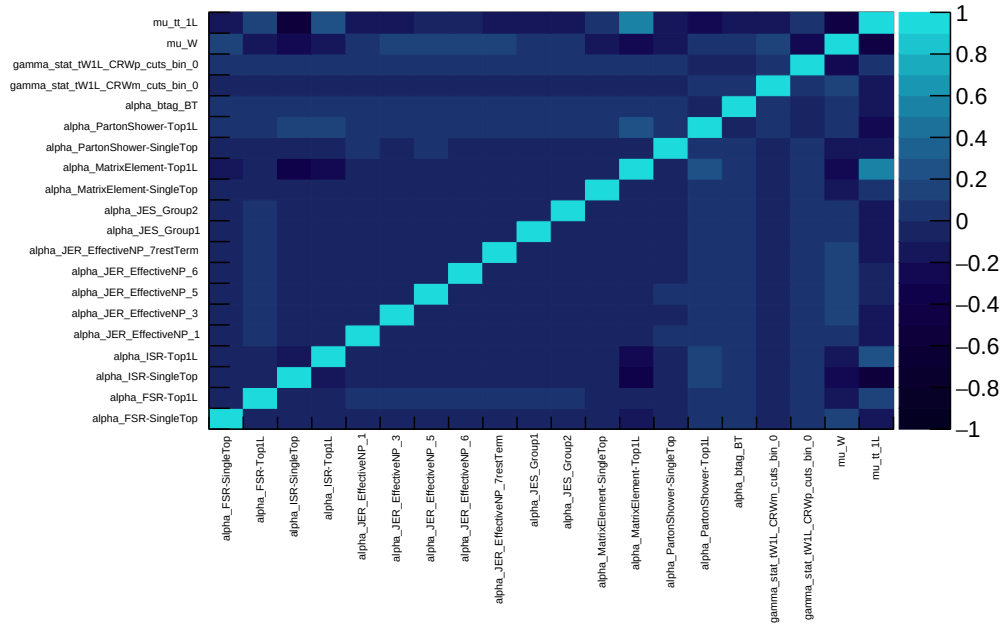

Figure 7.5: Correlations of the systematic uncertainties and the normalisation factors in the background-only fit for the single lepton channel. Only correlations with an absolute value of 0.1 or larger are shown.

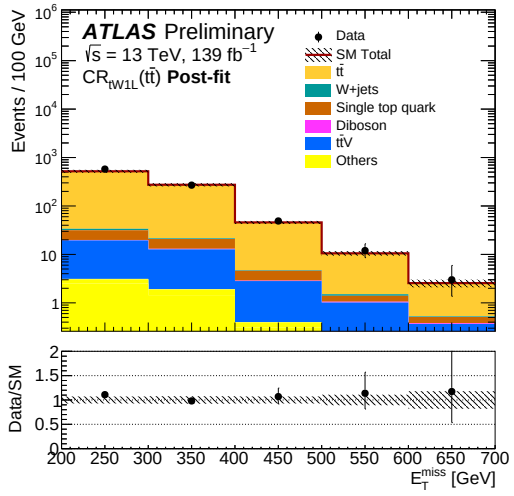

(a) $E_{\mathrm{T}}^{\mathrm{miss}}$ distribution in CR($t\bar{t}$)

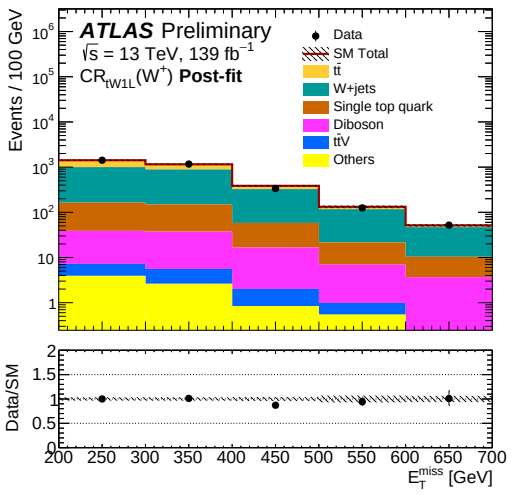

(b) $E_{\mathrm{T}}^{\mathrm{miss}}$ distribution in CR(W^+)

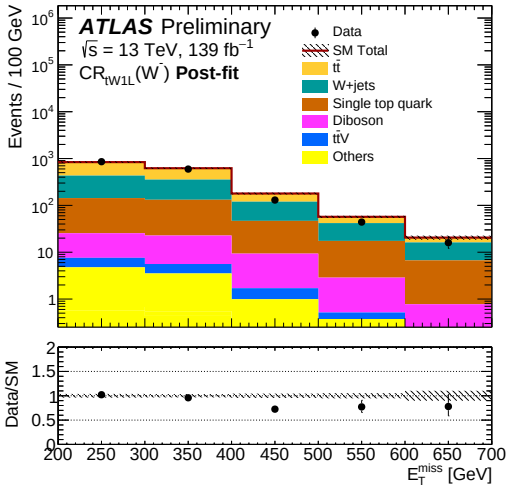

(c) $E_{\mathrm{T}}^{\mathrm{miss}}$ distribution in CR(W^-)

Figure 7.6: Post-fit distributions of the $E_{\mathrm{T}}^{\mathrm{miss}}$ variable in all CRs. Excellent agreement between data and the SM prediction is observed. The uncertainty band on the ratio contains the MC statistical, experimental and modelling uncertainties.

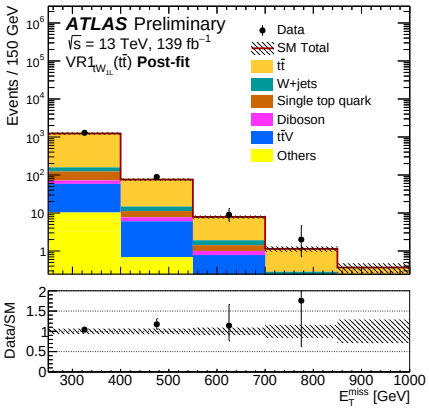

(a) $E_{\mathrm{T}}^{\mathrm{miss}}$ distribution in VR1($t\bar{t}$)

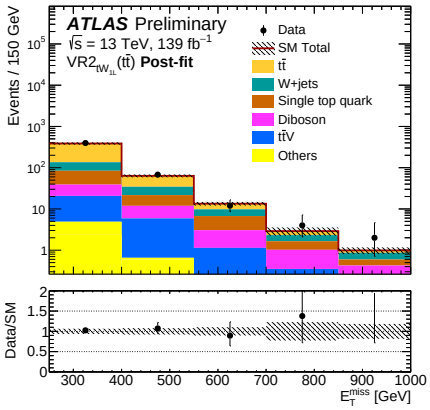

(b) $E_{\mathrm{T}}^{\mathrm{miss}}$ distribution in VR2($t\bar{t}$)

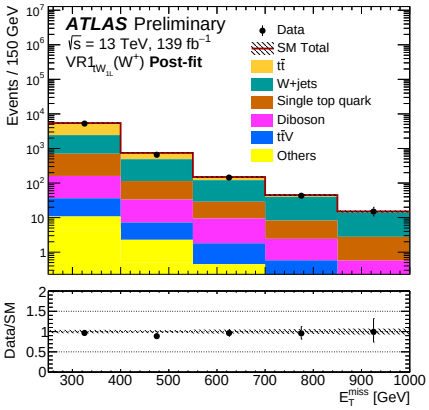

(c) $E_{\mathrm{T}}^{\mathrm{miss}}$ distribution in VR1(W^+)

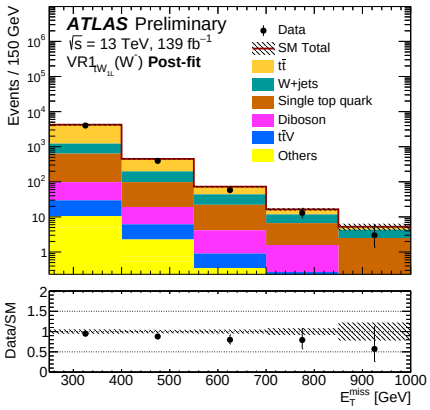

(d) $E_{\mathrm{T}}^{\mathrm{miss}}$ distribution in VR1(W^-)

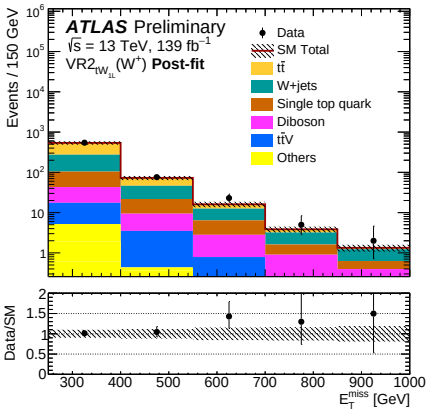

(e) $E_{\mathrm{T}}^{\mathrm{miss}}$ distribution in VR2(W^+)

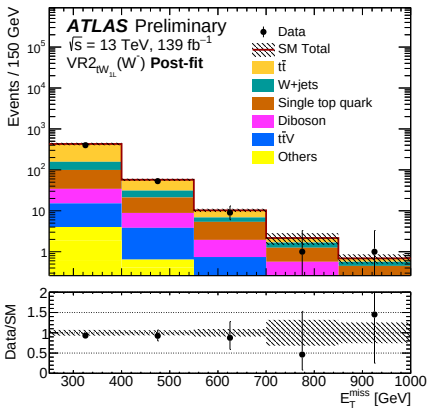

(f) $E_{\mathrm{T}}^{\mathrm{miss}}$ distribution in VR2(W^-)

Figure 7.7: Plots showing the $E_{\mathrm{T}}^{\mathrm{miss}}$ distribution in all VRs. Good agreement between data and the SM predictions in all regions is observed. The uncertainty band on the ratio includes MC statistical, experimental and modelling uncertainties.

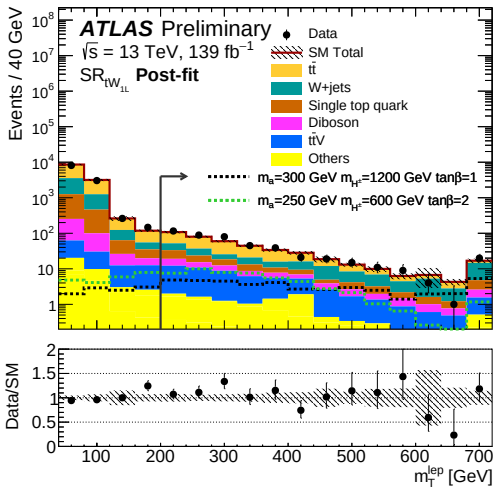

(a) m_{T}

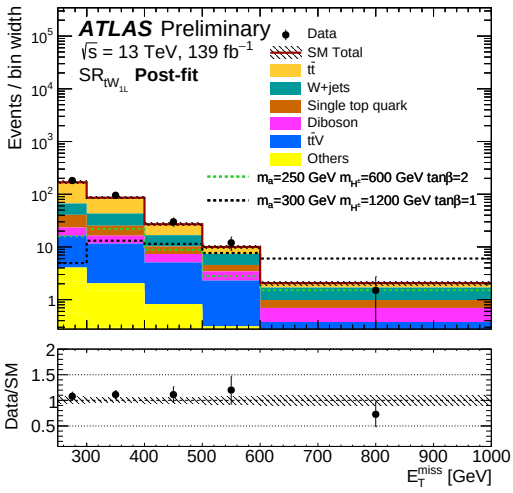

(b) $E_{\mathrm{T}}^{\mathrm{miss}}$

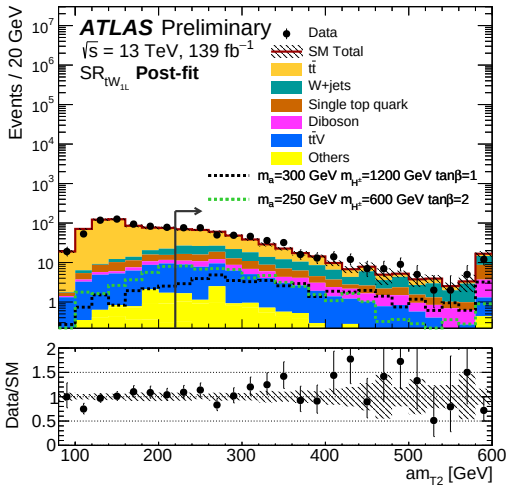

(c) am_{T2}

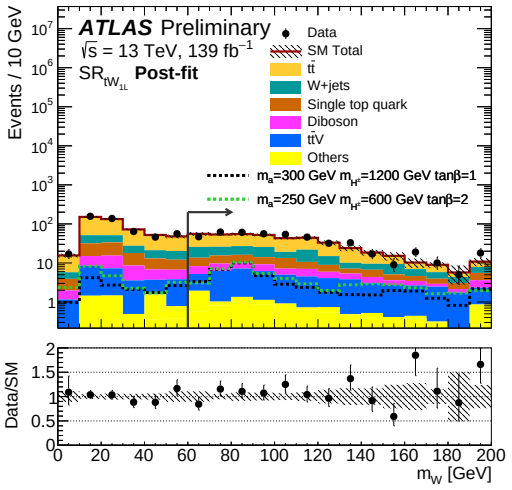

(d) $m_{\mathrm{W}}^{\mathrm{had}}$

Figure 7.8: Plots showing the post-fit N-1 distributions of the key kinematic variables. In these plots, all selections are applied except those on the variable being plotted. All uncertainties are included in the error band on the ratio. No significant excess is observed in the SR bins.

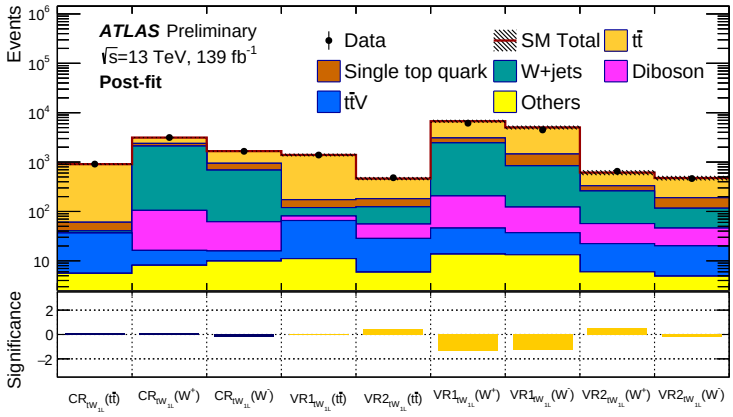

Figure 7.9: Summary plot showing the data/MC agreement in all control and validation regions for the single lepton channel of the search targeting the 2HDM+a tW+$E_{\mathrm{T}}^{\mathrm{miss}}$ signature. The uncertainty used to calculate the significance of the data/SM difference includes the statistical component on the MC and the data, as well as the total systematic uncertainty on the background estimate.

Model-dependent limits

In the absence of a significant excess, limits are set on the 2HDM+a model at 95% confidence limits using the previously described prescription. Model-dependent limits are set on the DMt and the DM$t + t\bar{t}$ signatures, in both the $m_a - m_{H\pm}$ and $m_{H\pm} - \tan\beta$ planes. A statistical combination of the 1ℓ and 2ℓ channel results is performed to maximise the sensivitity to the signal models. The fit is performed such that the individual background normalisations are constrained in their respective regions, such that there is no extrapolation of background estimates into vastly different phase space. For the DMt 1ℓ signature, $H^{\pm}$ masses are excluded upto 1250 GeV for $m_a = 100$ GeV, while for the DMt+$t\bar{t}$ signature masses above 1400 GeV are excluded. The observed limit of the statistical combination of the 1ℓ and 2ℓ channels is not as sensitive as the dedicated 1ℓ channel due to the 2σ excess in the 2ℓ SR.

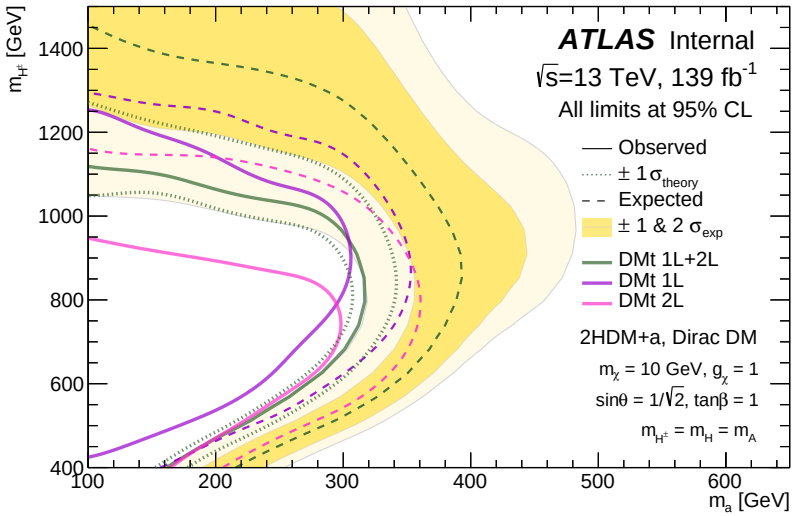

(a)

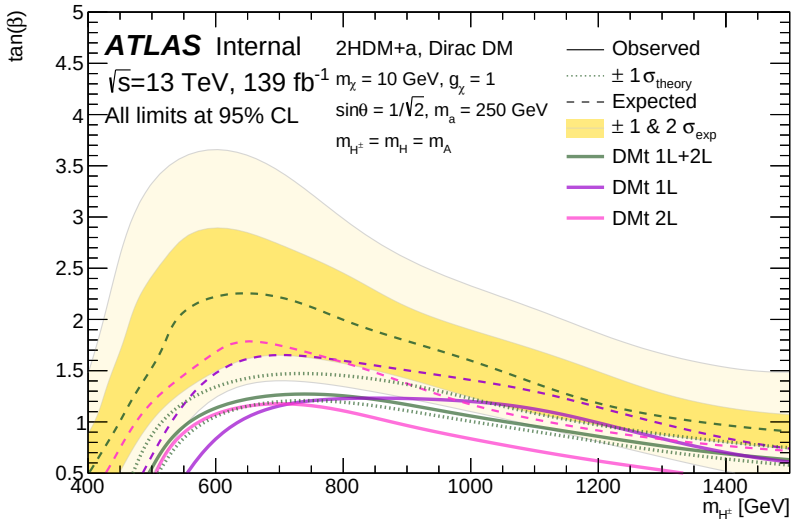

(b)

Figure 7.10: Plots showing the sensivitity to the 2HDM+a signal with the tW+$E_{\mathrm{T}}^{\mathrm{miss}}$ signature. Limits are shown in both the m_a-$m_{H^{\pm}}$ plane (a) and the $m_{H^{\pm}}$-tan(β) plane (b). Limits are shown for the analyses targeting the single lepton and di-lepton final states, along with the statistical combination of both channels.

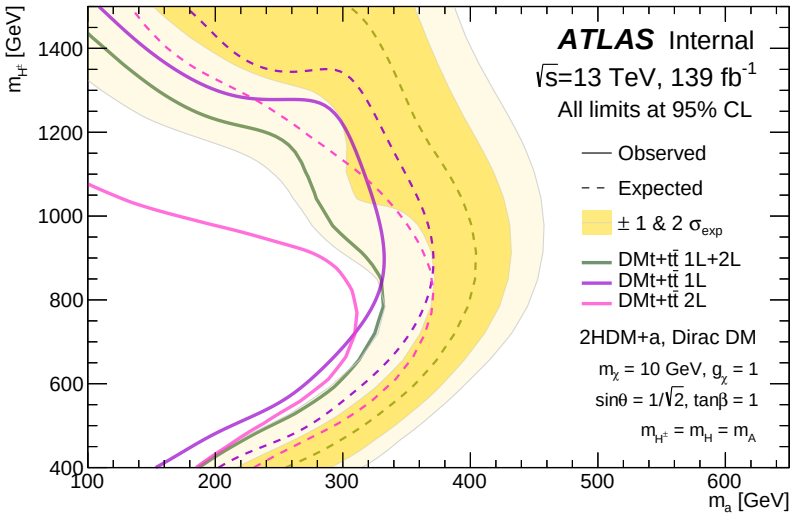

(a)

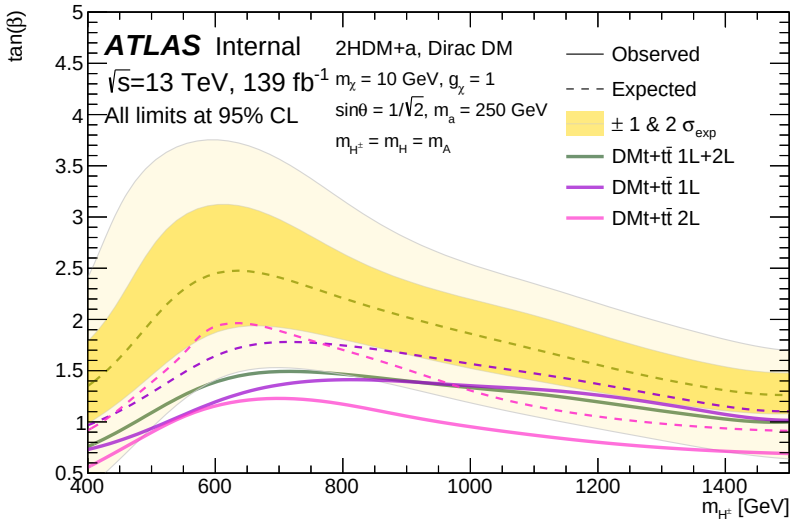

(b)

Figure 7.11: Plots showing the sensivitity to the 2HDM+a signal for both tW and $t\bar{t}$ signatures. Limits are shown in both the m_a-$m_{H^\pm}$ plane (a) and the $m_{H^\pm}$-tan(β) plane (b). Limits are shown for the analyses targeting the single lepton and di-lepton final states, along with the statistical combination of both channels.

Model-independent limits

In addition to model-dependent limits being set on the 2HDM+a signal model, with both tW and $tW + t\bar{t}$ signatures, 95% CL limits are set on any generic BSM processes using the model-independent fit strategy described in Section 5.5. The limits are presented as limits on the *visible* cross-section, $\sigma_{\text{vis}} = \epsilon \cdot A \cdot \sigma_{BSM}$, where ϵ is the signal selection efficiency, A is the detector acceptance, and σ_{vis} is the production cross-section for a generic BSM process. To set limits on a generic BSM process, the SR definition from Table 7.3 are modified, such that the individual SR bins have no upper $E_{\text{T}}^{\text{miss}}$ limit and rather only a lower $E_{\text{T}}^{\text{miss}}$ threshold. The yields in these modified, 'inclusive' SR bins are shown in Table 7.12. The results of the model-independent fit are shown in Table 7.13, as 95% CL limits on the expected and observed number of signal events.

Inclusive signal regions					
$E_{\text{T}}^{\text{miss}}$ threshold [GeV]	> 250	> 300	> 400	> 500	> 600
Observed events	469	287	96	36	12
Fitted SM bkg events	431 ± 27	262 ± 20	91 ± 10	36 ± 5	15.5 ± 2.8
$t\bar{t}$	213 ± 25	111 ± 18	28 ± 7	7.5 ± 2.9	2.3 ± 1.5
Single-top	43 ± 15	27 ± 12	9 ± 7	3.9 ± 3.8	$1.7^{+2.0}_{-1.7}$
W+jets	91 ± 8	63 ± 5	26 ± 3	12.0 ± 1.7	5.9 ± 1.1
Z+jets	3.8 ± 1.0	1.7 ± 0.7	0.6 ± 0.1	0.30 ± 0.05	0.15 ± 0.02
Diboson	26 ± 5	19.0 ± 3.9	9 ± 2	4.8 ± 1.0	2.6 ± 0.6
$t\bar{t}V$	47 ± 3	34.7 ± 2.4	15.3 ± 1.2	6.6 ± 0.5	2.5 ± 0.3
Others	7.5 ± 0.5	5.3 ± 0.4	2.3 ± 0.1	0.9 ± 0.1	0.40 ± 0.05

Table 7.12: Table showing the expected and observed yields in the modified signal regions for the determination of the model-independent limits. 'Others' includes the $t\bar{t}H$ and tWZ backgrounds.

Region	$\langle\epsilon\sigma\rangle_{\text{obs}}^{95}$[fb]	S_{obs}^{95}	S_{exp}^{95}
$\text{SR}_{1\text{L}}$ ($E_{\text{T}}^{\text{miss}} > 250$ GeV)	0.72	100.6	$66.7^{+32.7}_{-16.4}$
$\text{SR}_{1\text{L}}$ ($E_{\text{T}}^{\text{miss}} > 300$ GeV)	0.51	70.8	$54.1^{+16.0}_{-15.9}$
$\text{SR}_{1\text{L}}$ ($E_{\text{T}}^{\text{miss}} > 400$ GeV)	0.24	32.9	$29.4^{+10.1}_{-6.4}$
$\text{SR}_{1\text{L}}$ ($E_{\text{T}}^{\text{miss}} > 500$ GeV)	0.14	18.9	$18.7^{+7.6}_{-4.9}$
$\text{SR}_{1\text{L}}$ ($E_{\text{T}}^{\text{miss}} > 600$ GeV)	0.08	10.6	$12.0^{+2.7}_{-3.6}$

Table 7.13: Table showing the model-independent limits derived for the five modified inclusive SRs. Upper limits on the visible cross-sections of BSM physics between 0.08-0.72fb are excluded at 95% confidence limits, translating to an upper limit of around 100 events with a dataset of 139fb^{-1}.

Part III

High-Luminosity LHC studies

Chapter 8

Testbeam studies of ATLAS ITk pixel modules

The Run-2 period of data taking concluded in 2018, making way for the start of Long Shutdown 2 (LS2). As shown in Figure 8.1, wth LS2 comes the start of preparations for the next phase of the scientific programme of the LHC and ATLAS, the High-Luminosity phase. Following the completion of Run-3 of LHC operations, both ATLAS and LHC will go into Long Shutdown 3 (LS3), when a number of major upgrades of the detector will take place to cope with the new running conditions. The schedule for LHC operations and the subsequent upgrades are shown in Figure 8.1.

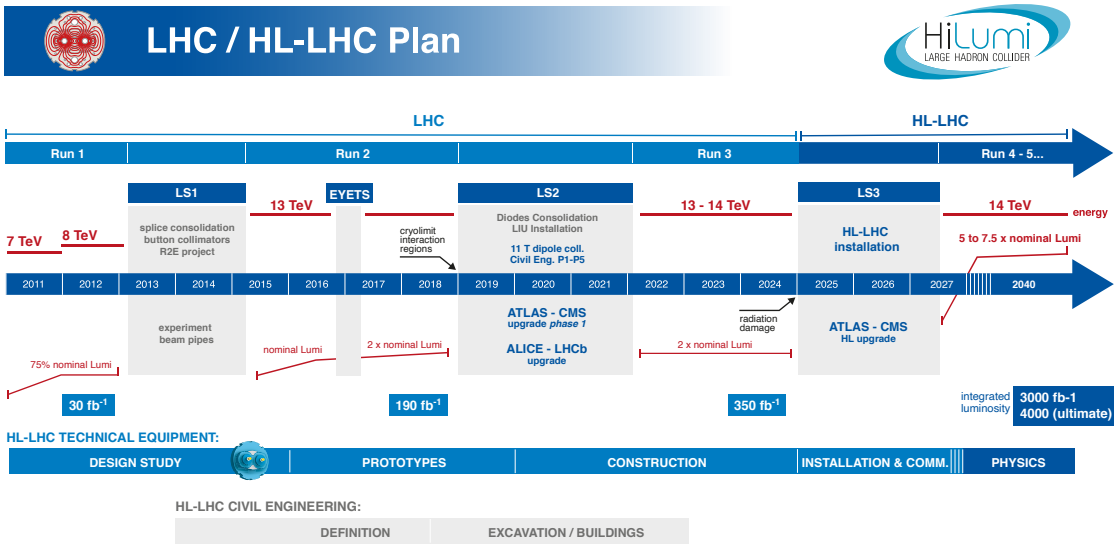

Figure 8.1: Figure showing the current schedule for LHC operations and eventual upgrades to the HL-LHC phase. [93]

The High-Luminosity LHC (HL-LHC) will begin running in the late-2020s, bringing instantaneous luminosities around 5 times higher than in Run-2, reaching $7.5 \times 10^{34}\,\mathrm{cm}^{-2}\mathrm{s}^{-1}$ at $\sqrt{s} = 14$ TeV. The total integrated luminosity to be recorded by ATLAS during this period is expected to total 3000-4000 fb^{-1}. Both the LHC and ATLAS will undergo numerous upgrades to prepare for the HL-LHC operations phase. The first set of upgrades to the ATLAS detector, known as the Phase I upgrades, are currently underway, taking place during the Long Shutdown 2 (LS2), between 2019-2021. The New Small Wheel (NSW) [94] will replace the current muon end-cap system, providing precision tracking and triggering capabilities. In addition, upgrades will be made to the electronics of the LAr calorimeter system, providing higher-granularity information to the L1 trigger [95].

During the HL-LHC phase in particular, the instantaneous luminosity is estimated to result in an average of 200 inelastic pp collisions in each bunch-crossing, with bunch-crossings occuring every 25 ns. Figure 8.2 shows an event display from a simulated $t\bar{t}$ ATLAS ITk with $\langle mu \rangle = 200$.

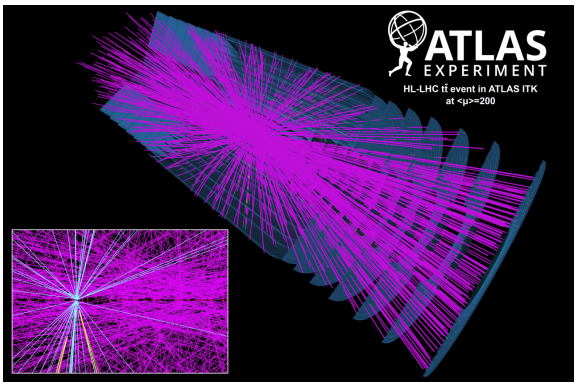

Figure 8.2: An event display of a simulated $t\bar{t}$ event in the ATLAS ITk at the HL-LHC, where there are an expected 200 interactions per bunch-crossing.

This instantaneous luminosity far exceeds the design of the ATLAS detector described in Chapter 2 and hence requires the installation of a new tracking detector with better performance and higher radiation tolerance, known as the ATLAS Inner Tracker (ITk). The ITk will be constructed based on full silicon micro-strip and hybrid pixel technologies, as these technologies are suited for high-occupancy, high-radiation environments. This Chapter documents studies on the performance of pixel modules for the upcoming ATLAS Inner Tracker (ITk) upgrade. In particular, test beam studies were performed using pixel modules based on FE-I4 front end ASICs.

8.1 ATLAS ITk upgrade

The ATLAS ITk, which is to be installed during the Phase II upgrades to the ATLAS detector, will replace the ATLAS ID during LS3. The ITk is an all silicon tracking detector, consisting of pixel and strip modules [96,97]. Figure 8.3 shows the most up-to-date ATLAS ITk layout, where the blue elements correspond to the strip detector modules, while the red elements correspond to the pixel detector modules.

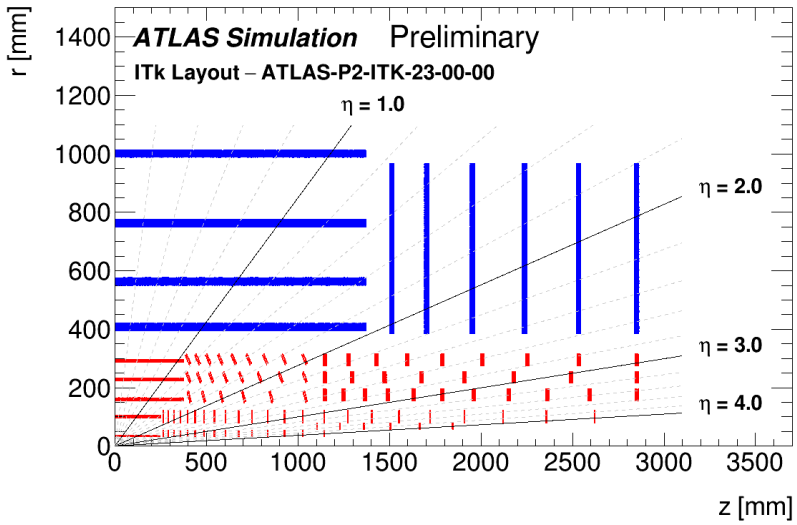

Figure 8.3: A schematic diagram, showing the ATLAS ITk layout for active detector elements. The detector elements shown in blue correspond to the strip detector, while the red elements correspond to the pixel detector.

The ITk aims to provide excellent tracking performance and efficiency, while operating in conditions where $\langle\mu\rangle = 200$, and also extending the tracking coverage upto $|\eta| < 4$. In addition to the challenging pileup conditions, the integrated radiation dose is expected to be as high as $3 \times 10^{16}\, n_{\text{eq}}/\text{cm}^2$ in the innermost layer, and hence the pixel sensor and readout electronics of the ITk must be extremely radiation-hard.

The pixel detector forms the innermost 5 layers and is surrounded by the strip detector. Between the two subdetectors, as many as 13 hits will be recorded for charged particles traversing the detector. The increase in the tracking granularity in the ITk is expected to improve the current track efficiency performance, despite the harsh pileup conditions, while the rate of fake tracks being reconstructed is expected to reduce significantly. Figure 8.4 shows the track reconstruction efficiency and fake rate as a function of $|\eta|$ for simulated $t\bar{t}$ events, comparing the ITk performance with $\langle\mu\rangle = 200$ to the Run-2 performance.

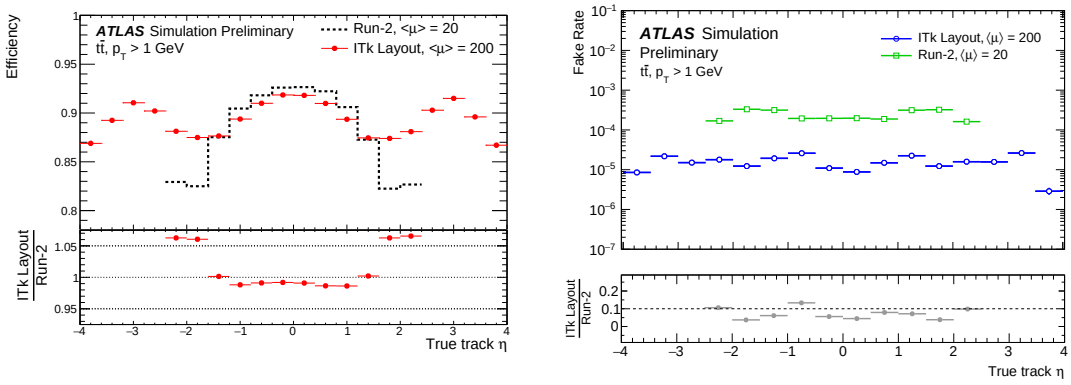

(a) (b)

Figure 8.4: Plots showing the track reconstruction efficiency (8.4a) and fake rate (8.4b) for simulated $t\bar{t}$ events, comparing the ITk performance with $\langle\mu\rangle = 200$ to the Run-2 performance [98].

8.2 Experimental setup

In order to characterise modules, test beam measurements are used to study the performance under conditions loosely mimicking those of the real detector. The device under test (DUT) is generally inserted between two arms of a beam telescope. Beam telescopes provide reference measurements with sub-pixel precision, allowing accurate track reconstruction for comparison with the hits measured by the DUTs. Both CERN and DESY have test beam facilities, the latter being described in the subsequent section.

The studies presented in this Chapter are on the performance of hybrid silicon pixel modules. Hybrid pixel modules combine both the pixel sensor and the read out chips by soldering the two together using bump-bonding.

DESY beam

DESY, the Deutsches Elektronen-Synchrotron, provides test beam facilities to experimental teams, allowing tests of the performance of detector devices. The DESY-II synchrotron [99], which begin operations in 1987, accelerates electrons or positrons, with momenta selectable between 1-6 GeV. A diagram showing the layout of the DESY-II test beam facility is shown in Figure 8.5.
The primary target, a 7 μm thick fiber, is placed in the beam orbit, which creates bremsstrahlung photons. The bremsstrahlung photons exit the DESY-II beam, travelling around 22m to hit the secondary targets. When these photons interact with the secondary target, electron-positron pairs are produced. The secondary targets are situated in front of the test beam facility dipole magnet, which allow the secondary electrons and positrons

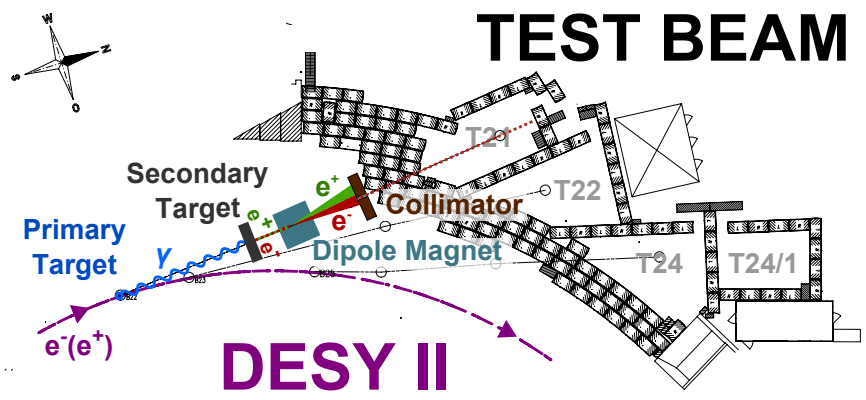

Figure 8.5: Diagram of the DESY-II test beam facility [99].

to be directed to three test beam halls, T21, T22 and T24.

EUDET setup

Test beam analyses at the DESY facility are performed using an EUDET-type beam telescope [100]. The telescope itself is a small tracking detector, comprising six silicon pixel sensors which are used to provide reference track hits, a triggering system which consists of four scintillators (two at the front of the telescope and two at the back) with photo multiplier tubes (PMTs) and a trigger logic unit (TLU), and finally a data acquisition (DAQ) system which reads out the hits and trigger information. A photograph of the EUDET telescope from a test beam in December 2018 is shown in Figure 8.6 for reference.

The six telescope sensor planes are arranged into two sets of three sensors with space between to insert a device-under-test (DUT). Telescope track hits are provided by these six planes, each of which has a MIMOSA 26 CMOS sensor. Each MIMOSA 26 sensor has 1152 columns and 576 rows of pixels, each of which is 18.4μm $\times$ 18.4μm. The total instrumented area of each telescope which can collect hit information, known as the active area, is 10.6 mm $\times$ 21.1 mm. A schematic diagram of the layout of the telescope planes is given in Figure 8.7.

Figure 8.6: A photograph of the EUDET telescope at DESY from a test beam in December 2018. Here, the six telescope planes are clearly visible, with two RD53a modules situated between the two groups of three telescope planes.

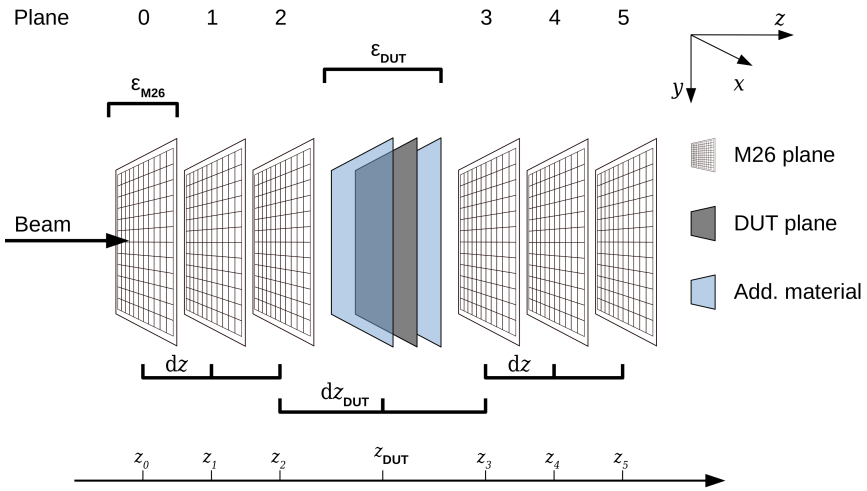

Figure 8.7: Schematic diagram of the layout of the six MIMOSA 26 telescope planes [100].

The telescope planes operate at a 80 MHz clock rate, with each row taking 16 cycles to be read out. This translates to the telescope being able to be fully read out approximately 8680 times per second. Reading out at this rate would produce huge amounts of data, much of which would be of no use to the subsequent analysis, and hence a trigger system is employed to only read out the telescope planes and DUTs when there is a signal, i.e. a particle passes through the telescope. When a particle enters the scintillator material, ionisation can occur which leads to the subsequent emission of photons. If all four PMTs

detect photons being emitted by their respective scintillators, the trigger is passed and the telescope and DUTs are read out.

8.3 Reconstruction and analysis

Reconstruction of test beam data is performed using the EUTelescope framework using a multi-step approach. The most important steps are *clustering*, *hit making*, *alignment* and finally *track-fitting*. A schematic diagram of the EUTelescope reconstruction steps is shown in Figure 8.8.

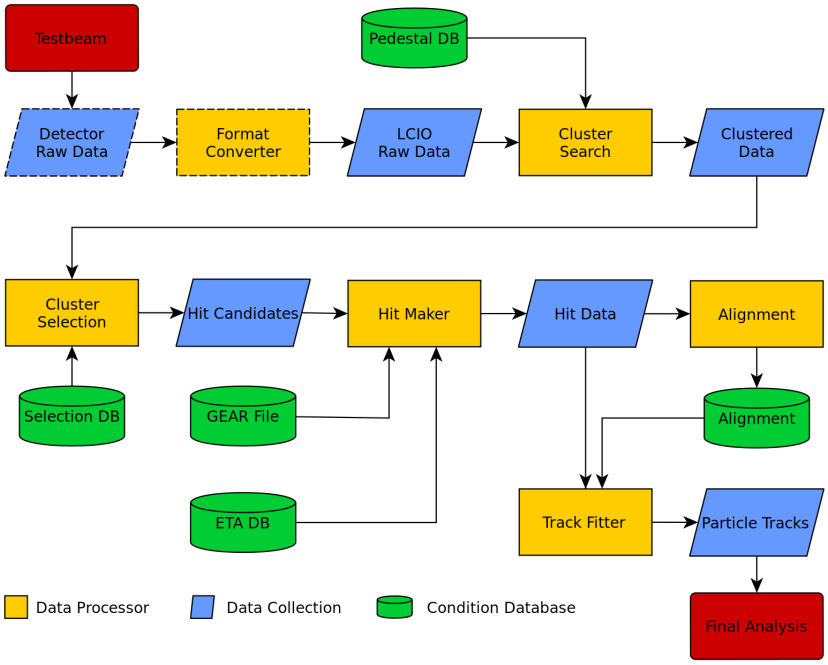

Figure 8.8: Diagram showing the workflow for reconstructing data taken at test beams, using the EUTelescope framework. [101]

In order to measure the efficiency of a DUT, the reconstructed tracks from the telescope planes are matched to hits in the DUT. The global efficiency of a DUT is given by

$$\epsilon_{\text{DUT}} = \frac{N_{\text{tracks, matched}}}{N_{\text{tracks}}} , \tag{8.3.1}$$

where N_{tracks} is the total number of telescope tracks and $N_{\text{tracks, matched}}$ is the subset of those which have a matching hit in the DUT. After HL-LHC radiation doses, the desired efficiency of each pixel module is to be above 97%. The in-pixel efficiency measures the efficiency within the pixel, and is calculated by taking the ratio of the number of tracks passing through a given pixel in the DUT which has a corresponding hit, divided by the number of tracks passing through the pixel. Pixels can be merged into $m \times n$ groups to

increase the available statistics.

Two FE-I4 modules [102] were used as the DUT in the following studies. These modules have 26880 pixels arranged in 80 columns and 336 rows, with an asymmetric pixel pitch of 250 μm by 50 μm. Hitmaps for the two FE-I4 modules are shown in Figure 8.9.

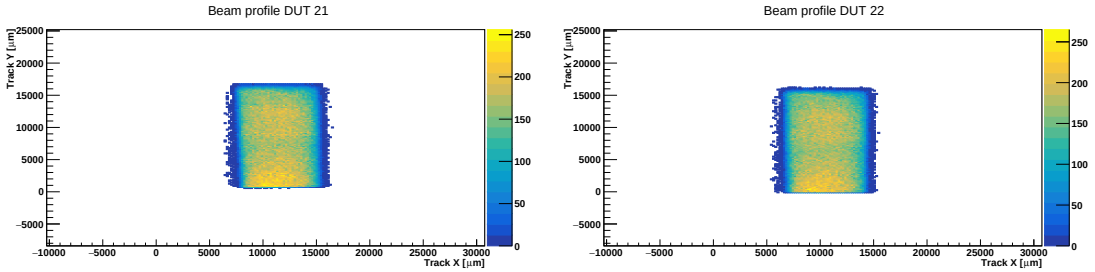

(a) (b)

Figure 8.9: Hitmaps for the two FE-I4 DUTs. All hits recorded are in the shadow of the scintillators, as hits on the sensor outside the scintillator area would not trigger the read out.

One FE-I4 module was irradiated to fluences representative of that expected in the HL-LHC, such that the efficiency could be compared with the efficiency at the start of HL-LHC operations. The global efficiency of the unirradiated module, 'DUT 21', was found to be 97.5%, while for the irradiated module, 'DUT 22', the global efficiency was found to be 95.1%. In order to account for reconstruction inefficiencies, the relative efficiency of the irradiated DUT to the unirradiated DUT is found by taking the ratio of their global efficiencies. The relative efficiency of the irradiated module is 97.5%. The global and in-pixel efficiency maps for these two modules are shown in Figure 8.10.

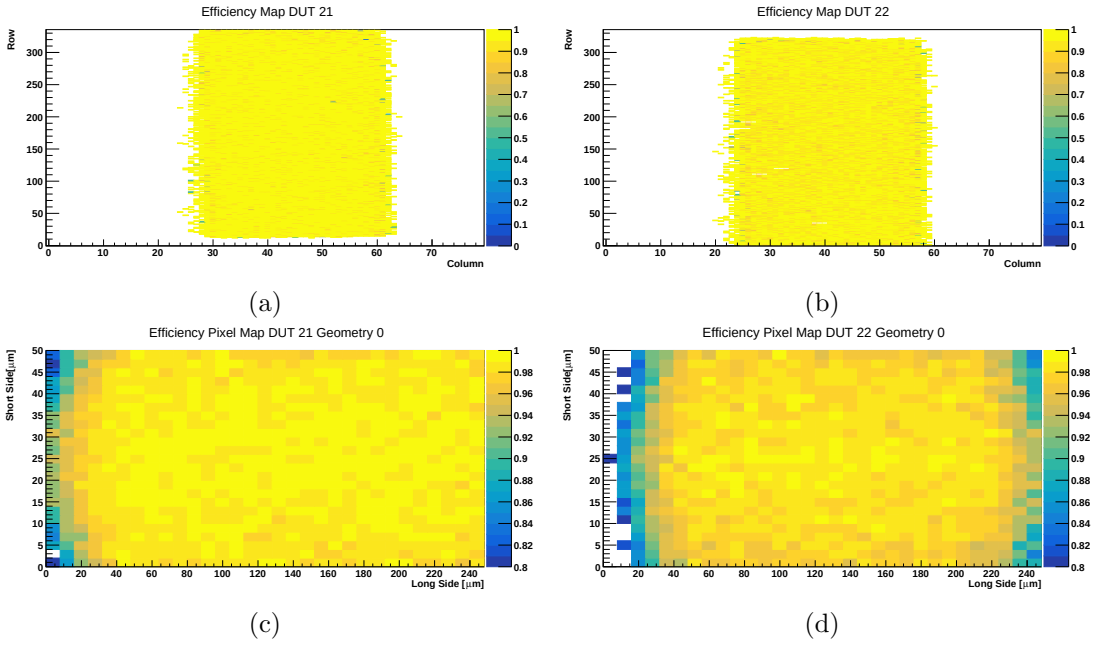

Figure 8.10: Plots showing the global (8.10a and 8.10b) and in-pixel efficiency maps (8.10c and 8.10d) for the two FE-I4 modules.

Chapter 9

Sensitivity to $\tilde{\chi}_1^{\pm}\tilde{\chi}_2^0$ pair-production at the HL-LHC

With the increased centre-of-mass energy and the expected 3000 fb^{-1} dataset, the physics analysis potential of the HL-LHC is unprecedented. Much of the HL-LHC physics program will be devoted to precision measurements of properties related to the Higgs boson and its relationship with the symmetry breaking mechanism of the electroweak sector of the SM. First sensitivity to the Higgs self-coupling is expected to be possible in the $HH \to b\bar{b}\gamma\gamma$ channel through both a conventional cut-and-count analysis [103] and a multivariate analysis [104]. This measurement will be used in combination with measurements in other final states, such as $b\bar{b}\tau\tau$ and $b\bar{b}b\bar{b}$ [105], further increasing sensitivity. It is also expected that measurements of the largest Higgs boson couplings to SM particles will be done with percent-level precision. Along with increased precision in measurements and sensitivity to SM properties, the HL-LHC will also bring increased sensitivity to TeV-scale new physics. This chapter describes one such prospects analysis, forming part of a plethora of sensitivity studies [4].

The analysis targets the same signal model as in Chapter 6, with a final state of a single electron/muon, two b-jets and $E_{\mathrm{T}}^{\mathrm{miss}}$. The sensitivity is assessed in the context of current expected HL-LHC conditions. Due to the huge dataset expected to be collected at the HL-LHC, the sensitivity is expected to reach far beyond the Run-2 sensitivity, and as such, mass up to 1500 GeV are considered for the $\tilde{\chi}_1^{\pm}/\tilde{\chi}_2^0$.

9.1 MC samples and detector simulation

The MC samples used for this analysis are generated using the same configurations as for the analysis detailed in Chapter 6. The MC samples used to model the $t\bar{t}$ and Wt-channel single top processes are generated with $\sqrt{s} = 14$ TeV, while all other SM background samples and the signal samples are generated at $\sqrt{s} = 13$ TeV.

In order to make meaningful predictions of sensitivity, a simulation of the ATLAS detector at the HL-LHC was developed through a set of parameterised smearing functions. These functions, known as the UpgradePerformanceFunctions, simulate the detector response by smearing the kinematic and angular properties of the physics objects, as well as providing additional collision vertices to simulate the pileup conditions at the HL-LHC. The treatment of each object relevant to this chapter will be discussed separately. Some shorthand will now be introduced for the following sections. $R(m, n)$ represents a random number drawn from a uniform distribution in the range m to n. $G(\mu, \sigma)$ represents a number drawn from a Gaussian distribution with a mean, μ, and a standard deviation, σ.

Leptons

The steps taken in the reconstruction of charged leptons are highly dependent on the generation of lepton being considered, but there are some common steps. Lepton ID working points are assigned for all three generations of charged leptons, and the detector response to the E_T for electrons and taus and p_T for muons is simulated. The charge-flip probability (the probability that the reconstructed lepton has the opposite charge to its true value), $P(\ell^{\pm}_{truth} \to \ell^{\mp}_{reco})$, is explicitly parameterised for electrons and is also possible for muons. Finally, the misreconstruction of an electron as a photon is parameterised.

A parameterisation of the lepton ID efficiencies is used in order to choose which lepton ID working points the lepton has passed. For each lepton generation there are three ID efficiency parameterisations, one corresponding to each working point. These parameterisations can be seen in Figure A.1. For a given lepton, the three ID efficiencies corresponding to the ID working points are retrieved, and all which satisfy $R(0, 1) < \epsilon^i_{ID}$, with $i = 1, 2, 3$, are passed.

The p_T resolution for leptons is simulated differently for muons than for electrons and taus. For the former, the key quantity is the charge (in units of e) to transverse momentum ratio, $\frac{q}{p_T}$, while for electrons and taus it is the energy, E. For both quantities, the 'reconstructed' value is as follows:

$$\begin{aligned} E_{reco} &= E_{truth} + G(0, \Delta E) \\ \left(\frac{q}{p_T}\right)_{reco} &= \left(\frac{q}{p_T}\right)_{truth} + G\left(0, \Delta\left(\frac{q}{p_T}\right)\right) \end{aligned} \tag{9.1.1}$$

Here, ΔE and $\Delta\frac{q}{p_T}$ denote the resolutions on the respective quantity. The reconstructed muon transverse momentum is then given by $p_T^{reco} = \left|\left(\frac{q}{p_T}\right)^{-1}_{reco}\right|$, while for electrons and taus it is given by $p_T^{reco} = p_T^{truth} \times \frac{E_{reco}}{E_{truth}}$.

The charge-flip probability for electrons is parameterised in η and differs slightly for the three ID working points, as can be seen in Figure A.1. The charge-flip probability is determined by the tightest working point which is passed by the electron. A charge-flip occurs if the following condition is satisfied; $R(0,1) < P(e^{\pm}_{truth} \rightarrow e^{\mp}_{reco})$. Muons, particularly high-p_T or η muons, can undergo a charge flip when the $\frac{q}{p_T}$ is smeared.

Finally, electrons being misreconstructed as a photons is simulated through a parameterisation in η. For electrons with a $p_T > 20$ GeV, the probability of an electron being reconstructed as a photon is 2% for electrons with $|\eta| < 1.37$ and is 5% for electrons with $|\eta| > 1.52$. An electron is misreconstructed as a photon if $R(0,1) < P(e \rightarrow \gamma)$.

Jets and flavour tagging

To simulate jet reconstruction, the first step of the detector simulation process is to smear the jet energy and p_T. The jet p_T is smeared by a multiplicative factor, $G\,(1, \Delta E)$, where ΔE represents the relative jet energy resolution determined from the parameterisation shown in Figure A.3a. The jet energy is smeared by multiplying the true jet energy by $\frac{p_T^{smeared}}{p_T^{truth}}$.

Jet flavour-tagging, in particular the tagging of jets originating from b-quarks, is of great importance to the study described in this chapter. The b-tagging working point used has a b-tagging efficiency $\epsilon_b = 70\%$, which has much-improved light-jet rejection compared to the $\epsilon_b = 85\%$ working point. The flavour-tag efficiency, ϵ^b_{ftag}, is parameterised in jet p_T and η, and can be seen in Figure A.3b. Jets which have originated from a b-quark at truth-level are b-tagged if $R(0,1) < \epsilon^b_{ftag}$. The misreconstruction of jets as electrons, taus and photons is simulated by parameterising the so-called 'fake rate'. This is rate at which an object is misreconstructed as another object.

$E_{\mathrm{T}}^{\mathbf{miss}}$

Smearing the $E_{\mathrm{T}}^{\mathrm{miss}}$ requires two steps. At truth-level, the missing transverse energy, $E^{miss}_{T,truth}$, is the sum of the transverse energies of all neutral particles in the event; in this study, only neutrinos and neutralinos contribute.

To account for mismeasurement due to pileup, $E^{miss}_{T,truth}$ is smeared by adding an additional term, $E^{miss}_{T,pileup}$, drawn randomly from the distribution shown in Figure A.4a. The $E_{\mathrm{T}}^{\mathrm{miss}}$ resolution, ΔE_T, is then determined from the parameterisation shown in Figure A.4b, using the sum of the neutral particle and pileup $E_{\mathrm{T}}^{\mathrm{miss}}$ components as an input. The final $E_{\mathrm{T}}^{\mathrm{miss}}$ is then give as:

$$E_T = E^{miss}_{T,truth} + G(0, \Delta E_T) \tag{9.1.2}$$

Kinematic distribution comparison

The effects of the detector simulation described in this section is illustrated in Figure 9.1 using simulated $t\bar{t}$ events. The 'truth-level' distributions include no detector effects, the 'truth-level with smearing' distributions include the detector simulation described in this section, and the 'reco-level' distrubutions are reconstructed using the full ATLAS detector simulation.

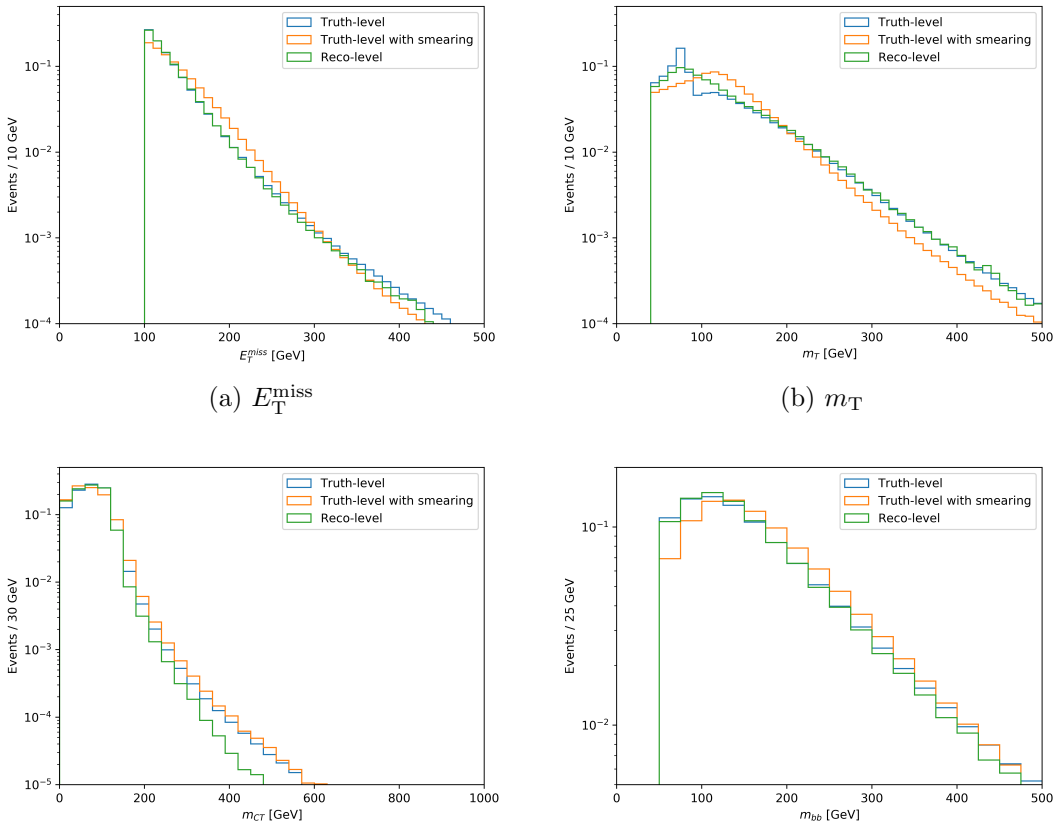

(a) $E_{\mathrm{T}}^{\mathrm{miss}}$ (b) m_{T}

(c) m_{CT} (d) m_{bb}

Figure 9.1: The E_T^{miss}, m_T, m_{CT} and m_{bb} distributions at truth-level, truth-level with the detector smearing described in this section, and a fully reconstructed samples. All distributions are normalised to unity to compare only the shape of the distributions and not normalisations.

9.2 Event selection

The object definitions used to reconstruct the leptons and jets are summarised in Table 9.1 and Table 9.2, respectively.

	Electrons	Muons
p_{T}	25 GeV	25 GeV
$\lvert\eta\rvert$	< 2.47	< 2.7
ID	Tight	Medium

Table 9.1: A summary of the object definitions for leptons in the HL-LHC projection.

	jets	b-jets
p_{T}	25 GeV	25 GeV
$\lvert\eta\rvert$	< 2.5	< 2.5
Jet radius (R)	0.4	0.4
b-tagging WP	-	70%

Table 9.2: A summary of the object definitions for jets in the HL-LHC projection.

Similarly to the 36.1fb^{-1} analysis described in Chapter 6, a number of preliminary selections are applied to select events with the single lepton, two b-jet topology, as shown in Table 9.3.

Preselection	
Leptons ($p_T \geq 25$ GeV)	$1e$ or 1μ
Jets ($p_T \geq 25$ GeV)	2 or 3
b-jets ($p_T \geq 25$ GeV)	2
m_{T}	≥ 40 GeV
m_{bb}	≥ 50 GeV
$E_{\mathrm{T}}^{\mathrm{miss}}$	≥ 200 GeV

Table 9.3: A summary of the preliminary selections used for for the HL-LHC projection.

The loose selections on m_{T} and m_{bb} are employed to reduce the impact of the combinatoric and multi-jet backgrounds, as described in Chapter 6, while the $E_{\mathrm{T}}^{\mathrm{miss}}$ selection is used to both reduce the SM background and target events containing two $\tilde{\chi}_1^0$ in the final state. The transverse momentum requirements of the leptons and jets are similar to those of the Run-2 analysis as it is assumed that this will be achievable at the HL-LHC. No trigger requirement is used as the analysis is MC-only.

Events passing the preliminary selections listed in Table 9.3 are used as inputs to BDT

classifiers. In this study, binary classification is performed such that the output of the BDT is a single value $\in [-1, 1]$. The key discriminatory variables which are given to the BDT classifiers as inputs are the $E_{\mathrm{T}}^{\mathrm{miss}}$, m_{T}, m_{CT}, m_{bb} and $\Delta R(\mathrm{b}_1, \mathrm{b}_2)$. Along with these, the transverse momentum of the lepton and the two b-jets are useful for background rejection. The distributions of $E_{\mathrm{T}}^{\mathrm{miss}}$, m_{T} and $\Delta R(\mathrm{b}_1, \mathrm{b}_2)$ for the signal are highly dependent upon the mass and the mass difference of the $\tilde{\chi}_2^0/\tilde{\chi}_1^{\pm}$ and $\tilde{\chi}_1^0$, and as such having one classifier which performs equally well across the entire phase space is extremely difficult to achieve. To aid in this, three BDT classifiers are trained, targeting 'low', 'intermediate' and 'high' mass-splittings, ΔM = m($\tilde{\chi}_1^{\pm}/\tilde{\chi}_2^0$) - m($\tilde{\chi}_1^0$). SR-Low targets $\Delta M < 300$ GeV, SR-Med targets $\Delta M \in [300, 600]$ GeV and SR-High targets $\Delta M > 600$ GeV. The signal grid, highlighted with the three targeted regions, is shown in Figure 9.2. Due to the limited number

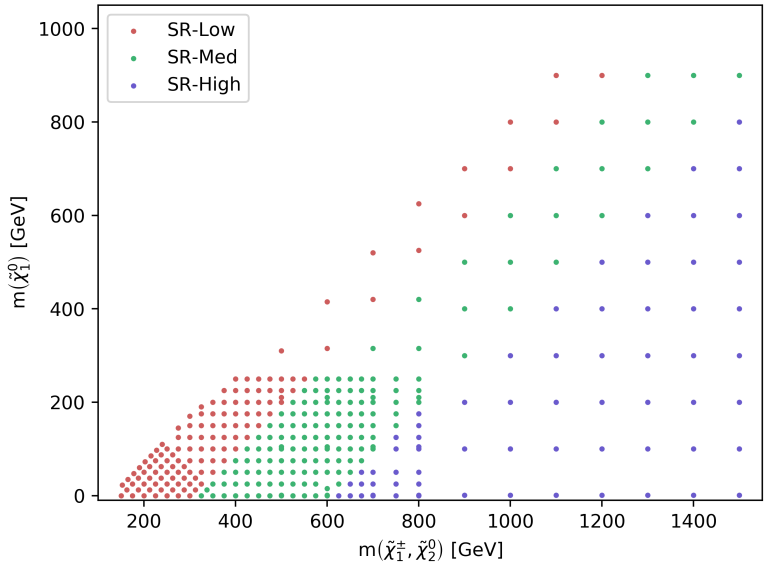

Figure 9.2: Plot showing the separation of the mass plane into the three defined categories.

of MC events in each individual signal sample, all signal samples in each mass-splitting regime ('low', 'intermediate' or 'high' ΔM) are summed together with an equal weight of 1. The sum of signals for each mass-splitting region provide a high-statistics signal sample on which to train the BDTs, with kinematic distributions representing a 'pseudo-average' of the individual signal samples. A benchmark signal is chosen from each mass-splittinBut g region for the purposes of comparing the kinematic distributions of signal and background, and for later deriving an optimal cut on the BDT output. The kinematic distributions forming inputs to the BDTs are shown, with benchmark signals overlaid, in Figures 9.3 and 9.4. The estimate for signal and background yields in the SRs is obtained by placing a cut on the output of the BDTs. The optimal cut value is derived by scanning over the BDT output with an increasing lower bound, and calculating the binomial significance, Z_n,

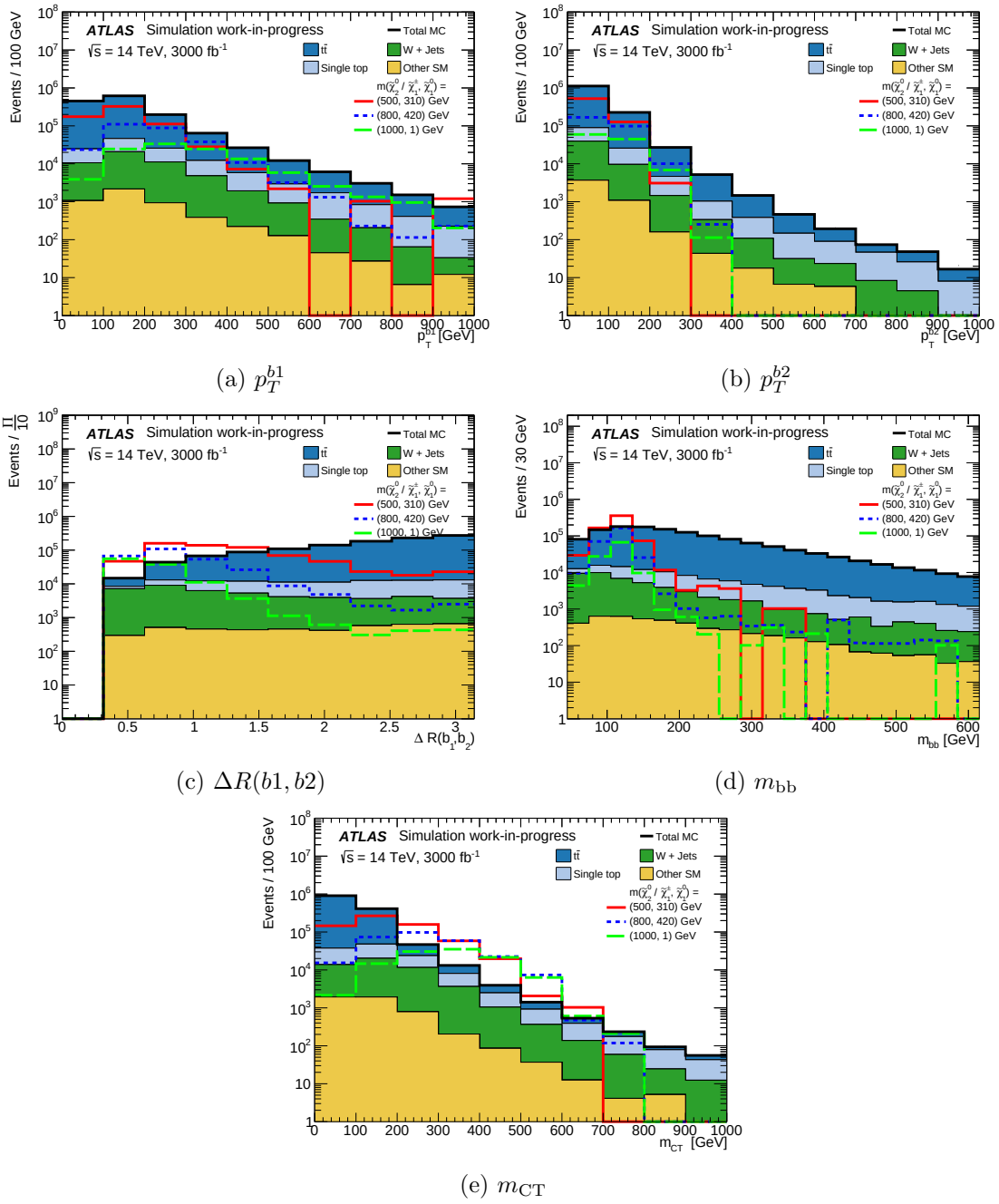

(a) p_T^{b1}

(b) p_T^{b2}

(c) $\Delta R(b1, b2)$

(d) m_{bb}

(e) m_{CT}

Figure 9.3: Kinematic and angular distributions for the BDT input variables at the preselection-level related to the b-jets.

for that region's benchmark model and the SM background. The optimal cuts are shown in Table 9.4.

The BDT output distributions for the SM backgrounds and the benchmark signal point for each region is shown in Figure 9.5. The arrows in these plots show the selection placed on the BDT output, which is labelled as 'MVA response'.

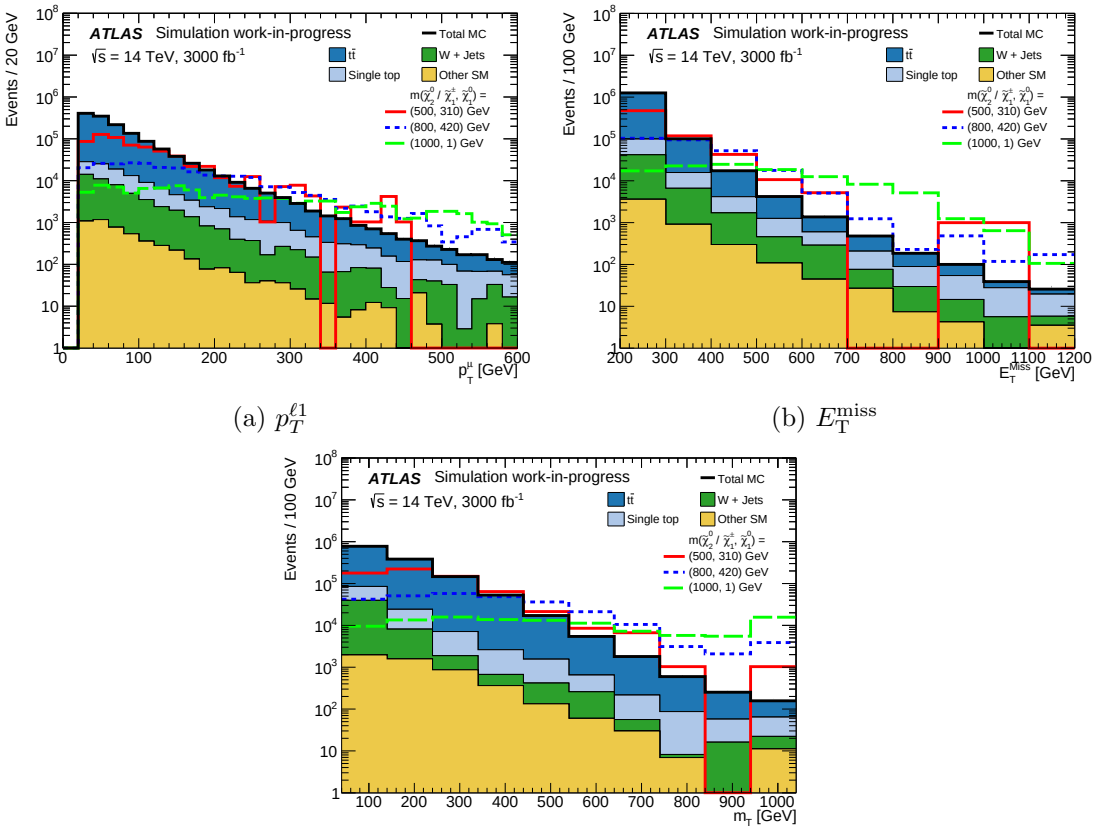

(a) $p_T^{\ell 1}$

(b) $E_{\mathrm{T}}^{\mathrm{miss}}$

(c) m_{T}

Figure 9.4: Kinematic and angular distributions for the BDT input variables at the preselection-level for the leptons and $E_{\mathrm{T}}^{\mathrm{miss}}$.

SR	Signal benchmark $m(\tilde{\chi}_1^{\pm}/\tilde{\chi}_2^0, \tilde{\chi}_1^0)$ [GeV]	BDT range
SR-M1	(500, 310)	> 0.25
SR-M2	(800, 420)	> 0.35
SR-M3	(1000, 1)	> 0.30

Table 9.4: Benchmark signal models and the corresponding optimised BDT output cut, derived by maximising the binomial significance, Z_n of the benchmark signal over the SM background.

9.3 Systematic uncertainties

A joint strategy between the ATLAS and CMS collaborations was adopted to have a coherent set of assumptions in the estimate of the systematic uncertaines for HL-LHC projection studies. For analyses with an existing Run-2 analysis, a prescription for extrapolating the current systematic uncertainties to 3000 fb^{-1} , where theoretical modelling uncertainties are expected to be half their current value. The extrapolation method for experimental

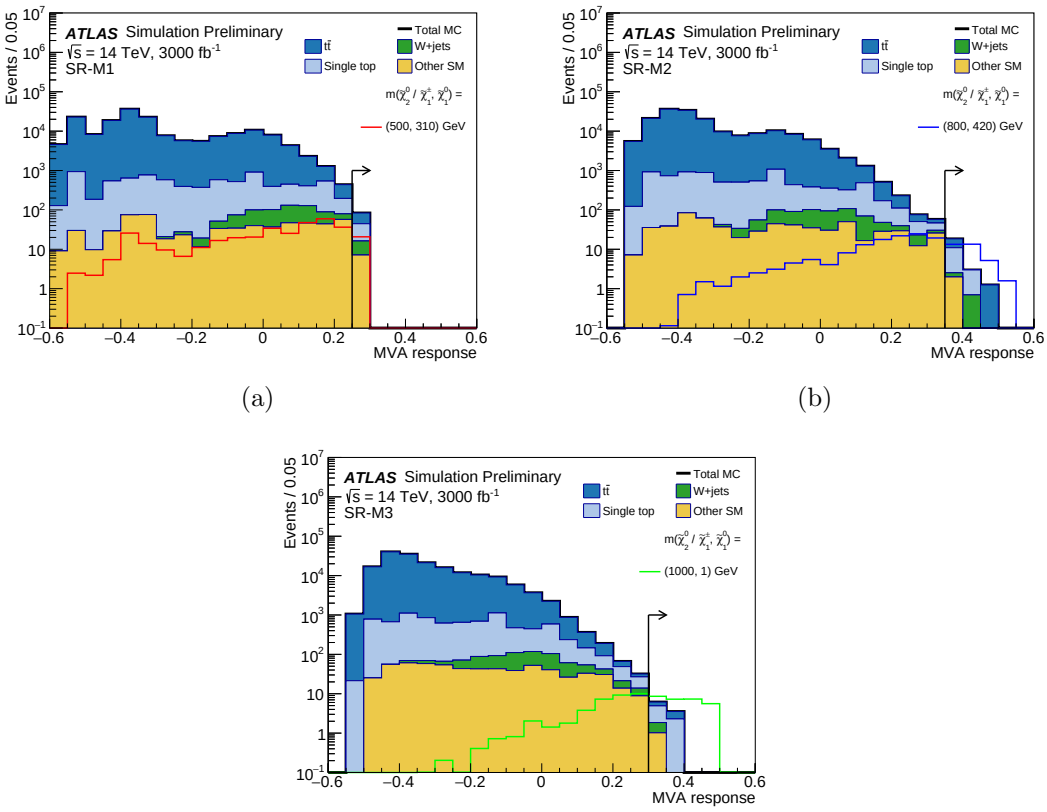

Figure 9.5: BDT outputs for HL-LHC projection. The arrow on each plot shows the cut placed on the BDT output, defining the SR.

uncertainties depend upon the systematic under consideration and are provided as multiplicative factors which are applied to the corresponding Run-2 systematic uncertainties.

In this study, the systematics from the Run-2 analysis described in Chapter 6 are extrapolated from SR1Lbb-High, which is the most kinematically similar SR to the regions presented in this analysis. The HL-LHC extrapolated uncertainties are shown in Table 9.5.

$1\ell + b\bar{b} + E_{\mathbf{T}}^{\mathbf{miss}}$ **channel**	
Uncertainty of region	All SRs
Total background uncertainty	18.1%
Systematic, jets	11.2%
Systematic, Wt modelling	10.0 %
Systematic, $t\bar{t}$ modelling	9.8 %
Systematic, $E_{\mathrm{T}}^{\mathrm{miss}}$	2.1%
Systematic, leptons	1.7%
Systematic, pileup	0.2%

Table 9.5: Table showing a summary of the experimental and modelling uncertainties in the SUSY Wh $1\ell + b\bar{b} + E_{\mathrm{T}}^{\mathrm{miss}}$ analysis. The uncertainties are expressed in terms of the number of events.

9.4 Results

The yields after the BDT cuts shown in Table 9.4 are shown below in Table 9.6. Entries denoted by '-' indicate there were no events of that particular process in the corresponding region.

Processes	SR-M1	SR-M2	SR-M3
$t\bar{t}$	38.9 ± 8.4	8.7 ± 3.3	2.5 ± 1.8
single top	28.3 ± 4.8	10.7 ± 3.2	5.4 ± 2.5
W+jets	22.2 ± 5.4	3.0 ± 2.0	2.0 ± 1.8
ttV	5.1 ± 2.4	2.0 ± 1.4	1.0 ± 1.0
Diboson	2.0 ± 2.0	-	-
total background	96.5 ± 11.8	24.4± 5.2	10.9 ± 3.4
$m(\tilde{\chi}_1^{\pm}/\tilde{\chi}_2^0, \tilde{\chi}_1^0) = (500, 300)$ GeV	20.7 ± 4.8	4.6 ± 2.3	1.0 ± 1.0
$m(\tilde{\chi}_1^{\pm}/\tilde{\chi}_2^0, \tilde{\chi}_1^0) = (800, 420)$ GeV	44.3 ± 2.3	33.6 ± 2.0	21.2 ± 1.6
$m(\tilde{\chi}_1^{\pm}/\tilde{\chi}_2^0, \tilde{\chi}_1^0) = (1000, 1)$ GeV	32.2 ± 1.8	31.9 ± 1.8	28.9 ± 1.7

Table 9.6: Expected signal and background yields. The errors are statistical uncertainties. Entries marked − indicate a negligible background contribution.

Figure 9.6 shows the 95% CL exclusion limit for this channel, as well as the 5σ discovery potential. The three signal regions are combined by taking the best expected sensitivity for each signal point. The systematics band, represented by the yellow area around the 95% CL exclusion line includes the extrapolated experimental and modelling systematics on the SM backgrounds, as well as the statistical uncertainty on all MC samples.

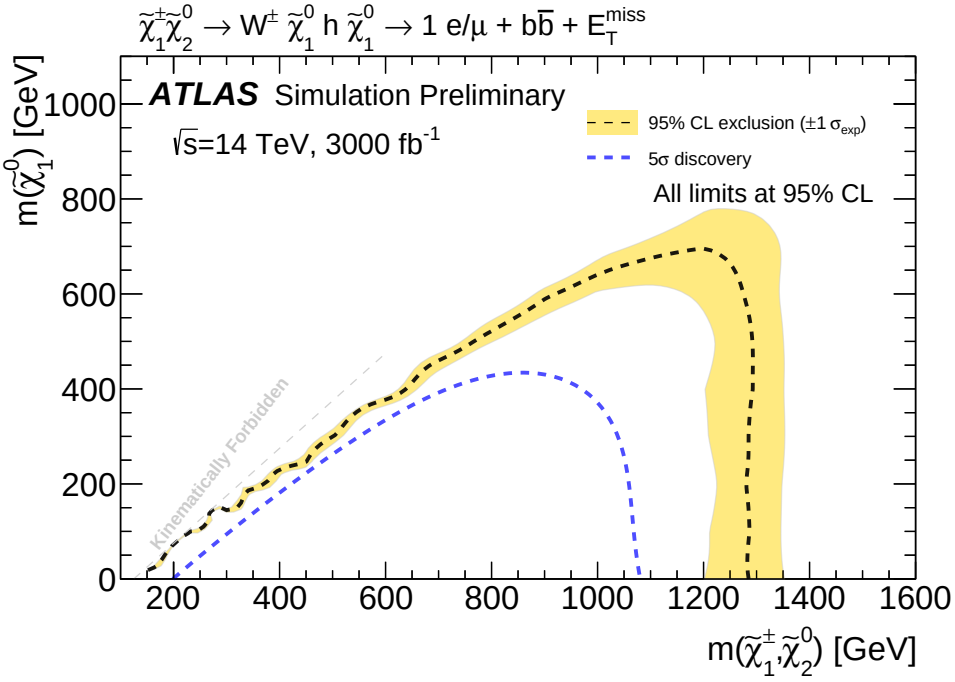

Figure 9.6: 95% CL exclusion limit and 5σ discovery limit for the analysis presented in this chapter.

As shown in Figure 9.6, it is expected that this channel can be excluded up to 1280 GeV, while there is discovery potential up to 1070 GeV. This far exceeds the exclusion limits at the end of Run-2, with results shown in Chapter 6 for both 36.1fb^{-1} and 139fb^{-1}. During this analysis, studies were performed using a both a conventional cut-based analysis and also using a deep neural network to perform binary classification of signal and background. These studies are included in Appendix A.

Chapter 10

Summary

At the time of writing, the ATLAS experiment has completed two periods of data-taking, Run-1 and Run-2, collecting data at the collision energy frontier and recording huge datasets. This data has been used to perform countless measurements of SM processes and parameters, along with a plethora of searches for New Physics, as motivated in Chapter 1. This Thesis has presented searches for two New Physics scenarios, with a collision energy of $\sqrt{s} = 13$ TeV.

Chapter 6 presents two searches targeting the pair-production of a chargino and next-to-lightest neutralino, decaying via $\tilde{\chi}_1^{\pm}\tilde{\chi}_2^0 \rightarrow Wh\tilde{\chi}_1^0\tilde{\chi}_1^0$ in the 1-lepton, 2 b-jets and $E_{\mathrm{T}}^{\mathrm{miss}}$ final state. The first of these searches used a dataset of 36.1 fb^{-1} taken in 2015 and 2016, and in the absence of an excess of events over the SM prediction set limits on the process at $\mathrm{m}(\tilde{\chi}_1^{\pm}/\tilde{\chi}_2^0) = 550$ GeV for a massless lightest neutralino. The sensitivity to this process was extended in the second analysis presented in Chapter 6, which utilised the full Run-2 dataset of 139 fb^{-1}, excluding the process upto 740 GeV in chargino/next-to-lightest neutralino mass. Finally, this Chapter presents early ML studies to discriminate this signal from the dominant top quark backgrounds. Both a fully-connected DNN and a BDT are trained to classify the signal from $t\bar{t}$ and Wt production in a three-way classification, showing promising discrimination. The results of this ML analysis will be presented in a future publication from ATLAS.

Chapter 7 presents a search for DM produced in association with a single top quark (Wt-channel), interpreted in the context of a 2HDM model with an additional pseudoscalar mediator, a, also utilising the full Run-2 139 fb^{-1} dataset. Chapter 7 focuses on the single lepton channel, but also presents the combined result with the two lepton channel. The single lepton analysis excludes the process of interest upto $m_{H^{\pm}} = 1250$ GeV for mediator masses upto 400 GeV. The sensitivity of this analysis to the production of DM in association with both a single top quark or a pair of top quarks is also presented, which extends the exclusion upto $m_{H^{\pm}} = 1400$ GeV.

Chapters 8 and 9 present studies related to the forthcoming upgrade of the LHC and ATLAS. Chapter 8 presents test beam studies performed on the FE-I4 modules in the ATLAS IBL, irradiated to an end of HL-LHC dose. The efficiency of the irradiated module was measured to be 97.5%, satisfying the efficiency requirement imposed for modules after HL-LHC operations. Finally, Chapter 9 presents a sensitivity projection for the process introduced in Chapter 6, using a parameterised HL-LHC ATLAS detector and with a dataset of 3000 fb^{-1} collected at $\sqrt{s} = 14$ TeV. The expected exclusion limit on this process is set at 1280 GeV, far exceeding the current limits.

While the searches for New Physics presented in this Thesis yielded only the SM, the prospect of observing New Physics at the LHC is very much alive. The program of searches on both ATLAS and CMS continues to push the boundaries of the detectors, and with novel techniques like ML being applied to the datasets collected, the collaborations are getting as much physics out of the recorded data as possible. With the advancements of such techniques, and the forthcoming upgrade to the LHC and ATLAS, the search for a hint of New Physics will probe both the SM and the available phase space for BSM processes to levels never before seen. In addition, inputs from experiments beyond the LHC, such as the g-2 experiment and direct and indirect DM detection experiments will further shape the future search program of ATLAS. Searches for New Physics at the energy frontier are very much in their infancy, and physicists will continue to narrow down the nature of physics beyond the SM over the coming years.

Appendix A

Sensitivity to $\tilde{\chi}_1^{\pm}\tilde{\chi}_2^0$ pair-production at the HL-LHC

The first part of this appendix is dedicated to documenting the detector simulation parameterisations detailed in Chapter 9.

A.1 Detector simulation parameterisations

Electrons

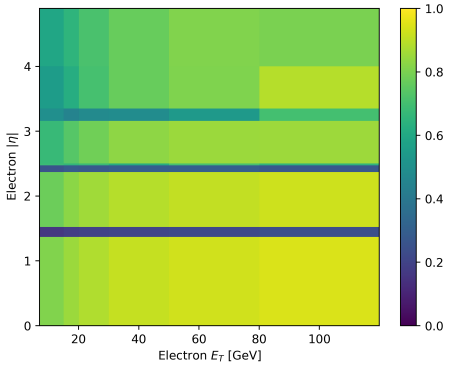

(a) ϵ_{rec} for 'loose' electron working point.

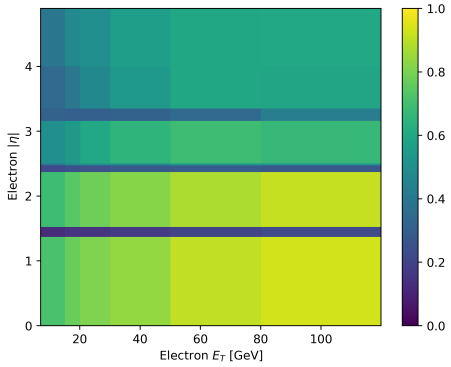

(b) ϵ_{rec} for 'medium' electron working point.

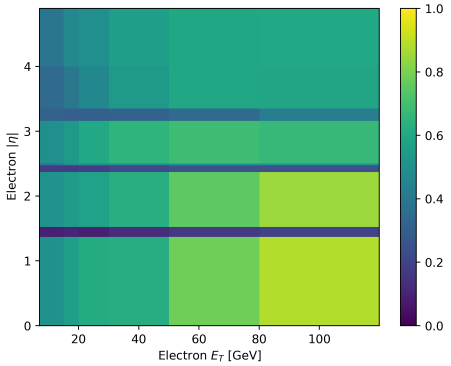

(c) ϵ_{rec} for 'tight' electron working point.

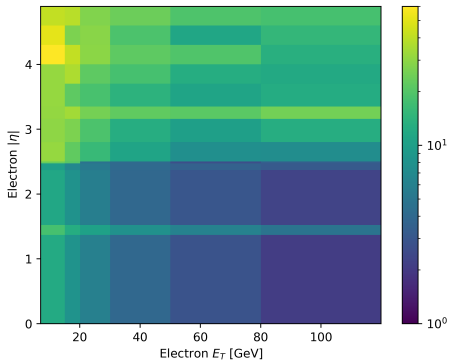

(d) Electron energy resolution (MeV).

Figure A.1: Electron ID efficiencies, energy resolution and charge-flip probability for the prospects study presented in Chapter 9. The

Muons

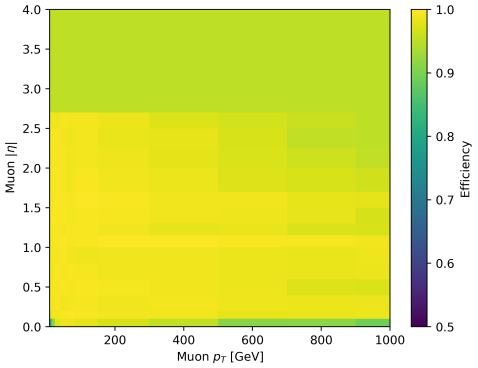

(a) ϵ_{rec} for 'loose' muon working point.

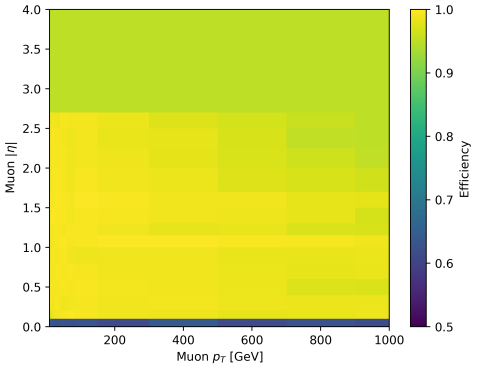

(b) ϵ_{rec} for 'tight' muon working point.

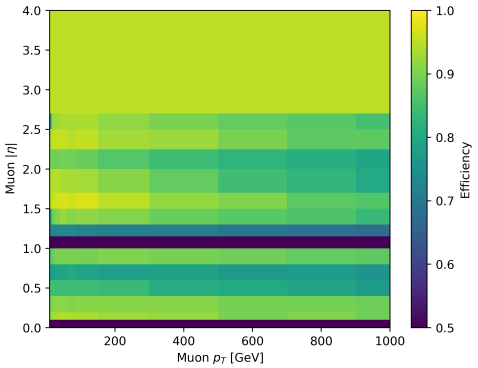

(c) ϵ_{rec} for 'high-p_T' muon working point.

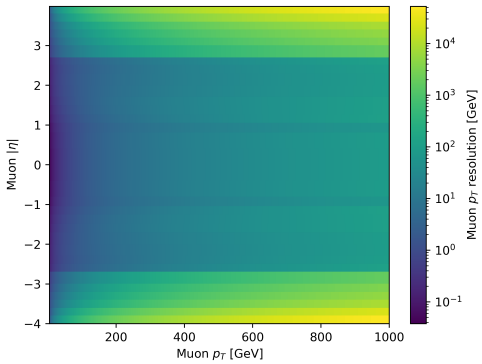

(d) Muon p_T resolution (MeV).

Figure A.2: Muon ID efficiencies and p_T resolution for the prospects study presented in Chapter 9. The

Jets

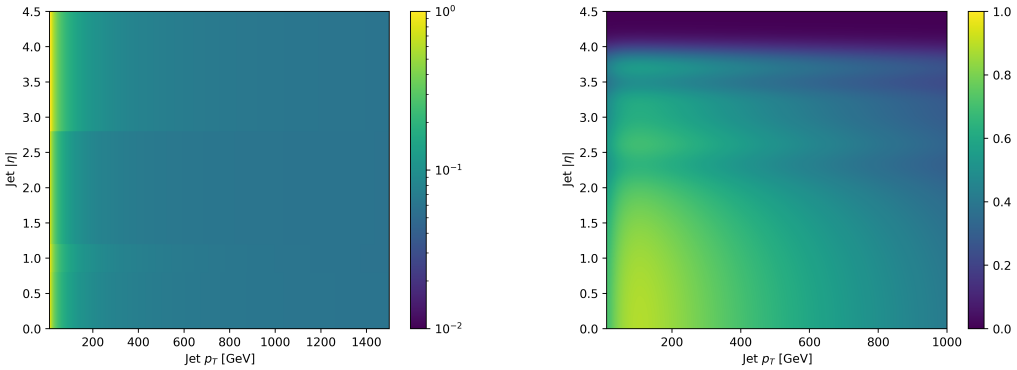

(a) (b)

Figure A.3: Parameterised relative jet energy resolution, shown in Figure A.3a, and parameterised b-tagging efficiency, shown in Figure A.3b, used in the HL-LHC detector simulation.

$E_{\mathrm{T}}^{\mathbf{miss}}$

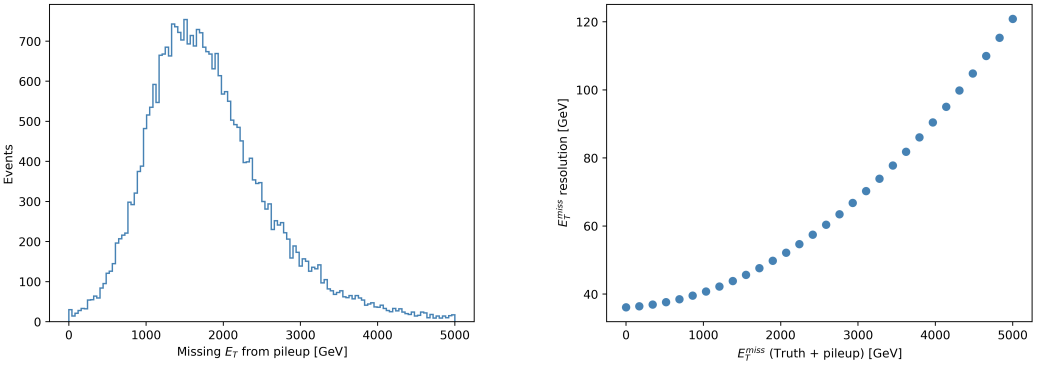

(a) (b)

Figure A.4: Parameterised $E_{\mathrm{T}}^{\mathrm{miss}}$ distribution from pileup, shown in Figure A.4a, and parameterised $E_{\mathrm{T}}^{\mathrm{miss}}$ resolution, shown in Figure A.4b, used in the HL-LHC detector simulation.

A.2 Cut & count studies

A reoptimisation of the signal regions defined in Table 6.2 was performed to compare the potential sensitivity of the conventional analysis to the multivariate analysis described in Chapter 9. During the reoptimisation, the selections on the m_{bb} and m_{CT} variables are unchanged from Table 6.2. A scan over the lower bound of the m_T and E_T^{miss} variables was performed in steps of 10 GeV, with no upper bound. The lack of an upper bound on these variables means the regions are able to overlap, and therefore lose their orthogonality. However, as the final fit result takes the best expected sensitivity for each point, the orthogonality of signal regions is not required. The cuts maximising the binomial significance, Z_n, for the benchmark signal points shown in Table 9.4 are chosen for the three signal regions. These cuts are summarised in Table A.1. The sensitivity to each signal

	SRLM	SRMM	SRHM
m_{bb}	$\in [105, 135]$		
m_{CT}	> 160		
$E_{\mathrm{T}}^{\mathrm{miss}}$	> 320	> 380	> 420
m_{T}	> 180	> 280	> 280

Table A.1: Reoptimised signal region selections for conventional analysis in order to compare sensitivity with the multivariate analysis described in Chapter 9. All cuts are in units of GeV.

point is assessed by calculating the binomial significance, Z_n, for each signal point in all three signal regions, and the combination of the regions takes the best expected significance for each point. The expected sensitivities can be seen in Figure A.5.

A.3 Deep learning studies

In addition to the the reoptimisation of the signal regions, described in the previous section, a study of the expected sensitivity using a DNN as a binary classifier was undertaken. A diagram of the DNN used in this study is shown in Figure A.6, and the model itself is implemented using Keras and Tensorflow. The inputs to the classifier are the same as described in Chapter 9for the BDT analysis, and the same procedure for separating the signal samples into three sets targetting different mass-splitting regimes is also the same. The DNN is trained on a GPU for a maximum of 10000 epochs, or until the accuracy of the classifier, evaluated using test data, has not improved in 2 epochs. To avoid overtraining, a dropout of 20% is used, such that upto 20% of the inputs to each layer can be ignored, at random, in each training epoch. Similarly to the BDT analysis described in Chapter 9, 3 classifiers are trained, one per mass-splitting region. The signal-background discrimination can be seen in Figure A.7.

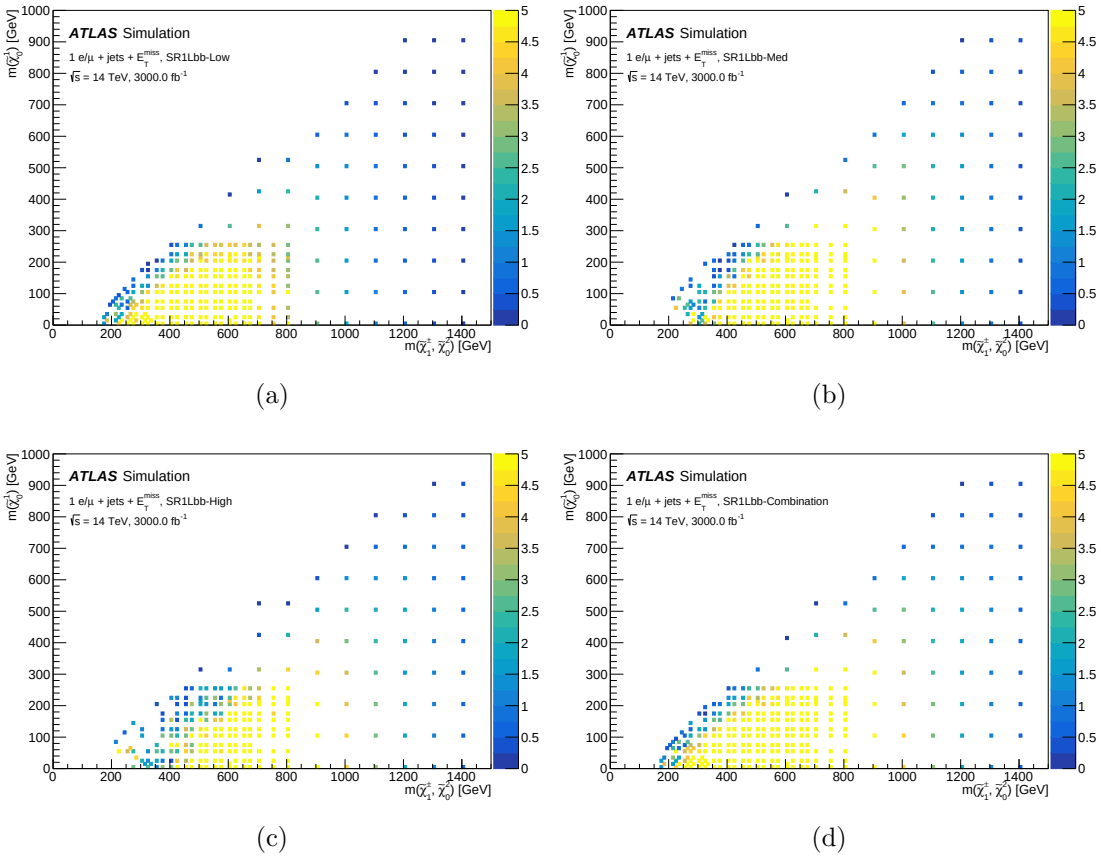

Figure A.5: Plots showing the binomial significance, Z_n, of each signal point in the reoptimised SRLM (A.5a), SRMM (A.5b), SRHM (A.5c), and the best expected combination (A.5d). All plots are produced assuming a total 15% background uncertainty.

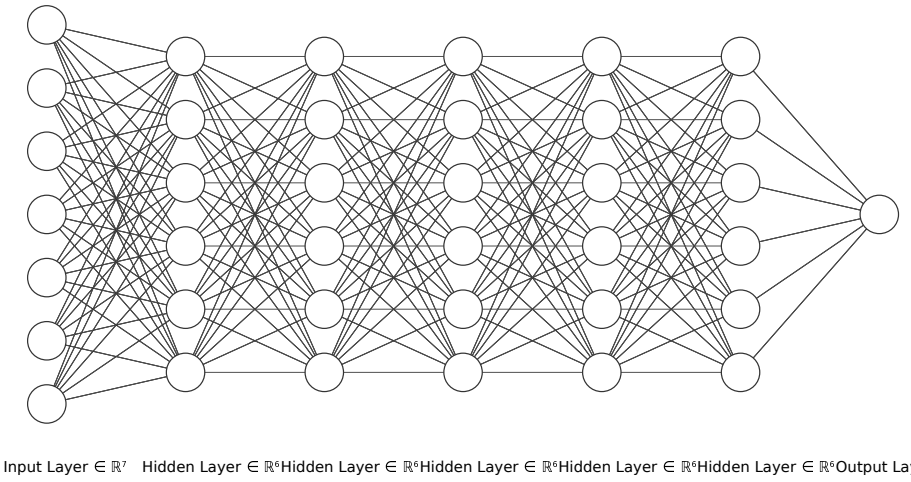

Figure A.6: A diagram showing the structure of the fully-connected Deep Neural Network tested as a binary classifier in the HL-LHC sensitivity study.

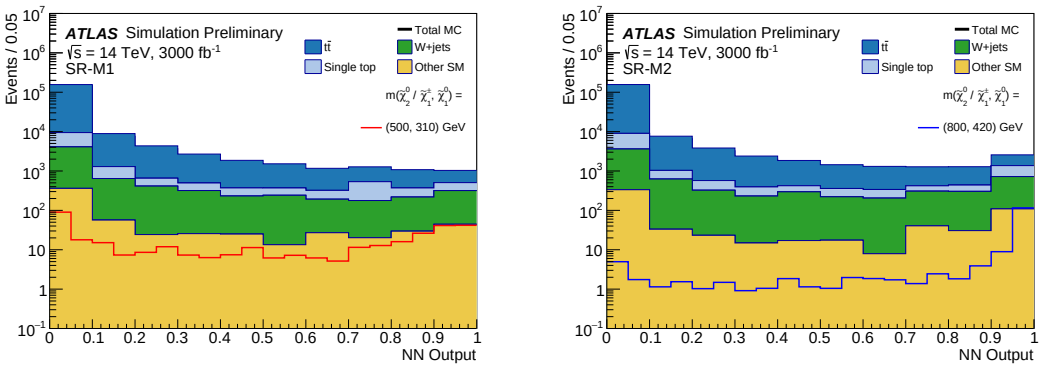

(a)

(b)

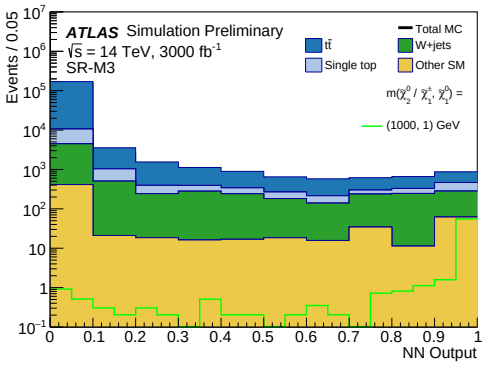

(c)

Figure A.7: Outputs for each of the DNN classifiers trained on the signal ensemble of each region and the dominant $t\bar{t}$ background.

The shape and range of the output of the DNN classifiers is due to the use of the sigmoid/softmax activiation on the output layer of the classifier, while TMVA performs a transformation of the form $y(x) = -\frac{1}{15}\left(\frac{1}{x} - 1\right)$ on the output of the classifier [73]. The DNN classifiers were not used in the final analysis as the sensitivity to the signal using a cut on the output of the DNN classifiers is much lower than for the BDT classifiers. While these studies were not performed due to time and resource constraints, it is expected that with larger MC statistics for the signal samples, fine-tuning of the DNN hyperparameters, and performing multi-class classification instead of binary classification, the DNN could achieve superior classification performance over the BDT classifiers.

A.4 Extending W+jets sample statistics

After applying all selections listed in Table 9.3 and the cuts on the BDT output listed in Table 9.4, the MC statistics in the W+jets sample was extremely low, such that the MC statistical uncertainty was $\sim 100\%$. For the final statistical analysis, a procedure was developed for extending the W+jets sample statistics in order to predict realistic yields and uncertainties. Using the detector simulation method described in Chapter 9, individual events in the nominal W+jets samples were smeared $N = 10$ times, to produce an extended sample with $\leq N$ times the input sample statistics. Due to the significant computing time of running this procedure, only B-filtered slices of the W+jets MC with $W \to e\nu/\mu\nu$ were used as the input for this procedure. A plot comparing the shape of the E_T^{miss} distribution for the nominal B-filtered samples with electrons, muons and taus and extended samples for B-filtered samples with electrons and muons is shown in Figure A.8.

The normalisation of the extended sample is corrected for the multiple smearing method by weighting each event by a factor $\frac{1}{N}$, and corrected for the missing $W \to \ell\nu$ slices by multiplying the expected yield of the extended sample by $N_{MC}^{nominal}/N_{MC}^{extended}$ evaluated at preselection level. The correction factor for the missing MC slices was found to be 1.21.

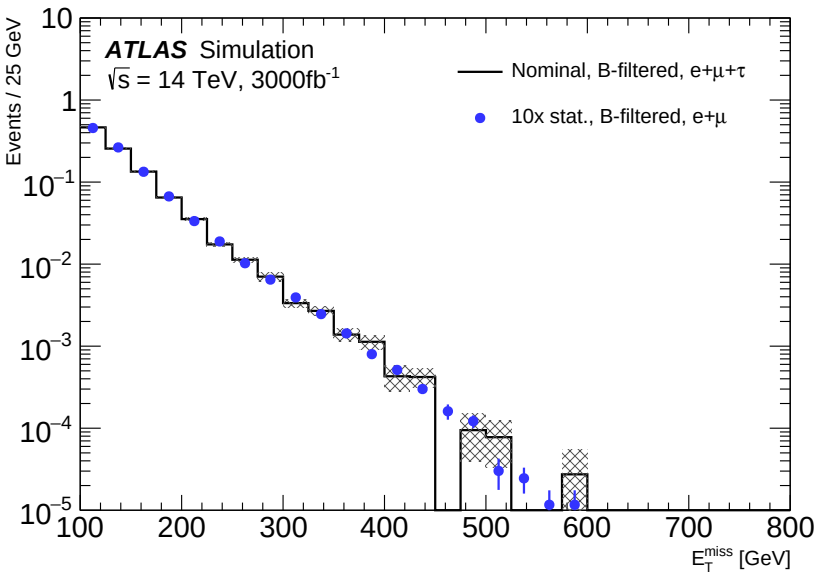

Figure A.8: A comparison of the E_T^{miss} distributions at preselection level for the nominal W+jets sample and the sample with extended MC statistics from the multiple event smearing method described in this section.

Bibliography

[1] ATLAS Collaboration. Search for chargino and neutralino production in final states with a Higgs boson and missing transverse momentum at $\sqrt{s} = 13$ TeV with the ATLAS detector. *Phys. Rev. D*, 100:012006, 2019.

[2] ATLAS Collaboration. Search for direct production of electroweakinos in final states with one lepton, missing transverse momentum and a Higgs boson decaying into two b-jets in pp collisions at $\sqrt{s} = 13$ TeV with the ATLAS detector. *Eur. Phys. J. C*, 80(8):691, 2020.

[3] ATLAS Collaboration. Search for dark matter associated production with a single top quark in $\sqrt{s} = 13$ TeV (pp) collisions with the ATLAS detector. Technical Report ATLAS-CONF-2020-034, 2020.

[4] X. C. Vidal et al. *Report from Working Group 3: Beyond the Standard Model physics at the HL-LHC and HE-LHC*, volume 7, pages 585–865. 2019.

[5] ATLAS Collaboration. Observation of a new particle in the search for the Standard Model Higgs boson with the ATLAS detector at the LHC. *Physics Letters B*, 716(1):1–29, 2012.

[6] CMS Collaboration. Observation of a new boson at a mass of 125 GeV with the CMS experiment at the LHC. *Physics Letters B*, 716(1):30–61, 2012.

[7] Super-Kamiokande Collaboration. Evidence for Oscillation of Atmospheric Neutrinos. *Physical Review Letters*, 81(8):1562–1567, 1998.

[8] X. Qian and P. Vogel. Neutrino mass hierarchy. *Progress in Particle and Nuclear Physics*, 83:1–30, 2015.

[9] LHCb Collaboration. Observation of the Resonant Character of the $Z(4430)^-$ State. *Phys. Rev. Lett.*, 112:222002, 2014.

[10] LHCb collaboration. Observation of structure in the J/ψ-pair mass spectrum. *Sci. Bull.*, (arXiv:2006.16957. LHCB-PAPER-2020-011), 2020.

[11] LHCb Collaboration. Observation of $J/\psi p$ Resonances Consistent with Pentaquark States in $\Lambda_b^0 \to J/\psi K^- p$ Decays. *Phys. Rev. Lett.*, 115:072001, 2015.

[12] LHCb Collaboration. Observation of a narrow pentaquark state, $P_c(4312)^+$, and of two-peak structure of the $P_c(4450)^+$. *Phys. Rev. Lett.*, 122(22):222001, 2019.

[13] M. Tanabashi et al. Review of Particle Physics. *Phys. Rev.*, D98(3):030001, 2018.

[14] M. Robinson et al. A Simple Introduction to Particle Physics. 2008.

[15] W. M. McClain. *Axioms of group theory*, pages 55–58. Springer New York, 2008.

[16] UA1 Collaboration. Experimental observation of isolated large transverse energy electrons with associated missing energy at s=540 GeV. *Physics Letters B*, 122(1):103 – 116, 1983.

[17] UA2 Collaboration. Observation of single isolated electrons of high transverse momentum in events with missing transverse energy at the CERN pp collider. *Physics Letters B*, 122(5):476 – 485, 1983.

[18] UA1 Collaboration. Experimental Observation of Lepton Pairs of Invariant Mass Around 95-GeV/c^2 at the CERN SPS Collider. *Phys. Lett. B*, 126:398–410, 1983.

[19] UA2 Collaboration. Evidence for $Z^0 \to e^+e^-$ at the CERN $\bar{p}p$ Collider. *Phys. Lett.*, 129B:130–140, 1983.

[20] D. de Florian et al. Handbook of LHC Higgs Cross Sections: 4. Deciphering the Nature of the Higgs Sector. 2016.

[21] V. Agrawal et al. Viable range of the mass scale of the standard model. *Physical Review D*, 57(9):5480–5492, 1998.

[22] P. Fisher et al. Neutrino mass and oscillation. *Annual Review of Nuclear and Particle Science*, 49(1):481–527, 1999.

[23] A. D. Sakharov. Violation of CP Invariance, C Asymmetry, and Baryon Asymmetry of the Universe. *Soviet Journal of Experimental and Theoretical Physics Letters*, 5:24, 1967.

[24] S. P. Martin. A Supersymmetry Primer. *Advanced Series on Directions in High Energy Physics*, page 1–98, 1998.

[25] M. Papucci et al. Natural SUSY endures. *Journal of High Energy Physics*, 2012(9), 2012.

[26] J. Abdallah et al. Simplified models for dark matter searches at the LHC. *Physics of the Dark Universe*, 9-10:8–23, 2015.

[27] ATLAS Collaboration. Constraints on mediator-based dark matter and scalar dark energy models using $\sqrt{s} = 13$ TeV pp collision data collected by the ATLAS detector. *Journal of High Energy Physics*, 2019(5), 2019.

[28] F. Kahlhoefer et al. Implications of unitarity and gauge invariance for simplified dark matter models. *Journal of High Energy Physics*, 2016(2), 2016.

[29] T. Abe et al. LHC Dark Matter Working Group: Next-generation spin-0 dark matter models. *Phys. Dark Univ.*, 27:100351, 2020.

[30] G.C. Branco et al. Theory and phenomenology of two-Higgs-doublet models. *Physics Reports*, 516(1-2):1–102, 2012.

[31] E. Mobs. The CERN accelerator complex - 2019. Complexe des accélérateurs du CERN - 2019. (CERN-GRAPHICS-2019-002), Jul 2019.

[32] W. Herr and B. Muratori. Concept of luminosity. *Proceedings of the CERN Accelerator School*, 2003.

[33] ATLAS Collaboration. Pileup Interactions and Data Taking Efficiency. `https://twiki.cern.ch/twiki/bin/view/AtlasPublic/LuminosityPublicResultsRun2`.

[34] A. Airapetian et al. *ATLAS: Detector and physics performance technical design report. Volume 1.* 1999.

[35] ATLAS Collaboration. The ATLAS Experiment at the CERN Large Hadron Collider. *JINST*, 3:S08003, 2008.

[36] M. Capeans et al. ATLAS Insertable B-Layer Technical Design Report. Technical Report CERN-LHCC-2010-013. ATLAS-TDR-19, 2010.

[37] ATLAS Collaboration. Standard Model Summary Plots Spring 2020. (ATL-PHYS-PUB-2020-010), 2020.

[38] G. Avoni et. al. The new LUCID-2 detector for luminosity measurement and monitoring in ATLAS. *JINST*, 13(07):P07017. 33 p, 2018.

[39] R. D. Ball et al. Parton distributions for the LHC run II. *Journal of High Energy Physics*, 2015(4), 2015.

[40] B. Andersson et al. A model for low-pT hadronic reactions with generalizations to hadron-nucleus and nucleus-nucleus collisions. *Nuclear Physics B*, 281(1):289 – 309, 1987.

[41] J. Winter et al. A modified cluster-hadronisation model. *The European Physical Journal C*, 36(3):381–395, 2004.

[42] ATLAS Collaboration. ATLAS Pythia 8 tunes to 7 TeV datas. (ATL-PHYS-PUB-2014-021), 2014.

[43] ATLAS Collaboration. The Pythia 8 A3 tune description of ATLAS minimum bias and inelastic measurements incorporating the Donnachie-Landshoff diffractive model. (ATL-PHYS-PUB-2016-017), 2016.

[44] S. Frixione et al. A positive-weight next-to-leading-order Monte Carlo for heavy flavour hadroproduction. *JHEP*, 09:126, 2007.

[45] P. Nason. A new method for combining NLO QCD with shower Monte Carlo algorithms. *JHEP*, 11:040, 2004.

[46] S. Frixione et al. Matching NLO QCD computations with parton shower simulations: the POWHEG method. *JHEP*, 11:070, 2007.

[47] S. Alioli et al. A general framework for implementing NLO calculations in shower Monte Carlo programs: the POWHEG BOX. *JHEP*, 06:043, 2010.

[48] ATLAS Collaboration. Further studies on simulation of top-quark production for the ATLAS experiment at $\sqrt{s} = 13$ TeV. Technical Report ATL-PHYS-PUB-2016-016, 2016.

[49] E. Re. Single-top Wt-channel production matched with parton showers using the POWHEG method. *Eur. Phys. J. C*, 71:1547, 2011.

[50] T. Gleisberg et al. Event generation with SHERPA 1.1. *JHEP*, 02:007, 2009.

[51] T. Gleisberg and S. Höche. Comix, a new matrix element generator. *JHEP*, 12:039, 2008.

[52] F. Cascioli et al. Scattering Amplitudes with Open Loops. *Phys. Rev. Lett.*, 108:111601, 2012.

[53] S. Schumann and F. Krauss. A parton shower algorithm based on Catani–Seymour dipole factorisation. *JHEP*, 03:038, 2008.

[54] S. Höche et al. QCD matrix elements + parton showers. The NLO case. *JHEP*, 04:027, 2013.

[55] R. D. Ball et al. Parton distributions with LHC data. *Nucl. Phys. B*, 867:244, 2013.

[56] S. Frixione et al. Single-top hadroproduction in association with a W boson. *Journal of High Energy Physics*, 2008(07):029–029, 2008.

[57] J. Pequenao and P. Schaffner. How ATLAS detects particles: diagram of particle paths in the detector. 2013.

[58] ATLAS Collaboration. Electron reconstruction and identification in the ATLAS experiment using the 2015 and 2016 LHC proton–proton collision data at $\sqrt{s} = 13$ TeV. *The European Physical Journal C*, 79(8), 2019.

[59] ATLAS Collaboration. Measurement of the photon identification efficiencies with the ATLAS detector using LHC Run 2 data collected in 2015 and 2016. *The European Physical Journal C*, 79(3), 2019.

[60] ATLAS Collaboration. Muon reconstruction performance of the ATLAS detector in proton–proton collision data at $\sqrt{s}$ s =13 TeV. *The European Physical Journal C*, 76(5), 2016.

[61] ATLAS Collaboration. Reconstruction of hadronic decay products of tau leptons with the ATLAS experiment. *The European Physical Journal C*, 76(5), 2016.

[62] ATLAS Collaboration. Topological cell clustering in the ATLAS calorimeters and its performance in LHC Run 1. *The European Physical Journal C*, 77(7), 2017.

[63] M. Livan and R. Wigmans. Misconceptions about Calorimetry. *Instruments*, 1(1):3, 2017.

[64] ATLAS Collaboration. Performance of pile-up mitigation techniques for jets in *pp* collisions at $\sqrt{s} = 8$ TeV using the ATLAS detector. *Eur. Phys. J. C*, 76(11):581, 2016.

[65] ATLAS Collaboration. ATLAS b-jet identification performance and efficiency measurement with $t\bar{t}$ events in pp collisions at $\sqrt{s} = 13$ TeV. *Eur. Phys. J. C*, 79(11):970, 2019.

[66] ATLAS Collaboration. Search for top-squark pair production in final states with one lepton, jets, and missing transverse momentum using 36 fb^{-1} of $\sqrt{s} = 13$ TeV pp collision data with the ATLAS detector. *Journal of High Energy Physics*, 2018(6), 2018.

[67] D. R. Tovey. On measuring the masses of pair-produced semi-invisibly decaying particles at hadron colliders. *Journal of High Energy Physics*, 2008(04):034–034, 2008.

[68] G. Polesello and D. R. Tovey. Supersymmetric particle mass measurement with the boost-corrected contransverse mass. *Journal of High Energy Physics*, 2010(3), 2010.

[69] C.G Lester and D.J Summers. Measuring masses of semi-invisibly decaying particle pairs produced at hadron colliders. *Physics Letters B*, 463(1):99–103, 1999.

[70] P. Konar et al. Dark matter particle spectroscopy at the LHC: generalizing MT2 to asymmetric event topologies. *Journal of High Energy Physics*, 2010(4), 2010.

[71] C. Lester and B. Nachman. Bisection-based asymmetric M T2 computation: a higher precision calculator than existing symmetric methods. *Journal of High Energy Physics*, 2015(3), 2015.

[72] W. Buttinger and M. Lefebvre. Formulae for Estimating Significance. Technical Report ATL-COM-GEN-2018-026, 2018.

[73] A. Hoecker et al. TMVA - Toolkit for Multivariate Data Analysis, 2007.

[74] H. Drucker and C. Cortes. Boosting Decision Trees. In *NIPS*, 1995.

[75] Y. Freund and R. E. Schapire. A Decision-Theoretic Generalization of On-Line Learning and an Application to Boosting. *J. Comput. Syst. Sci.*, 55(1):119–139, 1997.

[76] T. Chen and C. Guestrin. XGBoost. *Proceedings of the 22nd ACM SIGKDD International Conference on Knowledge Discovery and Data Mining*, 2016.

[77] S van der Meer. Calibration of the effective beam height in the ISR. Technical Report CERN-ISR-PO-68-31. ISR-PO-68-31, 1968.

[78] ATLAS Collaboration. Luminosity determination in pp collisions at $\sqrt{s}$ s = 8 TeV using the ATLAS detector at the LHC. *The European Physical Journal C*, 76(12), 2016.

[79] ATLAS Collaboration. Determination of jet calibration and energy resolution in proton-proton collisions at $\sqrt{s} = 8$ TeV using the ATLAS detector. Technical Report arXiv:1910.04482, 2019.

[80] ATLAS Collaboration. A method for the construction of strongly reduced representations of ATLAS experimental uncertainties and the application thereof to the jet energy scale. Technical Report ATL-PHYS-PUB-2015-014, 2015.

[81] ATLAS Collaboration. Jet energy resolution in proton-proton collisions at $\sqrt{\text{s}}$ = 7 TeV recorded in 2010 with the ATLAS detector. *The European Physical Journal C*, 73(3), 2013.

[82] ATLAS Collaboration. Performance of missing transverse momentum reconstruction with the ATLAS detector using proton–proton collisions at $\sqrt{s} = 13$ TeV. *The European Physical Journal C*, 78(11), 2018.

[83] J. Butterworth et al. PDF4LHC recommendations for LHC Run II. *Journal of Physics G: Nuclear and Particle Physics*, 43(2):023001, 2016.

[84] M. Baak et al. HistFitter software framework for statistical data analysis. *The European Physical Journal C*, 75(4), 2015.

[85] A L Read. Presentation of search results: theCLstechnique. *Journal of Physics G: Nuclear and Particle Physics*, 28(10):2693–2704, 2002.

[86] ATLAS Collaboration. Search for direct pair production of a chargino and a neutralino decaying to the 125 GeV Higgs boson in $\sqrt{s} = 8$ TeV pp collisions with the ATLAS detector. *Eur. Phys. J. C*, 75(5):208, 2015.

[87] ATLAS Collaboration. Search for chargino-neutralino production using recursive jigsaw reconstruction in final states with two or three charged leptons in proton-proton collisions at $\sqrt{s} = 13$ TeV with the ATLAS detector. *Phys. Rev. D*, 98(9):092012, 2018.

[88] ATLAS Collaboration. Search for chargino-neutralino production with mass splittings near the electroweak scale in three-lepton final states in $\sqrt{s} = 13$ TeV pp collisions with the ATLAS detector. *Physical Review D*, 101, 2020.

[89] P. Pani and G. Polesello. Dark matter production in association with a single top-quark at the LHC in a two-Higgs-doublet model with a pseudoscalar mediator. *Physics of the Dark Universe*, 21:8–15, 2018.

[90] A. Alloul et al. Feynrules 2.0 — a complete toolbox for tree-level phenomenology. *Computer Physics Communications*, 185(8):2250–2300, 2014.

[91] ATLAS Collaboration. Constraints on mediator-based dark matter and scalar dark energy models using $\sqrt{s} = 13$ TeV pp collision data collected by the ATLAS detector. *Journal of High Energy Physics*, 2019(5), 2019.

[92] F. Halzen et al. Charge asymmetry of weak boson production at the LHC and the charm content of the proton. *Physical Review D*, 88(7), 2013.

[93] High Luminosity LHC Project. Project Schedule. `https://project-hl-lhc-industry.web.cern.ch/content/project-schedule`, 2020.

[94] T. Kawamoto et al. New Small Wheel Technical Design Report. Technical Report CERN-LHCC-2013-006. ATLAS-TDR-020, 2013.

[95] ATLAS Collaboration. Technical Design Report for the Phase-I Upgrade of the ATLAS TDAQ System. Technical Report CERN-LHCC-2013-018. ATLAS-TDR-023, 2013.

[96] ATLAS Collaboration. Technical Design Report for the ATLAS Inner Tracker Pixel Detector. Technical Report CERN-LHCC-2017-021. ATLAS-TDR-030, 2017.

[97] ATLAS Collaboration. Technical Design Report for the ATLAS Inner Tracker Strip Detector. Technical Report CERN-LHCC-2017-005. ATLAS-TDR-025, 2017.

[98] ATLAS Collaboration. Expected Tracking Performance of the ATLAS Inner Tracker at the HL-LHC. Technical Report ATL-PHYS-PUB-2019-014, 2019.

[99] R. Diener et al. The DESY II test beam facility. *Nuclear Instruments and Methods in Physics Research Section A: Accelerators, Spectrometers, Detectors and Associated Equipment*, 922:265–286, 2019.

[100] H. Jansen et al. Performance of the EUDET-type beam telescopes. *EPJ Techniques and Instrumentation*, 3(1), 2016.

[101] D. R. Rodriguez and E. Rossi. EUTelescope Guide for ATLAS ITk Strip: Reconstruction and Analysis, 2017.

[102] M. Garcia-Sciveres et al. The FE-I4 pixel readout integrated circuit. *Nuclear Instruments and Methods in Physics Research Section A: Accelerators, Spectrometers, Detectors and Associated Equipment*, 636(1, Supplement):S155 – S159, 2011.

[103] ATLAS Collaboration. Study of the double Higgs production channel $H(\rightarrow b\bar{b})H(\rightarrow \gamma\gamma)$ with the ATLAS experiment at the HL-LHC. Technical Report ATL-PHYS-PUB-2017-001, 2017.

[104] J. Chang et al. Probing the trilinear Higgs boson self-coupling at the high-luminosity LHC via multivariate analysis. *Phys. Rev. D*, 101(1):016004, 2020.

[105] M. Cepeda et al. *Report from Working Group 2: Higgs Physics at the HL-LHC and HE-LHC*, volume 7, pages 221–584. 2019.